Modelling of ponderomotive laser self-focusing in a plasma with a hydrodynamic code in the context of direct-drive inertial confinement fusion

Alessandro Ruocco

université de BORDEAUX

Thesis

SUBMITTED IN PARTIAL FULFILLMENT OF THE REQUIREMENTS
FOR THE DEGREE OF

Doctor of Philosophy in Plasma Physics

UNIVERSITÉ DE BORDEAUX, ÉCOLE DOCTORALE DES SCIENCES ET DE L'INGÉNIEUR
SECTION : ASTROPHYSIQUE, PLASMAS, NUCLÉAIRE

Modelling of Ponderomotive Laser Self-Focusing in a Plasma with a Hydrodynamics Code in the Context of Direct-Drive Inertial Confinement Fusion

by

Alessandro Ruocco

supervised by

Vladimir Tikhonchuk

Guillaume Duchateau

Defended on the 27th of May 2020 in Talence (France)

Board of examiners:

Riconda, C.	Professor, University of Sorbonne, LULI (France)	**Rewiever**
Scott, R.	Researcher, CLF, STFC RAL (UK)	**Rewiever**
Lalanne, P.	Research Director, LP2N, CNRS (France)	**Examiner**
Debayle, A.	Researcher, CEA (France)	**Examiner**
Hüller, S.	Research Director, CPHT, CNRS (France)	**Examiner**
Tarisien, M.	Professor, Univesity of Bordeaux, CENBG (France)	**Examiner**
Tikhonchuk, V.	Professor, Univesity of Bordeaux, CELIA (France)	**Advisor**
Duchateau, G.	Researcher, CELIA, CEA (France)	**Co-advisor**

Contents

Abstract

Ponderomotive laser self-focusing poses a threat to the success of the inertial confinement fusion (ICF) program given that it locally enhances the laser intensity. This intensity amplification has two detrimental effects: i) undermining the uniformity of the shock wave launched into the target, and ii) increasing the probability of exciting laser-plasma instabilities. Despite several optical techniques have been implemented to smooth ponderomotive effects, they still remain a concern in case of crossing beams or in spike pulse-plasma interaction as in shock ignition.

In order to ameliorate the interpretation of experimental campaigns by means of radiation-hydrodynamics simulations, the Paraxial Complex Geometrical Optics (PCGO) module has been implemented in the hydrodynamics code CHIC in two-dimensional planar geometry: such a method is an improved version of the standard Ray-Tracing technique. PCGO accounts for nonlinear laser-plasma interaction such as ponderomotive force and hot electrons generation and propagation, usually neglected in hydrodynamic simulations. This approach is also used for creating spatially modulated laser beams by superposing Gaussian PCGO beamlets in the far-field. Their intensity envelope generates the intensity fluctuations. Although this PCGO-based method has improved the accuracy of CHIC simulations, the superposition of PCGO beamlets produces larger and longer speckles than real ones, and their self-focusing may be overestimated.

In this thesis, we develop a method for describing and controlling the excessive ponderomotive self-focusing developing in PCGO speckles while performing CHIC simulations. This study has been conducted in stationary plasmas. First, we investigate self-focusing of a single Gaussian PCGO beamlet in a homogeneous nonabsorbing plasma by comparing its behavior to a Gaussian-shaped beam modeled with the paraxial electromagnetic code HARMONY. This comparison allows to define the domain of beam power where the PCGO approximation is valid. We found that within 4 times the critical power, PCGO correctly reproduces HARMONY results. Afterwards, we consider the self-focusing of a PCGO speckle created by superposition of several beamlets, referred to as a multi-beamlet speckle. This speckle stands for a reference for any PCGO speckle created in CHIC. The reduction of the speckle intensity enhancement is quantified as a function of the number of superposed beamlets and by considering two strategies for multi-beamlet speckle shaping: random and regular. The latter configuration demonstrates better performances in controlling and reducing ponderomotive effects for a number of beamlets equal to three: our results show that the critical power of a three-beamlet speckle is twice higher compared to the critical power of a Gaussian beam with same characteristics. This novel speckle configuration has been implemented in CHIC and employed to generate multi-speckle beams whose speckle intensity distribution obeys to an exponential law. We then studied the self-focusing of a spatially

modulated beam (multi-speckle beam) in a homogeneous nonabsorbing plasma and show that our configuration allows to properly treat ponderomotive effects for different laser intensities: this method describes the speckle intensity statistics modification induced by speckle self-focusing and inter-speckle interaction as observed in electromagnetic simulations. The last part of the thesis is devoted to establish a baseline towards modelling of laser self-focusing in real ICF conditions. For this purpose, our results are extended to absorbing plasmas with a linear density profile. Speckle self-focusing is investigated here for different plasma lengths, and the effect of laser absorption is discussed. It is demonstrated that the proposed method of creation of a multi-beamlet speckle pattern operates in the conditions relevant to the direct-drive ICF. It allows to control efficiently the speckle self-focusing and its effect on the speckle intensity distribution in plasma.

Résumé de la thèse

L'auto-focalisation laser due à la force pondéromotrice constitue un obstacle au succès du programme de fusion par confinement inertiel (FCI) étant donné qu'elle augmente localement l'intensité laser. Cette amplification d'intensité a deux effets néfastes: i) diminuer l'uniformité de l'onde de choc lancée dans la cible, et ii) accroître la probabilité d'excitation des instabilités paramétriques. Bien que plusieurs techniques optiques aient été mises en œuvre pour atténuer les effets pondéromoteurs, ils restent une préoccupation en cas de croisement de faisceaux ou d'interaction avec une intensité laser élevée comme dans l'allumage par choc.

Afin d'améliorer l'interprétation des campagnes expérimentales au moyen de simulations hydrodynamiques, un module appelé Paraxial Complex Geometrical Optics (PCGO) a été implémenté dans le code hydrodynamique CHIC en géométrie plane bidimensionnelle : une telle méthode est une version améliorée de la technique standard du Ray-Tracing (RT). PCGO tient compte de l'interaction non linéaire laser-plasma telle que la force pondéromotrice et la génération et la propagation d'électrons chauds, généralement négligés dans les simulations hydrodynamiques. Cette approche est également utilisée pour créer des faisceaux laser spatialement modulés par superposition de faisceaux gaussiens PCGO : l'enveloppe d'intensité de ces faisceaux génère des fluctuations d'intensité (“ speckles ”) en champ lointain. Bien que cette méthode basée sur PCGO ait amélioré la précision des simulations CHIC, la superposition de faisceaux PCGO produit des speckles laser plus grands et plus longs que dans les expériences, et leur auto-focalisation peut être surestimée.

Dans cette thèse, nous développons une méthode pour décrire et contrôler l'auto-focalisation pondéromotrice des speckles dans un plasma stationnaire en utilisant CHIC dans le contexte de l'approche PCGO. Dans un premier temps, nous étudions l'auto-focalisation d'un faisceau PCGO gaussien dans un plasma homogène non absorbant en comparant son comportement à un faisceau de forme gaussienne modélisé avec le code HARMONY qui est basé sur une résolution paraxiale de l'équation d'Helmholtz. Cette comparaison permet de définir le domaine de la puissance du faisceau où l'approximation PCGO est valide. Nous montrons que jusqu'à 4 fois la puissance critique, PCGO reproduit correctement les résultats d'HARMONY. Ensuite, nous considérons l'auto-focalisation d'un speckle PCGO créé par superposition de plusieurs sous-faisceaux, appelé “ multi-beamlet speckle ”. Ce speckle représente une référence pour tout speckle PCGO créé dans CHIC. La réduction de l'augmentation de l'intensité du speckle est quantifiée en fonction du nombre de faisceaux superposés et en considérant deux stratégies pour la mise en forme du speckle à faisceaux multiples: aléatoire et régulière. Cette dernière configuration permet d'obtenir de meilleures performances pour contrôler et réduire les effets pondéromoteurs pour un nombre de faisceaux égal à trois: nos résultats montrent que la puissance critique d'un speckle à trois faisceaux est deux fois plus élevée que la puissance critique d'un faisceau gaussien de mêmes

caractéristiques. Cette nouvelle configuration de speckle a été implémentée dans CHIC et utilisée pour générer des faisceaux multi-speckle dont la distribution des intensités des speckles obéit à une loi exponentielle. Nous avons ensuite étudié l'auto-focalisation d'un faisceau modulé spatialement (faisceau multi-speckle) dans un plasma homogène non absorbant et montré que notre configuration de speckles permet de traiter correctement les effets pondéromoteurs pour différentes intensités laser: cette méthode décrit la modification des statistiques d'intensité de speckle induite par auto-focalisation du speckle et l'interaction entre speckles comme c'est observé dans des simulations électromagnétiques de référence. La dernière partie de la thèse est consacrée à établir une base pour la modélisation de l'autofocalisation laser dans des conditions FCI réelles. A cet effet, nos résultats sont étendus aux plasmas absorbants dont la densité présente un profile linéaire. L'auto-focalisation est étudiée ici pour différentes longueurs de plasma, et l'effet de l'absorption laser est discuté. Il est démontré que la méthode proposée pour la création d'une distribution de speckles aux faisceaux multiples fonctionne dans les conditions pertinentes pour la FCI an attaque directe. Elle permet de contrôler efficacement l'auto-focalisation du speckle et son effet sur la distribution de l'intensité des speckles dans le plasma.

Ringraziamenti

La tesi ha rappresentato per me un percorso di formazione e un momento di crescita fortemente caratterizzante e che mi ha segnato in positivo e in negativo su diversi aspetti della mia carriera e del mio carattere. Sicuramente, questo lavoro non sarebbe stato possibile senza l'aiuto e l'appoggio della miriade di persone che ho incontrato durante questo cammino. In quest'occasione, vorrei esprimere la mia gratitudine a ognuno di esse. Per primi, devo ringraziare i direttori del CELIA, Philippe Balcou e il suo successore Eric Mével, per avermi accolto al laboratorio e permesso di cominciare questo percorso. In particolare, non dimenticherò mai come Eric Mével si sia speso nell'ultima parte della mia tesi per permettermi di discutere nelle condizioni eccezionali causate dalla più grave pandemia che l'Europa abbia conosciuto dopo l'influenza spagnola del 1918-1920. Gli ultimi mesi turbolenti hanno segnato la vita di tutte le persone che conosco, e, in queste condizioni, concentrarsi sul terminare il proprio lavoro non è stato banale. Fortunatamente, a migliorare la situazione ha contribuito la sezione informatica del CELIA, Gaetan Corle e Richard Ferrere che mi hanno supportato tecnicamente quando avevo dei problemi informatici. Un grandissimo ringraziamento va ai miei supervisori, Vladimir Tikhonchuk e Guillaume Duchateau, per avermi inizialmente scelto e poi guidato con competenza e pazienza verso la fine di questo percorso tortuoso e per insegnato molto durante questi anni, e non solo scientificamente. Un grazie anche alla commissione di tesi, alla sua flessibilità e comprensione che mi ha permesso di addottorarmi in questo periodo un po' particolare: grazie a Caterina Riconda e Robbie Scott per aver accettato di correggere il mio manoscritto, a Stefan Hüller per aver concordato di presenziare la giuria, ma anche per i suoi preziosi consigli dispensati durante tutto il mio periodo di tesi, grazie ad Arnaud Debayle, Medhi Tarisien e Philippe Lalanne per i loro commenti espressi durante la discussione. Un grande ringraziamento va ad Arnaud Colaïtis, che ha saputo indirizzare ogni mia questione sul codice CHIC in maniera puntuale. Mi sento di esprimere un ringraziamento generale a tutti i ricercatori e professori del CELIA che mi hanno supportato scientificamente durante questi anni: Dimitri Batani, Philippe Nicolaï, Jean-Luc Feaugas, Jean-Luc deBois, Xavier Ribeyre, Edouard LeBel. Inoltre, ringrazio il gruppo di Rochester dove ho passato un paio di mesi durante il mio visiting: John Palastro, Valeri Goncharov, Andrei Maximov e Russ Follett.

Ma si sa, oltre al supporto tecnico e scientifico, si ha bisogno di uno svago, di un sostegno morale. Per questo devo ringraziare i miei colleghi/amici dottorandi e post-docs del CELIA. Con alcuni sono davvero cresciuto insieme, professionalmente e umanamente: grazie a Stéphane, mio 'camarade du bureau B7", con il quale ho imparato il francese e condiviso tanti dubbi, successi, frustrazioni e qualsiasi altra emozione si possa provare durante la tesi. Un grosso grazie a Gabri, che è stato per me un faro durante tutto il periodo del phd, e anche successivamente, per la sua amicizia e competenza in termini scientifici ma anche culinari. E come non

ringraziare il grande Pedro, per le sue disquisizioni linguistiche e le sue attenzioni mostrate nei miei confronti in ogni occasione che abbiamo condiviso. Queste tre persone hanno rappresentato e rappresenteranno per me il CELIA, siccome ho trascorso tutti i miei tre anni e mezzo in loro compagnia. Ma non ci sono stati solo loro, altre persone hanno segnato la mia vita in quel contesto: David, mio altro compagno di ufficio per ben due anni, i cui consigli mi hanno sempre sollevato nei momenti più bui, Alessandro T., per la sua simpatia e infinita disponibilità, Jonathan, il cui umorismo particolare mi ha sempre rallegrato, Julien, con cui discorrere è di una piacevolezza unica e la cui gentilezza colpisce in maniera profonda, Nicolas, Wendè, Nelson, Alain e Giedre, compagni di associazionismo, Erwan e Paul, amici di lab e di partite di calcio, Francesco, Edoardo, Lena, Guilhem, Dimitri, e, per finire, Donaldi, che non ha bisogno di altri aggettivi o descrizioni. Sono fortemente riconoscente poi al grande Fer, compañero madrileño rincontrato a Rochester e che ha alleggerito il freddo inverno nordamericano con la sua compagnia: mi mancano ancora infatti le nostre serate a suon di musica, di la Kapital e Lux!

A parte a ggente ro Celia, voglio ringraziare anche tutta la cricca internazionale formatasi a Bordeaux: il bel gruppone di italiani che mi ha supportato e con cui ho condiviso una marea di esperienze, a partire da Nadia e Giovanni, i pilastri "Ritals" di Bordeaux, e poi Gloria, Cristina, Silvia, Davide, Luigi, Sergio, Giuliana, Manuela, Edo, Marco, il gruppo di greci e greche simpaticissimi, quali Eva, Evy, Margarita e gli altri, Esma e Bertrand, i due finlandesi Mixu e Josuè, i canadesi Josh e Jenny.

Infine, è d'obbligo ringraziare chi da lontano mi ha sostenuto: la mia famiglia, tutta, e i miei amici napoletani, e in particolare Claudia, che ogni volta che li rivedo mi fanno sentire come se non avessi mai lasciato Napoli. Per ultimo, voglio ringraziare Sally, la compagna perfetta per me, che mi è stata vicino, supportato e sopportato durante tutto questo viaggio.

Remerciements

La thèse m'a marqué positivement et négativement sur différents aspects de ma carrière et de mon attitude. Ce travail n'aurait pas été possible sans l'aide et le soutien de nombreuses personnes que j'ai rencontrées au cours de ce parcours. A cette occasion, je voudrais exprimer ma gratitude à chacun d'eux. Tout d'abord, je dois remercier les directeurs du CELIA, Philippe Balcou et son successeur Eric Mével, de m'avoir accueilli au laboratoire et de m'avoir permis de commencer ce voyage. En particulier, je n'oublierai jamais comment Eric Mével s'est dépensé pendant la dernière partie de ma thèse pour me permettre de soutenir durant les moments difficiles de la pandémie. Pendant cette période, terminer le manuscrit n'était pas banal. Heureusement, la section informatique de CELIA, Gaetan Corle et Richard Ferrere ont beaucoup aidé non seulement récemment, mais depuis qu'ils ont commencé au CELIA. Un grand merci à mes encadrants, Vladimir Tikhonchuk et Guillaume Duchateau, de m'avoir choisi et de m'avoir ensuite guidé avec compétence et patience vers la fin de ce voyage tortueux. J'ai beaucoup appris sous leur direction, et pas seulement scientificament. Merci également au jury de thèse, pour sa flexibilité et sa compréhension, ce qui m'a permis d'obtenir ce doctorat même dans cette période particulière: merci à Caterina Riconda et Robbie Scott d'avoir accepté de réviser mon manuscrit, à Stefan Hüller pour pour ses précieux conseils tout au long de ma thèse, merci à Arnaud Debayle, Medhi Tarisien et

Philippe Lalanne pour leurs commentaires exprimés lors de la discussion. Un grand merci également à Arnaud Colaïtis, qui a su répondre à toutes mes questions sur le code CHIC de manière précise. Je voudrais remercier de manière générale tous les professeurs et chercheurs du CELIA qui m'ont soutenu scientifiquement durant ces années: Dimitri Batani, Philippe Nicolaï, Jean-Luc Feaugas, Jean-Luc deBois, Xavier Ribeyre, Edouard LeBel. Je remercie également l'équipe de Rochester où j'ai passé quelques mois pour mon visiting: John Palastro, Valeri Goncharov, Andrei Maximov et Russ Follett.

Mais en plus du soutien technique et scientifique, on avait besoin de soutien moral aussi. Pour cela, je dois remercier mes collègues/amis doctorants et post-doctorants du CELIA. Avec certains d'entre eux, j'ai vraiment grandi ensemble, professionnellement et humainement: grâce à Stéphane, mon "camarade du bureau B7", avec lequelle j'ai appris le français et partagé de nombreux doutes, succès, frustrations et toutes autres émotions que on peut ressentir pendant la thèse. Un grand merci à Gabri, qui a été un phare pour moi pendant toute la durée du doctorat, et aussi par la suite, pour son amitié et sa compétence scientifique mais aussi culinaire. Et comment ne pas remercier le grand Pedro, pour ses recherches linguistiques et sa gentillesse. Ces trois personnes représentaient et représenteront le CELIA pour moi, car j'ai passé tous mes trois ans et demi avec eux. Mais ce n'était pas seulement que eux, d'autres personnes ont marqué ma vie dans ce contexte: David, mon autre copain de bureau pendant deux ans, dont les conseils m'ont toujours remonté le moral dans les moments les plus sombres, Alessandro T., pour son affection et sympathie infini, Jonathan, dont humour particulier m'a toujours fait rire, Julien, une personne très sympa et dont gentillesse impressionne profondément, Nicolas, Wendè, Nelson, Alain et Giedre, mes camarades BOSCH, Erwan et Paul, amis de laboratoire et de football, Thibault, Victorien, Francesco, Edoardo, Lena, Guilhem, Dimitri et, enfin, Donaldi, qui n'a pas besoin d'autres adjectifs ou descriptions. Je suis également très reconnaissant envers Fer, mon ancien compagnon lors de mon Erasmus en Espagne que j'ai rencontré à Rochester et qui a réchauffé le froid hiver nord-américain: nos soirées musicales, la Kapital et Lux me manquent encore!

Outre le peuple du Celia, je tiens également à remercier tous les copains internationaux que j'ai rencontrés à Bordeaux: le sympathique groupe d'italiens qui m'ont soutenu et avec lesquelles j'ai partagé beaucoup d'expériences, à commencer par Nadia et Giovanni, les piliers " Ritals " de Bordeaux, puis Gloria, Cristina, Silvia, Davide, Luigi, Sergio, Giuliana, Manuela, Edo, Marco, le groupe de grecs, comme Eva, Evy, Margarita et les autres, Esma et Bertrand, les deux finlandais Mixu et Josuè, les canadiens Josh et Jenny.

Il faut remercier ceux qui m'ont soutenu d'Italie: ma famille, tous, et mes amis napolitains, et en particulier Claudia, qui chaque fois que je les vois me font sentir comme si je n'avais jamais quitté Naples. Enfin, je tiens à remercier Sally, la parfaite compagne pour moi, qui m'a soutenu et enduré tout au long de ce voyage français.

Acknowledgments

The thesis marked me positively and negatively on different aspects of my career and myself. Surely, this work would not have been possible without the help and support of lots of people I met during this path. On this occasion, I would like to express my gratitude to each of them. First of all, I must thank the directors of CELIA, Philippe Balcou and his successor Eric Mével, for welcoming me to the laboratory and allowing me to start

this journey. In particular, I appreciated how Eric Mével spent himself to allow me to hold my viva during the hard times of the covid pandemic. During this period, focusing on finishing what I started was not trivial. Fortunately, the IT section of CELIA, Gaetan Corle and Richard Ferrere helped a lot not only lately, but since they set foot at CELIA. I must acknowledge my supervisors, Vladimir Tikhonchuk and Guillaume Duchateau, for choosing me and then guided me with competence and patience towards the end of this tortuous journey. Thanks also to the thesis committee, for their flexibility and understanding, allowing me to get this PhD even in this particular period: thanks to Caterina Riconda and Robbie Scott for agreeing to revise my manuscript, to Stefan Hüller for his valuable advices throughout my thesis, thanks to Arnaud Debayle, Medhi Tarisien and Philippe Lalanne for their comments expressed during the discussion. Many thanks also to Arnaud Colaïtis, who has been able to address all my questions on the CHIC code in a precise manner. I would like to express a general thanks to all the CELIA professors who have scientifically supported me during these years: Dimitri Batani, Philippe Nicolaï, Jean-Luc Feaugas, Jean-Luc deBois, Xavier Ribeyre, Edouard LeBel. Also, I thank the Rochester team where I spent a couple of months for my visiting period: John Palastro, Valeri Goncharov, Andrei Maximov and Russ Follett.

But besides technical and scientific support, you need something else as weel, like moral support. For this I have to thank my colleagues/friends PhD students and post-docs of CELIA. With some of them I really grew up together, professionally and humanely: thanks to Stéphane, my 'camarade du bureau B7", with whom I learned French and shared many doubts, successes, frustrations and any other emotions you can feel during the thesis. A big thank to Gabri, who was a beacon for me during the whole period of the PhD, and also afterwards, for his friendship and competence in scientific but also culinary terms. And how not to thank the great Pedro, for his linguistic disquisitions and his affcections. These three people represented and will represent CELIA for me, as I spent all my three and a half years in their company. But it wasn't just them, other people have marked my life in that context: David, my other officemate for two years, whose advices have always cheered me up in the darkest moments, Alessandro T., for his fondness and infinite kindness, Jonathan, whose particular humor has always made me laugh me up, Julien, a very nice person to talk to and whose kindness deeply impresses, Nicolas, Wendè, Nelson, Alain and Giedre, my BOSCH fellows, Erwan and Paul, friends of lab and football mates, Thibault, Victorien, Francesco, Edoardo, Lena, Guilhem, Dimitri, and, finally, Donaldi, who needs no other adjectives or descriptions. I am also very grateful to Fer, my previous mate during my Erasmus in Spain whom I met again in Rochester and who made the cold North American winter warmer: I still miss our evenings with music, la Kapital and Lux!

Besides of the Celia people, I also want to thank all the international mates I have met Bordeaux: the nice group of Italians who supported me and with whom I shared a lot of experiences, starting from Nadia and Giovanni, the pillars of "Ritals" in Bordeaux, and then Gloria, Cristina, Silvia, Davide, Luigi, Sergio, Giuliana, Manuela, Edo, Marco, the group of very nice Greeks, such as Eva, Evy, Margarita and the others, Esma and Bertrand, the two Finns Mixu and Josuè, the Canadians Josh and Jenny.

Finally, it is a must to thank those who have supported me from Italy: my family, all of them, and my Neapolitan friends, who every time I see them make me feel as if I had never left Naples. Lastly, I want to thank Sally, the perfect companion for me, who has supported and endured throughout this French journey.

List of oral and poster presentations related to this work

In the following, there is the list of oral and poster presentations related to this thesis:

- July 2019 - 46^{th} **EPS Conference on Plasma Physics**, Milan (Italy). Oral presentation: "*Modeling of laser-plasma interaction in the shock ignition regime with LPSE: Comparison with particle in-cell simulations and experiments*".
- June 2019 - 49^{th} **Anomalous Absorption Conference**, Telluride (USA). Poster presentation: "*Modeling of laser-plasma interaction in the shock-ignition regime with LPSE: Comparison with particle-in-cell simulations and experiments*" (presented by Andrei Maximov, LLE (USA)).
- October 2018 - **First User Meeting LMJ-PETAL**, Le Barp (France). Poster presentation: "*Self-focusing of a laser beam into the plasma*".
- June 2018 - 9^{th} **Forum Intense Laser Plasma**, Ile d'Oleron (France). Oral presentation: "*2D self-focusing of a laser beam in a plasma: PCGO approach against paraxial*".
- March 2018 - 14^{th} **Direct-Drive and Fast-Ignition Workshop**, York (UK). Oral presentation: "*Self-focusing of a laser beam into the plasma*".
- February 2018 - 6^{th} **International Symposium on Optics and its Applications (OPTICS-2018)**, Trento (Italy). Oral presentation: "*Self focusing of laser beam into plasma*".
- July 2017 - **Summer School "Atoms and Plasmas in Super-Intense Laser Fields"**, Erice (Italy). Poster presentation: "*Self-focusing of a spatially and temporally modulated laser beam*".

List of publications in peer-reviewed journals related to this work

In the following, there is the list of publications in peer-reviewed journals related to this thesis:

- A. Ruocco, G. Duchateau, V. Tikhonchuk, and S. Hüller, "*Modeling of laser ponderomotive self-focusing in plasma within the paraxial complex geometrical optics approach*", Plasma Physics and Controlled Fusion Volume **61**, Number 11 (2019). doi: doi10.1088/1361-6587/ab467b

Introduction

Promise of a new energy source from nuclear fusion

The increasing of the world population and the negative impact of the conventional oil- and carbon-based energy sources on the environment push the research on finding new ways to produce energy. The major part of world power plants uses oil and coal as fuel, which poses several issues. On one hand, both oil and coal have limited supplies on Earth, and the growing of the world population makes them an insufficient resource for satisfying the whole energy needs on long time-scales. On the other hand, it is clear that the next generation of power plants should be more environmentally friendly in order to limit pollution and stop the global warming. Earth temperature increasing may lead to various negative scenarios not only for the mankind, but also for animals and plants: thinning of pole glaciers, expansion of the deserts and seasons perturbation are few of the inauspicious effects of global warming which threat all the living beings on Earth. Therefore the new forms of energy production must be oil- and carbon-free, provide as much electrical power as oil- and carbon-based power plants, and be built with the most up-to-date security technology in order to avoid power plant collapse due to potential catastrophes such as explosions, terrorist attacks, earthquakes, tsunami, etc.

From a scientific point of view, the characteristic of a power plant mostly depends on the fuel used. The energy sources can be divided in three macro-categories [1]:

- Fossil (gas, oil, carbon): sources in depletion and highly polluting;
- Renewable (solar, wind, bio-mass): sources which are naturally produced on human time-scale. They are the cleanest energy sources, but even the most optimistic previsions forecast that they will not be able to satisfy the entire world energy needs.
- Nuclear: fission and fusion. The former is very efficient, but it has many disadvantages, first of all the security and the treatment of radioactive waste. The latter represents a clean path to achieve energy production but still presents various scientific and technical issues [2].

Because of the continuous increase of the world population, we must develop the knowledge to make all the clean energy sources economically convenient and technologically efficient as much as possible. In fact, a single energy source would not suffice to satisfy the whole world energy needs. Nuclear fusion falls among the cleanest energy sources. Despite it was born and developed for military purposes [3], in the next we refer to nuclear fusion as conceived for civilian purposes, i.e. as energy source. In order to use fusion reactions for civilian needs, a reactor

should operate in a controlled environment at high temperatures, and we refer to nuclear fusion in the civilian context as *thermonuclear controlled fusion*. Many reasons support the development and the improvement of thermonuclear fusion-based power plants [4]:

- it is clean: the quantity of radioactive waste is minimal;
- the fusion fuel, constituted by Deuterium (D) and Tritium (T), is largely abundant in nature: Deuterium can be find in the seawater, while tritium is extracted through Lithium reactions;
- the fusion-based power plant is safer than fission-based power plant given that the fusion process is limited to a small amount of fuel and it can be stopped by switching off the mechanism which confines the environment where fusion occurs;
- it can produce a very high amount of energy with a small amount of fuel;
- it is easily replenished from seawater, which represents a very huge reservoir of deuterium.

In spite of these advantages and all the optimistic evaluations, the current technology does not allow to reach the desired energy gain from fusion reactions yet. In the following, we briefly describe nuclear fusion concepts and how they are related to energy production.

Nuclear fusion

Nuclear fusion consists of a reaction where two light nuclei inelastically interact and produce heavier nuclei with a positive energy yield, provided that they have enough energy to overcome the Coulomb repulsion [5]. In nuclear physics, a fusion reaction is characterized by its Q-value defined as:

$$Q = \left(\sum_r m_r - \sum_p m_p \right) c^2, \tag{1}$$

where the index r refers to reagents and p to products. The Q-value represents the energy released due to the mass change between reactors and products. The sign of Q indicates if the reaction is exothermic ($Q > 0$) or endothermic ($Q < 0$), respectively. In the first case, the reaction releases energy, in the second case it needs energy to occur. The Q-value can be expressed in terms of nucleons binding energy B

$$Q = \sum_p B_p - \sum_r B_r \tag{2}$$

where B is negative for all the isotopes. A *semi-empirical mass formula*, or *Weizsaecker formula* allows to express B in terms of empirical parameters [5].

Figure 1 shows the binding energy per nucleon as a function of the atomic mass A. The curve increases for light nuclei ($A < 56$), then slightly decreases for heavier nuclei. It follows from Eq. (2) that nuclear reactions are exothermic if lighter nuclei fuse to produce an heavier nucleus or when two heavy nuclei split in lighter fragments. The first case refers to nuclear fusion, the second case refers to nuclear fission. Fusing light nuclei is the source of stellar energy production: the star gravity confines the nuclei in the stellar interior. This

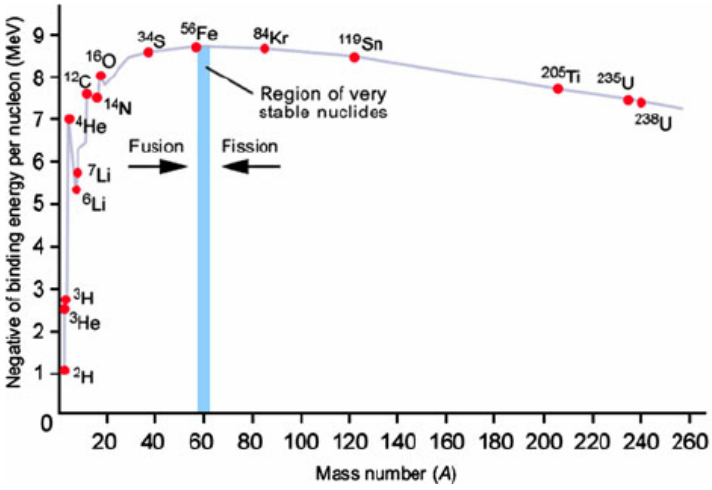

Figure 1: Binding energy per nucleon as a function of mass number. Exothermic reactions occur when two light nuclei ($A < 56$) fuse (nuclear fusion), or when a heavy nucleus ($A > 56$) breaks up in two lighter nuclides (nuclear fission). Reprinted from [6].

confinement creates very energetic, high temperature projectiles (the nuclei) such that the Coulomb barrier is overcome when they collide.

Besides the Q-value, other fusion parameters are:

- *cross section* σ: it stands for the probability to produce a fusion reaction when two nuclei collide. The cross section depends on the relative velocity of the particles. In case where we have two colliding beams of particles with a fixed relative velocity and denoted by the index 1 and 2 respectively, the probability that a particle in the beam 1 fuses with in a particle in beam 2 per unit length of interaction is $n_2\sigma$, where n_2 is the particle density of beam 2. The cross section unit is cm^2.

- *averaged reactivity* $\langle\sigma v\rangle$: the cross section σ accounts for two-particle interaction. When the number of interacting particles is large and the particles have a certain range of velocities, it is more convenient to define another quantity, called reactivity σv. The reactivity stands for the probability of reaction per unit of time and unit of density. Considering two beams of particles with a broad particle velocity range, the averaged reactivity reads

$$< \sigma v >= \int \sigma(v) v f(v) dv, \tag{3}$$

  where $f(v)$ stands for the distribution function of particles and depends on the relative velocity. The distribution function in the integral accounts for the fact that the particle of one beam can collide with a particle of the other beam within a large range of relative velocities.

- *reaction rate* $R_{1,2}$: it measures the number of reactions per unit of time and unit of volume occuring between the species i and j. It is defined as follows

$$R_{1,2} = \frac{n_1 n_2}{1 + \delta_{i,j}} < \sigma v > \tag{4}$$

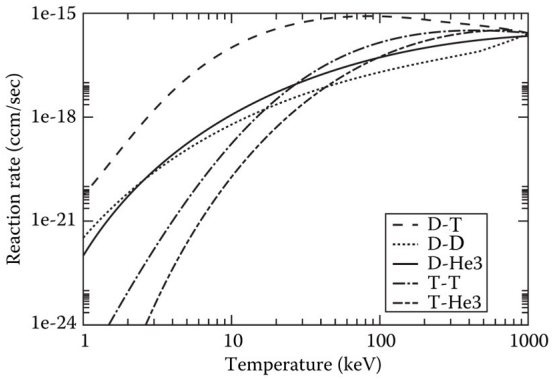

Figure 2: Reaction rate as a function of the temperature of the system for different fusion reactions. Here it is assumed that all the particles are in thermal equilibrium. Reprinted from [4].

where $i = 1$ and $j = 2$, $\delta_{i,j}$ is the Kronecker symbol which accounts for the symmetry of binary collisions: $\delta_{i,j} = 1$ if $i = j$, $\delta_{i,j} = 0$ otherwise.

Figure 2 displayes the fusion reaction rate as a function of the temperature of the system for different fusion reactions when all the particles are in thermal equilibrium. The Deuterium-Tritium reaction shows the highest reaction rate at the lowest temperatures ($T < 100$ keV), which makes the DT reaction the most suitable to harness thermonuclear fusion on Earth. Such a reaction has the following form

$$\mathrm{D}_1^2 + \mathrm{T}_1^3 \rightarrow \mathrm{He}_2^4 + \mathrm{n} \tag{5}$$

and it represents one of the most important reaction in thermonuclear fusion research. The energy released is $Q = 17.6$ MeV, and it is carried out by the neutrons and alpha-particles in form of kinetic energy.

Confinement of the fuel under extreme pressure and temperature is the only way to recreate the stellar interior on Earth and activate fusion reaction. From Fig. 2, it is clear that the system must reach temperatures above 10 keV in order to have a high reactivity. At such temperatures, the gas is completely ionized, becoming a plasma.

In the following, we describe how plasma can be created and confined on Earth, giving rise to thermonuclear controlled fusion. In particular, we describe one of the method used to plasma confinement: the inertial confinement fusion (ICF).

Inertial Confinement Fusion (ICF)

As previously seen, fusion reactions must occur in matter in plasma state. One of the most challenging issues dwells in confining such an ionized gas to densities and for times such that fusion reaction holds long enough to burn all the fusion fuel. Two main methods of plasma confinement have been pursued: a magnetic confinement

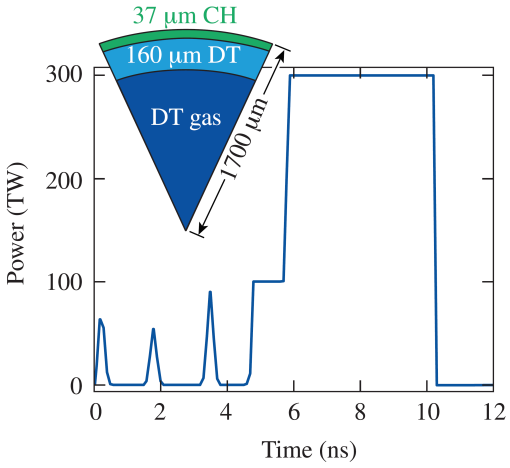

Figure 3: Example of a target and a laser pulse shape used in ICF direct-drive. Reprinted from [7].

(MCF) and an inertial confinement (ICF). In the next, we describe only the latter confinement technique given that this doctoral thesis is inspired by issues encountered in ICF.

In ICF [7–10], a capsule composed by a low-Z material called ablator covers the core of a DT fuel. The latter is turn divided in a cryogenic (solid) outer part and an inner DT gas. A high-power, nanosecond laser driver uniformly illuminates the target, in order to ablate the outer shell. The ablated material presents in form of plasma due to its high temperature. As a reaction to the ablation, the so-called rocket effect occurs: a shock wave propagates inward and implodes the capsule up to temperatures and densities necessary to ignite the fuel. Several configurations of ICF have been investigated. They can be divided in two main categories: *indirect-drive approach*, in which the target is placed inside a cylindrical metallic hohlraum and it is compressed by the x-rays produced by laser-hohlraum interaction, and *direct-drive approach*, where the lasers directly irradiate a spherical capsule. In the following sections, we describe in more details some characteristics of direct-drive ICF given that it represents the framework of this thesis.

ICF targets, laser pulse design and stages in ICF

The success of ICF program depends on the quality of beam-target coupling: higher energy gain requires to maximize absorption and minimize indesired instabilities that jeopardize all the fusion process. The target design has evolved from the dawn of ICF to nowadays in parallel to the progress of laser technology in order to conceive the most favorable beam-target scheme. At these days, the ICF target has a radius between 1.5-2.5 mm and presents two concentric layers [7]: a plastic (CH) layer of a thickness of 30-50 μm that serves as ablator and a cryogenic layer of DT ice with a thickness varying from 150 to 600 μm which covers the inner DT gas. The ablator and the cryogenic layer are referred to as target shell. The ablator interfaces with the laser, and its composition (CH plastic) aims to increase the rate of laser absorption and the ablation pressure. Figure 3 shows an example of an ICF target. The time-shape of the pulses currently used in the largest ICF facilities such as NIF [11] is schematically illustrated in the same picture: the laser pulse lasts around 10 ns, and three low-intensity, sharp pickets are launched before the main pulse in the first 4 ns. After 4 ns, the

laser intensity abruptly increases in two steps, and the power peak of 300 TW is reached at 6 ns, lasting until 10 ns. This constant part represents the main part of the laser pulse, responsible for the most laser-plasma interaction processes. This three-picket scheme allows to build the drive pressure needed for target compression in subsequent steps in order to avoid a steep rising of the shell entropy. The NIF laser operates at a wavelength of 0.35 μm, delivering an energy up to 2.1 MJ in this time interval. The peak laser intensity is above 10^{15} W/cm^2. Although this target and beam design predicts to achieve a 1-D gain of 48 [7], several processes may preclude the realization of such high gains in multi-dimensional geometry.

In the following, we briefly present the four stages of the laser-target interaction and the ICF process.

1. **Early stage and plasma corona formation**

   As soon as the laser pulse interacts with the capsule surface, a plasma is created by material ablation. Such a plasma moves outward and forms the target corona. Each one of the three pickets launches a shock wave traveling up to the inner part of the shell. At this stage, two regions can be identified: the interaction region and the transport region. In the first one, the laser interacts with the plasma corona. The laser propagates up to the critical surface, characterized by a certain value of the plasma density called *critical density*. The critical surface delimits the interaction region. Near this surface, laser energy is in part reflected and in part absorbed by inverse bremsstrahlung. About 10% of the absorbed laser energy is converted in x-ray radiation, whereas the main part is transferred to thermal electrons. Thanks to these electrons, the deposited laser energy is transported to the ablation surface, maintaining the target ablation. This process is called thermal transport characterized by the electron thermal conductivity. This last one stands for a coefficient which links the heat flux to the electron temperature gradient.

2. **Acceleration phase**

   The main part of the laser pulse is timed in such a way to launch a fourth shock wave that joins the previous shocks at the rear side of the shell and create a strong inwards propagating shock. This process initiates the compression of the internal fuel. The shock wave travels ahead of the ablation front. The efficiency of the compression depends on many factors: for instance, laser-plasma instabilities produced by nonlinear phenomena may degrade the compression efficiency. Plasma and laser conditions reached at this phase represent the environment of interest of this thesis. Among all the nonlinear processes, we concentrate on the ponderomotive laser self-focusing, which leads to a local intensity enhancement and filamentation instability. These nonlinear effects have a harmful consequence on the compression efficiency because: i) they break the laser uniformity by locally enhancing the laser intensity, and ii) they may support the excitation of three-wave instabilities, which may be a source of suprathermal electrons. These electrons enter the shell with an energy one-two orders of magnitude larger than the thermal electrons, thus they can penetrate the ablation front and preheat the fuel. Preheating the fuel is undesirable because it reduces its compressibility.

   Linear and nonlinear laser-plasma coupling are presented in Chapter 1. Non-linear ponderomotive force effects on laser-plasma dynamics are extensively treated in this thesis (see Chapters 2-3-4).

3. **Deceleration phase**

   When the shock wave arrives at the core, it bounces back and encounters the inward moving solid shell, causing its deceleration. In this way, the kinetic energy of the laser-accelerated shell is converted into internal energy. The fuel is then assembled: now it consists of a hot ($\sim 3-8$ keV), moderate density ($\sim 30-100$ g/cm^3) central hot spot surrounded by a colder ($\sim 200-400$ eV) but dense plasma layer ($\sim 300-1000$ g/cm^3). At this stage, fusion reactions take place.

4. **Ignition and burn phase**

   Fusion reaction takes place initially in the central hot spot. Ignition occurs if the energy gain in the hot spot overcomes the energy losses. The α-particles created in fusion reactions deposit their energy in the hot spot, supporting the reaction. Radiation, neutrons and electrons transport the energy outside the hot spot, cooling it. If the temperature of the hot spot increases, the fusion reactions propagate outside into the cold fuel. This process leads to the propagation of a burn wave, which is supposed to consume all the remaining fuel. About 80% of the fusion energy leaves the target in form of neutron kinetic energy. The α-particles and neutrons are absorbed by the reactor walls and their energy converted into thermal energy. Neutrons are used also to produce tritium in reactions with lithium placed in a blanket behind the chamber wall. Then the heat is used in turbines to generate electric energy. When all the capsule fuel is consumed, a new capsule would be introduced and irradiated by lasers, and the process restarts.

This procedure is repeated several times per second in order to produce the desired electric power and supply to the energy needed to maintain the power plant active (drivers, target fabrication and injection, debris removal).

Lawson's criterion and need for using high intensity lasers

In order to ignite the reactions in the hot spot, certain conditions must be attained: by definition, fuel ignites when the reaction self-sustains, which occurs when the energy released by the α-particles exceeds the loss due to the thermal transport outside the hot spot. The ignition conditions are expressed in terms of plasma density n and plasma confinement time τ: let us consider the plasma kinetic energy $E_K = 3nTV$, where T is plasma temperature in energy units, V is the hot spot volume and the factor three account for the three degrees of freedom that particles have. We also assume an equal number of deuterons and tritons, i.e. $n_D = n_T = n/2$. The energy produced during the plasma confinement time τ is $E_f = W_H \tau V$, where $W = n^2 < \sigma v > /4$ is the rate of fusion process. However, only the energy carried by alpha-particles has to be considered, which is $20\% E_f$. The remaining 80% carried by neutrons is lost because they leave the hot spot. In order to obtain an energy gain, we must have that $0.2E_f > E_K$, which rewritten in terms of $n\tau$ gives the Lawson's criterion:

$$n\tau > \frac{60T}{< \sigma v > Q_{DT}}. \tag{6}$$

For DT reactions, $Q_{DT} = 17.6$ MeV, and, with the temperature of the system in the range $T \sim 5-10$ keV in order to have a consistent fusion rate (see Fig. 2), the Lawson's criterion requires that:

$$n\tau \approx 10^{14} - 10^{15} \quad \text{s/cm}^3. \tag{7}$$

In ICF context, Eq. (7) is usually rewritten in terms of the hot spot areal density [8]:

$$\rho R_{hs} > 0.3 \quad \mathrm{g/cm^2}, \tag{8}$$

where ρ is the hot spot density, whereas R_{hs} is the hot spot radius. Once multiplied the areal density by the hot spot temperature, which is around 5 keV, one obtains the minimum pressure that needs to be attained in the hot spot to trigger the ignition, which is around 150 Gbar [7]. Since this pressure depends on the shell implosion velocity, one finds that the minimum implosion velocity v_{im} needed to generate a such hot-spot pressure is $v_{im} = 3 \times 10^7$ cm/s. On the other hand, hydrodynamic model of implosion [10] allows to relate the implosion velocity to laser and target parameters:

$$v_{im} = 1.63 \times 10^6 \alpha_{if}^{3/10} A_{if}^{1/2} \left(I_{15}/\lambda_{\mu m}\right)^{2/15} \mathrm{cm/s} \tag{9}$$

where α_{if} is the in-flight adiabat parameter, A_{if} is the in-flight aspect ratio, I_{15} is the laser intensity in PW/cm^2 units and $\lambda_{\mu m}$ is the laser wavelength in micron units. The adiabat α_{if} is defined as the ratio between the shell internal pressure and the pressure of a cold degenerate electron gas at the moment when the shell is accelerated to the velocity v_{im}. Such a parameter characterizes the fuel compressibility. The in-flight aspect ratio A_{if} is defined as the ratio of the capsule radius to the thickness at the same time. From theory and numerical simulations [10], one obtains typical values of A_{if} around 25-40, whereas α_{if} values lie in the range 1.5-4. Injecting those values of α_{if} and A_{if} into Eq. (9), we obtain that the laser intensity needed to create the correct implosion conditions ranges between 0.35 PW/cm^2 to 6 PW/cm^2 considering a laser wavelength $\lambda = 0.35$ μm. Despite this estimation is rather approximate, it gives an idea of the intensity range one must employ to accomplish ICF.

Alternative ICF schemes: shock ignition

Besides the conventional direct-drive scheme above presented, several other schemes have been developed in order to generate energy gains as high as possible: for example, magneto-inertial fusion [12] aims to improve the energy confinement by imposing an external magnetic field, or fast ignition [13], where the ignition is triggered by relativistic electrons generated by an ultraintense laser which is fired into a small gold cone imbedded the spherical fuel capsule. Among others, the shock ignition (SI) approach [14,15] promises ignition at a lower laser energy than conventional hot-spot schemes: in the first step, a 10-ns laser of intensities around 10^{14} W/cm^2 drives an implosion slower than in conventional direct-drive ICF, which reduces the occurrence of hydrodynamic instabilities. In the second step, a spike pulse of a few-hundred of picoseconds and of intensity above 5×10^{15} W/cm^2 launches a strong shock of hundreds of Mbar towards the target core. This shock wave must be strong enough to ignite the hot spot, and it is usually two, three times stronger than the shock wave launched by lasers in standard ICF approaches. Numerous studies have demonstrated very promising results [16–18]. One of the biggest concerns in SI is the generation of laser-plasma instabilities (LPIs) during the spike pulse-plasma interaction. These instabilities may have two main detrimental effects: i) scattering off of the laser light which weakens the strength and the symmetry of the shock wave, and ii) excitation of suprathermal electrons, which propagate towards the hot spot. These hot electrons might pose a serious preheat threat to the capsule or

rather contribute to increase the shock pressure, depending on their energy. The best scenario would involve hot electrons with a temperature in the range of 40-70 keV which depose their energy downstream the shock wave front, enhancing its strength [16, 19–21]. However, it is still not clear what are the best laser and target configurations for such electrons to deposit all their energy in that region. In this context, understanding the role of ponderomotive self-focusing may be crucial for the success of SI, even more relevant than in conventional ICF: it may decisively contribute to hot electrons creation. The level of its contribution is still under investigation.

Importance of modelling of ponderomotive self-focusing in radiation-hydrodynamics codes

As explained in the previous sections, high laser intensities are needed to compress the fuel to very high temperatures and densities in order to ignite the fusion reactions. At these intensities, laser-matter interaction has been widely studied in the literature, and several related phenomena have been identified [22]. Variation of dielectric proprieties of plasma due to laser electric field propagation constitutes one of the most notable process: under certain conditions, the refractive index of the plasma is modified and becomes laser intensity-dependent. Such a modification affects the laser propagation, and produces a self-consistent feedback on the whole laser-matter coupling. For instance, the medium refractive index may change such that to induce an enhancement of the laser intensity. In dielectrics, this effect is called *Optical Kerr effect* [23], whereas in plasmas it is referred to as *ponderomotive laser self-focusing* [24]. In this latter case, laser self-focusing occurs if the laser power (or intensity) overcomes a threshold value. In inertial confinement fusion conditions, laser intensities are above 10^{14} W/cm^2, and laser-induced ponderomotive force is expected to influence the laser propagation and the plasma dynamics: the beam ponderomotive pressure transversely pushes the plasma particles away from the beam axis, leading to a reduction of the laser traverse width because of the refractive index variation. The net effect is a local laser intensity enhancement, which i) reduces the uniformity of the shock wave launched into the target, and ii) enhances the probability of exciting laser-plasma instabilities, such as stimulated Raman scattering (SRS), two plasmon decay (TPD), stimulated Brillouin scattering (SBS). These instabilities may jeopardize the fuel ignition. It appears crucial to mitigate laser self-focusing in order for the ICF program to succeed. To do so, optical smoothing techniques have been introduced in laser facilities. One of them creates small-scale modulations of the laser intensity profile, known as speckle pattern. Spatial modulations in laser intensity are achieved by phase plates such as random phase plate (RPP) [25] or kinoform phase plates (KPP) [26], placed behind the focal lens: independently of the technique, the phase plate breaks the laser coherence, and small-scale spatial fluctuations in the far-field appears. Usually, the beam transverse profile is shaped as a flat-top with an average intensity imposed by the beam focal parameters. An exponential law characterize the probability distribution of the speckle intensity. According to such a statistics, a fraction of them carries an intensity several times higher than the average beam intensity. Instead, the smoothing by spectral dispersion (SSD) [27] introduces a temporal smoothing of the beam fluctuations by inducing a temporal variation of the speckles location on time-scales shorter than the hydrodynamic plasma response. Although all these techniques have improved the quality of laser-plasma coupling in the corona [7, 28], undesired nonlinear effects may still occur in the high-intensity

speckles, which represent the tail of the probability distribution: even though the average laser intensity is below the parametric instability threshold, the intensity of those speckle may overcome such thresholds. Furthermore, ponderomotive effects may be important when two or more beams cross each other because multi-beam-plasma interaction such as crossed beam energy transfer (CBET) [29–31] may occur: ponderomotive effects may induce an energy transfer between beams especially in flowing plasmas. Also, the spike laser-plasma coupling in the shock ignition context may be conditioned by ponderomotive self-focusing [32]. It is clear that any description of nonlinear laser-plasma coupling cannot exclude ponderomotive-related processes.

Nonlinear laser-plasma coupling involves different spatial- and time-scales. From a numerical point of view, these effects are studied with interaction codes, where propagation of a smoothed laser beam can be described within the paraxial [33–35] or nonparaxial [36] approximation. Despite their success in treating nonlinear laser-plasma coupling, these codes are limited to consider only the interaction between the laser and the target corona, neglecting other ICF processes such as target implosion and capsule ignition for instance. A full treatment of ICF demands macroscopic scales, multi-material laser-matter coupling, physics of the implosion, and other phenomena incompatible with the electromagnetic microscopic description due to computational costs and model limitations. Radiation-hydrodynamics codes instead accomplish those requirements because they operate at a macroscopic spatial-scale and at a long time-scale as needed for ICF. Thus, the majority of ICF physics can be included, and these codes represent the main numerical tool for describing the fusion process. Concerning the laser interaction with the corona, laser energy deposition is often modeled in a simplified way by using Ray-Tracing (RT) techniques [37]. Within the RT framework, the laser beams are represented by a bunch of infinitely thin rays, each of them carrying a fraction of the laser power and propagating in plasma according to Geometrical Optics (GO) laws. Despite the ray tracing is adopted in many hydrodynamics codes used in ICF research, it cannot straightforwardly account for i) laser speckle structure, ii) collisionless laser energy absorption and iii) nonlinear laser-plasma coupling processes, such as SRS, TPD and hot electrons generation and transport. The main challenge in improving hydrodynamics code efficiency is in-line evaluation of multi-scale effects along with an adequate implementation of laser smoothing techniques. In order to fulfill these goals, new modules have been implemented in the hydrocode CHIC [38]: they rely on the Paraxial Complex Geometrical Optics (PCGO) equations [39] and have been implemented in two-dimensional (2D) planar geometry [40]. The beamlets represent the basic elements of the PCGO description: they consist in rays with a defined Gaussian intensity profile, so they can be considered "thick" in contrast to the "thin" rays described within RT. This novel description has opened the possibilities for modelling of different laser-plasma coupling phenomena in CHIC, such as cross beam energy transfer, ponderomotive force and hot electrons generation and propagation [41]. Furthermore, it has allowed to develop methods to model of optical smoothing techniques in CHIC, as for instance the creation of spatially modulated beams. Laser intensity fluctuations are retrieved by randomly distributing the focal spots of the beamlets in the focal volume, where they propagate following their optical path. Combination of the beamlets allows to create a speckle pattern in the far-field, where a plasma (or a solid target) is placed. To be computationally efficient and compatible with the hydrodynamics spatial resolution, the PCGO model has to use a limited number of beamlets and speckles, at least an order of magnitude less than in reality. A typical

transverse size of a laser speckle is of a few microns, while the spatial resolution of hydrodynamic codes is about one order of magnitude larger than the laser wavelength. Thus, each PCGO speckle represents several real speckles in terms of dimension, and it is not clear how PCGO speckles behave under the influence of the ponderomotive force. The 2D planar geometry may introduce another shortcoming: scaling the real 3D speckle intensity profile (or 2D axisymmetric) to a 2D planar configuration with larger speckles overestimates the PCGO speckle power, while the intensity is preserved. Since the critical power in 3D and in 2D does not scale with the same factor, bigger PCGO speckles could be more prone to self-focus than real ones: analytic estimation gives that intensity enhancement in PCGO Gaussian speckles is twice higher than in smaller-scale real speckles of equivalent intensity. Consequently, ponderomotively-driven local intensity enhancement may be miscalculated in CHIC simulations, reducing the capability to interpret experimental results with CHIC. It is then necessary to develop a method which permits to assess the ponderomotively-induced intensity enhancement of a PCGO speckle to the same level as in real speckles.

Goals of this thesis

The goals of this thesis are i) to characterize the ponderomotive laser self-focusing in the radiation-hydrodynamics code CHIC within PCGO in two-dimensional planar geometry, ii) to find a method to reduce PCGO speckle ponderomotive intensity enhancement to a level compatible with the reality, and iii) to employ such a method in some relevant ICF situations. These objectives are achieved by studying ponderomotive self-focusing of different PCGO beams: a single Gaussian beam, referred to as a *beamlet*, a Gaussian speckle generated by superposing a few beamlets, called *multi-beamlet speckle*, and a *multi-speckle beam*, which stands for the PCGO version of spatially modulated beams.

First we have considered the self-focusing of a single beamlet. We have compared the beamlet self-focusing to simulations performed with the paraxial wave-based code HARMONY. We have found that PCGO model correctly describes the beamlet self-focusing in a homogeneous nonabsorbing plasma in the power regime explored and independently of the initial plasma density. In the same range of plasma density and beam power, we have then studied the self-focusing of a Gaussian speckle modelled as a multi-beamlet speckle. This speckle represents a prototype of any PCGO-generated speckles. Ponderomotively-induced intensity enhancement is decreased compared to the single beamlet case. This reduction can be quantified as a function of the number of superposed beamlets and by considering two strategies for multi-beamlet speckle shaping: random and deterministic. The latter configuration allows to better control the ponderomotive effects when three beamlets compose the speckle. The deterministic method has been used for creating a multi-speckle beam and we have then studied the self-focusing of such a beam in a homogeneous nonabsorbing plasma. We show that this method describes the speckle intensity statistics modification induced by speckle self-focusing and inter-speckle interaction as observed in electromagnetic simulations. At the end, all these results are extended to absorbing plasmas whose density exhibits a linear profile. Self-focusing of PCGO beams is investigated here for different plasma lengths, and the effect of laser absorption is discussed. This study demonstrated a validity of the multi-beamlet speckle approach and its efficiency for controlling the self-focusing.

Manuscript outline

This manuscript is organized as follows:

- **Chapter 1**: **State-of-the-art**:

  The first chapter provides guiding theoretical considerations on i) laser models, ii) plasma physics, iii) laser-plasma interaction and iv) the numerical tools employed to carry out this work: the electromagnetic code HARMONY and the radiation-hydrodynamics code CHIC. In this context, the Paraxial Complex Geometrical Optics theory and its implementation in CHIC are described. Illustration of laser ponderomotive effects constitutes a big part of the section concerning the laser-plasma interaction: a quantitative estimation of the error committed by approximating real speckles with larger PCGO speckles of same intensity is recovered.

- **Chapter 2**: **Self-focusing of a beamlet and a multi-beamlet speckle in homogeneous nonabsorbing plasmas**:

  This chapter addresses the issue of self-focusing of a beamlet and a multi-beamlet speckle in a homogeneous nonabsorbing plasma. First, we investigate self-focusing of a PCGO beamlet by comparing its behavior to a Gaussian-shaped beam modeled with the paraxial wave-based code HARMONY. This comparison provides a range of parameters where the PCGO approximation correctly describes the self-focusing of Gaussian beams. Then, we consider self-focusing of a PCGO multi-beamlet speckle, created by superposition of several beamlets. This speckle stands for a prototype for any PCGO speckle created in CHIC. The reduction of the speckle intensity enhancement is quantified as a function of the number of superposed beamlets and by considering two strategies for multi-beamlet speckle shaping: random and regular. We compare the two configurations in terms of controlling and reducing ponderomotive effects.

- **Chapter 3**: **Self-focusing of a spatially modulated beam within the PCGO framework in homogeneous nonabsorbing plasmas**:

  We adapt the PCGO-based method to create a multi-speckle beam by employing the best beamlets initialization scheme found in Chapter 2. We then study the self-focusing of a spatially modulated beam (multi-speckle beam) in a homogeneous nonabsorbing plasma and compare our results to former publications on speckles self-focusing.

- **Chapter 4**: **Laser self-focusing in plasmas with a linear density profile**:

  The last chapter is devoted to establish a baseline towards modelling of laser self-focusing in real ICF conditions. For this purpose, our results are extended to absorbing plasmas with density linearly increasing in space. PCGO beams self-focusing is investigated here for different plasma lengths, and the effect of laser absorption is discussed.

Conclusion summarizes the main results obtained in this work, identifying the potential perspectives.

Chapter 1

State-of-the-art

In this Chapter, we present the state-of-the-art of laser propagation modelling, plasma theory and laser-plasma interaction. In addition, we briefly describe the numerical tools employed in ICF studies. In Section 1.1, the main models for laser radiation dynamics are summarized: starting from the Maxwell's equations, we illustrate the features of simplified models implemented in radiation-hydrodynamics codes to describe laser propagation and absorption. Moreover, some features of spatially modulated beams are introduced. In Section 1.2, the kinetic and fluid plasma theories are reviewed, comprising linear plasma waves. Section 1.3 is devoted to the main laser-plasma coupling phenomena occurring in the ICF context. In Section 1.4, the codes used in this thesis are described.

1.1 Modeling of laser propagation

An important aspect of laser-plasma model in ICF is the accuracy of the description of light propagation and absorption. An accurate characterization of laser dynamics requires solving the Maxwell's equations coupled to the electric and magnetic fields sources. Finding such a solution is too demanding in terms of CPU time, especially while simulating realistic ICF long spatial- and time-scales. ICF-related phenomena occur over hydrodynamic scales, which are characterized by spatial lengths of a few hundreds of micrometers and time duration of many nanoseconds. Simplified models for laser propagation and laser-plasma interaction, which are consistent with such spatial and temporal scales, are seeked. In this sense, geometrical optics-based theories provide the fundamental mathematical background for a computationally efficient description of laser-plasma coupling. On the other hand, those theories stand for an oversimplified model, which neglect wave properties of the laser radiation and all the short spatial- and time-scales phenomena. Conversely, it has been demonstrated [42] that effects occurring on a scale of a few micrometers and a few picoseconds, the so-called kinetic scale, can be crucial for a correct interpretation of experimental results in realistic laser-plasma conditions. In order to include kinetic-like phenomena into hydrodynamics codes by using standard geometrical optics, novel multi-scale laser models, which account for reduced diffraction-like and kinetic-like effects, must be considered.

In the next subsections, we present various theories of laser light propagation. We start from the vectorial form of the Maxwell's equations [43] in Sec. 1.1.1, where we review some important properties of laser

propagation within the wave theory, where the electomagnetic radiation is approximated as a scalar field [44]. Within this approximation, the vectorial light properties, for instance wave polarization, are not accounted for. However, such a model describes several features of laser-plasma coupling, as illustrated in Section 1.3 [45, 46]. In Sec. 1.1.2 we present the paraxial approximation of the Helmholtz equation [39, 44], which holds for the majority of the cases encountered in ICF given that ICF pulses present high frequency and short wavelength compared to the scales of the system. Gaussian beams stand for the most useful solution of the paraxial equation: a presentation of their properties is given. Geometrical Optics (GO), which is the simplest approach to study linear laser-matter interaction, is then introduced [37, 39, 44, 47] in Sec. 1.1.3. Considering complex value of wave phase and amplitude allows to extend the GO to the Complex Geometrical Optics (CGO). The paraxial approximation of CGO gives rise to the Paraxial Complex Geometrical Optics (PCGO), presented in Sec. 1.1.4. This model combines some aspects of GO to wave optics, accounting for a reduced modelling of beam diffraction and in particular imposing a description of beam intensity. The PCGO implementation in radiation-hydrodynamics code CHIC has allowed to introduce nonlinear intensity-dependent multi-scale effects in laser plasma coupling [41], as illustrated at the end of this chapter.

1.1.1 From the Maxwell's equations to the Helmholtz equation

As the laser light consists of electromagnetic waves, its behavior can be described by solving the Maxwell's equations for the electric field vector $\mathbf{E}$ and the magnetic field vector $\mathbf{B}$. Considering a plasma electron and ion density n_e and n_i, respectively, the Maxwell's equations in the plasma write [43, 48]:

$$\nabla \cdot \mathbf{E} = 4\pi e \left(n_i - n_e\right), \tag{1.1}$$

$$\nabla \cdot \mathbf{B} = 0, \tag{1.2}$$

$$\nabla \times \mathbf{E} = -\frac{1}{c}\frac{\partial \mathbf{B}}{\partial t}, \tag{1.3}$$

$$\nabla \times \mathbf{B} = \frac{1}{c}\frac{\partial \mathbf{E}}{\partial t} + \frac{4\pi}{c}\mathbf{j}, \tag{1.4}$$

where $c \approx 3 \times 10^8$ m/s is light speed in the vacuum, e is the unitary electric charge and $\mathbf{j}$ stands for the density current. Equation (1.1) is referred to as *Gauss's law* for the electric field, Eq. (1.2) is referred to as *Gauss's law* for the magnetic field, Eq. (1.3) is referred to as *Faraday's law* and Eq. (1.4) is referred to as *Ampere's law*.

Although coupling the field sources related to the Maxwell's equations provides an accurate description of the electromagnetic radiation dynamics, one is able to find an analytic solution only in a very few cases. To gain some first insights on the radiation behaviour, it is useful to consider light propagation in vacuum. Then Eqs. (1.1)-(1.4) become [43]:

$$\nabla \cdot \mathbf{E} = 0, \tag{1.5}$$

$$\nabla \cdot \mathbf{B} = 0, \tag{1.6}$$

$$\nabla \times \mathbf{E} = -\frac{1}{c}\frac{\partial \mathbf{B}}{\partial t}, \tag{1.7}$$

$$\nabla \times \mathbf{B} = \frac{1}{c}\frac{\partial \mathbf{E}}{\partial t}, \tag{1.8}$$

In order to find an equation for the electric field solely, one takes the curl of Eq. (1.7), and the time derivative of Eq. (1.8). Merging them and accounting for Eqs. (1.5)-(1.6), one obtains an equation for the electric field $\mathbf{E}$ in vacuum:

$$\nabla^2 \mathbf{E} - \frac{1}{c^2}\frac{\partial^2 \mathbf{E}}{\partial t^2} = 0 \tag{1.9}$$

Equation (1.9) is known as *wave equation* because it describes the propagation of a wave. A similar equation is retrieved for the magnetic field. Equation (1.9) means that each component of the electric (and magnetic) field obeys to a wave equation.

As both electric and magnetic fields are perpendicular to the wave propagation direction and neglecting fields polarization variation, it is possible to describe the light as a scalar wave. Let us consider the electric field amplitude as a real part of a complex scalar quantity: $E = A_0(\mathbf{r}) \exp\left[i(\phi(\mathbf{r}) - \omega t)\right] = A(\mathbf{r}) \exp\left(-i\omega t\right)$, where $\phi(\mathbf{r})$ represents the wave phase, $A(\mathbf{r}) = A_0(\mathbf{r}) \exp i\phi(\mathbf{r})$ is the complex amplitude, $A_0(\mathbf{r})$ is the real amplitude such that $|E| = A_0(\mathbf{r})$, and ω is the wave frequency. The wavefronts are defined as surfaces perpendicular to the wavevector and are retrieved by imposing $\phi(\mathbf{r}) = const$. Hereinafter, the wave frequency is constant, and the wave is referred to as *monochromatic wave*. Injecting $E = A(\mathbf{r}) \exp(-i\omega t)$ into the wave equation (1.9), taking into account that $\omega/c = k$, we find the scalar version of the Helmholtz equation for the complex wave amplitude $A(\mathbf{r})$:

$$\nabla^2 A(\mathbf{r}) + k^2 A(\mathbf{r}) = 0. \tag{1.10}$$

Such an equation describes the spatial variation of the complex amplitude of a monochromatic wave with a frequency ω. The simplest solutions of the Helmholtz equation are:

- **plane waves**: $A(\mathbf{r}) = A_0 e^{i\mathbf{k}\cdot\mathbf{r}}$,

  where the vector $\mathbf{k}$ defines the direction of the wave propagation, A_0 is a constant and $\phi(\mathbf{r}) = i\mathbf{k} \cdot \mathbf{r}$. The wavefronts are planes perpendicular to the wavevector $\mathbf{k}$. Plane waves are characterized by a wavelength $\lambda = 2\pi/|\mathbf{k}|$. The wave intensity is $I_0 = cA_0^2/(8\pi)$. The intensity is thus constant everywhere in space and in time. As a consequence, plane waves carry an infinite amount of energy, which does not represent any realistic situation. Despite that, they stand for an useful approximation of the light wave, and they are employed to describe light propagation in electromagnetic codes as illustrated in Sec. 1.4.

- **spherical waves**: $A(\mathbf{r}) = \frac{A_0}{r} e^{ikr}$.

They stand for waves generated from a point source, where the vector $r = \sqrt{x^2+y^2+z^2}$ stands for the distance from the source, supposed place at $r_0 = 0$. The intensity $I_0 = c|A_0|^2/(8\pi r^2)$ decreases with the distance from the source, and the wavefronts are concentric spheres centred at it. If the observation point is placed at large distance from the wave source along the x-axis for example, the spherical wavefront can be locally approximated as a plane wave given that $kr \approx kx$.

- **paraboloidal waves**: $A(\mathbf{r}) = \frac{A_0(\mathbf{r})}{r} e^{ikx} e^{i\frac{z^2+y^2}{2x}}$

  At large distances from the source but where the plane approximation is still not applicable, the wavefront of a spherical wave assumes a paraboloid-like form: for an observer placed along the x-axis, if $x >> (y^2+z^2)^{1/2}$, the radius r can be approximated as follows

$$r = \sqrt{x^2+y^2+z^2} = x\sqrt{1+\frac{y^2+z^2}{x^2}} \approx x + \frac{y^2+z^2}{2x} \tag{1.11}$$

  The wavefront of the paraboloidal wave can be seen as a planar front modulated by a small curvature due to the transverse factor $\exp(i\frac{y^2+z^2}{2x})$. The paraboloidal wave represents a simplified expression of a Gaussian beam, which will be described in the next subsections.

1.1.2 Paraxial solutions of Helmholtz equation: Beam optics and Gaussian beams

The paraxial approximation is one of the most common assumptions made for modelling of ICF long pulses. A pulse can be considered paraxial when the wave propagation direction forms a small angle with the wavefront normal vector. One class of paraxial solutions has a cylindrical symmetry, which gives rise to optical beams. Study of such solutions has opened an optical domain, called *beam optics*. In general, beams are composed by a spatially confined wave energy with a narrow angular spreading. Gaussian beams are beams of a cylindrical shape, i.e. the wave energy is transversely "confined" within a cylinder. Even though Gaussian beams are an approximation of the Maxwell's equations solution, their behaviour well describes the evolution of different beams, such as collimated beams, cylindrical-shaped beams for instance. In the following, we describe the paraxial approximation and the Gaussian beam description of the light.

Paraxial solutions can be constructed directly by imposing a longitudinal spatially slowly variation of the wave amplitude along the propagation direction: $A(\mathbf{r}) = A_p(\mathbf{r})e^{ikx}$, where x is the propagation direction. The amplitude $A_p(\mathbf{r})$ varies slowly over distances of the order of λ. Mathematically, this reads

$$\left|\frac{\partial^2 A_p}{\partial x^2}\right| << k^2 \mid A_p \mid^2 . \tag{1.12}$$

The paraxial approximation of the Helmholtz equation is found by injecting $A(\mathbf{r}) = A_p(\mathbf{r})e^{ikx}$ in Eq. (1.10) and neglecting the second derivative in x:

$$\frac{\partial^2 A_p}{\partial y^2} + \frac{\partial^2 A_p}{\partial z^2} + 2ik\frac{\partial A_p}{\partial x} = 0. \tag{1.13}$$

The expression for a Gaussian beam is retrieved once noticing that the paraxial equation Eq. (1.13) can be rewritten in cylindrical coordinates as:

$$\frac{1}{r_\perp}\frac{\partial}{\partial r_\perp}\left(r_\perp\frac{\partial A_p}{\partial r}\right)+2ik\frac{\partial A_p}{\partial x}=0. \tag{1.14}$$

where $r_\perp=\sqrt{y^2+z^2}$ stands for the dimension transverse to the propagation direction x. The amplitude A_p can be presented in the following form [49]

$$A_p=e^{i\left(P(x)+\frac{kr_\perp^2}{2q(x)}\right)} \tag{1.15}$$

Such a function accounts for the cylindrical symmetry of the Helmholtz equation. The goal then is to find the expression for $P(x)$ and $q(x)$ such that A_p satisfies Eq. (1.14) in the subsequent orders of the paraxial parameter considering $kr_\perp >> 1$. Plugging Eq. (1.15) into Eq. (1.14), one obtains

$$-\frac{k^2r_\perp^2}{q^2}+i\frac{2k}{q}-2k\frac{dP}{dx}+\frac{k^2r_\perp^2}{q^2}\frac{dq}{dx}=0. \tag{1.16}$$

Isolating terms at zero-th and second order in $r_\perp$, one obtains the equations for q and P:

$$\frac{dP}{dx}=\frac{i}{q}. \tag{1.17}$$

$$\frac{dq}{dx}=1; \tag{1.18}$$

The first equation gives $q(x)=q_0+x$. In order to represent a beam solution, q_0 must be complex, otherwise no amplitude modulations would happen. So, we impose $q_0=ix_R$, where x_R is a real number. The quantity P then writes

$$iP=\ln\left(1-i\frac{x}{x_R}\right). \tag{1.19}$$

Manipulating the expressions of P and q, and injecting them into Eq. (1.15), the electric field amplitude in Cartesian coordinates reads

$$A(x,y,z)=A_0\frac{e^{-\frac{kx_Rr^2}{2(x^2+x_R^2)}}}{\sqrt{1+\left(\frac{x}{x_R}\right)^2}}e^{i\frac{kxr^2}{2(x^2+x_R^2)}}e^{i\tan^{-1}\left(\frac{x}{x_R}\right)}e^{ikx} \tag{1.20}$$

where A_0 is the amplitude of the electric field in the focal plane. Defining the minimum beam width called *beam waist* as

$$w_0^2=\frac{2x_R}{k}; \tag{1.21}$$

the curvature radius $R(x)$ as

$$R(x)=x\left[1+\left(\frac{x_R}{x}\right)^2\right] \tag{1.22}$$

and the Gouy phase shift as

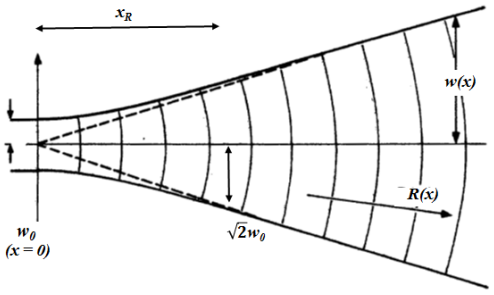

Figure 1.1: Illustration of Gaussian beam parameters in two dimensions. Adaptated from [49].

$$\phi_G(x) = \tan^{-1}\left(\frac{x}{x_R}\right); \tag{1.23}$$

the electric field amplitude assumes the well-known Gaussian form

$$A(x,y,z) = A_0 \frac{w_0}{w(x)} e^{-\frac{r_\perp^2}{w^2(x)}} e^{i\frac{kr_\perp^2}{2R(z)}} e^{i(kx+\phi_G(x))}, \tag{1.24}$$

where

$$w(x) = w_0\sqrt{1+\left(\frac{x}{x_R}\right)^2} \tag{1.25}$$

is the spatially dependent beam width. With our definitions, the minimum width occurs at $x = 0$, and x_R is redefined as:

$$x_R = \frac{kw_0^2}{2}. \tag{1.26}$$

Such a distance is called *Rayleigh length*, and it is the distance at which the beam radius increases by a factor of $\sqrt{2}$. Figure 1.1 shows a relation between the waist w_0 and the Rayleigh length, displaying how the wavefront curves far away from the focus spot placed at x =0. The Gaussian beam intensity is

$$I(r,x) = I_0 \frac{w_0^2}{w^2(x)} e^{-\frac{2r_\perp^2}{w^2(x)}}. \tag{1.27}$$

where $I_0 = c|A_0|^2/(8\pi)$ The beam power P is defined as the energy flowing over a surface per unit of time. Thus, in cylindrical coordinates it reads

$$P_{3D} = \int_0^\infty 2\pi I(r_\perp, x) r_\perp dr_\perp. \tag{1.28}$$

The index 3D refers to the three-dimensional geometry where the integral is performed in the (y,z) plane perpendicular to the propagation direction. Plugging Eq. (1.27) in Eq. (1.28), and solving the Gaussian integrals, one obtains that the expression of beam power in 3D reads

$$P_{3D} = \frac{\pi}{2} I_0 w_0^2. \tag{1.29}$$

It is useful to recover the Gaussian beam quantities in two dimensions, which stand for the geometry of the cases investigated in this thesis. Supposing that y is the transverse dimension, once adapted the Laplacian operator ∇^2 to the 2D case, the equation for P assumes the form

$$i\frac{P}{2} = \ln\left(1 - i\frac{x}{x_R}\right), \tag{1.30}$$

whereas the equation for q remains the same as well Eqs. (1.22)-(1.25). The only exception is the Gouy phase, which becomes $\phi_G^{2D}(x) = \tan^{-1}\sqrt{\frac{x}{x_R}}$. Finding the expression of P from Eq. (1.30), the electric field amplitude rewrites:

$$A(x,y,z) = A_0\sqrt{\frac{w_0}{w(x)}} e^{-\frac{y^2}{w^2(x)}} e^{i\frac{ky^2}{2R(x)}} e^{i(kx+\phi_G^{2D}(x))}. \tag{1.31}$$

Then, the intensity reads

$$I(x,y) = I_0 \frac{w_0}{w(x)} e^{-\frac{2y^2}{w^2(x)}}, \tag{1.32}$$

and the beam power becomes

$$P_{2D} = \int_{-\infty}^{+\infty} I(y,x) h dy = \sqrt{\frac{\pi}{2}} I_0 w_0 h \tag{1.33}$$

where h is the unitary length in the third (z) dimension and it is a constant added in order to preserve the correct units for the beam power.

In nonabsorbing medium, the beam power is conserved. Given the same maximum beam intensity I_0, in 3D geometry the power conservation gives that the on-axis intensity varies as

$$I(x)w^2(x) = I_0 w_0^2, \tag{1.34}$$

whereas in the 2D geometry the same expression rewrites as

$$I(x)w(x) = I_0 w_0. \tag{1.35}$$

Due to these differences in 2D and 3D dimensions, ponderomotive effects evolve in a distinctive way, as described in Sec. 1.3.2.1.

Besides beam optics, the slowly varying approximation is the base of the ray theories: for real values of the amplitude and phase, the Helmholtz equation gives rise to the Geometrical Optics (GO). The Complex Geometrical Optics (CGO) is an extension of the GO which includes diffraction effects, whereas the GO accounts only for ray propagation and refraction if the refraction index depends on spatial coordinates.

1.1.3 Ray optics

In this subsection, we review the eikonal approach for solving the Helmholtz equation starting from a nonabsorbing medium: we assume that the slowly varying approximation holds but we do not suppose a rectilinear propagation. Unlike the Gaussian beam description presented above, where the beam is not supposed to vary its direction, within this approach the wave is described by a ray defined by three vectors (or two in case of two-dimensional geometry): a vector parallel to the wave propagation direction, and two transverse vectors (or one transverse vector in two-dimension) which allow to account for propagation direction variation due to refraction in the medium. In a medium in fact, the Helmholtz equation (1.10) rewrites

$$\nabla^2 A(\mathbf{r}) + k^2 N^2 A(\mathbf{r}) = 0, \tag{1.36}$$

Injecting where $N = \sqrt{\varepsilon}$ is the medium refractive index, being ε the permittivity. To find the ray equations, the wave field amplitude A is decomposed in a series of terms by performing the so-called *Debye expansion*

$$A = \sum_{m=0}^{\infty} \frac{A_m(\mathbf{r})}{ik^m} e^{ik\phi(\mathbf{r})}. \tag{1.37}$$

Injecting Eq. (1.37) in Eq. (1.36), considering real values of $A_m(\mathbf{r})$ and $\phi(\mathbf{r})$, one obtains

$$\left(N^2 - |\nabla\phi|^2\right) A_0 + \frac{\nabla^2 A_0}{k^2} + \frac{1}{ik}\left[2\nabla\phi\cdot\nabla A_0 + A_0\nabla^2\phi\right] = 0. \tag{1.38}$$

Considering the zero-th order of k^{-1} in Eq. (1.38), one obtains

$$|\nabla\phi|^2 = N^2. \tag{1.39}$$

This equation is referred to as *eikonal equation* since $\phi(\mathbf{r}) = const$ gives a surface perpendicular to the propagation direction. The equation for the ray coordinates comes from Eq. (1.39) by invoking arguments from the differential geometry: considering that Eq. (1.39) generates a variety into the Hamilton-Jacobi space [50], it is known that Hamiltonian of the system is conserved along the ray trajectory:

$$H = \frac{1}{2}\left(\mathbf{p}^2 - N^2\right), \tag{1.40}$$

where we have defined $\mathbf{p} = \nabla\phi$. Introducing the ray coordinate τ, the position and the moment are related to the Hamiltonian by the canonical equations for the coordinate r_i and moment p_i

$$\frac{dr_i}{d\tau} = \frac{\partial H}{\partial p_i} \tag{1.41}$$

$$\frac{dp_i}{d\tau} = -\frac{\partial H}{\partial r_i} \tag{1.42}$$

whereas the equation for the eikonal ϕ rewrites

$$\frac{d\phi}{d\tau} = N. \tag{1.43}$$

Equations (1.41)-(1.42) can be rewritten as [39]

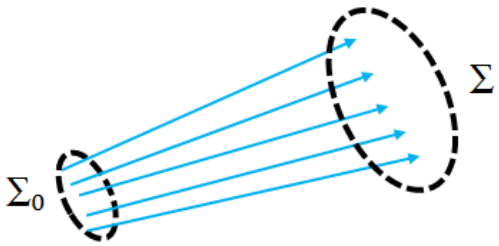

Figure 1.2: Illustration of rays (blue arrows) divergence due to refraction while propagating from a surface Σ_0 to a surface Σ.

$$\frac{d\mathbf{r}}{d\tau} = \mathbf{p} \tag{1.44}$$

$$\frac{d\mathbf{p}}{d\tau} = c^2 \frac{\nabla N^2}{2}. \tag{1.45}$$

The equation for the ray trajectory is found by combining Eq. (1.44) and Eq. (1.45):

$$\frac{d^2\mathbf{r}}{d\tau^2} = c^2 \frac{\nabla N^2}{2}. \tag{1.46}$$

Equation (1.46) defines the ray trajectory dynamics through its position $\mathbf{r}$ depending on the refractive index N, thus describing the ray path associated to the wave. Rays direction coincides with the propagation direction in isotropic media, and it is perpendicular to the surfaces defined by the equation $\phi(\mathbf{r}) = const$. From Eq. (1.43), one obtains the expression for the eikonal:

$$\phi = \phi_0 + \int_{\tau_0}^{\tau} N d\tau. \tag{1.47}$$

The ray amplitude is obtained by solving Eq. (1.38) for terms of the first order in k^{-1}:

$$2\nabla\phi \cdot \nabla A_0 + A_0 \nabla^2 \phi = 0 \tag{1.48}$$

Such an equation is solved by noting that the first term is the projection of ∇A_0 over the trajectory: $\nabla\phi \cdot \nabla A_0 = dA_0/d\Upsilon|\nabla\phi|$, where Υ is the arc length defined as $\Upsilon = N\tau$, and that $|p| = N$, one obtains

$$\frac{dA_0^2}{d\tau} + A_0^2 \nabla^2 \phi = 0. \tag{1.49}$$

The solution for the wave amplitude can be rewritten in the form

$$A_0^2(\tau) = \frac{A_0^2(\tau_0)}{\sqrt{J}} \tag{1.50}$$

where J is the ratio of the Jacobians of the transformation from the transverse coordinates (q_1, q_2) at the initial ray position τ_0 to the ray transverse coordinates at current ray position τ. Geometrically, the Jacobian J is the beam divergence when the ray propagates from a surface Σ_0 to a surface Σ. This feature can be seen in Fig. 1.2. It can be demonstrated that along the ray path in nonabsorbing plasmas the beam power $\mathbf{I}d\Sigma$ is

conserved, where $\mathbf{I} = (E^*\nabla E - E\nabla E^*)/(2ik)$ is the ray intensity [39, 47]. As a consequence, since the beam intensity is proportional to the square of the amplitude, one obtains that $\sqrt{J} = \sqrt{(N\Sigma)/(N_0\Sigma_0)}$, where N and N_0 are the refractive index at Σ and Σ_0, respectively. This property links the refractive index variation to the ray divergence describing the refraction of the rays.

Ray optics stands for the simplest approximation of light propagation: it considers laser beam evolution through the dynamics of thin rays, which interact with media through the refractive index. In weakly dissipative media, the power associated with the ray changes along the propagation direction. This fact is described by a complex permittivity ε with the imaginary part smaller than the real part:

$$\varepsilon = \varepsilon' + i\varepsilon'' \tag{1.51}$$

where $\varepsilon'' << \varepsilon'$. As a consequence, $N = N' + iN''$, with $N'' << N'$. Because of dissipation, the ray amplitude varies as

$$A_0^2(\tau) = \frac{A_0^2(\tau_0)}{\sqrt{J}} \exp\left(-k\int_{\tau_0}^{\tau} N'' d\tau\right), \tag{1.52}$$

where the exponential term accounts for absorption. Equations (1.46) and (1.52) are the basic equations of the Ray-Tracing techniques implemented in hydrodynamics codes for describing laser propagation and absorption [37]: in these codes, lasers are modelled as a bundle of thin rays, obeying to those equations.

1.1.4 Paraxial Complex Geometrical Optics (PCGO)

The GO formulation can be extended to the next order to the paraxial parameter $1/kr$, which allows to account for the beam diffraction and for the amplitude variation along the ray. Assuming the paraxial approximation, where the system scale length is much longer than the laser wavelength, the beam dynamics can be described by a bunch of rays weakly divergent or convergent around a central ray hereinafter called $\mathbf{r}_c$. Therefore, instead of solving Eq.(1.46) for all rays as in RT, it is convenient working within a frame along the central ray and rewrite Eq. (1.39) in it. Let this frame be (τ_c, q_1, q_2), where τ_c central ray tangent, q_1 and q_2 are the coordinates in the plane perpendicular to τ_c. The position of a neighboring ray $\mathbf{r}$ around the central ray can be written as $\mathbf{r} = \mathbf{r}_c + \mathbf{q}$, where $\mathbf{q} = q_1\mathbf{e}_1(\tau_c) + q_2\mathbf{e}_2(\tau_c)$, and $\mathbf{e}_i(\tau_c)$ perpendicular to the central ray tangent. Authors in [51] have demonstrated that a reference system (τ_c, q_1, q_2) where the unitary vector $\mathbf{e_1}$ is parallel to the ray normal and $\mathbf{e_2}$ is perpendicular to the plan τ_c and $\mathbf{e_1}$ can be always defined. In this particular frame, the eikonal equation Eq. (1.39) reads

$$\frac{1}{h^2}\left(\frac{\partial\phi}{\partial\tau_c}\right)^2 + \left(\frac{\partial\phi}{\partial q_1}\right)^2 + \left(\frac{\partial\phi}{\partial q_2}\right)^2 = \varepsilon(\mathbf{r}_c) + (\mathbf{q}\cdot\nabla)\varepsilon(\mathbf{r}_c) + \frac{1}{2}(\mathbf{q}\cdot\nabla)^2\varepsilon(\mathbf{r}_c) + O(|\varepsilon(\mathbf{r}_c)|^2), \tag{1.53}$$

where $h = N - (\mathbf{q}\cdot\nabla)N$ is the Lamé coefficient. Here the permittivity ε has been expanded around the central ray $\mathbf{q} = \mathbf{r} - \mathbf{r}_c$. In the next, we assume a 2D geometry defined by the coordinates (τ_c, q). The eikonal ϕ can be expanded around the central ray too, assuming the form

$$\phi = \phi_c(\tau_c) + \hat{\phi}(q, \tau_c) \tag{1.54}$$

where $\phi_c(\tau_c) = \int^{\tau_c} N'(\mathbf{r}_c)d\tau_c'$ is the central ray eikonal, and $\hat{\phi}$ complex value representing a small deviation with respect to the eikonal on the central ray. Let us assume that such a deviation has a quadratic form

$$\tilde{S}(\tau_c, q_1) = \frac{1}{2}Bq, \tag{1.55}$$

with B is the complex curvature wavefront. Injecting Eq. (1.55) into Eq. (1.53), one obtains a system of Riccati-like equations for B. In the two-dimensional geometry, the tensor B has only one component:

$$\frac{\partial B}{\partial \tau_c} + B^2(\tau_c) = \frac{1}{2}\frac{\partial \varepsilon(\mathbf{r}_c)}{\partial q^2} - \frac{3}{4\varepsilon(\mathbf{r}_c)}\left(\frac{\partial \varepsilon(\mathbf{r}_c)}{\partial q}\right)^2, \tag{1.56}$$

which can be further reduced to an ODEs system numerically solvable once presented the the curvature B as a product of two factors, $B = PQ^{-1}$. The electric field amplitude can be retrieved once considering the transport equation in the $(\tau_c, \mathbf{q})$ frame [41], for which an expression for A_0 is recovered:

$$\frac{2}{c^2h^2}\frac{\partial \phi}{\partial \tau_c}\frac{\partial A_0}{\partial \tau_c} + \left[\frac{1}{ch}\frac{\partial}{\partial \tau_c}\left(\frac{1}{ch}\frac{\partial \phi}{\partial \tau_c} + \frac{\partial^2 \phi}{\partial q^2}\right)\right]A_0 = 0, \tag{1.57}$$

Combining the solution of Eq. (1.57) with the solution of Eq. (1.56), imposing that $w(\tau_c) = \sqrt{2/(k\mathrm{Im B})}$ as beam width and $R(\tau_c) = \mathrm{Re B}/\sqrt{\varepsilon_c'}$ as wavefront curvature, one obtains:

$$A_0(\tau_c) = \frac{A_0}{\sqrt[4]{\varepsilon_c'}}\sqrt{\frac{w}{w_0}}e^{-k\int_{\tau_0}^{\tau_c'} N^{2''}d\tau_c'}e^{-\frac{q^2}{w_0^2}} \tag{1.58}$$

where weakly absorption has been accounted for through the exponential integral. The intensity along the beam propagation direction reads

$$I_0(\tau_c) = \frac{I_0}{\sqrt{\varepsilon_c'}}\frac{w}{w_0}e^{-k\int_{\tau_{0'}}^{\tau_c'} N^{2''}d\tau_c'} \tag{1.59}$$

PCGO works for a weakly dissipative medium within the validity of the paraxial approximation. The limits of the PCGO model are the following:

1. THE GO CONDITION

$$\frac{\lambda}{L} << 1 \tag{1.60}$$

where λ is the laser beam wavelength and L is the characteristic length of the system. That is the standard condition where a geometrical optics-based theory applies. In the ICF context, $\lambda = 0.35 - 1.05$ μm, whereas $L = 10 - 1000$ μm, so this condition is satisfied;

2. THE PARAXIAL CONDITION

$$\frac{\lambda}{w_0} << 1 \tag{1.61}$$

where w_0 is the beam waist. Equation (1.61) ensures that the paraxial approximation holds all along the ray trajectory. In the ICF context, $w_0 = 500$ μm, which is modulated on the scale of 2-3 μm representing the laser speckles. When modelling of Gaussian beams, such an approximation holds, whereas it may fail in describing small scale fluctuations of spatially modulated beams;

$$\frac{w_0}{L} << 1 \tag{1.62}$$

it states that a Gaussian beam-like profile holds all along the propagation.

From these conditions, it is clear that despite standard PCGO allows to describe Gaussian beams, its direct application to model of spatially modulated ICF beams may be inaccurate. However, the implementation of a reduced PCGO model in hydrodynamics codes has opened the possibility to introduce spatial fluctuations in the far-field by employing PCGO-like Gaussian beamlets, as described in Sec. 1.4.2.

Besides laser beams, hot electron generation, propagation and energy deposition have been included in hydrodynamics codes thanks to PCGO-related algorithms. Such a development has allowed to add kinetic effects in CHIC in a reduced formulation [41].

1.1.5 Optical smoothing techniques for ICF

Before going into the laser-plasma coupling, we briefly recall the principles of optical smoothing techniques introduced in ICF facilities, and describe in more details the spatial modulation techniques. Without any phase plate, although the beam profile appears smoothed in the near-field, aberrations accumulated along the beamline chain can produce distorsion and amplitude modulation in the far-field [52]. Such modulations expose the target to an uncontrolled nonuniform and non-symmetrical illumination, which seed hydrodynamic instabilities occurring during the acceleration and deceleration phase. The inhomogeneities can occur at short or long wavelengths. In the first case, they are due to imperfection of the target surface or single-beam intensity modulations. Long wavelength nonuniformities are mainly due to beams misalignment or beam energy redirection due to laser-plasma instabilities. The short wavelength nonuniformities can be naturally self-smoothed by plasma thermal conduction, which is not the case for the long wavelength ones. Several techniques for laser-induced spatial and temporal smoothing have been developed in order to achieve a high degree of target illumination uniformity and so minimize the seeding of hydrodynamic instabilities such as Rayleigh-Taylor and Richtmyer-Meshkov instabilities [53] and diminishing the occurrence of nonlinear laser-plasma interaction. Spatially modulated laser beams have been introduced in ICF from late 80s. Such methods consist in breaking the global coherent beam profile in a pattern of small-scale modulations called *speckles*. These fluctuations are generated by placing a phase plate behind the beam focal lens: this plate presents a regular element pattern which induces a random phase variation to each part of the beam passing through a given element. The phase variation depends on the type of the phase plate: for instance, a random discrete phase variation of 0 or π is induced by a Random Phase Plate (RPP) [25], whereas a random continuous phase variation is assigned to each part of the beam in case of Kinoform Phase Plates (KPP) [26] and Continuous Phase Plates (CPP) [54]. The main difference in these techniques is the level of the laser energy diffracted out of the focal spot, which is 20% in the RPP case, 5% in the KPP case and $\sim$ 1% in the CPP case. After passing through the phase plate, the beam is then broken in several small beamlets, each carrying a different phase. The interference of all the beamlets in the far-field generates a modulated intensity profile known as speckle pattern. The speckles size

and the number of speckles are related to the laser wavelength and the focal length: in vacuum, in the far-field, the speckles have a transverse coherent size of [55, 56]

$$w_s = \frac{f\lambda}{D}, \tag{1.63}$$

where f is the focal length and D is the lens diameter, and a longitudinal coherent size of

$$x_s = k w_B w_s, \tag{1.64}$$

where w_B is the waist of the beam. This method allows to redistribute the long wavelength energy non-uniformity to shorter wavelengths. Since the characteristic size of speckles is of the same order as the short wavelength non-uniformity of laser energy deposition, these non-uniformities can be rapidly smoothed by thermal conduction. Geometrical and optical considerations allow to estimate how the number of speckles in the far-field M scales with the number of phase plate elements q: in case of RPP for example, it can be demonstrated [55] that at a given RPP width D, the volume where the beamlets overlap scales as $f^4\lambda^3 q^{3/2}/D^4$. By considering Guassian speckles, the speckle volume can be approximated as $x_R w_s^2$. Since M can be considered as the ratio of the overlapping volume and the volume of a speckle, from Eqs. (1.63) and (1.64), one finds that M scales as $q^{3/2}$. Then, M is of the order of 10^3-10^4 [55].

Two important parameters characterize spatially modulated beams: the beam contrast and the probability distribution of the speckle intensity. At a given position, the contrast of a nonuniform beam is defined as [56]

$$C^2 = \frac{\langle I^2 \rangle_\perp - \langle I \rangle_\perp^2}{\langle I \rangle_\perp^2}, \tag{1.65}$$

where the $\langle\rangle_\perp$ stands for the spatial average performed in the transverse directions. Such a parameter quantifies the amplitude of the laser intensity fluctuations over an area comparable to the transverse beam size. In case of KPP or RPP beams, in the far-field C=100 %, which means that the amplitude of intensity fluctuations are comparable to the average intensity.

Since M is a large number, it is convenient to characterize the speckles intensity by using a statistical approach: it has been found that the probability $P(I_s)$ of finding a speckle of intensity I_s with respect the average beam intensity $< I >$ follows an exponential law [55, 56]:

$$P(I_s) \propto \exp\left(-\frac{I_s}{< I >}\right). \tag{1.66}$$

Consequently, there is a consistent part of the speckles which have an intensity smaller than $< I >$, whereas a fraction of them presents an intensity larger than $< I >$. These high-intensity speckles may be a source of nonlinear laser-plasma coupling effects. The role of ponderomotive force in a speckle pattern and its influence on speckle statistics and beam dynamics is investigated in Chapter 3.

1.2 Plasma physics

In this section, we review the essential features of plasma physics in order to be able to understand ICF coronal phenomena. In Section 1.2.1, plasma relevant parameters are presented. Section 1.2.2 concerns plasma theories,

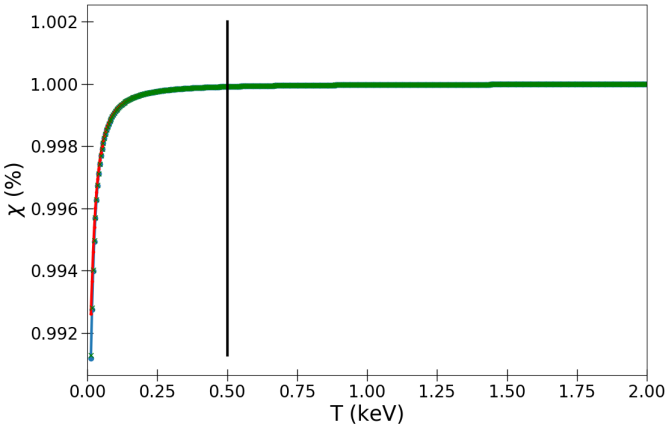

Figure 1.3: Ionization degree χ for an hydrogen gas (red line), a carbon gas (blue line) and a C_2H_2 gas (green line) as a function of the temperature of the system T.

starting from the plasma kinetic theory. Then fluid theory of plasmas is revised, along with the dispersion relations for longitudinal and transverse plasma waves.

1.2.1 Relevant parameters

As soon as ICF high power lasers irradiate a solid target, a gas generated by mass ablation propagates out-wards, opposite to the laser direction. Such a gas is quickly ionized by the laser, and the ionization degree $\chi = n_j/n_0^g$ of the species j composing the gas can be evaluated according to statistical mechanics considerations [10], n_0^g the neutral gas density and n_j the density of the ionized gas of species j. In case of ideal gas and first ionization of neutral atoms, the ionization degree is found by solving the *Saha equation*, which links χ, n_0^g and the gas temperature T_g [57–60]

$$\frac{\chi^2}{1-\chi} = \frac{2}{n_0^g}\left(\frac{2\pi m_e T_g}{h^2}\right)^{3/2} e^{-\frac{I_i}{T_g}}, \tag{1.67}$$

where m_e is the electron mass, h is the Planck constant, I_i is the first ionization energy of atoms, and T_g is in energy units. The ionization level according to Eq. (1.67) for an hydrogen gas (red line), a carbon gas (blue line) and a C_2H_2 gas (green line) is shown in Fig. 1.3 as a function of the gas temperature. In the fusion environment, the coronal temperature T_e is above 0.5 keV. Such a value is evidenced in the figure by the solid black line: above this temperature, the ionization degree is around 100% independently of the gas. In such conditions, the completely ionized gas is referred to as *plasma*. The plasma state represents the environment in which the laser propagates while ablating and compressing the target. The plasma corona size varies in time, since the laser ablates the material during its interaction with the target. The corona size depends also on the geometry of the experiment, on the ICF configuration (direct-drive or indirect-drive) and on the laser intensity. Typical plasma sizes range from 200-300 μm in case of OMEGA experiments [61] to 600-800 μm for NIF [11] and LMJ [62] experiments.

The most relevant parameters that characterize the plasma are the *Debye length* and the *plasma frequency*.

The *Debye length* λ_D refers to the length at which the standard Coulomb potential decreases by a factor of $1/e$. This parameter can be measured by introducing a test particle q_t into the plasma. Supposing this test particle at rest, the plasma particles of charge $-q_t$ surround the charge q_t because of the Coulomb attraction. Such a cloud shields the electric field generated by the test particle q_t and, according to the Poisson's equation (1.1), the Coulomb potential generated by q_t is reduced by a factor proportional to $\exp(-r/\lambda_D)$ [48, 63]. Assuming the quasi-neutrality condition, for which the plasma density reads $n_e = Zn_i$, where n_e and n_i are electron and ion densities respectively, Z the average ion charge, and with an electron temperature T_e and ion temperature T_i such that $T_e \neq T_i$, the Debye length for electrons λ_{De} and ions λ_{Di} read

$$\lambda_{De} = \sqrt{\frac{T_e}{4\pi e^2 n_e}} \qquad \lambda_{Di} = \sqrt{\frac{T_i}{4\pi Z^2 e^2 n_i}}, \tag{1.68}$$

where e stands for the unitary electric charge, and the temperatures are in energy units. The total Debye length $\lambda_D^{-1} = \lambda_{De}^{-1} + \lambda_{Di}^{-1}$ reads

$$\lambda_D = \sqrt{\frac{T_e}{4\pi e^2 n_e}} \frac{1}{1 + \sqrt{\frac{ZT_e}{T_i}}}. \tag{1.69}$$

For high Z or for high ion temperatures, $T_i >> ZT_e$ and the ion term in Eq. (1.69) can be neglected.

The plasma frequency ω_p stands for the characteristic frequency of a periodic plasma collective motion. Let us suppose that an ion slab and an electron slab are displaced by a certain length the one from the other in a collisionless plasma. The ion slab is supposed at rest. The charge displacement induces a violation of the local charge neutrality, which generates an electric field between the two slabs. Under the influence of this field, the electron slab oscillates with a frequency:

$$\omega_{pe} = \sqrt{\frac{4\pi n_e e^2}{m_e}}. \tag{1.70}$$

An analogous frequency can be defined for ions in case they can oscillate:

$$\omega_{pi} = \sqrt{\frac{4\pi n_i Z^2 e^2}{m_i}}, \tag{1.71}$$

where m_i is the ion mass. So, the total plasma frequency reads $\omega_p^2 = \omega_{pe}^2 + \omega_{pi}^2$. Since $m_i >> m_e$, the ions give a small contribution to the plasma frequency, which rewrites

$$\omega_p \approx \omega_{pe}. \tag{1.72}$$

In the following, we refer to ω_{pe} as the plasma frequency.

In a plasma, particles collectively interact via the Coulomb force. Due to the long-range nature of this force, collisions are most likely to deviate particles at small angles rather than large angles. The collision frequency measures the cumulative effect of a large amount of small angle collisions. Averaging over the particle distribution (which will be introduced in the next section), one can calculate the average collision frequency for particle-particle collision [48], recovering thus the electron-ion, electron-electron and ion-ion collision frequencies:

$$\nu_{ei} = \frac{4\sqrt{2\pi} n_i Z^2 e^4 \ln\Lambda}{3\sqrt{m_e} T_e^{3/2}}. \tag{1.73}$$

$$\nu_{ee} = \frac{\nu_{ei}}{Z}, \tag{1.74}$$

$$\nu_{ii} = \left(\frac{m_e}{m_i}\right)^{1/2} \left(\frac{T_e}{T_i}\right)^{3/2} Z^2 \nu_{ei}, \tag{1.75}$$

where $\ln\Lambda$ is the Coulomb logarithm, and Λ is the ratio of the maximum and minimum distances at which the two particles can collide. From Eqs. (1.73)-(1.75), it is clear that $\nu_{ei} > \nu_{ee} > \nu_{ii}$.

Starting from the parameters presented above, one can define the properties that a system must satisfy such that it can be considered as a plasma [63, 64]:

- $\lambda_D << L$;

  where L stands for the characteristic plasma length. This relation implies that the plasma size is larger than a Debye sphere. Furthermore, this condition allows to maintain plasma quasi-neutrality, avoiding particle recombination and keep the ionization rate constant;

- $\mu_n >> 1$;

  where $\mu_n = n\lambda_D^3$ measures the number of particles in the Debye sphere. As long as this condition holds, the plasma can be treated with statistical methods;

- $\nu_{ei}/\omega_{pe} \sim 1/\mu_n << 1$.

  Since collisions are single particle effects, whereas plasma oscillations stand for collective effects, from such an inequality follows that the plasma is a system where collective phenomena dominates over single particle processes. However, collisions play an important role in particles energy exchange and temperature relaxation.

In the following, we illustrate the two main plasma theories: the kinetic theory and the fluid theory.

1.2.2 Plasma models

Plasma description depends on the phenomenon under investigation, and in particular on their temporal- and spatial-scales. Considering the plasma as a many body system, methods from statistical physics appear natural tools for plasma modelling. The kinetic theory of plasma is presented in Section 1.2.2.1. In Section 1.2.2.2 we show how few assumptions on kinetic parameters allows to retrieve the fluid plasma equations.

1.2.2.1 Kinetic theory of plasmas

For $\mu_n >> 1$, and when the strength of collective effects overcome short-range particles interaction, the description of the plasma by kinetic models is quite accurate [48, 65]. Introducing a six-dimension space spanned by spatial $\mathbf{r} = (x, y, z)$ and velocity $\mathbf{v} = (v_x, v_y, v_z)$ coordinates, the dynamical state of a particle is represented by a point P in this space, which determines the spatial position and the velocity of the particle. In case of a system with a large number of particles on the Debye scale, the ensemble of dynamical states of all particles forms a continuous distribution in the 6-dimensional $(\mathbf{r}, \mathbf{v})$-space. For a two-component plasma, i.e. composed by electrons and one ion species, we define a single-particle distribution function $f_s = f_s(\mathbf{r}, \mathbf{v}, t)$ for every species s, where $s = i$ for ions, and $s = e$ for electrons, such that

$$d\mu_{n,s} = f_s(\mathbf{r}, \mathbf{v}, t) d\mathbf{V}, \tag{1.76}$$

where $d\mu_{n,s}$ stands for the number of particles of the species s contained in the infinitesimal volume $d\mathbf{V} = d\mathbf{r}d\mathbf{v}$. The distribution function f_s stands for the probability density to find $d\mu_{n,s}$ particles in the infinitesimal volume $d\mathbf{r}d\mathbf{v}$ if normalized as follows

$$\int_{\mathbf{V}} f_s(\mathbf{r}, \mathbf{v}, t) d\mathbf{r}d\mathbf{v} = \mu_{n,s}, \tag{1.77}$$

where the integral is intended to be calculated over the whole six-dimension volume $\mathbf{V}$. With this definition, the particle changing rate $d\mu_{n,s}/(dtd\mathbf{V}) = \partial f_s/\partial t$ in the volume $d\mathbf{V}$ reads

$$\frac{\partial f_s}{\partial t} = \left(\frac{\partial f_s}{\partial t}\right)_{stream} + \left(\frac{\partial f_s}{\partial t}\right)_{coll}. \tag{1.78}$$

The first term in the right-hand is called *streaming term*, whose variation is due to the total force acting on the particles, whereas the second term in the right hand-side stands for the contribution due to collisions among particles. The streaming term can be expressed in terms of the spatial and velocity derivatives [64]

$$\left(\frac{\partial f_s}{\partial t}\right)_{stream} = -\left(\mathbf{v} \cdot \nabla_{\mathbf{r}}\right) f_s - \frac{1}{m_s}\left(\mathbf{F}_s \cdot \nabla_{\mathbf{v}}\right) f_s, \tag{1.79}$$

where $\nabla_{\mathbf{r}} = (\partial_x, \partial_y, \partial_z)$ and $\nabla_{\mathbf{v}} = (\partial_{v_x}, \partial_{v_y}, \partial_{v_z})$ are the derivative operators in the spatial and velocity space respectively, and $\mathbf{F}_s$ stands for the total force acting on every species s. Injecting Eq. (1.79) into Eq. (1.78), this last one rewrites

$$\frac{\partial f_s}{\partial t} + \left(\mathbf{v} \cdot \nabla_{\mathbf{r}}\right) f_s + \frac{1}{m_s}\left(\mathbf{F}_s \cdot \nabla_{\mathbf{v}}\right) f_s = \left(\frac{\partial f_s}{\partial t}\right)_{coll}. \tag{1.80}$$

Equation (1.80) is called *Boltzmann equation* and describes the plasma dynamics far from the equilibrium. The third term in the left hand-side and the term in the right hand-side represent the total force and collisions, respectively. They govern the evolution of the plasma system. The particular form of the collision term depends on what kind of collisions are taken into account [48].

In collisionless plasmas, Eq. (1.80) becomes the *Vlasov equation* [66]

$$\frac{\partial f_s}{\partial t} + (\mathbf{v}\cdot\nabla_{\mathbf{r}})\, f_s + \frac{1}{m_s}\,(\mathbf{F}_s\cdot\nabla_{\mathbf{v}})\, f_s = 0. \tag{1.81}$$

In fusion plasmas, only the Lorentz force is supposed to act on plasma particle: $\mathbf{F}_s = q_s\,[\mathbf{E} + (1/c)\mathbf{v}\times\mathbf{B}]$, where q_s stands for electric charge of the species s and Eq. (1.81) reduces to

$$\frac{\partial f_s}{\partial t} + (\mathbf{v}\cdot\nabla_{\mathbf{r}})\, f_s + \frac{q_s}{m_s}\left[\mathbf{E} + \frac{\mathbf{v}\times\mathbf{B}}{c}\right]\cdot\nabla_{\mathbf{v}} f_s = 0. \tag{1.82}$$

The fields are generated by superposition of external and averaged fields. For electric field $\mathbf{E} = \mathbf{E}_s^{ext} + \mathbf{E}_s^{mean}$, and for magnetic field $\mathbf{B} = \mathbf{B}_s^{ext} + \mathbf{B}_s^{mean}$, where $\mathbf{E}_s^{mean}$ and $\mathbf{B}_s^{mean}$ are respectively the averaged electric field and magnetic field acting on a single particle produced by the other $\mu_{n,s} - 1$ charges. Specifically, the internal electric field $\mathbf{E}_s^{mean}$ and magnetic field $\mathbf{B}_s^{mean}$ acting on a particle are generated by the other $\mu_{n,s} - 1$ charges for electric field, and by the average density current due to $\mu_{n,s} - 1$ charges motion for the magnetic field. We refer to all the average fields as *self-consistent* fields. The self-consistency arises from the fact that their sources are strictly related to the distribution function, whose evolution strongly depends on the fields. In this picture, particles motion is thoroughly connected to the fields, and plasma processes are essentially due to this self-consistent coupling between charged particles and fields. This propriety makes the plasma an unique state of matter. In order to solve the problem of self-consistent fields and particles interaction, the Maxwell's equations (1.1)-(1.4) need to be coupled to the Vlasov equation Eq. (1.82), giving rise to the *Vlasov-Maxwell* system [63]. The field sources are calculated from the Vlasov equation, so the terms n and $\mathbf{j}$ in Eq. (1.1) and Eq. (1.4) stand for the particle density and the density current defined as follows:

$$n(\mathbf{r},t) = n^{ext} + n^{int} = n^{ext} + \sum_s n_s, \tag{1.83}$$

$$\mathbf{j}(\mathbf{r},t) = \mathbf{j}^{ext} + \mathbf{j}^{int} = \mathbf{j}^{ext} + \sum_s q_s n_s \mathbf{u}_s, \tag{1.84}$$

where

$$n_s = n_s(\mathbf{r},t) = \int f_s(\mathbf{r},\mathbf{v},t)d\mathbf{v} \tag{1.85}$$

and

$$\mathbf{u}_s = \mathbf{u}_s(\mathbf{r},t) = \frac{1}{n_s}\int \mathbf{v} f_s(\mathbf{r},\mathbf{v},t)d\mathbf{v} \tag{1.86}$$

are the particle density and the average velocity of particles of s-species, respectively. The Vlasov-Maxwell system along with Eqs. (1.83)-(1.86) describe the spatial-temporal self-consistent evolution of a collisionless plasma in the kinetic framework. Both particles and fields compose the entire state of plasma, which is defined by $\mathbf{E}(\mathbf{r},t)$, $\mathbf{B}(\mathbf{r},t)$ and $f_s(\mathbf{r},t)$.

In absence of external fields, the equilibrium distribution function tends to assume Maxwellian-like distribution, which in three dimensions reads [48]:

$$f_{s0} = n_s \left(\frac{m_s}{2\pi T_s} \right)^{3/2} \exp\left(-\frac{\mathrm{m_s v^2}}{2\mathrm{T_s}} \right). \tag{1.87}$$

where $v_{ts}^2 = T_s/m_s$ is the thermal velocity of particles of the species s, and the index 0 indicates the equilibrium state.

1.2.2.2 Fluid theory of plasmas

Despite its accuracy in describing plasma phenomena, implementation and running numerical codes based on kinetic description is too computationally expensive for ICF modelling. The distribution function can be calculated only in small plasma volumes and for short time-scales. This limits the application of the plasma kinetic theory to ICF, since the latter involves millimetre spatial-scales over nanosecond time-scales. The fluid plasma theory corresponds to an approximate version of the kinetic theory that: i) allows to retrieve the measurable macroscopic plasma quantities, such as pressure, temperature and density, ii) is less costly in terms of CPU time since the space where the equations are discretised is three-dimensional rather than six-dimensional, and iii) kinetic phenomena are approximated at hydrodynamic scales assuming that the distribution function of each speciesis close to the equilibrium. To summarize, the conditions under which plasmas can be described as a fluid are [65]

1. the characteristic time-scale is much longer than the plasma period and larger than the collision time $t_{macro} >> 1/\nu_e >> 1/\omega_{pe}$;

2. the spatial-scale of a significant change in macroscopic quantities is larger than the free mean path of the particles;

Under these assumptions, a plasma can be considered to be close to a local thermal equilibrium: each plasma species has a defined temperature if the condition of a local quasi-neutrality holds. Despite that, temperatures of electrons and ions can be different, because electron-ion temperature relaxation proceeds on hydrodynamic time-scales. In this case, plasma can be described as a single fluid with two temperatures. If the hydrodynamic time is larger than the time needed for the temperature to reach an equilibrium, $t_{macro} > (m_i/m_e)/\nu_{ei}$ equilibrium between the two species is established, and plasma can be described as a single fluid with a single temperature.

Some authors have introduced the fluid equations from euristical considerations [64, 68], but they can be obtained by integrating the Vlasov equation (1.81) [63] as well. To do so, we define the function Ψ_s^l, which is the general moment of order l related to the distribution function f_s, as:

$$\Psi_s^l = \langle \Psi(\mathbf{v}) \rangle_s = \frac{\int \Psi^l(\mathbf{v}) f_s d\mathbf{v}}{n_s(\mathbf{r}, t)}, \tag{1.88}$$

where the average is performed over the s-species distribution function. Once defined a particular form of the function $\Psi^l(\mathbf{v})$, one finds the expression of the moment of order l:

- The *moment of 0-th order* Ψ_s^0 is defined by $\Psi^0(\mathbf{v}) = 1$. It follows from Eq. (1.88) that $\Psi_s^0 = 1$, which means that the moment of *0-th* order is related to the particle density n_s;

- The *moment of 1-th order* Ψ_s^1 is defined by $\Psi^1(\mathbf{v}) = \mathbf{v}$. Thus, from Eq. (1.88) one obtains $n_s\Psi_s^1 = \mathbf{u}_s$. The first-order moment is related to the average particle velocity $\mathbf{u}_s$;

- The *moment of 2-nd order* Ψ_s^2 is defined by $\Psi^2(\mathbf{v}) = \frac{m_s \mathbf{v}:\mathbf{v}}{2}$, where : refers to the tensor product. The second-order moment can be related to the plasma pressure $P_s = \Psi_s^2 - m_s\mathbf{u}_s : \mathbf{u}_s$. The diagonal terms of P_s^{ii} is proportional to the plasma temperature T_s: $T_s = P_s^{ii}/n_s$, thus $T_s = p_s/n_s$ where $p_s = 1/3\sum_{i=x}^{y} P_s^{ii}$ is the average of the diagonal terms and denotes the isotropic pressure.

All along this thesis, we consider weakly dissipative plasmas, so collisions do not play an important role. In this context, the Vlasov equation represents our starting point for recovering the fluid equations. Thus, multiplying the Eq. (1.82) by Ψ^l and then integrating over the velocity distribution, one obtains the equation for the moment of order l related to the distribution function f_s:

$$\frac{\partial}{\partial t}\left(n_s\langle\Psi^l\rangle_s\right) + \nabla_{\mathbf{r}}\left(n_s\langle\Psi^l\mathbf{v}\rangle_s\right) - \frac{n_s q_s}{m_s}\left[\mathbf{E}\langle\nabla_{\mathbf{v}}\Psi^l\rangle_s - \langle\nabla_{\mathbf{v}}\Psi^l \cdot \frac{\mathbf{v}}{c} \times \mathbf{B}\rangle_s\right] = 0. \tag{1.89}$$

Solving Eq. (1.89) for $l = 0$ allows to retrieve the continuity equation:

$$\frac{\partial n_s}{\partial t} + \nabla\left(n_s\mathbf{u}_s\right) = 0. \tag{1.90}$$

From now on, $\nabla \equiv \nabla_{\mathbf{r}}$. This equation states that the total number of particles s does not change during the plasma evolution.

For $l = 1$, Eq. (1.89) describes the moment transferred to the species s for unit of volume by external and internal forces:

$$m_s n_s\left[\frac{\partial \mathbf{u}_s}{\partial t} + \left(\mathbf{u}_s \cdot \nabla_{\mathbf{r}}\right)\mathbf{u}_s\right] = -\nabla p_s - \nabla : \hat{\Pi}_s + q_s n_s\left[\mathbf{E} + \frac{1}{c}\mathbf{u}_s \times \mathbf{B}\right], \tag{1.91}$$

where $\hat{\Pi}_s$ stands for off-diagonal terms in the tensor of plasma pressure P_s, responsible for internal friction. The first two terms of the right hand-side are the gradient of the plasma pressure decomposed into its diagonal and off-diagonal part respectively, the third term is related to the Lorentz force.

The equation for the energy transfer is found once integrating Eq. (1.89) for $l = 2$

$$\frac{\partial(n_s K)}{\partial t} = -\nabla \cdot \mathbf{G} + \mathbf{j} \cdot \mathbf{E}. \tag{1.92}$$

Here, the plasma energy is written in terms of its total kinetic energy $K = 3/2 n_s T_s + 1/2 m_s n_s u_s^2$ due to microscopic thermal motion of the particles and average kinetic energy respectively. The term $G = \mathbf{q}_s + P_s : u_s + 3/2 n_s T_s \mathbf{u}_s + 1/2 n_s m_s u_s^2 \mathbf{u}_s$ represents the enegy flux composed by the density of thermal flux $\mathbf{q}_s = m_s\langle(\mathbf{v} - \mathbf{u}_s)^2(\mathbf{v} - \mathbf{u}_s)\rangle_s$, the work due to pressure $P_s : \mathbf{u}_s$, the energy transport due to fluid motion and the energy transport due to convection respectively. The second term at the right hand-side stands for the energy dissipation due internal current $\mathbf{j}_s$, the so-called *Joule heating* [43].

Equations (1.90)-(1.92) correspond to a hierarchical system where the equation of order l contains terms of the moment of order $l + 1$. Since the energy flux $\mathbf{q}_s$ corresponds to the moment of third order, and it appears in the moment equation of the second order, another equation is needed to close the system. One may

consider that at zero approximation, $\mathbf{q}_s = 0$, and so the system (1.90)-(1.92) is automatically satisfied. More accurate description of the plasma requires the knowledge of the energy flux, thus different approximations of the energy flux term have been developed. One of the most commun approximation dwells on the Spitzer-Härm theory, which derives the transport coefficients from the kinetic theory with the Landau collision integral [69]. Equations (1.90)-(1.92) are coupled to the Maxwell's equations and to an equation of state which relates the plasma pressure to the density and temperature.

In the next, we consider isotropic plasmas without external magnetic fields, so the plasma pressure tensor is diagonal. For the sake of clarity, here we rewrite the continuity and the moment equation, which are extensively used in the following to study plasma waves:

$$\frac{\partial n_s}{\partial t} + \nabla \left(n_s \mathbf{u}_s \right) = 0, \tag{1.93}$$

$$m_s n_s \left[\frac{\partial \mathbf{u}_s}{\partial t} + \left(\mathbf{u}_s \cdot \nabla \right) \mathbf{u}_s \right] = -\nabla P_s + q_s n_s \left[\mathbf{E} + \frac{1}{c} \mathbf{u}_s \times \mathbf{B} \right]. \tag{1.94}$$

These two equations must be coupled to an equation of state which links the density, pressure and temperature.

1.2.2.3 Waves in unmagnetized plasma

We describe here waves in an unmagnetized plasma within the fluid theory, retrieving the dispersion relation for longitudinal and transverse modes. In particular, we consider small perturbation from the equilibrium term, for which a linear theory can be developed. For these small amplitude waves, the hydrodynamic quantities can be split into an equilibrium and perturbation term: $n_e = n_{s0} + n_{s1}$, $\mathbf{u}_s = \mathbf{u}_{s0} + \mathbf{u}_{s1}$, $\mathbf{E} = \mathbf{E}_0 + \mathbf{E}_1$ and $\mathbf{B} = \mathbf{B}_0 + \mathbf{B}_1$. At the equilibrium, we assume $n_{s0} = const$, $\mathbf{u}_{s0} = 0$, $\mathbf{E}_0 = 0$ and $\mathbf{B}_0 = 0$.

Longitudinal electrostatic waves: Electron plasma waves Let us suppose $T_e \neq 0$ and ions at rest. In order to find electron plasma waves, we start from the fluid equations (1.93)-(1.94) for electrons only. The equation of state needed for closing the plasma system reads:

$$P_e = T_e n_e. \tag{1.95}$$

Accounting for the fact that the electron temperature is related to the density by the condition of adiabaticity, the plasma pressure gradient reads

$$\nabla P_e = \gamma T_e \nabla n_e. \tag{1.96}$$

where $\gamma = (g + 2/g)$ is the ratio of specific heats, depending on degree of freedom g for the electron motion. Injecting the expressions for small amplitude waves into Eq. (1.93)-Eq. (1.94) and neglecting all the quantities higher than the first order, we obtain linearized equations for the electron plasma wave. Performing then Fourier transform in space and time we have:

$$-i\omega n_{e1} + ikn_{e0}u_{e1} = 0 \tag{1.97}$$

$$-i\omega n_{e0} m_e u_{e1} = -3iT_e k n_{e1} - e n_{e0} E_1 \tag{1.98}$$

$$ikE_1 = -4\pi e n_{e1} \tag{1.99}$$

The condition of non-zero solution for this system of three linear equations gives the dispersion relation for an electron plasma wave:

$$\omega^2 = \omega_{pe}^2 + 3v_{te}^2 k^2. \tag{1.100}$$

Such a dispersion relation can be rewritten in terms of the Debye length as:

$$\omega = \omega_{pe}\sqrt{1 + 3k^2\lambda_D^2}. \tag{1.101}$$

It could be shown [48,63,64] that weakly damped electron plasma waves exist only if the thermal correction $3k^2\lambda_D^2$ is small, and consequently, $\omega \approx \omega_{pe}$. From Eq. (1.100), the electron waves, called also Langmuir waves, exist in plasma at a frequency approximately equal to the electron plasma frequency, with a small correction due to the thermal motion. When the thermal correction increases, the phase velocity of Langmuir waves approaches closer to the electron thermal velocity, and the wave may undergo Landau damping. This effect is not accounted for within the fluid description because it stands for a kinetic effect. Therefore, the linear fluid wave description applies when Landau damping is negligible, $k\lambda_D << 1$, otherwise the waves must be described within the kinetic approach.

Longitudinal electrostatic waves: ion acoustic waves As for electron plasma waves, we retrieve here the dispersion relation for ion acoustic waves in one-dimensional linear approximation by assuming that:

- electrons inertia is negligible, since $m_e << m_i$: the electrons move instantaneously along with ions;
- electrons are considered isothermal because their temperature is equilibrated on ion time-scale;
- ion equation of state is adiabatic, similar to the electron equation of state in the electron plasma wave.

With these hypotheses, the equations governing the plasma dynamics are

$$en_e E = -\frac{dP_e}{dx} = -T_e\frac{\partial n_e}{\partial x}; \tag{1.102}$$

$$\frac{\partial n_i}{\partial t} + \frac{\partial\left(n_i u_i\right)}{\partial x} = 0; \tag{1.103}$$

$$m_i n_i\left[\frac{\partial u_i}{\partial t} + v_i\frac{\partial u}{\partial x}_i\right] = -\frac{\partial P_i}{\partial x} + Zen_i E. \tag{1.104}$$

Linearizing such equations one obtains

$$en_{e0}E_1 = -T_e\frac{dn_{e1}}{dx}, \tag{1.105}$$

$$\frac{\partial n_{i1}}{\partial t} + n_{i0}\frac{\partial u_{i1}}{\partial x} = 0, \tag{1.106}$$

$$m_i n_{i0}\frac{\partial u_{i1}}{\partial t} = -3T_i\frac{\partial n_{i1}}{\partial x} + Zen_{i0}E_1 \tag{1.107}$$

where $\gamma_i = 3$. Combining the time derivative of Eq. (1.106), the spatial derivative of Eq. (1.107), accounting for Eq. (1.105) and the quasi-neutrality condition $Zn_i = n_e$, one has:

$$\frac{\partial^2 n_{i1}}{\partial t^2} - c_s^2\frac{\partial^2 n_{i1}}{\partial x^2} = 0, \tag{1.108}$$

where $c_s^2 = (3T_i + ZT_e)/m_i$ is the sound speed. This equation describes the propagation of ion acoustic waves (IAWs), and provides the dispersion relation of IAWs in the Fourier space:

$$\omega^2 = c_s^2 k^2. \tag{1.109}$$

If the quasi-neutrality condition is not satisfied, the dispersion relation Eq. (1.109) is corrected as follows [63]

$$\omega^2 = k^2\left(\frac{3T_i}{m_i} + \frac{ZT_e/m_i}{1 + k^2\lambda_D^2}\right). \tag{1.110}$$

So, for small value of $k^2\lambda_D^2$, one retrieves the Eq. (1.109). In cases where $k^2\lambda_D^2 >> 1$, one finds pure low frequency ion plasma oscillations at frequency ω_{pi}. In this range of wavelengths, the ion kinetic effects become important leading to Landau damping of ion plasma waves.

Transverse electromagnetic waves Transverse perturbation may propagate as an electromagnetic wave in plasmas. Since the electric field is perpendicular to the propagation direction, one has $\nabla \cdot \mathbf{E} = 0$ and $\nabla \cdot \mathbf{B} = 0$. In order to find the dispersion relation, one can consider ions to be at rest due to the large difference between ion and the electron mass. Furthermore, transverse wave does not produce plasma density perturbation, and $n_{e1} = 0$. The dispersion relation is found by linearizing the moment electron plasma equation and the Maxwell's equations:

$$m_e\frac{\partial \mathbf{u}_{e1}}{\partial t} = -e\mathbf{E}_1, \tag{1.111}$$

$$\mathbf{j}_{e1} = -en_{e0}\mathbf{u}_{e1}. \tag{1.112}$$

$$\nabla \times \mathbf{E_1} = -\frac{1}{c}\frac{\partial \mathbf{B_1}}{\partial t}, \tag{1.113}$$

$$\nabla \times \mathbf{B_1} = \frac{4\pi}{c}\mathbf{j}_{e1} + \frac{1}{c}\frac{\partial \mathbf{E_1}}{\partial t}, \tag{1.114}$$

A relation between the electric field and the density current is found by taking the time derivative of Eq. (1.112) and combining it with Eq. (1.111), giving

$$\frac{\partial \mathbf{j}_{e1}}{\partial t} = \frac{e^2 n_{e0}}{m_e}\mathbf{E}_1. \tag{1.115}$$

The relation dispersion of electromagnetic waves in plasmas is retrieved once combining the curl of Eq. (1.113) and the time derivative of Eq. (1.114), considering the one-dimensional problem and considering Eq. (1.115):

$$\omega^2 = \omega_{pe}^2 + c^2 k^2. \tag{1.116}$$

From this relation, the maximum density at which an electromagnetic wave can propagate can be evaluated. Defining the refraction index $N = ck/\omega$, Eq. (1.116) reads

$$N(x) = \sqrt{1 - \frac{\omega_{pe}^2(x)}{\omega^2}}. \tag{1.117}$$

For $\omega_{pe} > \omega$, the refractive index becomes imaginary, and the light cannot further penetrate the plasma being reflected. The density at which it occurs is called "*critical density*" n_c and it writes

$$n_c = \frac{m_e \omega^2}{4\pi e^2}. \tag{1.118}$$

The critical density expression can be rewritten as a function of the laser wavelength:

$$n_c = 1.1 \times 10^{21} \left(\frac{\lambda}{\mu\mathrm{m}}\right)^{-2}, \tag{1.119}$$

where n_c is in units of cm^{-3}. Accounting for Eq. (1.70) and Eq. (1.119), the refractive index can be also written in terms of the critical density and local plasma density:

$$N(x) = \sqrt{1 - \frac{n_e(x)}{n_c}}. \tag{1.120}$$

The plasma permittivity then reads

$$\varepsilon = N^2(x) = 1 - \frac{n_e(x)}{n_c}. \tag{1.121}$$

The dispersion relation for the the longitudinal and transverse plasma waves present the same frequency cut-off ω_{pe} which is proportional to the square root of the local plasma density. This is not the case for ion waves, which have much lower frequency. Figure 1.4 shows the dispersion relations for all the three waves. The green curve corresponds to the electron plasma wave Eq. (1.101), the blue curve refers to the ion acoustic wave Eq. (1.109), and the gray curve to the electromagnetic wave Eq. (1.116). The dashed line refers to the cut-off $\omega = \omega_{pe}$. The electron plasma dispersion curve a slightly diverges from the cut-off because the thermal term of Eq. (1.101) represents a small correction. The same frequency cut-off is evidenced also in the electromagnetic wave dispersion relation, whose frequency increases as a function of the wavevector k.

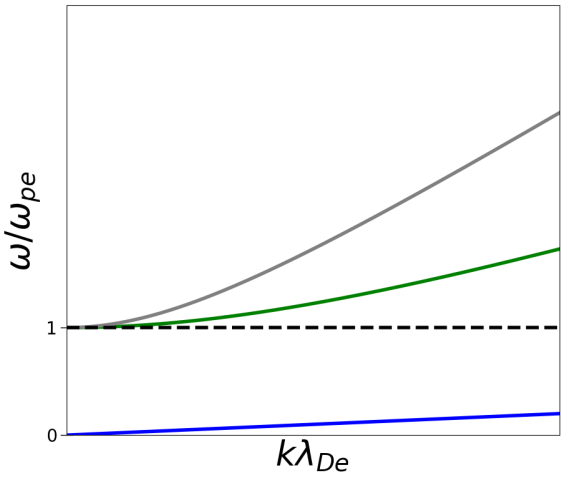

Figure 1.4: Dispersion relation of plasma waves. The gray curve corresponds to the electromagnetic wave, the green curve corresponds to the electron wave and the blue curve corresponds to the ion wave. The dashed line refers to the cut-off $\omega = \omega_{pe}$.

1.3 Laser-plasma coupling in ICF and SI

Depending on the laser intensity I_0 and the laser wavelength λ, laser-plasma interaction can be divided into three different regimes [60]: the low, the moderate and high intensity regime. The low intensity regime is characterized by $I_0\lambda^2 < 10^{14}$ W/cm^2 μm^2, and the laser-plasma coupling consists mainly of laser absorption due to collisional or resonance mechanisms. The moderate intensity regime, where 10^{14} W/cm^2 μm^2 $< I_0\lambda^2 < 10^{18}$ W/cm^2 μm^2, comprises low intensity effects competing with laser ponderomotive self-focusing and laser-plasma instabilities, as beam filamentation and parametric instabilities. For $I_0\lambda^2 > 10^{18}$ W/cm^2 μm^2, referred to as high intensity regime, the plasma electrons undergo relativistic motion, and relativistic effects take place. The regime explored in this thesis pertains to the second case, being the framework where ICF and SI laser-plasma coupling occurs.

In the following sections, we recall several laser-plasma interaction physics occurring at low and moderate regime.

1.3.1 Low intensity regime: linear laser-plasma coupling

1.3.1.1 Collisionless plasma: light reflection

Let us consider a monochromatic electric field $\mathbf{E}(\mathbf{r}, t) = \mathbf{E}_0(\mathbf{r}, t)e^{-i\omega t}$ propagating in a plasma, with a frequency ω higher than the electron plasma frequency. Ions are then considered at rest, and the fluid electron equations govern the plasma dynamics. Due to the low intensity assumption, second order effects can be disregarded. Also, for the nonrelativistic assumption, the term $\mathbf{u}\times\mathbf{B}$ does not play a role in the electron dynamics. According to these considerations, at the first order, the linearized density current rewrites $\mathbf{j}_e = \mathbf{j}_{e1}$, and Eq. (1.115) reads

$$\mathbf{j}_{e1} = -\frac{i\omega_{pe}^2}{4\pi\omega}\mathbf{E}_0(\mathbf{r},t)e^{-i\omega t}, \tag{1.122}$$

where we have assumed $\mathbf{j}_{e0} = 0$. Substituting Eq. (1.122) into Eq. (1.4), taking the curl of Eq. (1.3), combining them and considering standard vector identities, the electric field equation in the frequency domain writes [45]

$$\nabla^2\mathbf{E} - \nabla(\nabla\cdot\mathbf{E}) + \frac{\omega^2}{c^2}\varepsilon\mathbf{E} = 0, \tag{1.123}$$

where ε is the plasma permittivity defined in Eq. (1.121).

Plasma properties influence the solution of Eq. (1.123), and so the fields dynamics. If the plasma is homogeneous, then $\nabla(\nabla\cdot\mathbf{E}) = 0$ and $\nabla\varepsilon = 0$. If the wave amplitude is a plane wave such as $\mathbf{E}_0(\mathbf{r},t) = \mathbf{E}_0 e^{i\mathbf{k}\cdot\mathbf{r}}$ and $n_{e0} < n_c$, one retrieves the dispersion relation of electromagnetic waves in plasma as in Eq. (1.116). If $n_{e0} > n_c$, the radiation cannot enter the plasma and it is reflected at the plasma surface.

In case of inhomogeneous plasmas, if the plasma density at the plasma surface is smaller than n_c and then increases, the light propagates up to the critical density, being then reflected since it cannot propagate further. In order to analyse the light reflection neglecting energy loss, let us consider the propagation of a monochromatic wave in a collisionless plasma slab. We suppose that the plasma slab lies into the (x,y)-plane, and that an s-polarized planar wave entering the plasma with an angle of incidence θ with respect the plasma slab normal. The electric field amplitude rewrites $\mathbf{E}_0 = E_{0z}(x,y)\hat{z}$. Considering that the plasma density n_{e0} is inhomogeneous along the x-axis $n_{e0} = n_{e0}(x)$, and letting θ be the inclination of the wave vector with respect the plasma density gradient, Eq. (1.123) for the electric field amplitude rewrites

$$\frac{d^2E_{0z}}{dx^2} + \frac{d^2E_{0z}}{dy^2} + \frac{\omega^2}{c^2}\varepsilon(x)E_{0z} = 0. \tag{1.124}$$

Since the density gradient is orientated along x, the solution of Eq. (1.124) can be factorized as follows: $E_{0z} = E_{0z}(x)E_{0z}(y)$, and the term $E_{0z}(y)$ is retrieved once observed that the y component of the wavevector $\mathbf{k}$ must be conserved: $E_{0z}(y) = \exp(ik_y y)$, where $k_y = \omega\sin\theta/c$. Injecting $E_{0z}(y)$ in Eq. (1.124), one obtains

$$\frac{d^2E_{0z}}{dx^2} + \frac{\omega^2}{c^2}\left(\varepsilon(x) - \sin^2\theta\right)E_{0z} = 0. \tag{1.125}$$

According to Eq. (1.125), the light propagates up to the point where $\varepsilon(x) = \sin^2\theta$, and then it is reflected. If the plasma density varies linearly along x, i.e. $n_{e0} = n_c x/L$, where L is the position of the critical density, and supposing that the light enters the slab at $x = 0$, the turning point appears for $x = L\cos^2\theta$, so for densities less than the critical density. Figure 1.5 illustrates the light reflection for an s-polarized electric field propagating into a plasma slab. The dashed black line refers to the trajectory of the light. For $\theta = 0$, the turning point becomes $x = L$, and the wave trajectory resembles a straight line.

If the light is p-polarized, as displayed in the Figure 1.5 by the electric field vector $\mathbf{E}$ in blue, the wave undergoes resonant absorption. This effect can create energetic electrons and plays an important role in ICF even at low intensities, however the resonant absorption is not considered in this thesis.

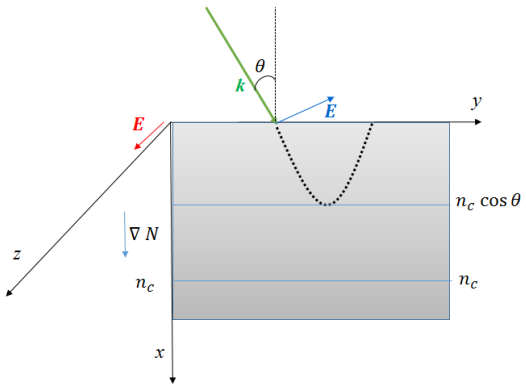

Figure 1.5: Light reflection in a plasma slab. The red electric field vector **E** refers to an s-polarized wave, the blue vector to a p-polarized wave.

1.3.1.2 Collisional effects: light absorption

We now review the effect of electron-ion collisions on the wave propagation. In order to describe this process, we solve Eq. (1.124) by using Wentzel-Kramers-Brillouin (WKB) approximation [45]. This method considers the slowly varying approximation used in Sec. 1.1, and allows to solve a system of linear differential equations with spatially varying coefficients. If the plasma permittivity slowly depends on the spatial coordinates, considering an electric field in the WKB approximation propagates along the x-axis, the electric field reads

$$E_{0z}(x) = \tilde{E}_0(x) e^{i\frac{\omega}{c}\int_0^x \Phi(x')dx'} \tag{1.126}$$

where the integral is taken along the wave trajectory. This expression supposes that the wave enters the plasma at $x = 0$. Plugging Eq. (1.126) into Eq. (1.124), we obtain an equation containing terms of different orders in derivatives with respect to x. At zero order, we find an equation for the phase (see Sec. 1.1)

$$\Phi(x') = \sqrt{\varepsilon}. \tag{1.127}$$

At first order, we obtain an equation for the wave amplitude. Posing at $x = 0$ the plasma-vacuum interface, and combining the first order solution to Eq. (1.127), the electric field reads

$$E_{0x} = \frac{E_v}{\sqrt[4]{\varepsilon}} e^{i\frac{\omega}{c}\int_0^x \sqrt{\varepsilon(x')}dx'} \tag{1.128}$$

where E_v is the electric field amplitude in the vacuum. From Eq. (1.128), it follows that the electric field amplitude decreases along the propagation direction if there is a positive imaginary part of plasma permittivity ε, which physically means that electron-ion collisions are accounted for. Let us consider electrons at thermal equilibrium, and ions acting as a fixed background which simply neutralizes the electron charge. For an electron fluid, the rate of electrons moment changes due to collisions with ions is

$$\left(\frac{\partial n_e \mathbf{u}_e}{\partial t}\right)_i = -\nu_{ei} n_e \mathbf{u}_e \tag{1.129}$$

Adding this term to Eq. (1.115), the density current reads

$$\mathbf{j} = -\imath \frac{e^2 n_e \mathbf{E}}{m_e(\omega + \imath\nu_{ei})}. \tag{1.130}$$

and the permittivity ε becomes a complex value: in fact, solving the dispersion equation for electromagnetic modes propagating as in Sec. 1.2.2.2, considering a complex density current, and supposing that $\nu_{ei} << \omega$, accounting for $n_e/n_c = \omega_{pe}^2/\omega^2$, the plasma permittivity from Eq. (1.121) can be rewritten as

$$\varepsilon = 1 - \frac{\omega_{pe}^2}{\omega(\omega + \imath\nu_{ei})}. \tag{1.131}$$

Consequently, the dispersion relation for electromagnetic waves becomes

$$\omega^2 = c^2k^2 + \omega_{pe}^2 \left(1 - \frac{\imath\nu_{ei}}{\omega}\right). \tag{1.132}$$

Substituting Eq. (1.131) in Eq. (1.128) allows to find a solution for electric field in an absorbing plasma in the WKB approximation.

In an inhomogeneous plasma, the most of light absorption occurs around the critical density. However, it is useful to evaluate the rate of the power absorption along the whole spatial density profile. The spatial rate of intensity variation reads

$$\frac{dI}{dx} = -\kappa I, \tag{1.133}$$

where κ is the spatial collisional damping rate which is equal to two times the imaginary part of the k-vector. To evaluate κ, one may consider that the collision frequency depends on plasma density through Eq. (1.73), and solving Eq. (1.132) to find an expression for the wavevector k. In a plasma of spatial-varying density the spatial damping rate can be rewritten as follows [60]

$$\kappa = \left(\frac{\nu_{ei}(n_e(x))}{c}\right)\left(\frac{n_e(x)}{n_c}\right)\left(1 - \frac{n_e(x)}{n_c}\right)^{-1/2}, \tag{1.134}$$

from which it implies that if the wave goes through a slab of plasma of a length L, the fraction of power absorbed reads

$$f_A = 1 - \exp\left(-\int_0^L \kappa dx\right), \tag{1.135}$$

where $f = (I_{inc} - I_{out})/I_{inc}$, and I_{out} and I_{inc} are the outgoing and incident intensity, respectively. Equation (1.135) is valid for any plasma profile, and its integral depends on the plasma density profile. In Chapter 4, we solve this equation for a linear plasma density profile.

1.3.2 Moderate intensity regime: Nonlinear laser-plasma coupling

In this section, nonlinear effects for 10^{14} W/cm^2 μm^2 $< I_0\lambda^2 < 10^{18}$ W/cm^2 μm^2 are reviewed, especially the ones treated in this thesis: laser beam self-focusing and filamentation instability, with a short excursion into parametric instabilities.

1.3.2.1 Ponderomotive force in laser-plasma coupling

High intensity laser beams exert on the plasma electrons a *ponderomotive force*, which acts transversally to the laser propagation direction in case of long laser pulses. In order to recover the expression for the ponderomotive force, we consider a high frequency laser which does not directly perturb the ion dynamics on laser oscillation time-scales. The ions provide a background of positive charge and their behavior will be retrieved from the feedback of the electron motion on longer time-scales. We start by determing an expression for the ponderomotive force acting on one electron [60]. After that, we extend the problem to a plasma with an electron density n_{e0}, and eventually we see how ions are influenced by electron motion.

When the laser beam interacts with an electron, the particle experiences the Lorentz force, and its velocity dynamics changes accordingly to the moment equation:

$$m_e \frac{d\mathbf{u}_e}{dt} = -e\left[\mathbf{E} + \frac{\mathbf{u}_e}{c} \times \mathbf{B}\right]. \tag{1.136}$$

The electric and magnetic fields are described as components of a monochromatic wave, which we present as $\mathbf{E}(\mathbf{r},t) = \mathbf{E}_0(\mathbf{r})\cos\omega t$, and $\mathbf{B}(\mathbf{r},t) = -c/\omega\nabla\times\mathbf{E}_0(\mathbf{r})\sin\omega t = \mathbf{B}_0(\mathbf{r})\sin\omega t$. We note that the two fields affect the electron motion at different orders since relativistic effects are weak in this intensity regime. Thus, $e\mathbf{u}\times\mathbf{B}/c$ is of the second order compared to than $e\mathbf{E}$. So, considering that at the equilibrium $\mathbf{u}_{e0} = 0$, linearizing Eq. (1.136), the electron velocity evaluated at position $\mathbf{r}_0$ reads

$$\mathbf{u}_{e1}(\mathbf{r}_0) = -\frac{e\mathbf{E}_0(\mathbf{r}_0)\sin\omega t}{m_e\omega}. \tag{1.137}$$

The expression for $\mathbf{r}_1$ is obtained once integrating Eq. (1.137) from Newton's law $\mathbf{u}_{e1}(\mathbf{r}_0) = d\mathbf{r}_1/dt$:

$$\mathbf{r}_1 = \frac{e\mathbf{E}_0(\mathbf{r}_0)\cos\omega t}{m_e\omega^2}. \tag{1.138}$$

The electron oscillates in the light field at a frequency ω. In order to evaluate the complete dynamics, we must account for the second order effects induced by the magnetic field, i.e. modification of the electron dynamics at the position $\mathbf{r}_1$. Here, a Taylor's expansion of the electric field around the position $\mathbf{r}_1$ gives: $\mathbf{E}_0 = \mathbf{E}_0(\mathbf{r}_0) + (\mathbf{r}_1\cdot\nabla)\mathbf{E}_0(\mathbf{r}_0)$. Consequently, the moment equation at the second order reads

$$m_e \frac{d\mathbf{u}_{e2}}{dt} = -e\left[(\mathbf{r}_1\cdot\nabla)\mathbf{E}_0(\mathbf{r}_0) + \frac{\mathbf{u}_{e1}}{c}\times\mathbf{B}_0(\mathbf{r}_0)\right]. \tag{1.139}$$

Substituting Eq. (1.138) in Eq. (1.139), averaging over the oscillation period $T = 2\pi/\omega$ and recalling some vectorial algebra relations, we obtain the average force $\mathbf{f}_P^e$ acting over an electron:

$$\mathbf{f}_P^e = m_e\langle\frac{d\mathbf{u}_{e2}}{dt}\rangle_T = -\frac{e^2}{4m_e\omega^2}\nabla\mathbf{E}_0^2. \tag{1.140}$$

The ponderomotive potential ϕ_P is defined from Eq. (1.140):

$$\phi_P = -\frac{e}{4m_e\omega^2}\mathbf{E}_0^2. \tag{1.141}$$

For a plasma of electron density n_{e0}, the ponderomotive force acting on a unit of volume writes

$$\mathbf{F}_P = n_{e0}\mathbf{f}_P^e = -\frac{\omega_{pe}^2}{16\pi\omega^2}\nabla\mathbf{E}_0^2. \tag{1.142}$$

Equation (1.142) describes a plasma perturbation over a time-scale longer than the electron oscillation period due to the laser intensity gradient: the electrons are transversely pushed in the direction where the intensity decreases. Such a displacement creates an electric charge separation that induces a Coulomb potential ϕ_c tending to restore the charge neutrality between electrons and ions. The total force acting on the electron fluid $\mathbf{F}_e^{tot}$ is

$$\mathbf{F}_e^{tot} = \mathbf{F}_P^e - n_{e0}e\mathbf{E}_{cs}, \tag{1.143}$$

where $\mathbf{E}_{cs} = -\nabla\phi_c$ is the electrostatic restoring field. The ion motion is influenced by such a charge separation through the potential ϕ_c, and the force acting on the ions reads $\mathbf{F}_i^{tot}$

$$\mathbf{F}_i^{tot} = n_{i0}Ze\mathbf{E}_{cs}. \tag{1.144}$$

where Ze ion charge. Combining Eqs. (1.143) and (1.144), when the quasi-neutrality is re-established, the total force acting on the plasma reads

$$\mathbf{F}_e^{tot} + \mathbf{F}_i^{tot} = \mathbf{F}_P^e. \tag{1.145}$$

From these considerations, it is clear that the ponderomotive force changes the ion dynamics as well, and it must be included into the ion equation (1.108). To do so, let us consider that the electrons constitute an isothermal fluid, the electron pressure gradient reads $\nabla P_e = T_e\nabla n_e$. The ion fluid can be described by an adiabatic equation of state: $\nabla P_i = 3T_i\nabla n_i$. In order to find the ion dynamics, let us consider the equations for the electron and ion momenta including the ponderomotive force. They read respectively

$$m_e n_e\frac{\partial\mathbf{u}_e}{\partial t} + n_e m_e(\mathbf{u_e}\cdot\nabla)\mathbf{u_e} = -T_e\nabla n_e + en_e\nabla\phi_c + en_e\nabla\phi_P, \tag{1.146}$$

$$m_i n_i\frac{\partial\mathbf{u}_i}{\partial t} + n_i m_i(\mathbf{u_i}\cdot\nabla)\mathbf{u_i} = -3T_i\nabla n_i - Zen_i\nabla\phi_c, \tag{1.147}$$

In the low frequency limit, the electron inertia can be disregarded. Considering then a decomposition into an unperturbed term denoted with index "0" and small perturbation contribution with index "1", and plugging the electron pressure expression into Eq. (1.146), the Coulomb potential from Eq. (1.146) reads:

$$en_e\nabla\phi_c = T_e\nabla n_{e1} - en_e\nabla\phi_p \tag{1.148}$$

Injecting this expression into Eq. (1.147), accounting for ion density conservation equation at first order, and expanding also the ion response into an equilibrium and small perturbation terms, one obtains

$$m_i n_{i0}\frac{d\mathbf{u}_{i1}}{dt} = -3T_i\nabla n_{i1} - ZT_e\nabla n_{i1} + Zen_i\nabla\phi_p. \tag{1.149}$$

Taking the gradient of Eq. (1.149), and considering Eq. (1.141), the equation of the ion dynamics becomes

$$\left(\partial_t^2 - c_s^2\nabla^2\right)\frac{n_{i1}}{n_{i0}} = -c_s^2\frac{\omega_{pe}^2}{16\pi\omega^2}\nabla^2\mathbf{E}_0^2. \tag{1.150}$$

From Eq. (1.150), at a stationary state, the ion density locally depends on the laser intensity

$$\frac{\delta n}{n_{i0}} = -\beta E_0^2. \tag{1.151}$$

where $\delta n = n_i(x)/n_{i0} - 1$ is the amplitude of the plasma density perturbation and $\beta = e^2/[4m_e\omega^2(T_e + 3T_i/Z)]$. However, to include strong density nonlinearity and reproduce the Boltzmann density depletion as described in [70, 71], the term n_{i1}/n_{i0} is usually replaced by $\log(1 - n_{i1}/n_{i0})$, and the plasma response reads

$$\frac{\delta n}{n_{i0}} = e^{-\beta E_0^2} - 1. \tag{1.152}$$

As a consequence, in the moderate intensity regime, the plasma density can be strongly modified by the laser ponderomotive force. The density modification induces an increase of the refraction index near the laser beam axis. The field then experiences a refractive index gradient which makes the plasma acting as a convergent lens. Such a behaviour can be better illustrated when considering the laser described as a Gaussian beam.

Self-focusing of a Gaussian beam. Let us review the effect of ponderomotive force when a beam has a Gaussian profile [24]. We consider a nonlinear stationary solution Eq. (1.152) for a plasma response to the laser propagation. With this assumption and supposing a monochromatic field $E = \mathrm{Re}[\mathrm{E}_0 \exp(-\mathrm{i}\omega\mathrm{t})]$, the electric field as in Eq. (1.123) rewrites

$$-\omega^2 E_0 + c^2\nabla^2 E_0 = -\omega_{pe}^2 e^{-\beta E_0^2} E_0. \tag{1.153}$$

Supposing a spatially slowing varying electromagnetic field, the wave reads $E_0(\mathbf{r}, t) = A(\mathbf{r})\exp(\imath kx)$, where $A(\mathbf{r})$ stands for the slowing varying amplitude in space. Equation (1.153) becomes

$$-2\imath kc^2\frac{\partial A}{\partial x} + c^2\nabla_\perp^2 A - \Gamma^2 A + \omega_{pe}^2 A[1 - \exp(-\beta\left|A\right|^2)] = 0, \tag{1.154}$$

where $k^2c^2 + \omega_{pe}^2 - \omega^2 = \Gamma^2$ corresponds to dispersion relation shift due to electron density perturbation, $\nabla_\perp$ is the transverse gradient.

Assuming the geometrical optics framework, $A(\mathbf{r})$ can be decomposed in an amplitude and phase:

$$A(\mathbf{r}) = A_0(\mathbf{r})\exp(\imath k\phi),$$

Assuming axially symmetric beams, introducing the transverse coordinate $r_\perp$, Eq.(1.154) can be split into two equations for the real and imaginary part, respectively:

$$-c^2k^2A_0\left[2\frac{\partial\phi}{\partial x} + \left(\frac{\partial\phi}{\partial r_\perp}\right)^2\right] + c^2\left(\frac{1}{r_\perp}\frac{\partial A_0}{\partial r_\perp} + \frac{\partial^2 A_0}{\partial r_\perp^2}\right) + \omega_{pe}^2 A_0[1 - \exp(-\beta\left|A_0\right|^2)] - \Gamma^2 A_0 = 0, \tag{1.155}$$

$$2\left(\frac{\partial A_0}{\partial x}+\frac{\partial\phi}{\partial r}\frac{\partial A_0}{\partial r_\perp}\right)+A_0\left(\frac{1}{r_\perp}\frac{\partial\phi}{\partial r_\perp}+\frac{\partial^2\phi}{\partial r_\perp^2}\right)=0, \tag{1.156}$$

At this point, we assume that the amplitude A_0 has a Gaussian profile:

$$A_0^2=\frac{E_0^2}{f^{1+m}}\exp\Big(-\frac{2r_\perp^2}{w_0^2f^2}\Big), \tag{1.157}$$

where $f=w(x)/w_0$ dimensionless beam width, and $m=0$ or 1 depending if the problem is two- or three-dimensional, respectively. In order to reproduce a Gaussian beam profile, the phase ϕ writes (see Sec. 1.1.2)

$$\phi(x,r)=\frac{r_\perp^2}{2f}\frac{df}{dx}+\tilde{\phi}(x), \tag{1.158}$$

which depends on $r_\perp$ and x. Here we have also added a term $\tilde{\phi}(x)$ which accounts for a nonlinear perturbation of the phase.

Since we are considering paraxial beams, $r_\perp^2<<(w_0^2f^2)$, Eq. (1.155) is split in two equations of the 0-th and 2-nd order in $r_\perp$. At the 0-th order in $r_\perp$, accounting for Eqs. (1.157) and (1.158), Eq.(1.156) produces the equation for the phase $\tilde{\Phi}$:

$$\frac{d\tilde{\phi}}{dx}=-\frac{2}{w_0^2k^2f^2}+\frac{\omega_{pe}^2-\Gamma^2}{2c^2k^2}-\frac{\omega_{pe}^2}{2c^2k^2}\exp\left(-\frac{\beta E_0^2}{f^{m+1}}\right). \tag{1.159}$$

Hence, $\tilde{\Phi}$ takes into account the contribution of nonlinear effects to the eikonal. At 2-nd order in $r_\perp$, we retrieve the equation for f

$$\frac{d^2f}{dx^2}=\frac{4}{k^2w_0^4f^3}-\frac{2\beta E_0^2}{k^2w_0^2f^{m+2}}\frac{\omega_{pe}^2}{c^2}\exp(-\beta E_0^2/f^{m+1}). \tag{1.160}$$

The first term in the right hand-side describes the beam diffraction, whereas the second term is responsible for the ponderomotive effects.

The difference between the 2D and 3D geometry in Eq. (1.160) dwells in the power of f in the ponderomotive term: while in 3D, the ponderomotive term scales as $\exp(-\beta E_0^2/f^2)/f^3$, in 2D it scales as $\exp(-\beta E_0^2/f)/f^2$. This is explained by energy conservation arguments: in 3D the power of a Gaussian beam is proportional to $1/f^2$, where in 2D to $1/f$, according to Eqs. (1.33) and (1.28). As a consequence, ponderomotive effects are expected to be stronger in 3D than in 2D.

An important parameter for ponderomotive effects evaluation is the critical power. Early studies of critical power started in the 60s were related to the Kerr effect induced by lasers propagating in dielectrics [72–74], and then in plasmas [24, 75–79]. From [24], the threshold condition at which the ponderomotive effects equilibrate the diffraction requires that the beam propagates in the density channel without changing its width when it enters the plasma region with a planar wavefront, i.e. the beam is focused at the vacuum-plasma interface. As a consequence of diffraction and ponderomotive effects equilibrium, the beam remains self-trapped inside the plasma channel with no width modification. In the 3D case (m=1), this is recovered by imposing in Eq. (1.160) that the second time derivative of f is zero, giving

$$E_{0c}^2 = \frac{\mathtt{Re}\left[\mathcal{W}\left(\frac{-2c^2}{w_0^2\omega_{pe}^2}\right)\right]}{\beta}, \tag{1.161}$$

where E_{0c} is the critical electric field amplitude to obtain a steady state and $\mathtt{Re}\,[\mathcal{W}]$ stands for the real-value of the Lambert function $\mathcal{W}$ [80]. This function $\mathcal{W}(a)$ is the solution of equation $\mathcal{W}\exp(\mathcal{W}) = \alpha$, with α being a real number. Once supposing $w_0 >> c/\omega_{pe}$, the condition Eq. (1.161) can be expressed in terms of laser intensity:

$$I_0^c = 8\,\frac{n_c^2(T_e + 3T_i/Z)c^3}{n_{e0}w_0^2\omega^2}\sqrt{1 - \frac{n_{e0}}{n_c}}, \tag{1.162}$$

where I_0^c is called *critical intensity*, and it gives the characteristic laser intensity at which ponderomotive effects begin to affect the beam dynamics when the beam is focused on the plasma-vacuum interface. In 3D, the total power P carried out by the laser beam is calculated from Eq. (1.28). Then, the critical power of a Gaussian beam propagating into an underdense plasma (corresponding to the limit $w_0 >> c/\omega_{pe}$) in cylindrical symmetry reads [81, 82]:

$$P_c^{3D} = 1.86 \times 4\pi\,\frac{n_c^2(T_e + 3T_i/Z)c^3}{n_{e0}\omega^2}\sqrt{1 - \frac{n_{e0}}{n_c}}, \tag{1.163}$$

where the coefficient 1.86 was calculated numerically in Ref. [83].

The critical power depends on the dimension of the problem. In 2D, the power depends on the beam waist because of a lower dimension. Accounting for Eq. (1.33) and Eq. (1.28), the conversion from the 3D critical power to 2D critical power while keeping the same critical intensity Eq. (1.162) (in the limit $w_0 >> c/\omega_{pe}$) and the same beam width reads

$$P_c^{2D} = \frac{hP_c^{3D}}{\sqrt{\pi}w_0}, \tag{1.164}$$

where h is the unit length in the third dimension. When the power of a Gaussian beam overcomes the critical power, whether in 2D or 3D geometry, the beam width decreases and the laser intensity increases. Figure 1.6a illustrates a solution of Eq. (1.160) for $I_0/I_0^c = 3$ and for the initial condition $f_0 = 1$, which corresponds to a beam entering the plasma with a plane wavefront in 2D (m=0). The intensity enhancement according to Eq. (1.35) $I_{max}/I_0 = 1/f$ (green line) and the dimensionless beam width f (red line) are plotted as a function of x in Fig. 1.6a. The ponderomotive force induces a density depletion according to Eq. (1.152) or Eq. (1.151). In such a density channel, the laser intensity increases and beam width decreases. After reaching the first maximum, diffraction prevails over the ponderomotive force, and the beam begins to diverge, until the initial conditions are restored, so the beam converges again. The beam is then trapped inside the density cavity, undergoing oscillations. The beam width reduction stage is called *beam ponderomotive self-focusing* because it is due to ponderomotive effects. In this stationary solution, laser self-focusing is characterized by the intensity enhancement I_{max}/I_0: the stronger the beam power is, the higher the intensity enhancement appears. However, the intensity enhancement depends on the geometry, as displayed in Fig. 1.6b: here, I_{max}/I_0 evaluated in 3D (orange line) and in 2D (blue line) from Eq. (1.160) for m=1 and m=0, respectively. It is compared for different values of the initial beam intensity I_0/I_0^c. In 3D, $I_{max}/I_0 = 1/f^2$ according to Eq. (1.34). In both cases,

the ponderomotive force induces beam self-focusing for $I_0/I_0^c > 1$, but in 3D ponderomotive effects are more important than in 2D given that plasma depletion takes place in two transverse dimensions. This scenario concerns the situation where a speckle is described as a Gaussian beam with the same width w_0 in 2D and 3D geometry. In cases where the beam intensity is the same, but the width of the beam is different in 2D and 3D geometry, Eq. (1.164) writes:

$$P_c^{2D} = \frac{hP_c^{3D}}{\sqrt{\pi}} \frac{w_{2D}}{w_{3D}^2}, \tag{1.165}$$

where w_{2D} and w_{3D} are the speckle width in 2D and 3D, and $h = 1$ cm is an artificial length introduced to have the right intensity and power units. Notably this case occurs when modelling of ICF experiments with hydrodynamic codes, and in particular in this work, where we study two-dimensional self-focusing with the hydrodynamic code CHIC within the PCGO framework: all along this thesis, we consider 2D speckles several times larger than real far-field speckles as encountered when performing full hydrodynamic simulations of ICF-like laser-target interaction.

Another quantity used to understand the strength of ponderomotive effects is the self-focusing length L_{sf}. This stands for the distance at which the beam reaches its maximum intensity due to ponderomotively-induced focusing. Independently on the dimension, a semi-empirical relation between L_{sf} and the Rayleigh length of a Gaussian beam x_R has been found [84,85]:

$$L_{sf} = \frac{0.367 x_R}{\sqrt{\left(p^{1/2} - 0.852\right)^2 - 0.0219}}, \tag{1.166}$$

where p stands for the ratio between the speckle power and its critical power in 3D or 2D geometry. Ponderomotive effects are relevant if plasma length is larger than L_{sf}, otherwise the beam dynamics is unaffected by self-focusing. In Chapter 4, we apply Eq. (1.166) to compare this analytic estimation to PCGO-CHIC simulations for plasmas with a linear density profile.

As mentioned above, ponderomotive self-focusing theory has been considered in the stationary state. This approximation is accurate for low powers. Since the beam width reduces and the intensity increases, the self-focusing can trigger other laser-plasma instabilities, such as filamentation instability [71,86]. In these cases, the steady state solution is no longer valid, and the beam can break in filaments behind the self-focusing position. The conditions for filamentation instability are summarized in Section 1.3.4.1.

1.3.3 Self-focusing in the PCGO framework

In this section, we evaluate the intensity enhancement in speckles described within the PCGO model. Two aspects must be considered: first, the PCGO speckles are of a larger size, contain more power and, consequently, stronger self-focused. Second, PCGO model is considered in two dimensions, and self-focusing is weaker than in the real 3D world. We demonstrate here that competition of these two factors leads to an overestimation of the speckle intensity enhancement by modelling of realistic speckles by larger 2D speckles for conditions relevant to NIF-scale experiments. Let us consider a NIF-size laser with a 400 TW power distributed over 200 beams and equipped with phase plates producing 10^4 speckles. The single beam power is 2 TW, whereas

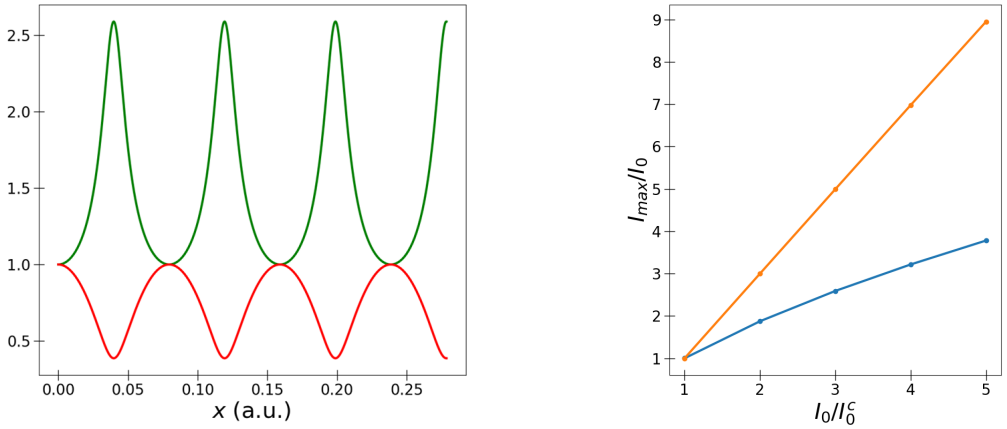

(a) (b)

Figure 1.6: (a) Laser intensity enhancement I_{max}/I_0 (green line) and dimensionless width f (red line) as a function of the coordinate x along the beam propagation direction for $I_0/I_0^c = 3$ from solution of Eq. (1.160) with m=0 (2D). (b) Comparison I_{max}/I_0 for 2D (blue line) and 3D (orange line) as function of I_0/I_0^c.

the average speckle power $\hat{p}_s$ is computed by dividing the beam power to 10^4, giving $\hat{p}_s^{3D} = 200$ MW. For speckles with a width of 2 μm, from Eq. (1.163) considering a laser wavelength $\lambda = 0.35$ μm, plasma density $n_{e0}/n_c = 0.1$ and temperature $T_e = 3$ keV, the critical power P_c^{3D} is around $P_{3D}^c = 430$ MW, thus the ratio $p_{3D} = \hat{p}_s^{3D}/P_c^{3D} \sim 0.46$. In a 2D planar geometry as in CHIC, the speckles can be several times to one order of magnitude larger than optical speckles: in this example we consider $w_{2D} = 20\lambda$, as it is typical in ICF hydrodynamics simulations. Calculating the power for a single 2D speckle from Eq. (1.33) by conserving the same intensity as evaluated for the three-dimensional geometry, computing the equivalent 2D critical power P_c^{2D} for a larger 2D speckle from Eq. (1.165), one finds that the power ratio is $p_{2D} = P_{2D}/P_c^{2D} \sim 2$. Therefore, converting the power of a small 3D speckle to a larger 2D speckles leads to an overestimation of the speckle power compared to its critical power of $p_{2D}/p_{3D} \sim 2.6$. As a consequence, for the same beam average intensity, the intensity enhancements retrieved in 2D are systematically overestimated compared to 3D, as observed from Fig. 1.6b as well: supposing that in 3D one has $p_{3D} = 1$, no relevant intensity enhancement takes place. In 2D, the power ratio reads $p_{2D} = 2.6$, and an intensity enhancement 2-3 times larger than in 3D case is found. In order to account for this overestimation and decrease the PCGO speckle intensity enhancement at the same level of a real 3D speckle, in Chapter 2 we propose a method for controlling and reduce the PCGO speckle intensity enhancement by combining several Gaussian beamlets in a single speckle.

1.3.4 Laser-plasma instabilities

The most important laser-plasma instabilities (LPIs) in ICF can be divided in two categories: modulation instabilities and parametric instabilities [45, 87]. In the next subsections, we briefly recall the main feature of filamentation instability. Then we describes some properties of parametric instabilities relevant to ICF. Examples of three-wave instabilities are illustrated in Appendix.

1.3.4.1 Filamentation instability

The filamentation instability [71, 88] is a process similar to laser self-focusing: the ponderomotive self-focusing produces a global enhancement of a laser beam intensity, while filamentation corresponds to small-scale spatial modulations of the laser intensity profile, which can turn into an instability if such modulations are amplified. Following Refs. [71, 86], the ponderomotive filamentation is evaluated by considering the spatial amplification of initial laser intensity modulations once neglected all the thermal effects. Considering a perturbation, with a wavenumber κ_{fil} in the direction perpendicular to the laser propagation direction, the growth rate κ_{fil} as a function of the wavevector modulation k reads:

$$\kappa_{fil}^2 = \frac{k^2}{4N}\left(\frac{n_{e0}}{2n_c}\frac{Z}{Z+1}\frac{u_{osc}^2}{v_{te}^2} - \frac{k^2c^2}{\omega^2}\right). \tag{1.167}$$

where $u_{osc} = eE_0/m_e\omega$. The maximum wavenumber at which the instability develops is found by equating the term in the parenthesis of Eq. (1.167) to zero:

$$k_{max} = \frac{\omega}{c}\sqrt{\frac{n_{e0}}{2n_c}}\sqrt{\frac{Z}{Z+1}}\frac{u_{osc}}{v_{te}}. \tag{1.168}$$

This means that the filamentation takes place for the modulations of laser intensity with $k < k_{max}$. In Chapter 2 we discuss ponderomotive filamentation instability for a Gaussian beam, showing that the filamentation instability takes place under the condition $k_{max}w_0 > 1$ and when the inverse of the spatial growth rate κ_{fil} is smaller than the plasma length. This brings to a larger threshold power than the critical power for the ponderomotive self-focusing. More details on filamentation instabity and on the growth rate as a function of modes are given in Chapter 2.

1.3.4.2 Parametric instabilities

High intensity lasers of frequency ω and wavenumber $\mathbf{k}$ can act as a pump and resonantly amplify the plasma modes described in Sec. 1.2.2.3 [45, 46, 87]: the longitudinal modes such as electron plasma waves or Langmuir Waves (LW) and Ion Acoustic Waves (IAW), and transverse mode such as electromagnetic waves (EM). Invoking energy and moment conservation laws from quantum mechanics, the resonant conditions for excitation of a pair of daughter waves are

$$\omega = \omega_{d1} + \omega_{d2}, \tag{1.169}$$

$$\mathbf{k} = \mathbf{k}_{d1} + \mathbf{k}_{d2}, \tag{1.170}$$

where ω_{d1} and ω_{d2} are the frequencies of the daughter waves 1 and 2 respectively, and $\mathbf{k}_{d1}$ and $\mathbf{k}_{d2}$ are their wavenumber. The instabilities develop from amplification of the electron oscillation in the pump wave field, which enhances the amplitude of the daughter waves. Let us suppose that one of daughter wave is an electromagnetic wave of amplitude E_{EM}. Its amplification from a small seed E_{seed} can be of convective- or absolute-type: in case of convective instability, it locally grows and spreads out along the direction of wave propagation $E_{EM} = E_{seed}\exp\kappa_x x$, where κ_x is the spatial gain. In case of absolute instability, the instability is spatially

localized, and the daughter wave amplitude grows in time as $E_{EM} = E_{seed} \exp \gamma_t t$, where γ_t is the temporal growth rate. Once established the nature of the instability, the spatial gain determines whether its amplification takes place. The growth rate depends on the plasma conditions: in a homogeneous plasma [87, 89–92], the instability develops if the intrinsic growth rate γ_0 is larger than $\gamma_{th}^{conv} = (\nu_{d1}\nu_{d2})^{1/2}$, where ν_{d1} and ν_{d2} stand for the dissipation rates of the daughter waves 1 and 2 respectively. The absolute instability develops in case of oppositely propagating daughter waves, that is, $V_{d1}V_{d2} < 0$, where V_{d1} and V_{d2} are the group velocities of the two daughter waves. The instability develops if $\gamma_0 > \gamma_{th}^{abs} = |V_{d1}V_{d2}|/2\,[\nu_{d1}/|V_{d1}| + \nu_{d2}/|V_{d2}|]$. The instability is convective if $V_{d1}V_{d2} > 0$ or $\gamma_{th}^{conv} < \gamma_0 < \gamma_{th}^{abs}$ when $V_{d1}V_{d2} < 0$.

The most important instabilities in ICF are stimulated Raman scattering (SRS), stimulated Brillouin scattering (SBS) and the two-plasmons decay (TPD): SRS and SBS consist in excitation of a scattered electromagnetic and electron plasma in case of SRS or an ion acoustic wave in case of SBS. In TPD, the pump decays in two electron plasma waves. In Appendix, we describe in more details SRS and SBS, which may compete with ponderomotive self-focusing in an underdense plasma.

1.3.5 Competition of laser-plasma phenomena in ICF plasmas. Plasma-induced incoherence

The success of the ICF strongly depends on the quality of the laser-plasma coupling: the most favorable scenario consists in laser absorption occurring near the critical density by inverse bremsstrahlung. The absorbed laser energy is transformed into the electron internal energy, and increased plasma pressure launches the compression waves that converge to the target center, generating the required conditions for ignition (see Introduction). Laser-plasma instabilities degrade the compression efficiency by accelerating suprathermal electrons and by scattering the light energy away from plasma. SRS and TPD contribute to the former process [93–99], whereas SBS and SRS cause laser scattering [29, 100]. SRS- and TPD-generated hot electrons can penetrate the overdense plasma region up to the target core, where they deposit their energy. The preheated target is harder to compress, making fuel ignition less likely to occur. Laser scattering decreases the absorbed energy and compromises the uniformity of illumination, reducing the compression symmetry to the point where the ignition conditions no longer hold. In this scenario, laser self-focusing plays a role by inducing a local laser intensity enhancement, which reduces the illumination uniformity and increases the possibility to excite parametric instabilities. In addition, the laser self-focusing may amplify filamentation instability, further degrading the laser-plasma coupling. An overview on laser absorption, laser-plasma instabilities and self-focusing occurring in the underdense plasma corona as a function of the plasma density is presented in Fig. 1.7. This picture allows to identify the regions where each instability operates and where they compete.

Laser self-focusing, filamentation instability [101–103] and SBS are serious concerns for all ICF schemes since they can occur all along the underdense plasma profile. Moreover, a process similar to SBS called cross-beam energy transfer (CBET) can be produced by resonant excitation of IAWs when two laser beams of the same frequency cross each other in a plasma flowing with a near sonic velocity, thus, enabling an energy exchange between them [29, 30]. It was estimated that in the OMEGA experiments CBET is responsible for reduction of absorption and drive pressure by 30-40% [104]. Ponderomotively-driven nonlinear plasma response may create a

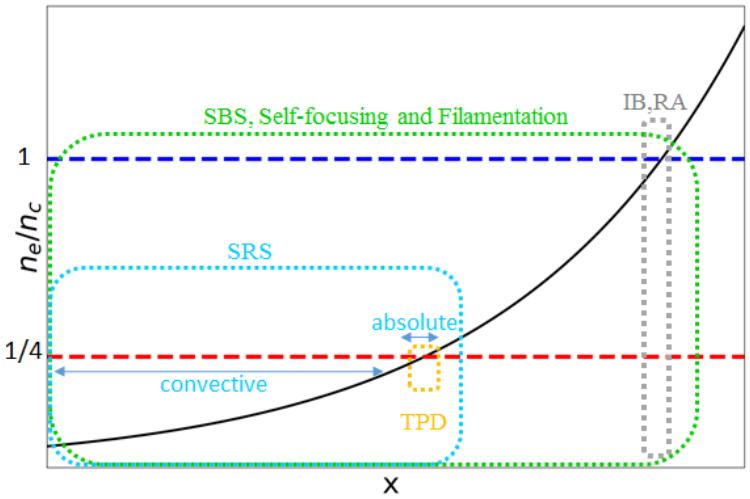

Figure 1.7: Occurrence of laser-plasma instabilities in an underdense ICF plasma profile.

favorable environment for CBET, worsening the situation [31]. Another process which leads to a local intensity amplification and can influence the laser-plasma coupling all along the underdense collisional plasma is the thermal self-focusing [105]. Similarly to the ponderomotive counterpart, plasma changes its local properties under the influence of the laser: whereas in case of ponderomotively-driven intensity enhancement such an effect is due to the expulsion of the fluid from the laser axis, in the thermal self-focusing the collisional-induced plasma heating provokes an hydrodynamics expansion which changes the index of refraction in the same way as in ponderomotive self-focusing. Thus, the thermal self-focusing influences the laser dynamics only in conjunction with laser absorption. Assuming $n_e << n_c$, the critical intensity $I_0^{c,th}$ for the thermal self-focusing to occur reads [106, 107]

$$\frac{I_0^{c,th}}{cn_cT_e} = \frac{n_c}{n_e}\frac{\kappa_0}{k^2w_0^4\nu_{ei}}, \tag{1.171}$$

where κ_0 is the Spitzer thermal conductivity $\kappa_0 = (128/3\pi)(Z+0.24)/(Z+4.2)v_{te}^2/\nu_{ei}$. Equation (1.171) is obtained within the classical theory of electron collisional transport, and has to be compared to the threshold of the ponderomotive. The latter can be rewritten as follows:

$$\frac{I_0^{c,pond}}{cn_cT_e} = \frac{n_c}{n_e}\frac{8}{k^2w_0^2}. \tag{1.172}$$

As a consequence, the difference between thermal and ponderomotive self-focusing is given by the factor

$$\frac{I_0^{c,th}}{I_0^{c,pond}} = \frac{\kappa_0}{8w_0^2\nu_{ei}}. \tag{1.173}$$

In Chapter 4 we study how thermal self-focusing influence the laser-plasma coupling along with laser absorption and ponderomotive self-focusing.

Absolute SRS and TPD can be excited near the quarter critical density. In ICF experiments, TPD dominates at laser intensities below 1 PW/cm^2, while the absolute SRS becomes more important at higher laser intensities

where longer density profiles and hotter plasmas are produced. In these latter cases, the convective back- and side-scattering SRS at lower densities $n_e/n_c < 0.25$ becomes important.

In case of the shock ignition scheme, the implosion laser pulse has a lower intensity than standard ICF pulses, so instabilities are not expected to take place. The instabilities instead highly concerns the spike pulse-plasma interaction [16, 17, 32]: the experimental results have shown a strong convective backward SRS, and a weaker absolute SRS [108, 109]. However, since the absolute SRS is generated deeper inside the plasma, the scattered light could be partially absorbed while travelling outwards. TPD seems to be less important than SRS [110]. Simulations and experiments evaluate the relative importance of SRS and TPD in terms of hot electron production. It has been proved that moderate suprathermal electrons with temperature of 60 keV produced by SRS could be beneficial by increasing the amplitude of the shock wave launched by the spike pulse [20]. TPD produces more energetic electrons with temperatures around 100 keV, which are undesirable for the shock ignition scheme [112, 113].

The laser beam spatial smoothing techniques described in Sec. 1.1.5 along with temporal [27] and polarization [114] smoothing have demonstrated capabilities to mitigate the filamentation instability in the standard ICF approach [115–117]: the target preheat has been reduced thanks to the reduced amount of hot electrons and laser self-focusing suppression. In the shock ignition approach, since the spike pulse has an intensity one order of magnitude higher than ICF standard pulses, filamentation may develop in the speckles at small-scales [32]. Therefore, the filamentation and ponderomotive self-focusing may dominate the laser-plasma coupling in this case, thus enabling onset of the parametric instabilities. In addition, backscattered light generated in small-scale hot spots has been evidenced [32, 118, 119]. Several other techniques have been considered in order to control the parametric instabilities, such as broadband pulses [120] or Spike Trains of Uneven Duration and Delay pulses [121]. Their efficiency have been demonstrated both numerically and analytically and they need to be tested on a real ICF/SI platforms.

The compression efficiency may also benefit from the plasma induced laser incoherence which relaxes speckles self-focusing and suppresses backward SBS. This phenomenon consists in a reduction of the degree of spatial and temporal coherence of a spatially modulated beam due to small-scale plasma density fluctuations generated by a combination of ponderomotive self-focusing, filamentation instability and forward SBS [122–125]. A typical signature of this process is angular and spectral broadening of the forward scattered light, which corresponds to an increasing of the spatial and temporal incoherence. At high intensities, plasma-induced incoherence is generated by interference of ion acoustic waves produced inside a self-focused speckle which interacts with IAWs excited in other speckles. These multiple interactions may lead to a stabilization of speckle self-focusing because of spreading plasma density fluctuations between the speckles. In Chapter 3, we extensively study plasma smoothing by means of PCGO-CHIC simulations.

1.4 Numerical tools

In this section, we describe numerical tools which are used for modelling of laser-plasma coupling at intermediate and long spatial- and temporal-scales: the electromagnetic code HARMONY and the hydrodynamics code

CHIC. HARMONY solves the electromagnetic wave equation in a quasi-monochromatic approximation for the electric field along with the nonlinear fluid equations for the plasma response and is dedicated to study filamentation, laser self-focusing and SBS in 2D paraxial approximation. Then we illustrate the radiation-hydrodynamics code CHIC and the modules based on PCGO allowing to account for nonlinear laser-plasma interaction and, in particular, laser self-focusing.

1.4.1 The electromagnetic code Harmony

HARMONY [34] is a 2D electromagnetic code describing backward SBS, laser self-focusing and filamentation in a plasma with density smaller than the critical density. The ion density perturbation and the plasma fluid velocity are decomposed in a slowly varying part describing processes like self-focusing and near-forward SBS, and a fast varying part describing harmonics IAWs driven by backward SBS:

$$n = n_0 + \sum_{m=1} n_m e^{2imkx} + c.c. \tag{1.174}$$

$$\mathbf{u} = \mathbf{u}_0 + \sum_{m=1} \mathbf{u}_m e^{2imkx} + c.c., \tag{1.175}$$

where the terms with the index 0 refer to the initial large scale profiles, the terms with $m = 1$ stand for the fundamental IAW driven by backward SBS and the terms with $m > 1$ describe the harmonics of the principal IAW. The plasma fluid equations at the large scale are similar to Eqs. (1.93) and (1.94) where source terms due to nonlinear IAW harmonics are added:

$$\frac{\partial n_0}{\partial t} + \nabla \left(n_0 \mathbf{u}_0 \right) = \left(\frac{\partial n_m}{\partial t} \right)_{IAW} \tag{1.176}$$

$$\frac{d(n_0 \mathbf{u}_0)}{dt} + c_s^2 \nabla n_0 = \frac{e n_0}{m_i} \nabla \phi_P + \left(\frac{\partial n_m \mathbf{u}_m}{\partial t} \right)_{IAW} \tag{1.177}$$

where the first term at right hand-side of Eq. (1.177) contains the ponderomotive potential as defined in Eq. (1.141). Correspondingly, the electric field is retrieved by solving the paraxial wave equations for the forward-propagating component $\mathbf{E}_+$ and backward-propagating component $\mathbf{E}_-$:

$$\left[\frac{\partial}{\partial t} + V_{g+} \frac{d}{dx} + \nu_d - i \frac{c^2}{2\omega} \frac{\partial^2}{\partial y^2} \right] \mathbf{E}_+ = -i \frac{\omega}{2 n_c} \left[n_1 \mathbf{E}_- + \delta n \mathbf{E}_+ \right] \tag{1.178}$$

$$\left[\frac{\partial}{\partial t} + V_{g-} \frac{\partial}{\partial x} + \nu_d - i \frac{c^2}{2\omega} \frac{\partial^2}{\partial y^2} \right] \mathbf{E}_- = -i \frac{\omega}{2 n_c} \left[n_1^* \mathbf{E}_+ + \delta n \mathbf{E}_- \right] \tag{1.179}$$

where δn is the slow density perturbation, whose coupling to the electric wave gives rise to the beam self-focusing, V_{g+} and V_{g-} stand for the group velocities of the forward- and backward-propagating light respectively, and ν_d denotes the damping of these two waves.

In this thesis, HARMONY is run in a simplified mode without the backscattered wave $E_- = 0$ and without right hand-side terms in Eqs. (1.176)-(1.177). Consequently, the hydrodynamic response is described by two equations in a 2D geometry, assuming an isothermal plasma at a constant temperature. The boundary electric

field $E(x=0,y,t)=E_0(y,t)$ is defined by setting E_0 as a Gaussian profile. Such a shape can change during the wave propagation due to laser-plasma interactions.

Since in HARMONY beams are described by an electric field having amplitude and phase, it provides an accurate description of the ponderomotive self-focusing, standing as a reference for validation of nonlinear self-focusing of PCGO beams described in Chapter 2.

1.4.2 Radiation-hydrodynamics code CHIC

Inertial fusion-related phenomena involve longer spatial and time-scales than the ones accessible with electromagnetic codes. To satisfy the need of simulating numerically the physical processes on such scales, hydrodynamics codes have been developed. The CHIC code stands for one of them: it is based on the Lagrangian formulation of single fluid equations, supposing a plasma composed by electrons and ions with two different temperatures [38]:

$$\frac{\partial \rho}{\partial t} + \nabla(\rho \mathbf{U}) = 0 \tag{1.180}$$

$$\rho\left[\frac{\partial \mathbf{U}}{\partial t} + (\mathbf{U}\cdot\nabla)\mathbf{U}\right] = -\nabla P + F_{\text{ext}} \tag{1.181}$$

where $\rho = m_e n_e + m_i n_i$ is the plasma mass density, $P = P_e + P_i$ is the total plasma pressure and $\rho\mathbf{U} = m_e n_e \mathbf{u}_e + m_i n_i \mathbf{u}_i$ is the hydrodynamic plasma flow. These equations assume that at any time electrons and ions are separately thermalized and they respect the quasi-neutrality condition $n_e = Z n_i$. The term F_{ext} stands for the forces acting on the plasma besides thermal pressure, as for example the ponderomotive force. Further two equations accounting for energy evolution of ions and electrons respectively are included:

$$\rho\left[\frac{\partial}{\partial t} + (\mathbf{U}\cdot\nabla)\right]\epsilon_e + \nabla\cdot\mathbf{q}_e = -P_e\nabla\cdot\mathbf{U} - 2\alpha\frac{m_e}{m_i}n_e\nu_{ei}(T_e - T_i) + \epsilon_{\text{ext}} \tag{1.182}$$

$$\rho\left[\frac{\partial}{\partial t} + (\mathbf{U}\cdot\nabla)\right]\epsilon_i + \nabla\cdot\mathbf{q}_i = -P_i\nabla\cdot\mathbf{U} + 2\alpha\frac{m_e}{m_i}n_e\nu_{ei}(T_e - T_i) \tag{1.183}$$

where ϵ_e and ϵ_i are the electron and ion specific internal energy respectively, $\mathbf{q}_e$ and $\mathbf{q}_i$ are the electrons and ions energy flux, ϵ_{ext} refers to other energy sources (or sinks), and α is a free parameter varying between [1, 1.5] accounting for non-ideal effects in the electron-ion coupling. The electron and ion heat fluxes are calculated from the Spitzer-Härm theory [69] with a flux limiter for electrons. The code uses tables for the equation of state. Built on a Lagrangian non-structured mesh, the CHIC code includes an Artibrary Lagrangian-Eulerian (ALE), option which improves the code robustness in case of strong mesh distortions [38].

Concerning the laser description, the code includes a laser beam propagation and energy deposition modelled with the standard Ray-Tracing. The incident laser beam is split into an ensemble of thin rays each of them carrying a fraction of laser power and obeying to laws of geometrical optics described in Sec. 1.1.3. The refraction of the ray in an inhomogeneous plasma is due to the variation of the refraction index in inside the cells. However, ray tracing does not consider beam diffraction, and laser intensity in plasma is not efficiently evaluated, providing only the values of laser power deposited in each cell at each time step. As a consequence, F_{ext} is usually neglected. Thus it is desirable to replace the standard ray tracing technique with a laser

propagation model which computes the laser intensity and then accounts for intensity-dependent phenomena and for diffraction effects.

To improve laser descripion and laser-plasma coupling in CHIC, a simplified version of PCGO has been implemented in two-dimensional planar geometry: such a model is referred to as *thick-ray* model [40]. In this approach, a ray is represented by a beamlet with a Gaussian intensity profile, characterized by initial power P_0, spatial width w_0 and central coordinate $\mathbf{r}_0$. The beamlet trajectory $\mathbf{r}_0(\tau_c)$ along the curvilinear ray coordinate τ_c obeys to the geometrical optics equation (1.46). The intensity profile is related to the complex wavefront curvature B as described in Sec. 1.1.4. In Cartesian coordinates and for nonabsorbing plasma for instance, the intensity profile of the thick beamlet projected into the hydrodynamics grid from Eq. (1.59) reads

$$I(x,y) = I_0(x) e^{-2\frac{y^2}{w^2(x)}}, \tag{1.184}$$

where x is the longitudinal coordinate and y the transverse coordinate. By solving Eq. (1.46), one retrieves the propagation path of thick ray centroid, whereas Eq. (1.184) gives the beam intensity. The beam deposes its energy in each cell along its trajectory according to Eq. (1.133), which accounts for electron-ion collisions (inverse Bremsstrahlung). As the laser intensity is known everywhere in the plasma, the ponderomotive force has been implemented as an external force acting on plasma through the term $F_{\text{ext}} = -en_e\nabla\phi_p$ (see Sec. 1.3), by projecting the ponderomotive potential ϕ_p into each cell. At each time step than, this external force induces a transverse motion of the plasma, with the subsequent variation of local plasma density as described by the stationary linear (Eq. (1.151)) or nonlinear (Eq. (1.152)) plasma response.

Implementation of the PCGO model has allowed to describe energy transfer between crossing laser beams [126]. Furthermore, the knowledge of laser intensity has lead to inline models for generation and propagation of hot electrons [127]: when the laser intensity exceeds the value of SRS- or TPD- thresholds in a cell, an electron beam is generated from this cell. Such an electron beam has a kinetic energy related to the laser intensity by scaling laws [128], and it propagates in plasmas following a straight trajectory with a defined aperture. Definition of such scaling laws is still subject of several studies. Moreover, in its current status, only transfer of the laser energy to hot electrons is considered, neglecting scattering light processes. Despite that, the PCGO-related hot-electron algorithm has demonstrated several successes in analysing experimental results [21, 41, 111, 129].

The PCGO implementation in CHIC has provided the possibility to create beams of different spatial shapes and with spatial-scale modulations [130]. In particular, PCGO allows to mimic the spatial fluctuations introduced by phase plates by superposition of Gaussian beamlets: each PCGO beamlet propagates according to Eq. (1.46), and with an intensity profile defined by Eq.(1.184), while the plasma density and temperature profiles are provided by the hydrodynamic equations (1.180)-(1.183) updated at each time step. The phase variation along the beamlet trajectory is not considered when thick beamlets are used to create a speckle pattern. Thus, the local laser intensity in plasma $I(x,y)$ is calculated as a sum of N_b neighbor beamlets intensities $I_j(x(\tau_j), y(\tau_j))$ [40, 130]:

$$I(x,y) = \sum_{j=1}^{N_b} I_j(x(\tau_j), y(\tau_j)), \tag{1.185}$$

where $(x(\tau_j), y(\tau_j))$ is the closest position on the trajectory of the beamlet from the observation point (x, y) where the total beam intensity is evaluated: only a limited number of beamlets passing at a distance of the order of the beamlet width contribute to the local intensity. The laser presents local intensity maxima in area where two or more beamlets cross each others. Each local maximum represents a speckle. Knowing the local intensity, one can calculate for example the ponderomotive pressure in plasma as a sum of all ponderomotive pressures locally induced by the nearby beamlets: $U_p = n_{e0}/(2cn_c) \sum_{j=1}^{N_b} I_j(\tau_j, q_j)$.

As already mentioned, the PCGO model used in CHIC does not account for beamlets interference when modelling of spatially modulated beams, and the number of speckles is at least one order of magnitude less than in reality. Moreover, diffraction limits the PCGO resolution to a few laser wavelengths, and the speckles must be several times larger than the real ones, which is compatible with the spatial resolution required in hydrodynamics simulations, restrained to values of 5-10 laser wavelengths. These dimensions are larger than the typical width of laser speckles of 2-3 laser wavelengths. As a first consequence, a realistic contrast of 100% (see Sec. 1.1.5) cannot be achieved within the current PCGO-CHIC approximation, where the contrast reaches a few tens of percent and depends on the number of beamlets. Another consequence of neglecting the beamlet phase concerns the probabiltiy distribution of speckles intensity: in the current PCGO algorithm used to create KPP beams, the statistics of speckle intensity is retrieved only if PCGO simulations are averaged over several realizations [130].

Two-dimensional speckles larger than real ones overestimate the effects of the ponderomotive force as discussed in Sec. 1.3.2.1. In order to apply the 2D planar PCGO-CHIC model to realistic situations, a modification of speckles initialization is required. A novel algorithm to create a PCGO spatially modulated beam which allows to relax speckle intensity enhancement by a factor of 2-3 is needed. In this way, 2D large speckle reproduces the intensity enhancement compatible to what is observed for real speckles. In Chapter 2 we study in details the self-focusing of a PCGO beamlet comparing our results to HARMONY simulations. Afterwards we introduce an algorithm that allows to decrease the ponderomotive force of the speckle by a factor of 2 while creating Gaussian speckles by superposing PCGO beamlets. This procedure is then extended to spatially modulated beams in Chapter 3, where self-focusing of a spatially modulated beam is described, showing how the new algorithm permits to account for other speckle characteristics such as the variation of the probability distribution of the speckle intensity. Whereas in Chapters 2 and 3 we consider homogeneous nonabsorbing plasmas, in Chapter 4 we investigate PCGO beams propagation in absorbing plasma with a linear density profile in order to approach ICF situations.

Chapter 2

Self-focusing of a beamlet and a multi-beamlet speckle in homogeneous nonabsorbing plasmas

2.1 Introduction

Unlike Ray-Tracing, the thick-ray approach describes the propagation of beams with a prescribed Gaussian intensity profile, which we call beamlets. Intensity-profile-related effects, such as ponderomotive force, previously not modelled in radiation-hydrodynamics codes, are now computed in CHIC since the implementation of the PCGO model. Moreover, this version of PCGO is used to create spatially modulated laser beams by superposing several beamlets to create the intensity fluctuations in the far-field (see Sec 1.4.2). Although this approach has improved the CHIC accuracy in interpreting ICF experiments and in designing ICF targets, the PCGO multi-beamlet speckle structure cannot accurately account for small spatial fluctuations: superposition of PCGO beamlets produces larger and longer speckles than in real cases, carrying then more power than real speckles. As a consequence ponderomotive-induced PCGO speckle self-focusing may be overestimated compared to the same effect occurring at smaller scales in spatially modulated beams. A method that makes the ponderomotive-driven PCGO speckle intensity enhancement comparable to what obtained with in 3D speckles (see Sec. 1.3.3) needs to be assessed.

In this chapter, we discuss the accuracy of the thick-ray model in describing the ponderomotive self-focusing of a Gaussian-shaped beam in homogeneous nonabsorbing plasmas. First, we investigate ponderomotive self-focusing of a PCGO beamlet by comparing its dynamics to a Gaussian-shaped beam modelled with the paraxial wave-based code HARMONY [34]. We vary plasma and beam conditions in order to define the domain of plasma density and beam power where the thick-ray approximation is valid. Then, in the second part we study the self-focusing of a PCGO speckle created by superposition of several beamlets, referred to as *multi-beamlet speckle*. This speckle stands for a reference of any PCGO speckle created in CHIC while modelling of spatially

modulated beams. In our study, we quantify the reduction of the speckle intensity enhancement as a function of the number N_b of superposed beamlets and by considering two strategies for multi-beamlet speckle shaping: random and regular. In the first one, at each realization the focal spot and the inclination of each thick beamlet are chosen randomly. This method does not impose an initial shape to the multi-beamlet speckle. The regular shaping method consists in configuring a priori the beamlets parameters such that the multi-beamlet speckle has a defined Gaussian intensity profile.

2.2 Self-focusing of a single beamlet

Propagation of a single beamlet by means of PCGO-CHIC in an underdense plasma with an ionization charge $Z = 3.5$ and atomic mass $A = 6.5$ corresponding to a plastic CH plasma is considered here. The thick-ray results are compared to numerical results obtained via HARMONY simulations for the same initial plasma conditions and beam profile. Laser absorption, plasma heating and hot-electron-source packages have been switched off. In this way, parametric instabilities, hot electron generation and thermal self-focusing are excluded and plasma dynamics is solely dominated by the ponderomotive force. The ponderomotive effects are evaluated by measuring the laser intensity enhancement in plasma, which is the main quantity to analyze for discriminating ponderomotive-induced consequences.

The input parameters set for CHIC and HARMONY are such as to generate a Gaussian beam with initial waist $w_0 \approx 21$ μm, and wavelength $\lambda = 1.05\,\mu$m. The Gaussian beam enters the plasma with a negative curvature wavefront given that the focal plane (x_f, y_f) is placed at $\approx (1100\lambda, 100\lambda)$ inside a plasma of size $(2500\lambda \times 200\lambda)$. The plasma temperature is $T_{\text{eff}} = 1$ keV, where $T_{\text{eff}} = T_e\,(1 + 3T_i/ZT_e)$, with $T_e = 3T_i$. In order to explore different regimes, two parameters have been varied: the plasma density n_{e0} and the laser power P^{2D}. We have chosen: n_{e0}/n_c=0.01; 0.05; 0.1 and $p_{2c} = P^{2D}/P_c^{2D} = 1;\ 2;\ 4;\ 6$, where the value of the beam power and the critical power P_c^{2D} are recalculated for each plasma density according to Eqs. (1.163) and (1.164). The laser pulse has a step-like temporal shape lasting $t_f = 250$ ps, long enough to attain a quasi-stationary state for $t > t_{c_s}$ where $t_{c_s} = w_0/c_s \approx 70 - 80$ ps. This state is systematically achieved in case of thick-ray simulations at around $t_s = 2.5\ t_{cs} \approx 200$ ps. Before that, the beam intensity oscillates in position and amplitude. Quasi-stationary states were not fully attained in HARMONY simulations for large powers because of filamentation instability, whereas at low powers the situation is very similar to the PCGO solution. We proceed to analyse CHIC results in Section 2.2.1, and then compare them to HARMONY simulations and theoretical estimations in Sec. 2.2.2.

2.2.1 Analysis of PCGO-CHIC results

For $p_{2c} \geq 2$ and at any density, an increase of beam intensity as a function of the initial beam power occurs, with a consequent beam width reduction. This is illustrated in Figs. 2.1a-2.1b: Figure 2.1a shows the initial beam condition common to all the cases and displays the initial laser intensity distribution $I(x, y)$ normalized to the initial intensity peak $I_0 = I_{\max}(x_f, y_f, t = 0)$. Figure 2.1b refers to the normalized intensity $I(x, y)/I_0$ at $t = 210$ ps and for $n_{e0}/n_c = 0.1$ and $p_{2c} = 2$. Since collisions are neglected, and since the thick-ray model conserves the

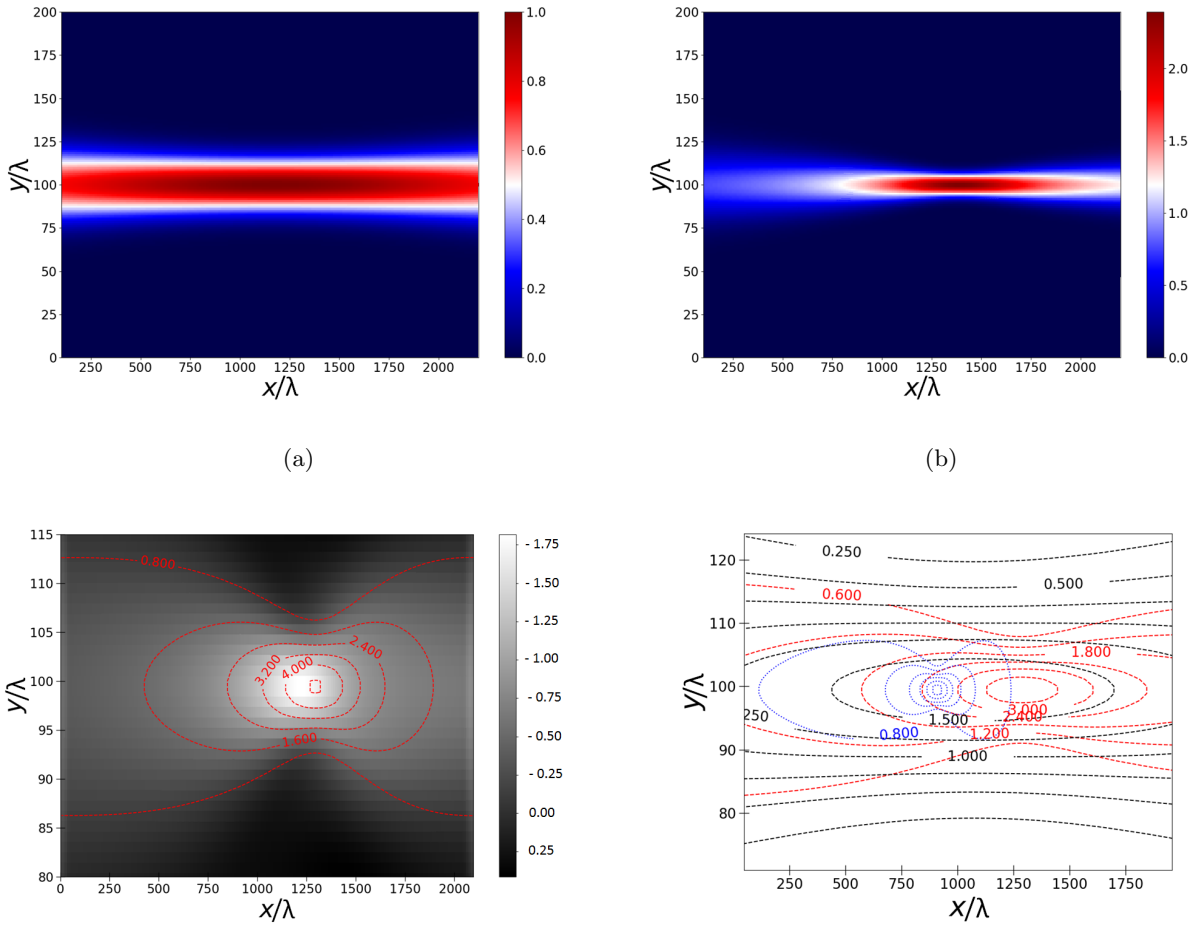

Figure 2.1: Normalized laser intensity distribution in plasma $I(x,y)/I_0$ for $p_{2c} = 2$ and for a) $t = 0$ and b) $t = 210$ ps. c) Amplitude of the density perturbation $\delta n(x,y)/n_{e0}$ (%), represented by the gray bar, superimposed to the contour lines of the laser intensity for $n_{e0}/n_c = 0.1$ and $p_{2c} = 2$ at $t = 210$ ps. d) Laser intensity contour lines. The black lines refer to the initial beam intensity, the red and blue contour lines refer to $t = 210$ ps and for a power of $p_{2c} = 2$ and $p_{2c} = 4$, respectively. The spatial coordinates are in units of the laser wavelength λ. In all the figures, the laser enters from the left side.

energy, the laser power must not vary during the simulation. Thus, whilst the beam width is reduced around the self-focusing position as consequence of self-focusing, the on-axis laser intensity must increase according to the relation

$$I(x,0,t) = \frac{w_0}{w(x,t)} I_0. \tag{2.1}$$

Figure 2.1b qualitatively shows this width reduction if compared to Figure 2.1a.

As described in Sec. 1.3.2.1, self-focusing derives from on-axis ponderomotively-induced density depletion, as displayed Fig. 2.1c: here the red lines are the contour plots of the beam intensity for $n_{e0}/n_c = 0.1$ and

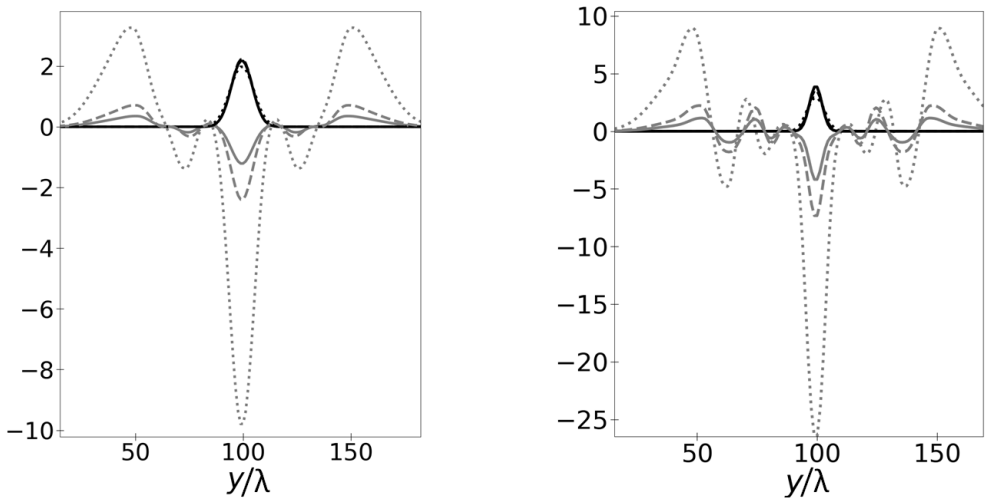

(a) (b)

Figure 2.2: Transverse line-outs of the normalized intensity $I(x_{sf}, y)/I_0$ (black lines) and density variation $\delta n(x_{sf}, y)/n_{e0}$ (gray lines) profiles for a) $p_{2c} = 2$ and b) $p_{2c} = 4$ at self-focusing position x_{sf} for $t = 210$ ps. The solid lines refer to the case $n_{e0}/n_c = 0.1$, the dashed lines to the case $n_{e0}/n_c = 0.05$, the dotted lines to the case $n_{e0}/n_c = 0.01$. The transverse spatial coordinate is in units of the laser wavelength λ.

$p_{2c} = 2$ at $t = 210$ ps, superposed to the amplitude of the density perturbation $\delta n(x, y)/n_{e0}$ (%) represented by a gray color bar for the same laser and plasma conditions. As expected, the contours reproduce the shape of the density channel, demonstrating that the laser intensity dynamics and the evolution of the density perturbation are strictly connected. More information on the laser intensity contours and beam shape variation due to self-focusing can be found in Fig. 2.1d. Here the black contour lines refer to the initial beam intensity, the red and blue contour lines refer to a beam power of $p_{2c} = 2$ and $p_{2c} = 4$ respectively and taken at $t = 210$ ps. As shown in this picture, the beam width is reduced for a higher beam power, with a consequent beam-shape modification: especially for $p_{2c} = 4$ (blue lines), the beamlet width is strongly reduced. Before a stationary state is set in, a transient stage during which the beam intensity undergoes a fluctuated evolution in time. The amplitude of such fluctuations increases with beamlet power and is independent of the initial plasma conditions. Eventually, at around $t_s = 210$ ps, the PCGO simulations attain a stationary state where the Gaussian-like structure of the beamlet is retrieved. In fact, for $t > t_s$ and for any plasma condition and beam power, all the self-focused PCGO beamlets obey to the Gaussian-related relation Eq. (2.1).

In Fig. 2.2, transverse line-outs of the normalized intensity $I(x_{sf}, y)/I_0$ (black lines) and the amplitude of the density perturbation $n(x_{sf}, y)/n_0 - 1$ at the self-focusing position x_{sf} and for $t > t_s$ are presented. We consider the density perturbation and the beam intensity in the same plot in order to evidence a correlation between the density decrease inside the plasma channels and the beam intensity enhancement. The solid lines refer to the case $n_{e0}/n_c = 0.1$, the dashed lines refer to the case $n_{e0}/n_c = 0.05$, the dotted lines refer to the case $n_{e0}/n_c = 0.01$. Figure 2.2a displays the case $p_{2c} = 2$, whereas Fig. 2.2b refers to the case $p_{2c} = 4$.

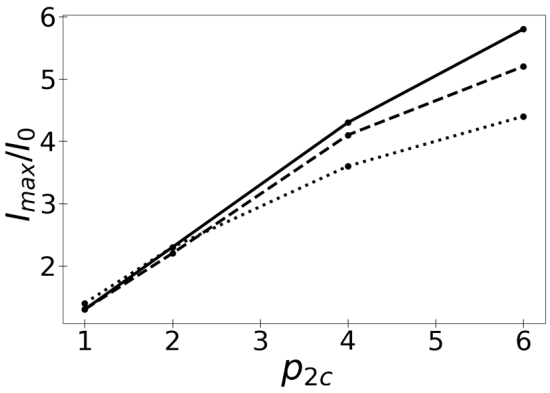

Figure 2.3: Laser intensity enhancement I_{max}/I_0 when a steady state is attained. The solid lines refer to the case $n_{e0}/n_c = 0.1$, the dashed lines to the case $n_{e0}/n_c = 0.05$, the dotted lines to the case $n_{e0}/n_c = 0.01$.

The transverse gradient of the laser intensity is the origin of the ponderomotive force-induced plasma density channeling. The width of the density channel coincides with the beam waist independently of p_{2c} and n_{e0}/n_c. The beam intensity enhancement weakly varies as a function of plasma density. On the other hand, the depth of the density channel depends on the initial beam power and initial plasma density, in agreement with the stationary theory presented in Sec. 1.3.2.1: at a given power, the density depletion is inversely proportional to the initial density, thus changing density from $n_{e0}/n_c = 0.1$ to $n_{e0}/n_c = 0.01$ amplifies the depth of density channel by a factor of 10, as also illustrated in the figures once comparing the solid and dotted gray lines. At a given density n_{e0}/n_c, instead, increasing the initial beam power enhances the effects of the ponderomotive force-induced plasma expulsion, resulting in an almost-linear dependence of plasma density response to the beam intensity enhancement, which in turn depends on the beam power: an intensity enhancement of two-times corresponds to a depth of the density channel two times larger, as evidenced in Fig. 2.2 if comparing for instance black dotted lines for the intensity enhancements and the gray dotted lines for the amplitude of the density cavities.

Figure 2.3 shows the beam intensity enhancement as a function of the beam power when the stationary state is reached, i.e. for $t > t_s$. For $p_{2c} \leq 2$, the intensity enhancement does not depend on n_{e0}/n_c. In the panel, the solid lines refer to the case $n_{e0}/n_c = 0.1$, the dashed lines to the case $n_{e0}/n_c = 0.05$, the dotted lines to the case $n_{e0}/n_c = 0.01$. The intensity enhancement quasi-linearly increases as a function of the beam power up to $p_{2c} \approx 4$, exhibiting a slight saturation above such a power and especially at lower densities. At so high power, the plasma density affects the beam self-focusing, since the intensity enhancement decreases at lower densities. This is due to the nonlinear density response to the laser intensity according to Eq. (1.152). This phenomenon is investigated in more details in the next section.

The density amplitude peak $[|\delta n|/n_c]_{max}$ as a function of the beam power is shown in Fig. 2.4. The solid lines refer to the case $n_{e0}/n_c = 0.1$, the dashed lines to the case $n_{e0}/n_c = 0.05$, the dotted lines to the case $n_{e0}/n_c = 0.01$. As previously anticipated, the density response strongly depends on the initial plasma density, whereas a weaker but still important dependence on beam power can be also noted. This is especially true at lower densities, where highly nonlinear density perturbation and nonlinear stage of self-focusing occur. A

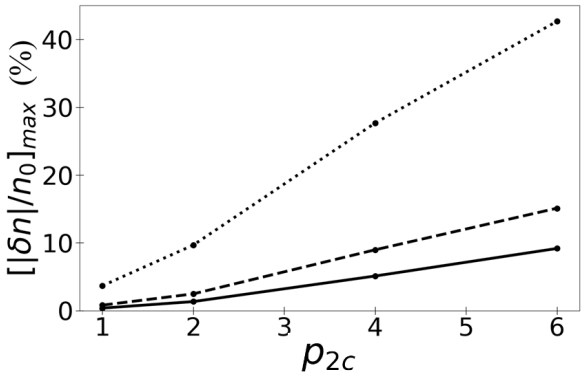

Figure 2.4: Amplitude of density perturbation $\delta n/n_{e0}$ (%) when a steady state is attained. The solid lines refer to the case $n_{e0}/n_c = 0.1$, the dashed lines to the case $n_{e0}/n_c = 0.05$, the dotted lines to the case $n_{e0}/n_c = 0.01$.

strong plasma nonlinearity may correspond to a less accurate solution of hydrodynamics equations (1.180)-(1.182), leading to a less pronounced beam intensity enhancement. This is probably the case for $n_{e0}/n_c = 0.01$ (dotted curve) at powers above 4 times the critical power.

Figure 2.5 depicts the displacement Δx_{sf} of the intensity peak position x_{sf} at $t = 210$ ps with respect to the initial longitudinal focus position of the beamlet x_f: $\Delta x_{sf} = (x_{sf} - x_f)/\lambda$. This parameter measures the self-focusing length. For $\Delta x_{sf} > 0$, the beam self-focuses behind its initial focus spot, whereas for $\Delta x_{sf} < 0$ it self-focuses ahead, which is observed only for $p_{2c} > 4$ and for $\delta n_{e0}/n_c \geq 0.05$. For $p_{2c} = 1$ the intensity maximum is shifted by around 600λ independently of the plasma density. For $p_{2c} > 1$ instead, at a given power the intensity peak moves deeper into the plasma as plasma density decreases. In contrast with the results on the intensity enhancement, the self-focusing position strongly depends on the initial laser power but very weakly

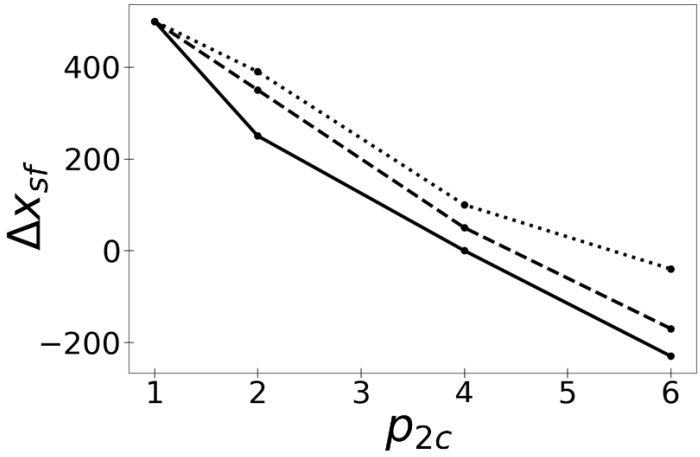

Figure 2.5: Displacement of intensity peak Δx_{sf} as a function of the beamlet power p_{2c} when a steady state is attained. The solid lines refer to the case $n_{e0}/n_c = 0.1$, the dashed lines to the case $n_{e0}/n_c = 0.05$, the dotted lines to the case $n_{e0}/n_c = 0.01$. The longitudinal spatial coordinate is in units of the laser wavelength λ.

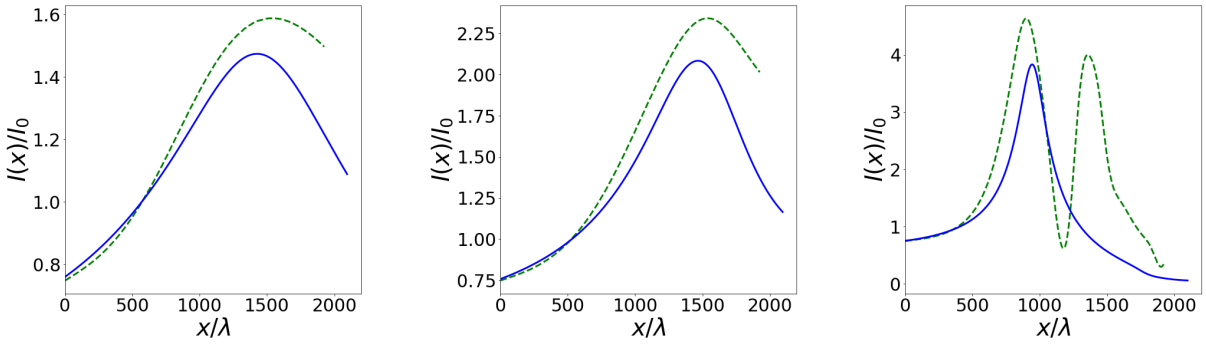

(a) (b) (c)

Figure 2.6: On-axis intensity normalized to the initial intensity maximum $I(x)/I_0$ as a function of the longitudinal coordinate x at $t \approx 200$ ps. The solid blue line and the dashed green curve correspond to thick-ray and HARMONY simulations respectively: (a) $n_{e0}/n_c = 0.1$ and $p_{2c} = 1$, (b) $n_{e0}/n_c = 0.05$ and $p_{2c} = 2$, (c) $n_{e0}/n_c = 0.01$ and $p_{2c} = 6$. The longitudinal spatial coordinate is in units of the laser wavelength λ. In all the figures, the laser enters from the left side.

on plasma density. At any densities, Δx_{sf} decreases as the beam power increases, i.e. when the beam power increases x_{sf} approaches to x_f. The cases $p_{2c} = 6$ stand for exceptions to this tendency: the beamlet self-focus before to the initial focus spot position highlighting the strength of ponderomotive force at this power: the displacement of the self-focusing position with respect to the initial focus spot linerly depends on the beam power, consistently with the analytic formula Eq. (1.166).

A more detailed discussion about the accuracy of solutions described in this section is presented in the next section, where we compare the PCGO results to HARMONY simulations and analytic evaluation for similar conditions.

2.2.2 Comparison to Harmony results

In this section, we compare the thick-beamlet results presented in the previous section to simulations performed with the HARMONY code. As above noted, the thick-ray simulations achieve a steady state for $t \sim t_s = 210$ ps, which corresponds to about $2.5t_{cs}$. Quasi-stationary states were not fully reached in HARMONY simulations for large powers because of filamentation instability, which stands for the only difference between PCGO-CHIC and HARMONY simulations from the laser-plasma interaction point of view. Nevertheless, the beam intensity dynamics stabilizes and can be compared to the CHIC results.

Figure 2.6 displays the on-axis intensity profile normalized to the initial maximum intensity $I(x)/I_0$ as a function of the longitudinal normalized coordinate for thick-ray (solid blue line) and HARMONY (dashed green line) simulations at $t = 200$ ps. Figures 2.6a and 2.6b refer to the case $p_{2c} = 1$ and $n_{e0}/n_c = 0.1$, and $p_{2c} = 2$ and $n_{e0}/n_c = 0.05$ respectively, and show a good agreement between thick-ray and HARMONY results, with a difference of less than 10% in the peak intensity and self-focusing position.

In contrast, for the case of $p_{2c} = 6$ and $n_{e0}/n_c = 0.01$ shown in Fig. 2.6c, the beam does not keep a Gaussian profile in HARMONY simulations: a second peak appears after the first main peak. The on-axis intensity then

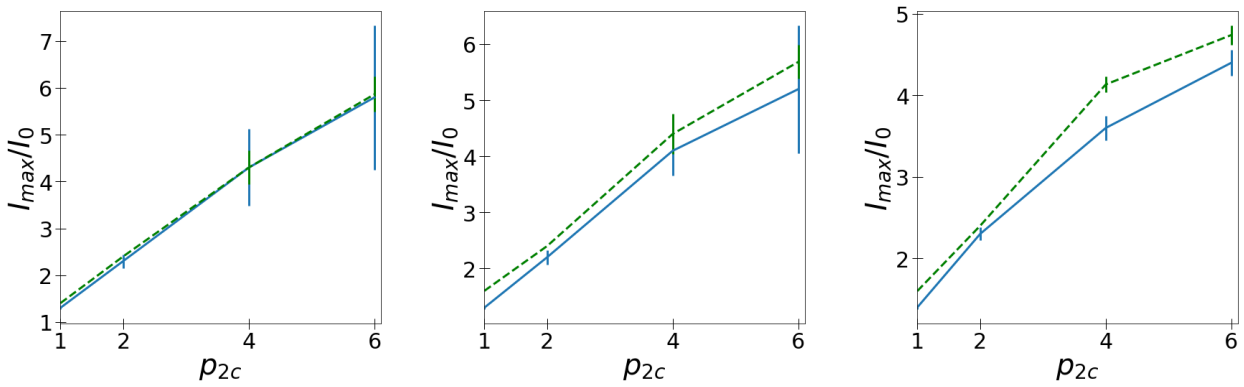

(a) (b) (c)

Figure 2.7: Intensity enhancement I_{max}/I_0 evaluated after the self-focusing as a function of the normalized laser beam power p_{2c} for various plasma densities: (a) $n_{e0}/n_c = 0.1$, (b) $n_{e0}/n_c = 0.05$, (c) $n_{e0}/n_c = 0.01$. The error bars represent the standard deviation of the time-averaged intensity enhancement. Blue and dashed green lines correspond to the thick-ray and HARMONY results respectively.

is influenced by the filamentation instability in case of HARMONY simulations. The latter cannot be described within the thick-ray approach, and hence the on-axis profiles look considerably different. Despite that, the intensity enhancement observed in PCGO simulations recovers within a difference of 20% the first peak position and the related intensity amplification evidenced in HARMONY runs.

Figure 2.7 summarizes the main results of the simulations performed: the intensity enhancement I_{max}/I_0 is shown as a function of the beam power and for various densities. The dashed green lines represent the HARMONY results, whereas the blue lines the thick-ray results. The error bars represent the standard deviation of intensity enhancement for times $t > t_{c_s}$, due to intensity oscillations in time. Large error bars for the thick-ray curves at high powers are due to the fact that the beamlet waist attains small value close to the limit of validity of the paraxial approximation. For $p_{2c} \geq 4$ and at any density, HARMONY simulations follow the theory prediction for filamentation instability [86]: strong self-focusing leads the laser intensity to concentrate in a first peak, which afterwards breaks in filaments. The main filament carries more than 90% of the initial beam power and propagates along the same initial beam direction, whereas side filaments carry the remaining beam energy. Dashed green lines for $p_{2c} \geq 4$ in Fig. 2.7 represent the intensity enhancement of the main filament. As shown in Fig. 2.7a, PCGO and HARMONY predictions are in good agreement for $n_{e0}/n_c = 0.1$. At lower density, the smaller the initial plasma density is, the larger divergence between the PCGO and HARMONY curves is, as one can see in Figs. 2.7b-2.7c for $n_{e0}/n_c = 0.05$ and $n_{e0}/n_c = 0.01$, with a larger difference for $n_{e0}/n_c = 0.01$ at higher powers because of filamentation instability. However, the difference remains within 15%-20%, which is still satisfactory.

Figure 2.8 presents the steady-state spatial gain for ponderomotive filamentation κ_{fil} multiplied by the plasma length $L = 0.2$ cm as a function of the wave number of laser modulations that can be developed in the plasma for $n_{e0}/n_c = 0.1$, $Z = 3.5$, $T_{\text{eff}} = 1$ keV and laser wavelength $\lambda = 1.05$ μm according to Eq. (1.167). The green line corresponds to the case $p_{2c} = 6$, the red line corresponds to the case $p_{2c} = 2.5$, the

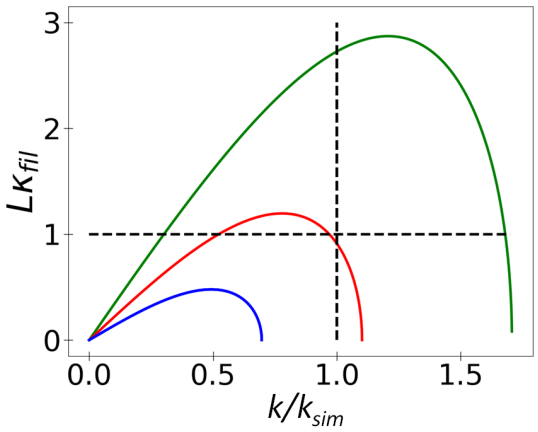

Figure 2.8: Spatial growth rate of filamentation instability κ_{fil} as a function of wave numbers that can develop in plasma k for $n_{e0}/n_c = 0.1$, $Z = 3.5$ and $T_{\text{eff}} = 1$ keV from Eq. (1.167). The green line corresponds to the case $p_{2c} = 6$, the red line corresponds to the case $p_{2c} = 2.5$, the blue line corresponds to the case $p_{2c} = 1$, whereas the vertical dashed black line displays the the wavevector cut-off k_{sim}. The horizontal dashed black line corresponds to the threshold condition $L\kappa_{fil} = 1$.

blue line corresponds to the case $p_{2c} = 1$, whereas the vertical dashed black line displays the wavevector cut-off k_{sim} evaluated by considering that the beamlet modulations occur over a scale of a length comparable to the beamlet diameter, approximated as $2w_0$, thus $k_{sim} = \pi/w_0$. The horizontal dashed black line corresponds to the threshold condition $L\kappa_{fil} = 1$.

Filamentation instability occurs for $L\kappa_{fil} > 1$ and if $k_{sim} < k_{max}$, where k_{max} is the value of k for which $\kappa_{fil} = 0$, and it is given by Eq. (1.168). The first inequality stands for the condition where the perturbation can be spatially amplified inside the plasma of length L. From these curves, it is evident that the modulations become unstable for $p_{2c} > 2.5$, confirming the previous predictions from HARMONY simulations: filamentation instability does not influence the Gaussian beam-plasma coupling for $p_{2c} \leq 2$. Comparing these analytic results to the plane wave solution with the same plasma conditions, the latter undergoes filamentation instability as soon as $p_{2c} \sim 1$. This difference is due to the fact that for a plane wave a broader range of wavenumbers can be amplified. As a result, the filamentation instability affects the plane wave propagation as soon as its power overcomes the critical power.

The nature of plasma response may explain the difference at lower densities. Figure 2.9 shows the amplitude of density perturbations at the self-focusing position x_{sf}: the blue lines refer to CHIC simulations, the green lines refer to HARMONY simulations. The red and purple dashed lines stand for the theoretical estimation of the amplitude of the density response according to Eqs. (1.151) and (1.152) respectively: I_{max} is replaced by the intensity enhancement observed in CHIC simulation (see Fig. 2.7, blue curves). Agreement between theoretical predictions, thick-ray and HARMONY results is excellent for n_{e0}/n_c=0.1, as shown in Fig. 2.9a. The case $n_{e0}/n_c = 0.05$ is illustrated in Fig. 2.9b: for $p_{2c} \leq 2$ the agreement is still good, whereas for $p_{2c} > 2$, a difference between HARMONY and CHIC curves suggests that the laser-plasma coupling in thick-ray model fails

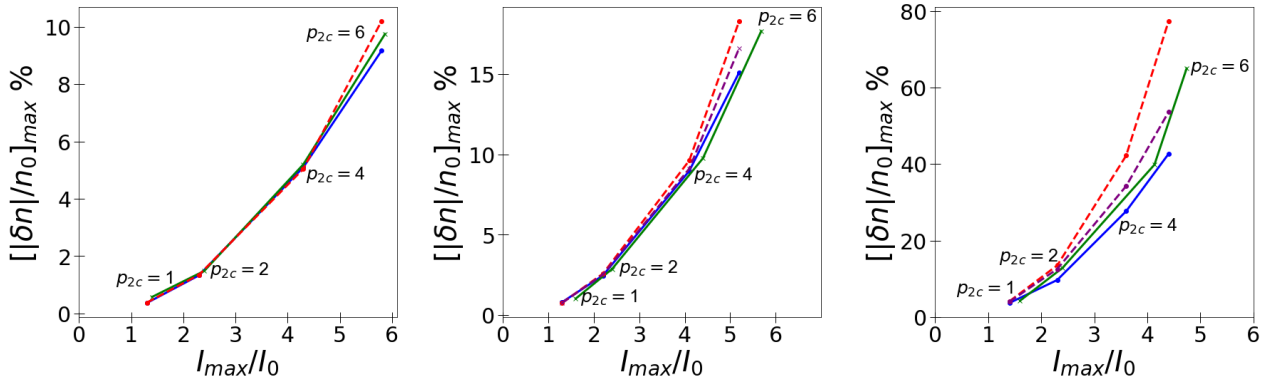

(a) (b) (c)

Figure 2.9: Amplitude of the density perturbation $[|\delta n|/n_{e0}]_{max}$ (%) as a function of laser intensity enhancement I_{max}/I_0 for various densities: (a) $n_{e0}/n_c = 0.1$, (b) $n_{e0}/n_c = 0.05$, (c) $n_{e0}/n_c = 0.01$. The green and the blue lines refer to HARMONY and PCGO-CHIC results respectively, the red and purple dashed lines to the amplitude of density perturbation estimated with the thick-ray intensity amplification according to linear theory, Eq. (1.151), and nonlinear theory, Eq. (1.152), respectively.

to correctly describe the laser and plasma dynamics: the density perturbation, exceeding 10%, becomes strongly nonlinear. Despite the filamention instability affects the laser beam evolution in the HARMONY simulations, a difference between the CHIC and HARMONY solutions remains less than 5-10%. At $n_{e0}/n_c = 0.01$ (see Fig. 2.9c) the nonlinearity in the plasma response appears at smaller power, $p_{2c} \approx 2$: the theoretical predictions for CHIC density response and intensity enhancement are better approximated by the nonlinear relation (purple dashed curve), but the simulations still underestimate the density response for higher beam powers. Thus, the density response in CHIC simulations results less accurate, leading to differences compared to theoretical predictions and HARMONY results. However, the difference remains lower than 20%, which is still satisfactory. For $p_c > 2$, the above theoretical considerations do not apply to HARMONY results due to filamentation instability, thus any relation between intensity enhancement and density perturbation no longer holds.

2.2.3 Conclusion on single-beamlet self-focusing

In this section, we summarize the main results on single-beamlet self-focusing. For $p_{2c} \geq 2$, the Gaussian thick-ray beamlet undergoes self-focusing for any plasma condition: the on-axis beam intensity increases, leading to a reduced beam width. The laser intensity enhancement weakly depends on the plasma density. Instead, higher initial beam powers correspond to larger intensity enhancements. The displacement of the beam peak intensity due to self-focusing follows the same tendency as the intensity enhancement, i.e. it is greatly reduced while increasing the beam power, whereas dependence on the plasma density is less important. However, only for $p_{2c} = 6$ and $n_{e0}/n_c \geq 0.05$ the self-focusing position is placed ahead the initial focal spot, otherwise it occurs behind it at distances that decrease with the beam power. The density response depends strongly on the initial plasma density: a strong nonlinear density perturbation with $[|\delta n|/n_0]_{max} > 10\%$ is excited for $p_{2c} \geq 2$ and $n_{e0}/n_c = 0.01$, whereas for higher densities, the response does not exceed the 10% for any power. One can

test the reliability of the PCGO-based thick-ray approach in describing beam self-focusing by comparing these results to electromagnetic code outcomes and theoretical estimations. Thick beamlets cannot break in filaments because the filamentation instability is not compatible with the assumption that PCGO beamlets must keep a Gaussian shape all along their propagation. Therefore, filamentation instability sets an upper limit for accurate description of Gaussian beam dynamics within the thick-ray approximation. The full-wave description predicts filamentation instability for $p_{2c} \geq 4$. Independently of the plasma density, more accurate theoretical evaluations set the threshold power for filamentation instability in case of Gaussian beams at $p_{2c} = 2.5$. In fact, in agreement with HARMONY simulations and differently from the plane wave results, the self-focusing of a Gaussian beam takes place at powers lower than the threshold of a filamentation instability because only perturbations with the wavelength smaller than the beam diameter can be excited. The simulations show that for $p_{2c} < 2.5$, Gaussian beam undergoes intensity amplification, whereas for $p_{2c} > 2.5$, filamentation instability develops. Despite filamentation instability is excited and it cannot be described with PCGO, one can safely extend the thick-ray model validity to $p_{2c} \leq 6$ as only one of the instability-induced filaments carries the dominant part of beam energy, and PCGO reproduces the most important self-focusing characteristics of such a filament. We also found that at low densities, the coupling between the hydrodynamic response in CHIC and the intensity enhancement predicted by the thick-ray model becomes less accurate because of the nonlinear plasma response. However, this issue is less important when considering a realistic density profile as encountered in ICF. Since the critical power is inversely proportional to the density, beam self-focusing is most likely to occur at high densities.

2.3 Self-focusing of a multi-beamlet speckle

In this section, we consider the propagation of a multi-beamlet speckle and its intensity enhancement is compared to the intensity amplification in a single thick beamlet. This is done in order to define the method that allows to better control ponderomotive effects in a multi-beamlet speckle. The plasma conditions are the same as in Sec. 2.2.2, keeping the density fixed at $n_{e0}/n_c = 0.1$ and with a plasma temperature $T_{\text{eff}} = 1$ keV. With these conditions, the thick-ray approximation is as accurate as possible in describing single-beamlet self-focusing. Therefore, the results shown in Section 2.2.2 represent the reference case for the multi-beamlet speckle study. Two methods of multi-beamlet speckle formation are compared: a random beamlets configuration and a regular beamlets configuration. In the random configuration, several thick beamlets are arbitrarily focused in a limited area, so the speckle shape is varied in each realization. Conversely, in the regular shaping, the beamlets are focused in a way to form a speckle with a prescribed Gaussian shape. In both cases, the initial multi-beamlet speckle power is equally split over the N_b beamlets: $P_b = P_s/N_b$, where P_s is the whole speckle power, whereas P_b is the beamlet power. Four different values of beam power are considered: $p_{2c} = P_s/P_c^{2D} = 1; 2; 4; 6$, where P_c^{2D} is evaluated according to Eq. (1.164). The number of beamlets N_b is varied from 3 to 5. The total power is equally split over the thick beamlets. Then, for $N_b = 3$, each thick beamlet carries 33% of P_s, for $N_b = 4$ it carries 25% of P_s and for $N_b = 5$ it carries the 20% of P_s. Such a power splitting recreates the speckles as conceived in the standard thick-ray-based approach for designing spatially modulated beams: there, the most

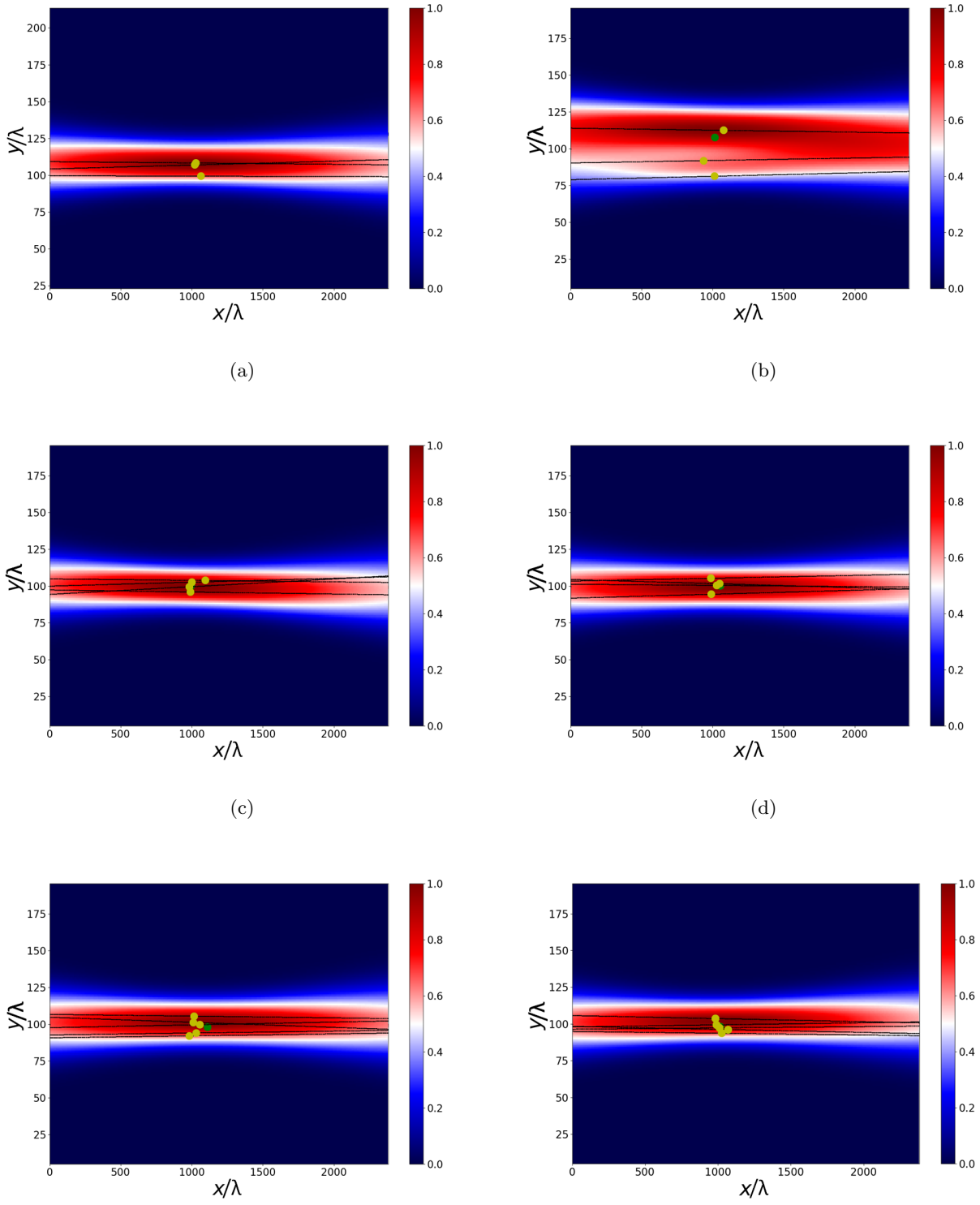

Figure 2.10: Beam intensity in plasma normalized to the maximum intensity in plasma (color bar) in two different runs within the random speckle shaping method for $N_b = 3$ in a) and b), for $N_b = 4$ in c) and d) and $N_b = 5$ in e) and f). The black curves show the beamlet trajectories. The yellow and green points stand for beamlet focal position. The spatial coordinates are in units of the laser wavelength λ. The laser enters from the left side.

intense speckles are composed by beamlets having approximately the same power, which facilitates occurrence of ponderomotive effects.

We remark that in this chapter only self-focusing of an isolated multi-beamlet speckle is analyzed, whereas in Chapter 3 we consider multi-speckle beams.

2.3.1 Multi-beamlet speckle: random speckle shaping

Evolution of a multi-beamlet speckle created with the method of random shaping is studied here. Thick beamlets having a waist of 20λ are randomly focused in plasma in a focal zone of size ($40\lambda \times 20\lambda$), giving a multi-beamlet speckle focusing point located around $(1000\lambda, 100\lambda)$. The angles of incidence of the beamlets have been changed in each simulation, being randomly chosen in the interval between $\hat{\theta}$ and $-\hat{\theta}$, where $\hat{\theta} = 0.2^{\circ}$ is the averaged multi-beamlet speckle divergence. The values of beamlets angles of incidence and the size of the focusing box have been chosen to reproduce a not too distorted multi-beamlet speckle, with an intensity envelope sufficiently close to a Gaussian-shaped beam. For each realization, the simulation time is $t_f = 250$ ps. In order to accumulate statistics and investigate average behavior of such a multi-beamlet speckle, we performed 5 simulations for each case for a given speckle power P_s. Figure 2.10 presents an example of a random beamlet configuration and related multi-beamlet speckle intensity distribution for $N_b = 3$ in a) and b), for $N_b = 4$ in c) and d), and for $N_b = 5$ in e) and f) with two different initial focusing parameters. The black curves show the thick beamlets trajectories, the yellow points stand for beamlet focusing spots, whereas the green points for the multi-beamlet speckle focus position. This set of pictures illustrates the randomness of the beamlets configuration inside the speckle and its influence on the multi-beamlet speckle shape. In the following, we show how such a random beamlets configuration affects the speckle self-focusing. Figure 2.11 shows the laser intensity enhancement averaged over 5 simulations $(I_{max}/I_0)_{aver}$. The solid blue line refers to the single-beamlet intensity

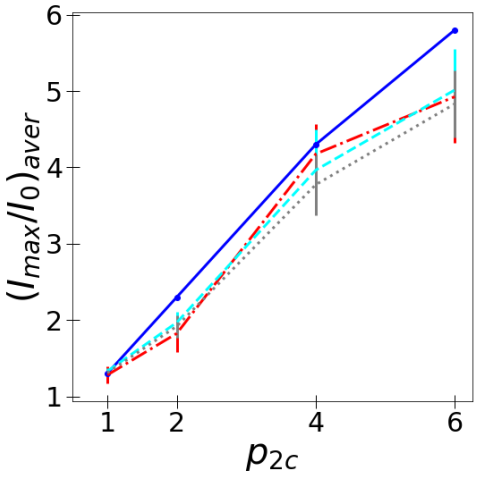

Figure 2.11: Laser intensity enhancement averaged over 5 simulations $(I_{max}/I_0)_{aver}$ when a stationary state as reached in function of the beam power for n_{e0}/n_c=0.1. The solid blue line refers to the single-beamlet case (see Fig. 2.7a), the red dashed dotted line to $N_b = 3$, the dashed cyan line to $N_b = 4$ and the dotted gray line $N_b = 5$. The error bars refer to the standard deviation of the average.

amplification described in Sec. 2.2.2 (see Fig. 2.7a), other lines refer to multi-beamlet cases: the red dashed dotted line refers to the case $N_b = 3$; the dashed cyan line to the case $N_b = 4$ and the gray dotted line to the case $N_b = 5$. The intensity enhancement in a multi-beamlet speckle is reduced with respect to the single-beamlet case: the maximum reduction is 15% for high power ($p_{2c} = 6$), with a weak dependence on N_b only for $p_{2c} \geq 2$. Since the thick beamlets carry a fraction of the total speckle power, the speckle-plasma dynamics is modified: the local plasma density perturbation is less deep and broader along the density channel compared to the single-beamlet case presented in Sec. 2.2.2. Due to the aleatory location of the beamlet focus positions in a very small area, their overlap reproduces almost the same ponderomotive force as in the single-beamlet case. Thus, randomly superposed thick beamlets just slightly reduce the intensity amplification compared to a single-beamlet with the same power. The reduction however cannot be deterministically quantified from the initial beamlets configuration, since the multi-beamlet speckle profile is not a priori defined. Other simulations performed but not not reported here show that increasing the number of beamlets beyond $N_b = 5$, the intensity enhancement for such multi-beamlet speckles follows the same tendency as for $N_b \leq 5$, demonstrating that ponderomotive effects weakly depend on N_b in case of the random configuration method. Also, simulations performed with different power splitting show that if one beamlet carries more than 50% of the total power, it governs the multi-beamlet speckle self-focusing similarly to the single-beamlet case. Therefore, unequal distribution of the speckle power over the beamlets is not considered for implementation in the PCGO algorithm developed for multi-speckle beams.

2.3.2 Multi-beamlet speckle: regular speckle shaping

In this section we study a multi-beamlet speckle containing 3 and 4 regularly focused beamlets. This choice is motivated by the results of the previous section: the self-focusing depends weakly on the number of beamlets. We present two relevant cases of multi-beamlet speckles composed by three superposed beamlets in Fig. 2.12a and four superposed beamlets in Fig. 2.12b. In case of $N_b = 3$, the focus point of the speckle represented by the green spot is located at $(1000\lambda, 100\lambda)$: the outer beamlets enter the plasma with angles of incidence of $\pm$ 0.02° with respect to the central beamlet which propagates parallel to the x axis, i.e. the speckle axis. The positions of the beamlets focusing spots (yellow points) are placed at: $(900\lambda, 110\lambda)$, $(1100\lambda, 100\lambda)$ and $(1300\lambda, 90\lambda)$ respectively. For $N_b = 4$, in Fig. 2.12b, the two central thick beamlets are focused at $(800\lambda, 100\lambda)$ with an angle of incidence of $\pm$ 0.01° respectively, whilst the outer beamlets are focused at $(1200\lambda, 110\lambda)$ and $(1200\lambda, 90\lambda)$ with an angle of incidence of $\pm$ 0.02°. The transverse and longitudinal speckle intensity profiles for each case are shown in Figs 2.12c-2.12d, respectively. The solid blue lines stand for a reference Gaussian profile, whereas the dashed dotted red line and the dashed cyan line stand for $N_b = 3$ and $N_b = 4$, respectively. Figure 2.12c refers to the transverse profiles at the focus position, whereas Fig. 2.12d refers to the longitudinal profiles. The matching with the Gaussian longitudinal and transverse profiles is correct in all cases.

Figure 2.13b shows the intensity enhancement in a speckle formed with three beamlets compared to single-beamlet simulations presented in Sec. 2.2.2 (solid blue line in Fig. 2.7a). The intensity enhancement I_{max}/I_0 is taken when a quasi-stationary state is established. The error bars refer to the standard deviation of the time-averaged intensity enhancement since the maximum peak intensity varies slightly in position and amplitude.

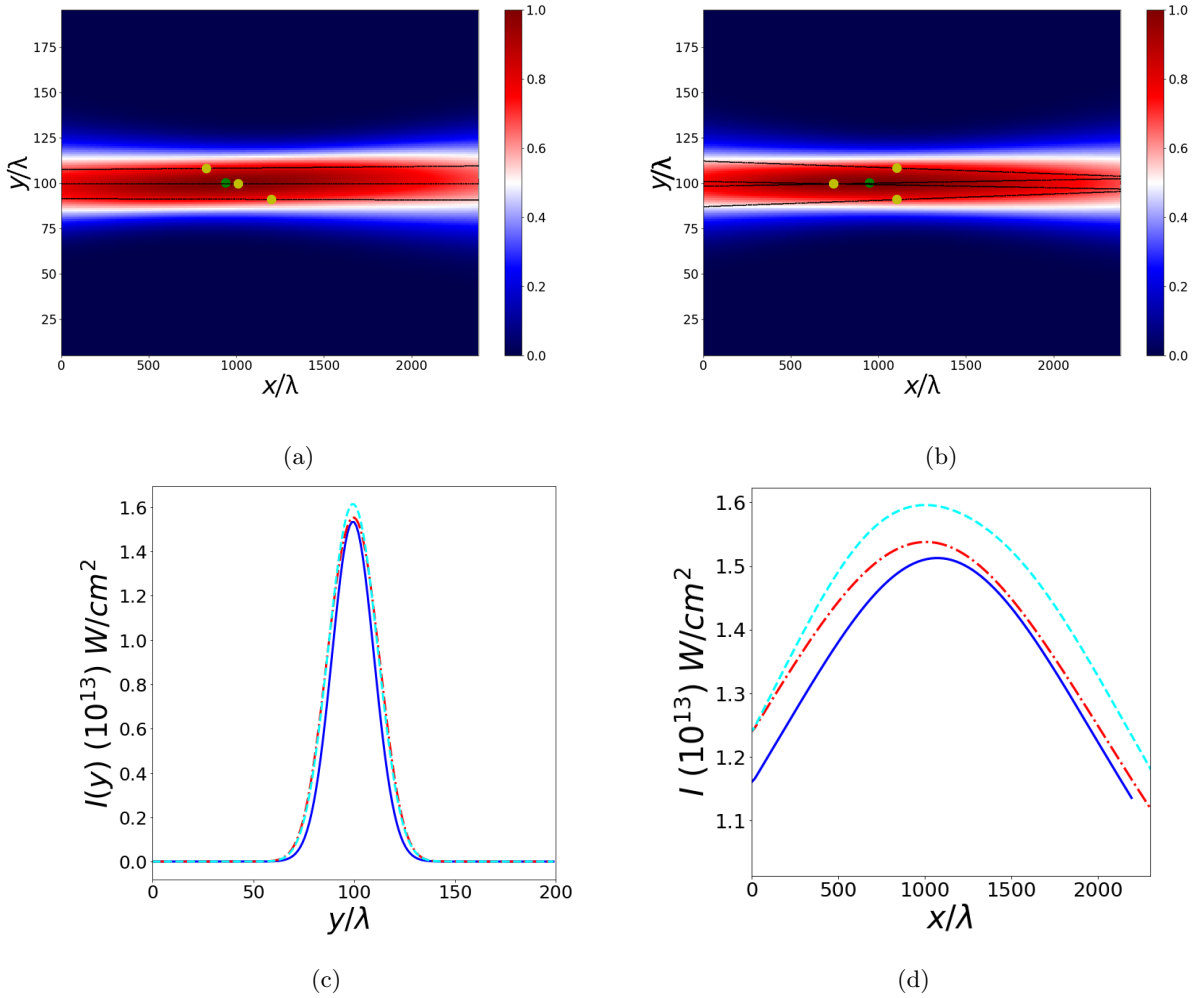

Figure 2.12: Example of regular multi-beamlet speckle shaping for $N_b = 3$ (a) and $N_b = 4$ (b). The beamlet power is P/N_b, where P is the speckle power. The blue dashed curves show the beamlets trajectories. Addition of all beamlet intensities gives rise to multi-beamlet speckle intensity indicated by the color bar. The intensity is normalized to the maximum speckle intensity. The green points stand for the multi-beamlet speckle focus position, whereas the red points stand for the beamlet focusing points. c) Laser intensity transverse cut in the focal plane and d) longitudinal laser intensity distribution along the beam propagation direction for the single-beamlet (solid blue line) and a regularly shaped multi-beamlet speckle for $N_b = 3$ (red dashed dotted line) and $N_b = 4$ (dashed cyan line) in case $p_{2c} = 1$. The total intensity profile is given by the sum of beamlet intensities inizialised in the far-field as shown in 2.12a for $N_b = 3$ and in 2.12b for $N_b = 4$. In panels a, b and d, the laser enters from the left. The spatial coordinates are in units of the laser wavelength λ.

The dashed red line refers to the case where the multi-beamlet speckle power is set equal to single-beamlet cases (see Sec. 2.2.2), so $p_{2d} = P_s/P_c^{2D} = P_{2D}/P_c^{2D}$, where P_{2D} is the power of a single beamlet as described in Sec. 2.2.2. The laser intensity enhancement is reduced in a multi-beamlet speckle. Similarly to the case of a random multi-beamlet, since the thick beamlets do not fully overlap, they create a longer density channel along the speckle axis than in the single-beamlet case. Such a density channel is shallower compared to the case of a

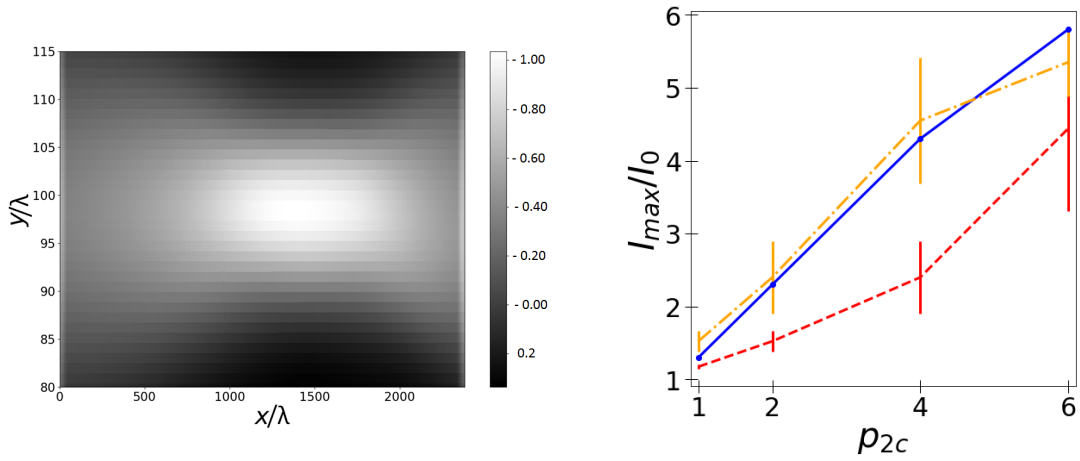

(a) (b)

Figure 2.13: a) Amplitude of the density perturbation $\delta n(x,y)/n_0$ (%) induced by a three-beamlet regularly shaped speckle for $n_{e0}/n_c = 0.1$ and $p_{2c} = 2$ at $t = 210$ ps. b) Laser intensity enhancement I_{max}/I_0 as a function of the beam power. Comparison between the single-beamlet and speckle with regular shaping for $N_b = 3$. The plasma density is $n_{e0}/n_c = 0.1$. The solid blue curves refer to single-beamlet results (solid blue curve in Fig. 2.7a). The red dashed lines refer to the case where the multi-beamlet speckle critical power is defined according to Eq. (1.164), the orange dashed dotted lines show the intensity enhancement assuming that the speckle critical power is twice the value defined by Eq. (1.164).

single-beamlet, leading to a weaker self-focusing. This feature can be seen by comparing the density channels produced by a single-beamlet as in Fig. 2.1c to the three-beamlet speckle. The latter one is shown in Fig. 2.13a for the same plasma conditions and at the same time: the density channel in the second case is larger and longer than in the single-beamlet case, and the amplitude of the density perturbation in the three-beamlet case is 75% smaller than in the single-beamlet case. Despite that, the density channel is sufficiently deep to refract the beamlets trajectories and guide them along the channel axis, resulting in spraying of beamlets and breaking of the initial speckle shape. All these effects contribute to self-focusing suppression compared to the case of a single beamlet carrying the same power.

Self-focusing of a speckle can be characterized by the ratio of the effective speckle length x_s to the speckle width w_0. In analogy to Gaussian beams, the longitudinal length of regularly shaped multi-beamlet speckle x_s is defined as a distance from the speckle intensity maximum to where the intensity decreases by a factor of $\sqrt{2}$. At early time, before self-focusing develops, the multi-beamlet speckle has a quasi-Gaussian profile (see Fig. 2.12a and Figs. 2.12c-2.12d), and $[x_s\lambda/(w_0^2\pi)]_{t=0} \approx 1$. For a single beamlet, $x_s \equiv x_R$, and $[x_R\lambda/(w_0^2\pi)] = 1$ independently of the time, given that Eq. (1.26) must be satisfied due to PCGO ansatz. For a multi-beamlet speckle, this aspect ratio changes in time because each beamlet produces the ponderomotive force independently. Consequently, the aspect ratio increases with time by a factor varying between 1.5 and 2.6. Thus, the self-focusing zone is in average around 2 times longer than in the single-beamlet case. This modification of the speckle shape explains reduction of the intensity enhancement in the speckle. Increase of the aspect ratio in a self-focused speckle is illustrated in Fig. 2.14. The intensity contours with black lines correspond to the single-

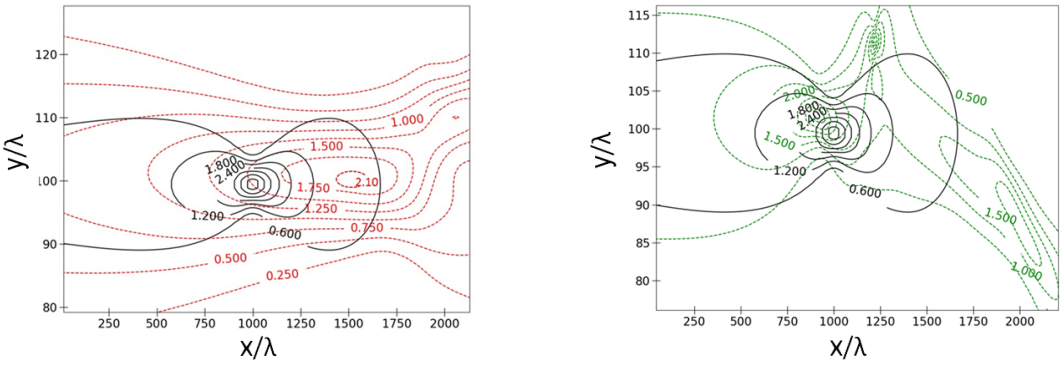

(a) (b)

Figure 2.14: Laser intensity contour plot in plasma at time 200 ps. In both panels, the solid black lines refer to the case of a single-beamlet with $p_{2c} = 4$ at $t = 200$ ps. The red dashed lines in (a) refer to the speckle with $N_b = 3$ having the same power as the single-beamlet. The green dashed lines in (b) corresponds to a three-beamlet speckle with power $\eta = 2$ times bigger. The intensity is normalized to the initial maximum intensity in plasma. The spatial coordinates are in units of the laser wavelength λ. In all the figures, the laser enters from the left side.

beamlet self-focusing with $p_{2c} = 4$. The red and green dashed lines correspond to the three-beamlet speckle self-focusing having the same power as the single-beamlet in Fig. 2.14a, and a power twice bigger in Fig. 2.14b respectively. The aspect ratio of single-beamlet remains constant, equal to the initial value, i.e. approximately one. Considering for the black lines that the beam width is 5λ and that the beamlet intensity enhancement is 4.5 (see Fig. 2.7a), the longitudinal length where intensity decreases by a factor $\sqrt{2}$ is $\approx 100\lambda$, which gives an aspect ratio ~ 1.12. Calculating the aspect ratio for the three-beamlet speckle in Fig. 2.14a, one obtains a number around 1.7.

Evaluating the aspect ratio for a speckle with a power twice higher (Fig. 2.14b), one finds it is around 1.3. Consequently, in order to obtain approximately the same aspect ratio as of a single-beamlet, we redefine the power of the multi-beamlet speckle as twice larger than the single-beamlet power. One can account for this by redefining the critical power for such a three-beamlet speckle $\tilde{P}_{c,speckle}$ as $\tilde{P}_{c,speckle} = \eta P_c^{2D}$, where $\eta = 2$ corresponds to the aspect ratio of the multi-beamlet speckle having the same power as the single-beamlet. Rerunning the simulations for a three-beamlet speckle of same characteristics as earlier but with a power $p_{2c} = P_s/\tilde{P}_{c,speckle}$, one obtains the dashed orange line in Fig. 2.13b, where the intensity enhancement of the multi-beamlet speckle becomes comparable to the single-beamlet case. Thus multiplying the speckle critical power by η allows to retrieve the single-beamlet results in terms of intensity amplification. Or, from a different point of view, one can state that superposing three beamlets in the configuration shown in Fig. 2.12a leads to a reduction of self-focusing effects roughly quantified by the increasing of the critical power by a factor of $\eta = 2$. Besides the intensity amplification in plasma, also the speckle shape around the self-focusing position is very similar to the single-beamlet, as one can see in Fig. 2.14b. However, despite rescaling the critical

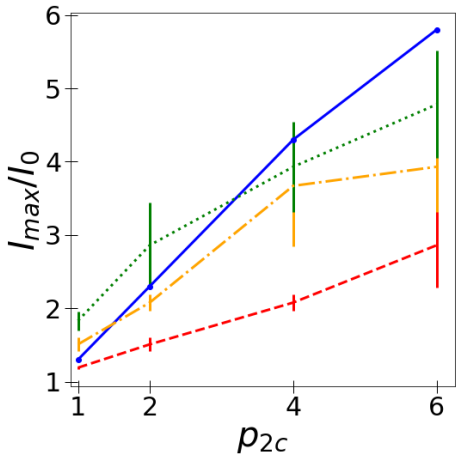

Figure 2.15: Laser intensity enhancement I_{max}/I_0 as a function of the beam power. Comparison between the single-beamlet and speckle with regular shaping for $N_b = 4$ (b). The plasma density is $n_{e0}/n_c = 0.1$. The solid blue curves refer to single-beamlet results (solid blue curve in Fig. 2.7a). The red dashed lines refer to the case where the multi-beamlet speckle critical power is defined according to Eq. (1.164), the orange dashed dotted lines show the intensity enhancement assuming that the speckle critical power is twice the value defined by Eq. (1.164), the dotted green line refers to the case where the critical power is multiplied by a factor of 3.

power of a three-beamlet speckle allows to retrieve the intensity enhancement in plasma, several features of the standard Gaussian beam propagation are lost. This is evidenced in Fig. 2.14b: the self-focusing position of the three-beamlet speckle, located around $(900\lambda, 100\lambda)$, is shifted from the position of the single-beamlet case, and deviated from the initial multi-beamlet speckle propagation axis. The three-beamlet speckle shape is modified behind the focus because of beamlets refraction in the density channel. The beamlets trajectories are deviated, creating other local intensity maxima, as the one at the position $(1200\lambda, 112\lambda)$. Although this process resembles beam spraying with a prescribed number of filaments equal to the number of beamlets, this phenomenon is a consequence of neglecting the field phases while combining the beamlets intensities, and it stands as an artifact of the model.

The results for a four-beamlet speckle self-focusing with an initial beamlet configuration as in Fig. 2.12b are displayed in Fig. 2.15. Here the intensity enhancement I_{max}/I_0 is shown as a function of a four-beamlet speckle power defined as $p_{2c} = P_s/P_c^{2D}$ (red dashed line), and a single-beamlet power (solid blue line). Superposition of four beamlets decreases the intensity enhancement by 50% in average. These results, similarly to the previous case $N_b = 3$ could be reduced to the single-beamlet case by introducing a multiplicative factor $\eta \approx 2 - 3$ in the critical speckle power. In Fig. 2.15, the orange dashed dotted line and the green dotted line correspond to the case for which $p_{2c} = P_s/\tilde{P}_{c,speckle}$, with $\eta = 2$ and $\eta = 3$ respectively. However, the agreement is satisfactory for $\eta = 2$ for $p_{2d} < 4$. Instead, a larger discrepancy occurs for η=3 at $p_{2d} > 4$. This simplified reduction is not as accurate as in the case of three beamlets. It means that the considerations made for the three beamlets speckle does not completely hold for the case $N_b = 4$, showing that the process is strongly related to the initial beamlet configuration.

2.3.3 Conclusion on multi-beamlet speckle self-focusing

We conclude this section by commenting the results obtained in cases of randomly and regularly shaped multi-beamlet speckles. The random method allows to decrease the ponderomotive effects, but the effect is weak: an average decreasing of 10-15% is not enough to approach the intensity enhancement theoretically predicted in 3D speckles. Moreover, although here we used a very small focusing box in order to keep the speckle shape close to a Gaussian beam, the control of speckle characteristics is still difficult: in the standard thick-ray method used to create spatially modulated beams, the focusing box is at least one order of magnitude larger, thus the speckles loss the Gaussian symmetry. This may lead to an uncontrolled self-focusing, which would strongly depend on the random superposition of the beamlets inside the speckle.

In the case of regularly-shaped speckles, the ponderomotive effects are better controlled. The reduction of self-focusing is better attained through superposition of three and four thick beamlets, and it is quantified by introducing a scaling factor in the multi-beamlet speckle power. In the case $N_b = 3$ such a reduction can be accounted for by rescaling the three-beamlet speckle critical power by a factor $\eta = 2$. The value of this factor is justified by increase of the speckle aspect ratio. For $N_b = 4$, ponderomotive effects are also suppressed, but relation to the aspect ratio is more complicated. This is due to the fact that the control of self-focusing depends on several parameters, such as the initial beamlet focusing positions and angles of incidence. Moreover, the whole speckle dynamics is affected by the interaction of beamlets when ponderomotive effects occur. The factor η stands as a rough description of all such effects, which gives an acceptable agreement in a limited number of cases. Notably, the redefinition of the critical power of a three-beamlet speckle allows to reduce the PCGO speckle intensity enhancement of the desired factor as estimated in Sec. 1.3.3.

2.4 Conclusion

We have studied ponderomotive self-focusing of a laser beam in plasma within the PCGO-based approach implemented in the hydrodynamic code CHIC, the thick-ray model. The validity domain of the thick-ray approximation is defined by comparison to the paraxial wave-based code HARMONY while simulating self-focusing of a Gaussian beam. A good agreement is found for beam powers less than four times the critical power. From $p_{2c} > 2$, Gaussian beams undergo filamentation instability and then break in filaments. Such a phenomenon cannot occur within the thick-ray approximation due to the geometrical optics limitation. However, thick-ray simulations retrieve the laser intensity enhancement up to six times the critical power when comparing to the intensity enhancement of the main filament in the HARMONY simulations. This assessment is confirmed for plasma density in the range $n_{e0}/n_c = 0.01 - 0.1$ and temperature 1 keV pertinent to ICF conditions in the target corona. A better agreement between the thick-ray approximation and HARMONY results has been found for $n_{e0}/n_c = 0.1 - 0.05$ where the density depletion is less important.

In order to model the situation of multiple speckles in an optically smoothed laser beam, a superposition of a limited number N_b of thick beamlets created within the thick-ray model has been considered. The goal was to overcome the fact that beamlets and multi-beamlet speckles are larger than real speckles. So they carry a higher power than real laser speckles, and therefore self-focusing is overestimated. To correct the unrealistic self-

focusing in a multi-beamlet speckle, two methods of speckle shaping have been presented: random and regular with $N_b = 3 - 5$ beamlets. Their superposition in intensity, with a weight (here of $1/N_b$) for each of them, is considered. We found that this approach results in a reduced self-focusing with respect to a single thick beamlet carrying the same power. In both cases of random and regular, a reduction of intensity enhancement has been evidenced. For the case of a regular multi-beamlet shaping, this reduction can be quantitatively accounted for by considering an effective increase of the critical power by a factor of η compared to the critical power of a Gaussian beam of the same width. This factor is approximately equal to the aspect ratio of the self-focused multi-beamlet speckle. In case of $N_b = 3$, $\eta \simeq 2$, and for $N_b = 4$, $\eta \simeq 2 - 3$. The validity of this approximation is limited to the case where the initial multi-beamlet speckle power is limited to a few times the critical power, and, furthermore, where the initial multi-beamlet configuration corresponds to a Gaussian shape as illustrated in Sec. 2.3.2.

Employing the method of regularly overlapping three beamlets to build PCGO speckles, one is able to reduce the intensity amplification by a factor of 2. This feature is demonstrated in a 2D planar geometry, where the PCGO formalism has been implemented. Therefore, with this method, one can systematically account for the 3D speckle intensity amplification overestimation of around 2 as seen in Sec. 1.3.3. This represents a step forward to correctly account three-dimensional nonlinear effects in a reduced geometry with simplified models.

In Chapter 3, self-focusing of spatially modulated beams configured by adapting the regular beamlet initialization is investigated.

Chapter 3

Self-focusing of a spatially modulated beam within the PCGO framework in homogeneous nonabsorbing plasmas

Although numerical [115,131] and experimental [132,133] investigations have evidenced that optical smoothing techniques reduce the occurrence of laser-plasma instabilities by decreasing speckle ponderomotive self-focusing, the latter can still affect the laser-plasma coupling especially in regions where beams cross each others or within the shock ignition context. Despite its importance, ponderomotive effects have been always neglected in hydrodynamic simulations because the standard ray-tracing method used in these codes cannot straightforwardly account for nonlinear laser-plasma coupling. The advent of PCGO-based algorithm provides an opportunity to approximate the beamlet diffraction along with some intensity-related features of laser-plasma interaction. In addition, beams with spatial intensity modulations can be designed by superposing several beamlets: within the PCGO algorithm implemented in the hydrodynamic code CHIC, a set of randomly generated beamlets propagate inside the plasma to form an arbitrary spatial configuration of speckles. In this scheme, the intensity probability distribution is not controlled. In Chapter 2 we showed that controlling of self-focusing effects can be achieved by regularly distributing the beamlets inside the speckles.

In this chapter, we describe a new method for generating a speckle pattern within PCGO-CHIC based on results obtained in Chapter 2. In this novel approach, the speckles are created by regular superposition of three Gaussian beamlets with intensities chosen such that speckle intensity probability distribution obeys to Eq. (1.66). Such a method is referred to as *semi-deterministic algorithm*, in contrast to the standard PCGO method called *random algorithm*. In both PCGO approaches, in contrast with real interference of optical beamlets, the number of speckles in the far-field is not linked to number of phase plate elements given that the speckles are directly defined in the far-field (semi-deterministic algorithm) or on the simulation boundary (random algorithm). Both schemes neglect the beamlet phases while computing the intensity envelope. In this context then, the number of speckle is related to the number of beamlets and can be controlled in the input.

We show here that the semi-deterministic approach improves the description of laser-plasma coupling in regimes where ponderomotive effects develop. In fact, the PCGO speckle pattern conserves some aspects of real self-focused speckles after re-normalization of PCGO speckle power by the factor introduced in Chapter 2. This re-normalization has been proved by comparing our results to simulations performed with electromagnetic codes. We are then confident that the novel algorithm permits to better describe intensity amplification of PCGO speckles when compared to real speckles.

The chapter is organized as follows: the algorithm for creating the PCGO speckle pattern is illustrated in Sec. 3.1. A detailed study of the plasma response, speckle self-focusing on short- and long-time scales and the overall beam evolution are presented in Sec. 3.2. A comparison to results obtained in previous publications is discussed in Sec. 3.3, whereas the advantages of such a method compared to the random algorithm for creating speckle patterns are discussed in Sec. 3.4. A summary of our results is presented in Sec. 3.5.

3.1 Creation of spatially modulated beams with PCGO in CHIC

In this section, we describe the two PCGO-based algorithms implemented in the hydrodynamics code CHIC and dedicated to generation of spatially modulated beams: in Sec. 3.1.1, the random approach is reviewed. In 3.1.2, the new semi-deterministic method, which is built on the results obtained in Chapter 2, is presented. In both cases, the speckle pattern is intended stationary all along the simulation, i.e. the coherence time of the speckles is longer than any simulation time. This is because we are not considering temporal smoothing techniques.

3.1.1 Random speckle pattern

In the PCGO standard approach, the speckle pattern is created by randomly projecting several Gaussian beamlets from the simulation boundaries to the far-field in three steps: the first step concerns the definition of the flat-top profile, by inserting value of the beam width in the far-field w_B, the beam power P_B, the order of the Super-Gaussian profile n and the beam focus spot (x_B, y_B). The average beam intensity $< I >$ is a-posterior computed through the relation

$$< I >= \frac{P_B}{\int_{-l_y}^{l_y} e^{-2\left|\frac{y}{w_B}\right|^n} dy}, \tag{3.1}$$

where l_y is few times larger than w_B. Once defined the spatial intensity distribution inside the simulation region, i.e. in the far-field, a Fast Fourier Transform back-propagates such an intensity distribution to the simulation boundaries, called virtual sphere in the following, in order to recreate at this position the corresponding intensity profile. At the same position, a sphere called virtual sphere is defined. The second step, named beam-splitting, consists in definition of N_b thick beamlets on the virtual sphere, with the intensity envelope reproducing the incident laser beam profile. The beamlets are initialized equidistantly with width w_0^b. The final stage consists in projecting the beamlets from their origin to their focus spot positions, which are randomly chosen inside a focusing box designed in the input. The dimension of the focusing box is related to the longitudinal speckle

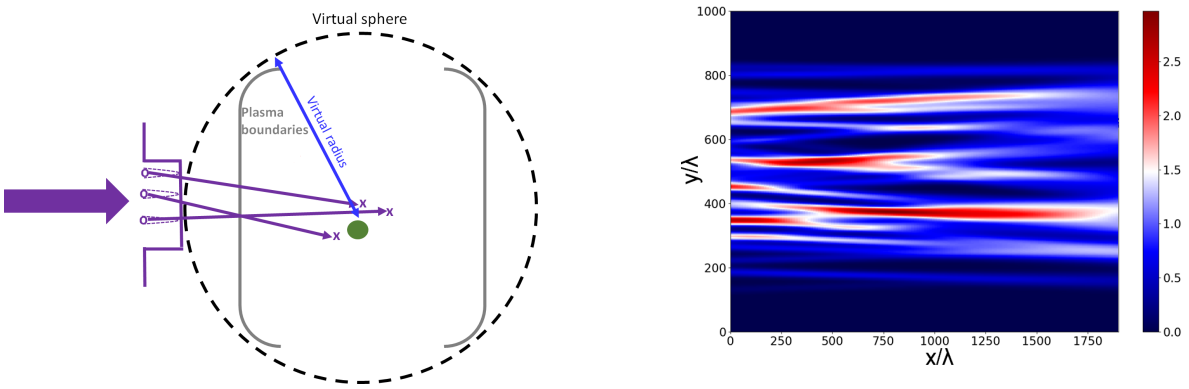

(a) (b)

Figure 3.1: Random algorithm: (a) scheme of the thick-ray algorithm implemented in the hydrodynamic code CHIC and generating a random speckle pattern. b) Laser intensity in the plasma normalized to the average intensity realized with the random algorithm. The laser comes from the left side. The spatial coordinates are in laser wavelength units.

size x_s, defined by Eq. (1.64), the speckle waist w_s, defined by Eq. (1.63), and the total beam width w_B. Eventually, the beamlets superposition in the simulation domain creates spatial modulations in the far-field. Figure 3.1a schematically presents all the process: the intensity of the incoming flat-top beam (purple curve) is distributed over N_b equidistant beamlets (dotted purple curves) on the virtual sphere (dashed black circle). The beamlets focus positions (purple crosses) are randomly chosen inside a box around the beam focus spot (green spot). The angle of incidence θ_b^j of the beamlet j is automatically evaluated by the algorithm once fixed the position where the beamlet is generated on the virtual sphere and the focused spot position randomly determined. Figure 3.1b shows the results of one realization by employing the random algorithm: it depicts the initial laser intensity distribution normalized to the beam average intensity $< I >$ in the far-field. The beam focus spot is located around $(500\lambda, 500\lambda)$. Local intensity maxima arise in areas where beamlets cross each others. These maxima represent the speckle pattern, which is localized within the focusing box defined by the input parameters. For each realization, the speckle intensity distribution does not reproduce the probability law Eq. (1.66) because the algorithm does not account for it. In order to reproduce the speckle statistics, one may repeat the same simulation for several times: for example, to obtain the speckle intensity statistics for 1000 speckles, one may perform 50 runs when considering a number of PCGO speckles equal to 20 for each run. Such method of speckle initialization limits the applicability of PCGO for investigating the ponderomotive effects in spatially modulated beam because the speckle intensity statistics cannot be controlled in a single realization. For more details on the random algorithm and application to ICF see Ref. [41].

3.1.2 Semi-deterministic speckle pattern

In the random approach, the speckle pattern is produced by superposition of randomly distributed beamlets generated from a given beam intensity profile. This method gives rise to random intensity fluctuations, with

speckle characteristics not a priori determined. Despite it was successfully applied for modeling some ICF-related phenomena, introduction of speckle statistical properties is needed in order to account for high intensity speckles especially when self-focusing effects are comprised. In Chapter 2 we demonstrated that a regular distribution of the beamlets inside a speckle provides a better control the individual speckle self-focusing. In order to extend these results to a spatially modulated beam, we developed an algorithm which regularly distributes the beamlets inside each speckle. In addition, this method assigns to each beamlet an intensity such that the probability distribution of the speckle statistics obeys to an exponential law. The algorithm operates as follows: first, the number of speckles N_s and the beam width w_B are fixed in the input. Then, the speckle width w_s is computed:

$$w_s = \frac{w_B}{N_s}. \tag{3.2}$$

From this equation, in order to remain within both PCGO and hydrodynamics limitations, it follows that $w_s = 15\lambda - 60\lambda$, depending on the laser wavelength. That sets an upper limit to the number of speckles, which spans between 15-50. Once defined the optical characteristics of speckles, the algorithm confers to each speckle a random intensity value within a range such that the ensemble of speckle intensities obey to Eq. (1.66). Despite the number of speckles created within the PCGO algorithm is smaller than the number of optical speckles, we choose the speckle intensities such that the intensity interval ranges from one tenth to three/four times the average beam intensity as in real speckle patterns.

By varying the spatial proprieties of the beamlet configuration, different spatial speckle distributions can be explored: patterns where inter-speckle distance is randomly varied, or speckles with arbitrary inclinations with respect to the laser beam axis. In the design used throughout this chapter, the beamlets are initialized to form parallel speckles with a constant transverse distance between them: considering that the beam focus spot is located at (x_B^f, y_B^f), the transverse focus spot coordinate y_s^j of the jth speckle is:

$$y_s^j = y_B^f + (N_s - 2j) y_w w_s, \tag{3.3}$$

where y_w is a numerical factor introduced from the input permitting to increase or decrease the focusing box area. The longitudinal spot coordinate x_s^j of the jth speckle is randomly chosen in the interval $\left[x_B^f - x_s; x_B^f + x_s\right]$. Then, the speckle-splitting process takes place: around each speckle focus spot position, three beamlets are initialized by starting with their focus spot positions. These beamlets are geometrically placed such that the central one has the same focus spot coordinates as the relative speckle, whereas the two outer beamlets are shifted to $(x_s^j \pm 0.15x_s, y_s^j \pm w_s/2)$, respectively. The beamlets have the same width, equal to the speckles width. We note that only one degree of freedom on the longitudinal spatial positions of beamlets focus spots is considered in this version of semi-deterministic method, whereas in the random algorithm there are two spatial degrees of freedom, longitudinal and transverse. At the next step, the speckle-splitting method equally divides the speckle intensity I_s over the three beamlets, thus $I_b = I_s/3$, where I_b refers to the beamlets intensity. Similarly to the random method, the last step consists in a back-propagating Fast Fourier Transform, which evaluates the beamlet properties over the virtual sphere, where they are initialized. The virtual sphere must be close enough to the simulation boundaries such that the beamlet wave vectors are approximately parallel to the beam axis. At the end of the initialization, the beam presents a small-scale modulations in form of

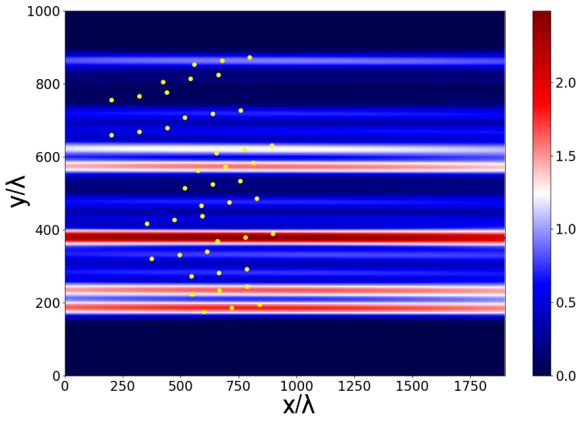

Figure 3.2: Semi-deterministic speckle pattern: laser intensity normalized to the average intensity in the far-field. The yellow points stand for the beamlet focus spots. The laser comes from the left side. The spatial coordinates are in laser wavelength units.

Gaussian-like three-beamlet speckles, each of them having a transverse and longitudinal intensity profile similar to the profiles studied in Chapter 2 for the regularly-focused three-beamlet speckle.

This semi-regular beamlets distribution produces the intensity distribution pattern as displayed in Fig. 3.2: here the color bar represents the beam intensity normalized to the average beam intensity $< I >$. The speckle pattern is clearly recognizable: each speckle consists of three-regularly focused beamlets with prescribed focusing spots (yellow dots) parallel to the beam axis. The beam parameters are similar to the ones in Fig. 3.1b: the beam focus spot position is $(500\lambda, 500\lambda)$, and its width is $w_B \approx 350\lambda$.

It is interesting to compare some features of spatially modulated beams produced by the random and semi-deterministic algorithm: Figure 3.3a shows transverse line-outs in the intensity profile of Fig. 3.1b (green line) and Fig. 3.2 (red line) at the beam focus spot position. The beam width created with both algorithms is comparable. Since the number of beamlets, speckles and speckle size are similar, the beam presents the same contrast independently of the algorithm, i.e. around 30%. In both cases, the order n of the Super-Gaussian envelope is 10. In Fig. 3.3b, the speckle abundance M as a function of speckle intensity normalized to the average beam intensity is shown. The dashed blue line refers to the exponential speckle abundance described by Eq. (1.66), the solid red line refers to one run realized with the semi-deterministic approach, the green lines refer to two different realizations by using the random algorithm. Since the semi-deterministic method is principally built by assigning a certain intensity to the speckles such that their intensities obey to Eq. (1.66), the speckle abundance reproduces quite well the analytic formula. Instead, two different realizations with the random algorithm correspond to two different intensity probability distributions: the speckle statistics arbitrarily varies at each run.

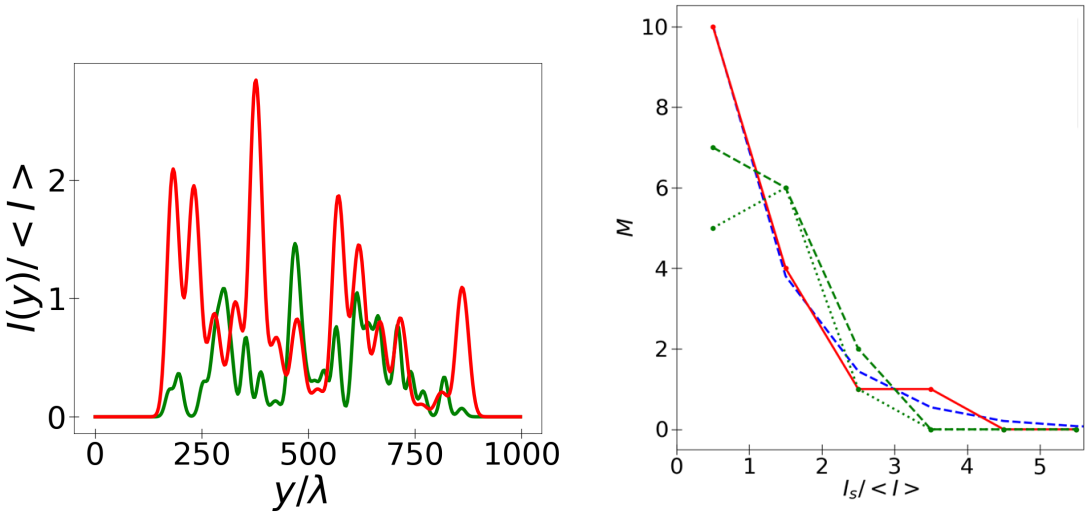

Figure 3.3: a) Transverse line-outs of laser intensity at $(500\lambda, 500\lambda)$ in case of random (green line) and semi-deterministic (red line) speckle pattern. b) Initial speckles abundance M: analytic results from Eq. (1.66) (blue dashed line), results from semi-deterministic pattern for a single realization (red line) and results for two realizations with a random pattern (dashed and dotted green line).

3.2 Self-focusing of a spatially modulated beam

In this section, we present the results of self-focusing of spatially modulated beam generated with the semi-deterministic algorithm. The plasma conditions are the same as in Chapter 2: the beam propagates into a homogeneous CH plasma ($Z = 3.5$) with density $n_{e0}/n_c = 0.1$ and temperature $T_e = 3T_i = 1$ keV. The plasma

$< I > /I_c^s$	I_s^{max}/I_c^s	I_s^{min}/I_c^s
0.2	0.5	0.016
0.35	0.9	0.3
0.5	1.2	0.07
0.85	2.1	0.1
1.25	3	0.15
2	5	0.5
2.5	6.2	0.65

Table 3.1: Parameters of set of simulations conducted with semi-deterministic PCGO model: First column: laser beam average intensity considered in the simulations. Second column: intensity of the most intense speckle normalized to the Gaussian beam critical intensity. Third column: intensity of the most intense speckle normalized to the three-beamlet beam critical intensity.

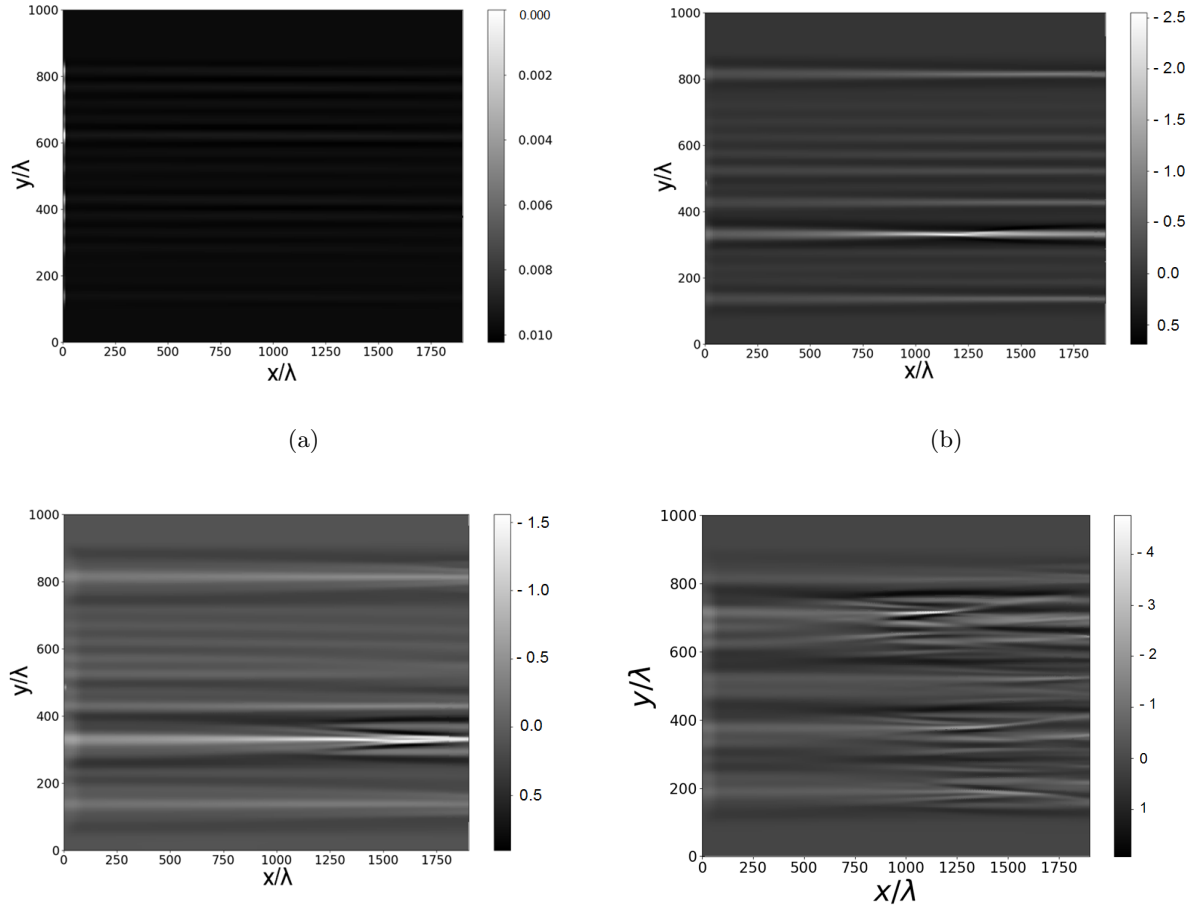

Figure 3.4: Density perturbation $\delta n/n_{e0}$ (%) for the case $< I > /I_c^s = 0.85$ at (a) t=10 ps, b) t=100 ps c) t=210 ps. Panel d) shows the case $< I > /I_c^s = 2$ and t=210 ps.

box has a longitudinal dimension of 2000λ, and a transverse dimension of 1000λ. The speckle pattern is shown in Fig. 3.2, with a speckle width of $w_s \approx 20\lambda$ equal to beamlets waist w_b^j. The beam is composed by 15 equidistant speckles, whose distance is larger than w_s, as displayed in the figure. With these parameters, the Gaussian beam critical intensity is $I_0^c = 1.5 \times 10^{13}$ W/cm^2 for the laser wavelength of 1.05 μm and coincides to the value given in Chapter 2. Hence, comparison between a single three-beamlet speckle from Chapter 2 and a three-beamlet speckle as in a speckle pattern can be assessed. The red line in Fig. 3.3b represents the speckles intensity statistics for all the cases considered.

The speckle pattern behavior is explored by considering different average laser intensities: we have performed 7 simulations lasting $t_f = 550$ ps, which is several times longer than the transit time of IAWs through a speckle. The goal here is to investigate individual speckle self-focusing at short time-scales along with inter-speckle interaction due to interference of IAWs for long time-scales. Table 3.1 shows the list of the average beam intensities considered: the first column in Table 3.1 refers to the average beam intensity normalized to the speckle critical intensity. Such a quantity is defined as following:

$$I_s^c = \frac{2P_{2D}^c}{\int_{-l_y}^{l_y} e^{-2\left|\frac{y}{w_B}\right|^n} dy}. \tag{3.4}$$

where P_{2D}^c stands for the critical power of a Gaussian beam with the order $n = 10$. Here we accounted for the fact that the three-beamlet speckle has a critical power twice higher than a Gaussian beamlet, as discovered in Chapter 2. The second column refers to the intensity of the most intense speckle normalized to the three-beamlet critical intensity, and the third column refers to the intensity of the less intense speckle normalized to the three-beamlet critical intensity. These cases range from the one where only one speckle has an intensity able to trigger self-focusing effects, i.e. $< I > /I_c^s = 0.2$ to the one where more than 60% of the speckles have an intensity at least equal to the three-beamlet critical intensity, as for the case $< I > /I_c^s = 2.5$. In Section 3.2.1 we study how the plasma perturbation forms inside the speckle area, whereas in Section 3.2.2 we relate the plasma perturbation to the ponderomotive effects in speckles at short and long time. As in the previous chapter, laser-plasma coupling consists in only ponderomotive force, then the modules which account for laser absorption and other nonlinear laser-plasma phenomena are switched off.

3.2.1 Plasma dynamics

In this section, we analyze the plasma response caused by the ponderomotive force induced by the regular speckle pattern. Figure 3.4 shows the plasma perturbation $\delta n/n_{e0}$ for $< I > /I_c^s = 0.85$ as a function of the normalized spatial coordinates for (a) $t = 10$ ps, (b) $t = 100$ ps and (c) $t = 280$ ps. The gray bar stands for the amplitude of the density perturbation $\delta n/n_{e0}$ (%). Figure 3.4a illustrates how the regular speckle pattern imprints its structure onto the plasma for times when self-focusing is not yet established but the plasma density modulation due to the ponderomotive force has already started. For longer times, the IAWs generated inside the speckles area transversely propagate outside it: Fig. 3.4b refers to a time when the IAWs have not left yet the speckles, whereas Fig. 3.4c displays the effect of IAWs interference, which occurs when IAWs cover a distance greater than $2w_s/c_s \sim 180$ ps. Reduction of the maximum amplitude when comparing Fig. 3.4c to Fig. 3.4b is due to decrease of ponderomotive effects induced by plasma smoothing.

By analyzing the evolution of plasma response with time and laser intensity, we find out that density perturbations with amplitude above 1% lead to strong modification of the intensity distribution in plasma, which occurs for $< I > /I_c^s > 0.5$. For beam intensities $< I > /I_c^s > 1$, the plasma density appears strongly modified behind the speckles self-focusing positions, as shown in Fig. 3.4d for $< I > /I_c^s = 2$ at $t = 210$ ps. Behind the main self-focusing area placed at $x > 1250\lambda$, the density channels are distorted, and the overall plasma density profile appears strongly perturbated. This behavior is due to two phenomena: firstly, the amplitude of IAWs is sufficiently large to create high-amplitude density perturbations, inducing a strong plasma perturbation even in low-intensity speckles which self-focus. As a side effect, a larger amount of speckles is deformed, they lose their Gaussian symmetry because beamlets significantly deviate from their initial direction of propagation due to refraction in deep density channels. Both effects are analyzed in more details in the forthcoming sections.

Figure 3.5a shows line-outs of the density perturbation $\delta n/n_{e0}$ as a function of the transverse coordinate at $x = 1700\lambda$ and $t = 75$ ps for: $< I > /I_c^s = 0.2$ (solid black curve), $< I > /I_c^s = 0.5$ (dashed red curve),

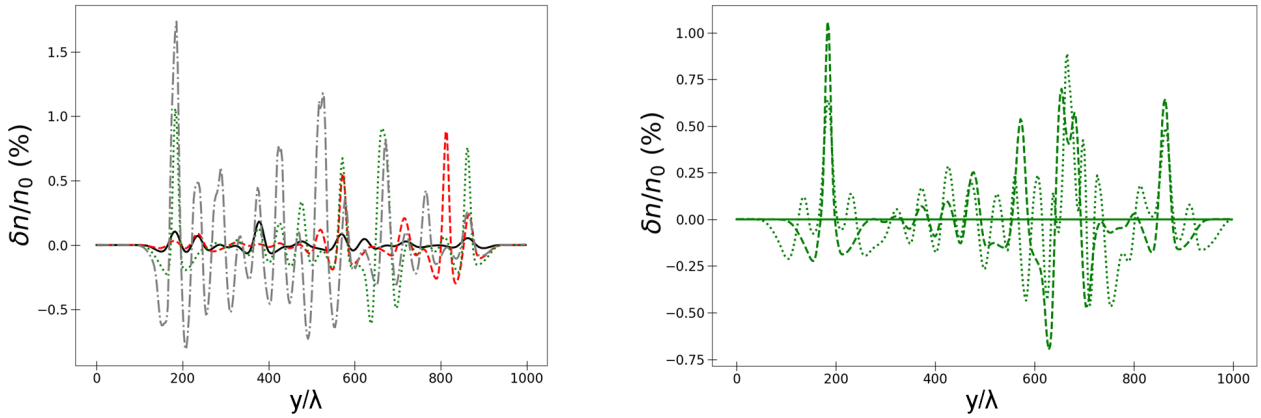

(a) (b)

Figure 3.5: Transverse line-outs of density perturbation $\delta n/n_{e0}$ a) at $x = 1700\lambda$ and $t = 75$ ps for $< I > /I_c^s = 0.2$ (solid black curve), $< I > /I_c^s = 0.5$ (dashed red curve), $< I > /I_c^s = 0.85$ (dotted green curve) and $< I > /I_c^s = 2$ (dashed-dotted gray curve); b) for $< I > /I_c^s = 1$ at around x=1700λ for $t = 1$ ps (solid green line), $t = 150$ ps (dashed green line) and $t = 300$ ps (dotted green line).

$< I > /I_c^s = 0.85$ (dotted green curve) and $< I > /I_c^s = 2$ (dashed-dotted gray curve). The amplitude of density perturbation depends on the speckle intensity: according to Eq. (1.152), higher initial intensity corresponds to a higher intensity enhancement, which leads to a density response of higher amplitude. In this panels, one notes that nonlinear density response occurs for $< I > /I_c^s > 0.5$. Generation and propagation of IAWs at $x = 1700\lambda$ for $< I > /I_c^s = 0.5$ is shown in Figure 3.5b: the solid green line refers to time $t = 1$ ps, the dotted green line to $t = 150$ ps and the dashed green line to $t = 300$ ps. At $t = 1$ ps, the density is not perturbed, thus the IAWs amplitude is zero. At $t = 150$ ps, peaks in the density transverse profile related to the occurrence of IAWs clearly appear. Such waves propagate in transverse direction, and interfere with others waves for times larger than $2w_c/c_s$: the double peak at around $y = 650\lambda$ for the dashed line illustrates this feature. This double peak structure stabilizes at $t = 300$ ps, as evidenced by the dotted line.

Figure 3.6a displayes the spatial Fourier transform of the data presented in Fig. 3.5: the solid black curve refers to $< I > /I_c^s = 0.2$, the dashed red curve refers to $< I > /I_c^s = 0.5$, the dotted green curve to $< I > /I_c^s = 0.85$, and the dashed-dotted gray curve to $< I > /I_c^s = 2$. As expected, at larger powers, different modes with several wave vectors k_y are produced since self-focusing develops in more speckles. Thus, the wave vector cut-off moves towards larger $|k_y|$. Furthermore, the amplitude of such density perturbations increases with the beam average intensity. It is interesting to note that modes with smaller k_y are produced for any beam average intensity, whereas, when the beam intensity increases, modes with larger $|k_y|$ are excited too. Figure 3.6b shows evolution of density perturbation spectrum for $t = 1$ ps (solid green line), $t = 150$ ps (dashed green curve) and $t = 300$ ps (dotted green line) for $< I > /I_c^s = 0.85$. The case $t = 150$ ps refers to independent speckle self-focusing, i.e. when IAWs interference has not occurred yet, whereas at $t = 300$ ps, IAWs have already propagated a distance larger than inter-speckle distance. As a consequence of IAWs

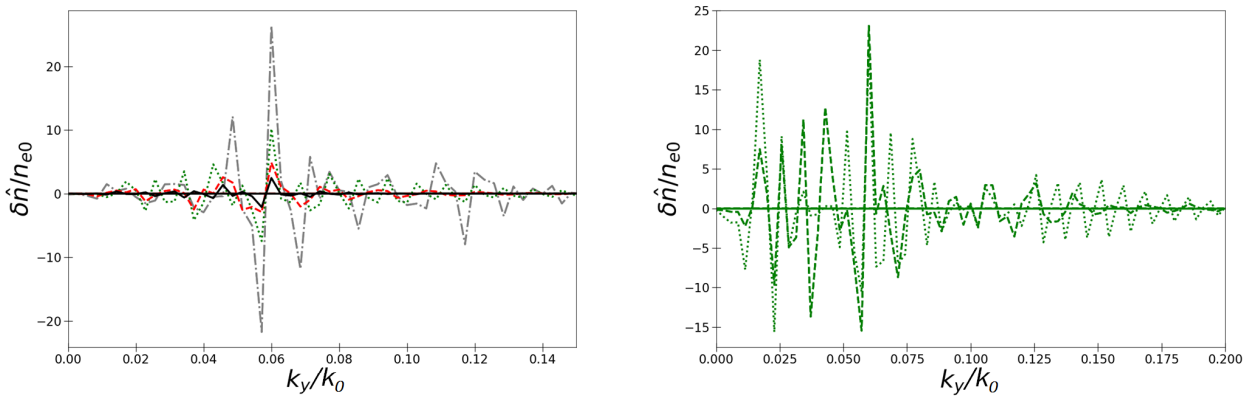

(a)

(b)

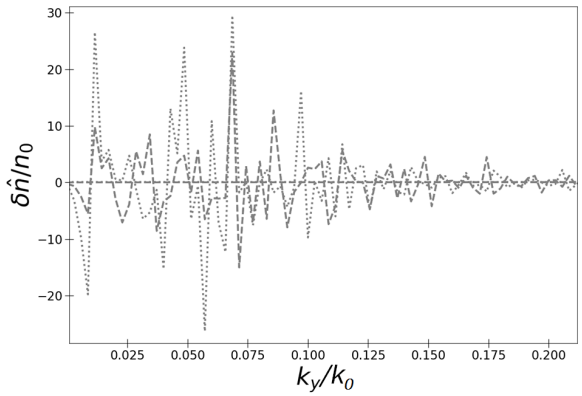

(c)

Figure 3.6: Spatial Fourier Transform of the transverse line-outs of density perturbation $\delta n/n_{e0}$ at $x = 1700\lambda$ and t=75 ps a) for $< I > /I_c^s = 0.2$ (solid black curve), $< I > /I_c^s = 0.5$ (dashed red curve), $< I > /I_c^s = 0.85$ (dotted green curve) and $< I > /I_c^s = 2$ (dashed-dotted gray curve); b) for $< I > /I_c^s = 0.85$ at $x = 1700\lambda$ for $t = 1$ ps (solid green line), $t = 150$ ps (dashed green curve) and $t = 300$ ps (dotted green line); c) for $< I > /I_c^s = 2$ at $x = 1700\lambda$ for $t = 150$ ps (dashed gray curve) and $t = 300$ ps (dotted gray line). In all panels, the wave vectors k_y are normalized to the laser wave vector $k = \omega/c$.

interference, the amplitude of density perturbation is reduced in average for $t = 300$ ps because of mode mixing. Figure 3.6c displays spectrum of density perturbations for $t = 150$ ps (dashed gray curve) and $t = 300$ ps (dotted gray curve) for the case $< I > /I_c^s = 2$. Comparing density perturbations for $< I > /I_c^s = 0.85$ and for $< I > /I_c^s = 2$ at $t = 300$ ps (dotted lines), one can note that whereas for $< I > /I_c^s = 0.85$ the density amplitude in the range of small wave numbers $0 < |k_y| < 0.1$ is approximately constant, for $< I > /I_c^s = 2$ it has a maximum at $k_y \sim 0.03k_0$ and decreases with increasing $|k_y|$. This is explained by the fact that the wavenumber $k_y = 0.03k_0$ corresponds to the speckle width $w_s = 20\lambda$. IAWs with this wavenumber are excited directly by the ponderomotive force in speckles. By contrast, the larger wave numbers are generated by nonlinear interaction of IAWs which increases with their amplitude and therefore can be observed at higher intensities. Consequently,

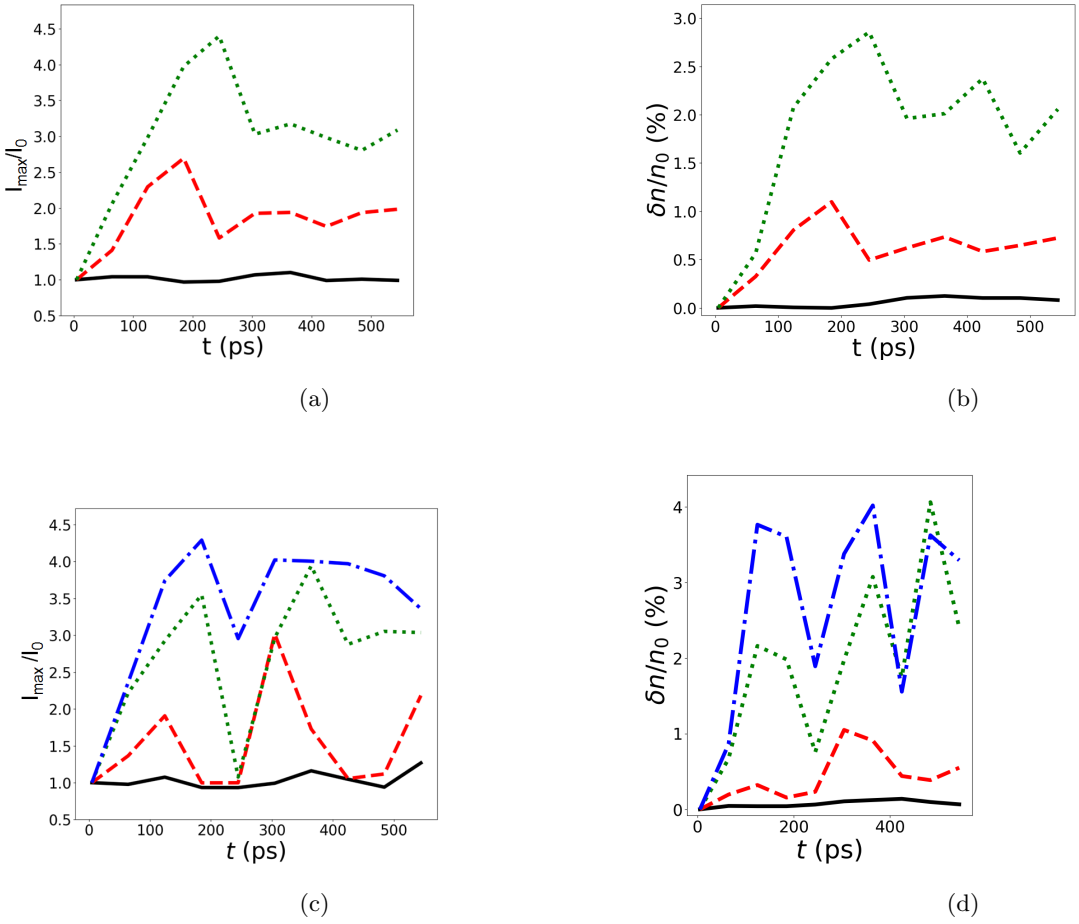

Figure 3.7: Intensity enhancement I_{max}/I_0 in a) and c) and amplitude of plasma perturbation $\delta n/n_{e0}$ in b) and d) as a function of time for selected speckles and for $< I > /I_s = 0.85$ (upper figures) and $< I > /I_s = 2$ (bottom figures). The black solid lines refer to speckle intensity I_s/I_c^s <0.5, the dashed red lines to I_s/I_c^s ≈1, the dotted green lines to $I_s/I_c^s \approx 2$, the dashed-dotted blue lines to I_s/I_c^s ≈3.

for the case $< I > /I_c^s = 2$ the less intense speckles can also undergo self-focusing even if at short time scale they do not present any noticeable intensity enhancement. This example demonstrates a reduction of plasma smoothing effect on the speckles self-focusing due to strong density perturbation.

3.2.2 Speckle dynamics and relation to the plasma perturbation

A relation between density amplitude and intensity enhancement is illustrated in Fig. 3.7, which displays the intensity enhancement I_{max}/I_0 (panels on the left) and the amplitude of the density perturbation $\delta n/n_{e0}$ (panels on the right) for selected speckles. The average beam intensity is $< I > /I_c^s = 0.85$ (upper panels) and $< I > /I_c^s = 2$ (bottom panels). The black solid lines refer to a speckle with intensity I_s/I_c^s <0.5, the dashed red lines refer to a speckle with intensity $I_s/I_c^s \approx 1$, the dotted green lines refer to a speckle with intensity $I_s/I_c^s \approx 2$, the dashed-dotted blue lines refer to a speckle with intensity $I_s/I_c^s \approx 3$. In Figs. 3.7a-3.7c, speckles with intensity smaller than I_c^s do not undergo self-focusing. This is in agreement with results found

in Chapter 2. On the other hand, for speckles with intensity larger than I_c^s, an increase of the intensity occurs for $0 < t < 150$ ps. At times longer than ~ 150 ps, IAWs generated inside one speckle reach the edge of the neighbor speckle, interacting with the counter-propagating IAW excited over there.

At the beginning, for times $150 < t < 180$ ps, the IAWs interference changes the amplitude of the density perturbation, and the speckle dynamics is perturbed as observed in panels on the right. Then, when the IAWs reach the core of the density cavity for times $t \sim 200 - 240$ ps, the density depletion varies depending on the IAW amplitude, and the speckle dynamics is modified accordingly. This can be seen in Fig. 3.7, but some differences emerge between the upper ($< I > /I_s = 0.85$) and bottom ($< I > /I_s = 2$) plots after the IAW interference at $t \approx 150$ ps. In case of $< I > /I_s = 0.85$ only one speckle has $I_s/I_c^s > 1$ (dotted green lines), its intensity decreases for $150 < t < 200$ ps. This is due to the fact that the neighbors of this speckle have a very low intensity ($< I_c^s$), and they do not generate a density perturbation strong enough to fill the density channel created by the most intense speckle. Thus, interference of the IAWs proceeds in a linear regime so speckle self-focusing reaches a stationary state for $t = 3w_s/c_s > 250$ ps, i.e. after the passage of the first IAW across the density channels. This linear plasma density perturbation saturates the intensity enhancement and to lead the system in a quasi-stationary state. The dynamics of speckles having $I_s/I_c^s = 1$ (red curve) and $I_s/I_c^s < 0.5$ in the upper panel presents the same structure. Small oscillations are due IAWs traveling across density channels, which occurs for times $t = (2m + 1)w_s/c_s$, being m an integer number.

For $< I > /I_s = 2$ (bottom panels in Fig. 3.7), where at least 6 speckles have $I_s/I_c^s >1$, the scenario is very different: IAWs interference drastically change the amplitude of density perturbations, the intensity enhancement and the relation between them over long times. For the most intense speckles, the intensity enhancement at short time is saturated already due to breaking of the speckle symmetry. The dashed-dotted blue lines in Figs. 3.7c-3.7d illustrate respectively the behavior of the intensity enhancement and the density amplitude as a function of time for this speckle. Both the density amplitude and intensity enhancement are strongly affected by the IAWs interference for $t > 150$ ps: this is due to the fact that its neighbor speckle has an intensity $I_s/I_c^s > 2$, its density perturbation amplitude and intensity enhancement are displayed by green lines in Fig. 3.7b and Fig. 3.7c, respectively. At longer times, more IAWs interact, penetrate the speckles and fill the density depletion caused by the ponderomotive force, but strong self-focused speckles are less sensitive to the plasma smoothing. On the other hand instead, high-amplitude IAWs boost an important intensity amplification in the less intense speckles too, as shown in Fig. 3.7c for $t > 250$ ps. However, in all cases, when the intensity enhancement increases more than 3-4 times, the speckle breaks down, and its intensity enhancement saturate. The combined effects of speckle breaking, plasma smoothing and strong self-focusing induce high-amplitude oscillations in the speckle dynamics, and no steady state is attained.

In the next sections, the results at short time, when the independent speckle self-focusing is expected to coincide to the results obtained in Chapter 2, and the consequence of plasma smoothing and high-amplitude plasma perturbations for longer times are studied separately.

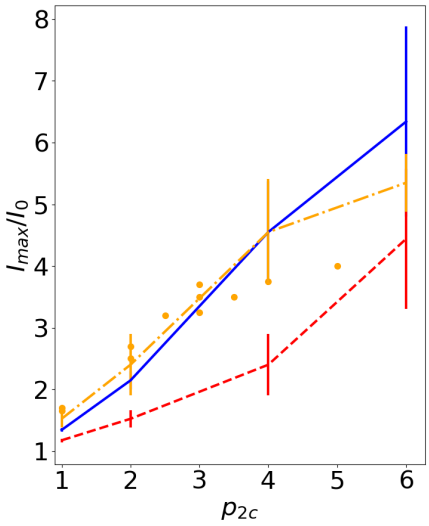

Figure 3.8: Comparison of the speckle intensity enhancement for a short time to the results obtained in Chapter 2. The blue line refers to the time-averaged intensity enhancement for a single beamlet, the red dashed line refers to the time-averaged intensity enhancement for a single three-beamlet case, the orange dashed-dotted line refers to the time-averaged intensity enhancement for a single three-beamlet case as a function of $p_{2c} = P_s/2P_c$, and the yellow dots stand for the intensity enhancement of several three-beamlet speckles composing the multi-speckle pattern as a function of $p_{2c} = P_s/2P_c$. The error bars refer to the standard deviation of the time average. The new results are presented without error bars for the sake of clarity.

3.2.3 Speckle self-focusing at short times: comparison to the single speckle case

Assuming the dynamics of each speckle can be considered independent before that IAWs excited in different speckles interact between each other, the individual speckle self-focusing can be studied by evaluating short time dynamics, i.e. for time up to $t \sim 150$ ps. This is very long time compared to other instabilities time-scales, which grow on a few picoseconds. However, since the packages modelling of those phenomena are turned off, other nonlinear laser-plasma instabilities do not affect our simulations. More details on the importance of other instabilities on ponderomotive self-focusing are presented in Chapter 4.

The individual speckle self-focusing time evolution can be compared to the long time dynamics, when the IAWs interfere and the speckle self-focusing is affected by the collective dynamics. At a short time-scale indeed, one expects to retrieve the single speckle behavior as described in Chapter 2. Figure 3.8 presents the results of Chapter 2 where the intensity enhancements of several three-beamlet speckles from the current study have been added: the blue line refers to the time-averaged intensity enhancement for a single beamlet, the red dashed line refers to the time-averaged intensity enhancement for a single three-beamlet speckle, the orange dashed-dotted line refers to the time-averaged intensity enhancement for a single three-beamlet case as a function of normalized power $p_{2c} = P_s/2P_c$. The yellow dots stand for the intensity enhancement of three-beamlet speckles composing a multi-speckle pattern as a function of $p_{2c} = P_s/2P_c$ averaged over a time interval of 50 ps around $t = 150$ ps. These points are recovered from different cases we have studied. The error bars refer to the standard deviation

of the time average. The dots do not present any error bars for the sake of clarity of the plot. The panel shows that in the multi-speckle pattern the single speckle behavior at a short time is very close to the single three-beamlet speckle for speckle powers less than 4, and that this feature does not depend on a particular multi-speckle case. Furthermore, the factor $\eta = 2$ introduced in Chapter 2 in order to account for self-focusing effects in three-beamlet speckles correctly describes the intensity enhancement in the multi-speckle case for a short time speckle self-focusing. When the speckle power exceeds 5-6 times the normalized critical power $p_{2c} = P_s/2P_c$, the power of all beamlets exceeds at least 4 times their critical power, so individual beamlet dynamics overcomes the collective behavior: the beamlets strongly refract, spreading out from the speckle area and breaking the speckle symmetry. This phenomenon leads to a saturation of the intensity enhancement, and at this speckle power the multi-beamlet PCGO solution underestimates the ponderomotive effects with respect to the single beamlet case, as already observed in Chapter 2.

3.2.4 Long time dynamics

As demonstrated in Sec. 3.2.2, plasma density perturbations excited inside the speckles at short time affect self-focusing at longer times. Depending on the IAWs amplitude, the speckle self-focusing can reach a steady state or strongly oscillate at long times. In particular, when IAWs develop in nonlinear regime, their interaction with the less intense speckles leads to value of intensity enhancement comparable to the most intense speckle. In order to measure a correlation within the speckle pattern, one may calculate a ratio between the intensity enhancement of the most and less intense speckle for a given case, denoted by i. The dependence of this ratio on the multi-speckle beam intensity is presented in Fig. 3.9a: the blue line refers to the value of i at around $t = 150$ ps, where the hydrodynamic inter-speckle coupling has not occurred yet. The black line refers to i

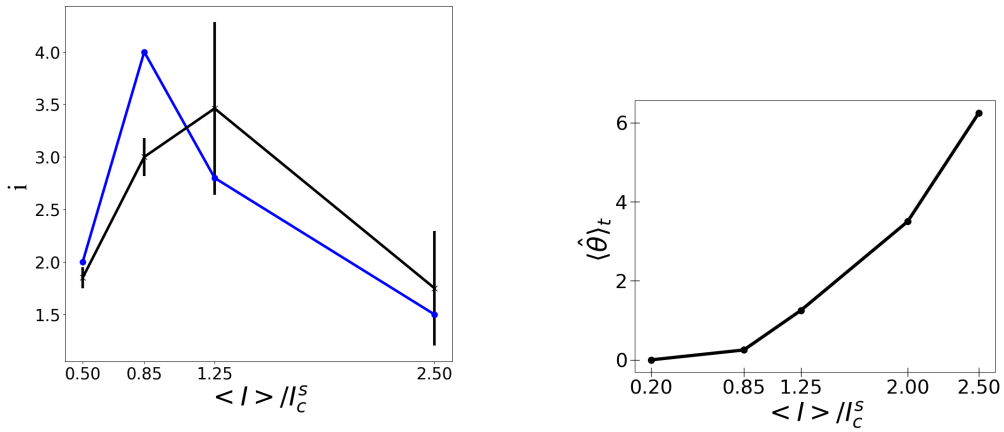

(a) (b)

Figure 3.9: a) Ratio between the intensity enhancement of the most intense and less intense speckle i as a function of the beam intensity. The blue curve refers to the intensity enhancement at $t = 120$ ps, whereas the black line to the time-average for $t > 120$ ps. b) Time-average of the beamlets average divergence $\langle\hat{\theta}\rangle_t$ as a function of the average beam intensity.

averaged over the rest of the simulation ($150 < t < 550$ ps). The error bars stand for the standard deviation. For $< I > /I_s = 0.5$, a difference between the most and less intense speckle in terms of intensity enhancement is very small; this is due to the fact that the amplitude of plasma perturbation is very weak, and there is no intensity enhancement in the weakest speckle. On the contrary, a strong difference between the short time and long time behavior is observed for $< I > /I_s = 0.85$: the most intense speckle experiences the effect of mixing of density perturbations: a combination of linear density perturbations smooths the intensity enhancement of the most intense speckle. Consequently, the ratio i decreases over a long time. For $< I > /I_s > 0.85$ instead, we observe that at a long time, the ratio i decreases similarly to the case of $< I > /I_s = 0.5$. However, unlike the $< I > /I_s = 0.5$ case, this reduction is explained by strong self-focusing effects which overcome plasma smoothing: at a short time, the intensity enhancement of the most intense speckles is saturated given that the speckle breaks due to beamlets divergence. On the other hand, the less intense speckles have an initial power sufficient to develop self-focusing, although weaker than the most intense speckles. These two processes going in opposite directions explain the fact that the ratio i does not exceed 2-3. This argument applies also to the long time evolution, since nonlinear plasma perturbation induces strong oscillations of the intensity enhancement in all speckles. The larger error bars for $< I > /I_s > 0.85$ highlight this point. Thus, increasing the beam intensity up to $< I > /I_s = 2.5$, both speckle breaking and self-focusing of less intense speckles reduce the importance of the plasma smoothing since more speckles enter in the self-focusing regime and IAWs amplitude non-linearly develops.

Figure 3.9b shows the time-averaged total beamlets deviation with respect to the initial straight beamlet trajectories for several cases. The angle $\langle\hat{\theta}\rangle_t$ measures the beamlets divergence, and it characterizes the beamlet spreading behind the speckle self-focusing position. The divergence increases with the average laser intensity, which explains why the speckles deviate from their initial Gaussian profile. This is particularly true for $< I > /I_c^s > 1$, where the average beamlets divergence above one degree is measured. As described already in Chapter 2, this effect is due to the fact that the speckle envelope emerges from an uncorrelated sum of Gaussian beamlets intensities.

3.2.5 Overall beam dynamics

In this section, we analyze the overall beam dynamics by considering the evolution of the beam contrast and the time-averaged speckle statistics. Figure 3.10a presents time dependence of the contrast variation $\Delta C/C_{en}(t)$, where $\Delta C = C_{exit} - C_{en}$ is the difference between the beam contrast evaluated at the exit C_{exit} and the entry C_{en} of the plasma box, respectively for $< I > /I_s = 0.2$ (solid black line), $< I > /I_s = 0.85$ (dashed blue line) and $< I > /I_s = 2$ (dotted green line). The value of the contrast at the entry is $C_{en} = 30\%$ and does not vary in time. The value of C_{exit} is around 30% as well, but it changes in time because of speckles self-focusing.

In case of a very low laser beam intensity, i.e. for $< I > /I_s = 0.2$, the contrast variation increases for times less the IAWs transit time ($t = 150$ ps), then it oscillates around $\approx 5\%$ with a period of around 200 ps and with a small amplitude. This is due to the fact that speckles do not appreciably self-focus, and the speckle pattern is slightly perturbed by the ponderomotively-induced density modulations. Increasing the beam intensity by four times leads to an enhancement of the contrast variation by about 6 times, as evidenced by the case of

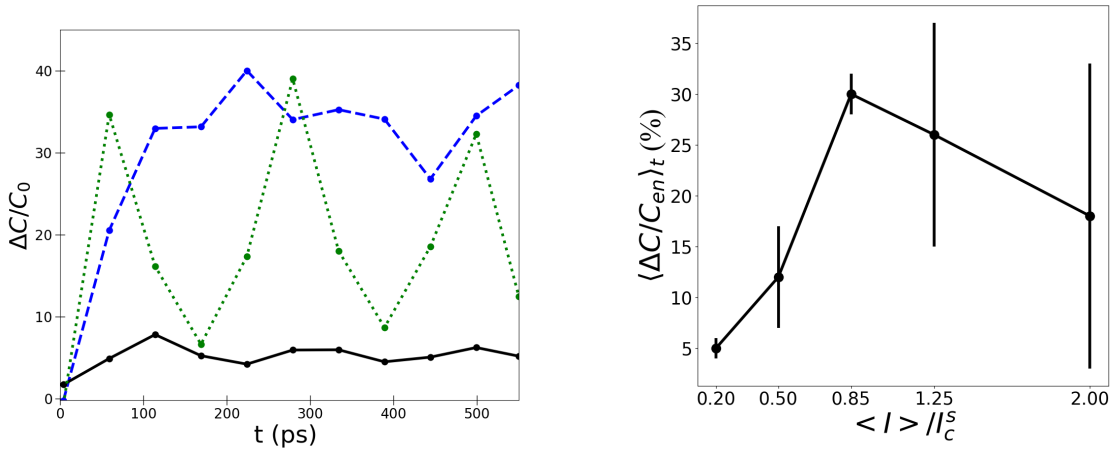

(a) (b)

Figure 3.10: a) Contrast variation dynamics $\Delta C/C_{en}(t)$ for $< I > /I_s = 0.2$ (solid black line), $< I > /I_s = 0.85$ (dashed blue line) and $< I > /I_s = 2$ (dotted green line). b) Time-averaged contrast variation $\langle \Delta C/C_{en} \rangle_t$ for different cases.

$< I > /I_s = 0.85$. A stationary state giving a 30% of contrast variation sets at about the same time interval as for the lower intensity case. In this case, there are no periodic oscillations, whereas the steady state value of 30% indicates that speckles are self-focused and reduced in their transverse size. This is due to the fact that an equilibrium between the plasma smoothing and the beamlets divergence is established, and the contrast saturates given that the intensity enhancement of the speckles is saturated (see also Fig. 3.7a).

In case of beam intensity $< I > /I_s = 2$ (green line), the scenario drastically changes: the time dependence of the contrast variation presents the same periodic structure as the $< I > /I_s = 0.2$ case but shifted in time for around 80 ps. The contrast variation reaches its maximum at 80 ps, then falls, before rising again at the same maximum and oscillates until the end of the simulation. These strong oscillations of the contrast variation are due to combination of two effects already discussed, but here evidenced at two different time scales: after the first 80 ps, the most intense speckles break, and the beamlets spread behind the main self-focus position. This leads to reduction of the beam fluctuations between 80 and 160 ps. Then, IAW interference takes place (for $t \approx 150$ ps), which smooths the speckles symmetry breaking by redistributing the intensity enhancement over all the speckles. This feature repeats periodically since the nonlinear plasma response induces strong intensity enhancements also in less intense speckles. As a result, the contrast variation strongly oscillates at an average value of 20% with an oscillation amplitude of around 15%. Figure 3.10b shows time-averaged contrast variation $\langle \Delta C/C_{en} \rangle_t$ as a function of the overall beam intensity and summarizes all the results concerning the contrast. The error bars stand for the standard deviation. As already pointed out, the time-averaged contrast variation increases with the beam intensity up to $< I > /I_s = 0.85$, then, it decreases presenting high amplitude oscillations, illustrated here with larger error bars for $< I > /I_s = 1.25$ and $< I > /I_s = 2$. This is in agreement with the results shown in Fig. 3.9a.

Another important parameter that characterizes the beam dynamics is the probability distribution of the

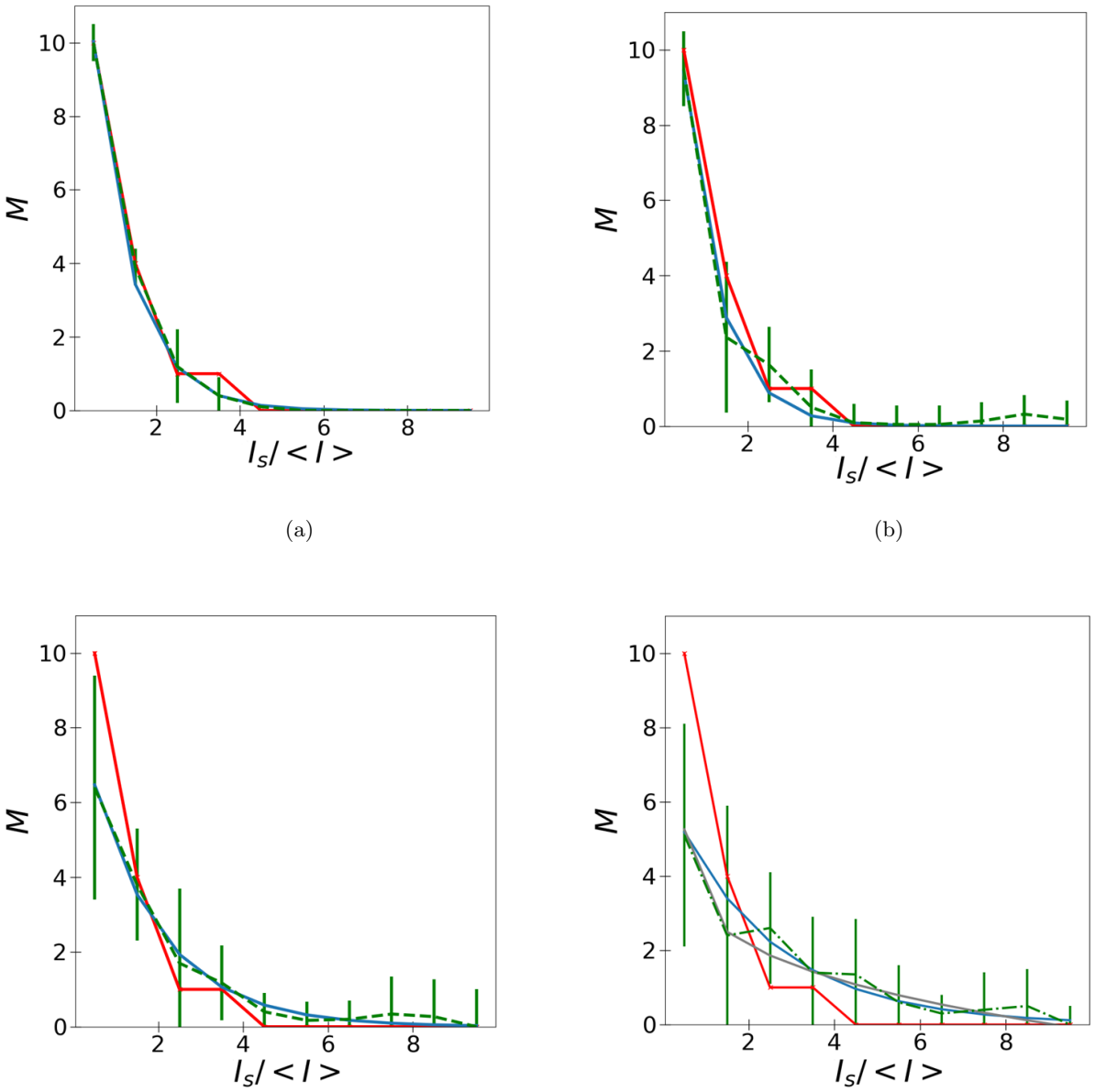

Figure 3.11: Abundance of speckles M as a function of speckle intensity normalized to the average beam intensity for a) $< I > /I_s = 0.2$, b) $< I > /I_s = 0.85$, c) $< I > /I_s = 1.25$ and d) $< I > /I_s = 2$. The green lines with error bars correspond to the time-averaged simulations data, the red lines refer to the reference initial statistics, the dashed blue and solid gray lines correspond to an exponential and power fit of the data, respectively.

speckle intensities. As already mentioned, all the cases considered are initialized with an exponential speckle statistics. But ponderomotive self-focusing can substantially change the relation between the speckles abundance and their intensity, as shown in Fig. 3.11. In this set of figures, the solid red lines refer to the reference initial speckle intensity distribution, the solid green lines refer to the time-averaged speckle abundance, the blue lines refer to the the exponential fit of the simulations data, whereas the solid gray lines refer to the fit by

$< I > /I_c^s$	a	b	α	β	γ
initial statistics	9.8	1.13			
0.2	10	1.1			
0.85	3	1.2			
1.25	6.3	0.5			
2	5.2	0.3	-2.8	-3.1	5.3

Table 3.2: Coefficients for the exponential fit $M = ae^{b<I>/I_s+c}$ and the power fit $M = \alpha\,(< I > /I_s)^{\beta} + \gamma$ of the speckle probability distribution.

a power function. Figure 3.11a shows the case $< I > /I_s = 0.2$, where only the most intense speckle has a power comparable to the speckle critical power. In this case, no appreciable change of the speckle statistics is evidenced, and the exponential fit gives an exponential factor of 1.1, very close to the initial exponential factor 1.13 as reported in Table 3.2. Figure 3.11b displays the case $< I > /I_s = 0.85$, where around 20% of speckles have a power above the multi-beamlet critical power. Here, self-focusing effect and plasma smoothing play an important role in the beam dynamics, and the abundance profile presents a bump in the tail of intensity distribution. Thus, the exponential fit still holds closely to the initial shape. The abundance modifies for $< I > /I_s = 1.25$ as illustrated in Fig. 3.11c, where the number of speckles having intensity above the multi-beamlet critical intensity is around 40%-50%. Here, the speckle-plasma interaction and beamlets divergence play an important role. The speckle statistics is strongly affected in both low- and high-intensity domains, but an exponential fit is preserved, with an exponential coefficient two times smaller as evidenced in Table 3.2. Increasing the power at the point where 80% of speckles have intensity above the multi-beamlet critical intensity leads to deviation from the exponential fit towards a power fit, as shown in Fig. 3.11d for the case $< I > /I_s = 2$: here, the data can be interpolated with an exponential coefficient of 0.3, or more accurately by a power function with a power index -3.1. In this case, more than two speckles have an intensity 4-6 times higher than the average beam intensity $< I >$ which implies a complicate interplay between nonlinear hydrodynamics and beamlets spreading. As a consequence, the speckle statistics substantially changes from the initial exponential shape and a larger probability for intense speckles is observed. A summary of the coefficients used for the fits is displayed in Table 3.2.

In conclusion, we can identify two regimes of multi-speckle beam self-focusing: a low and high intensity regime. The first one concerns beam intensity $< I > /I_s$ below 0.85-1.25: here the time-averaged speckle intensity statistics can be approximated as an exponential. In these cases, plasma-induced smoothing dominates and speckles do not reach a large intensity enhancement over all the simulation duration. The speckle intensity statistics modifies by increasing the average beam intensity, until ponderomotive effects overcome the plasma smoothing: in this situation, the speckle statistics show more high intensity speckles and the intensity distribution tends to a power law. These phenomena are observed as the average beam intensity overcomes $< I > /I_s \approx 0.85 - 1$. We observe a gradual transition between the low to the high intensity regimes.

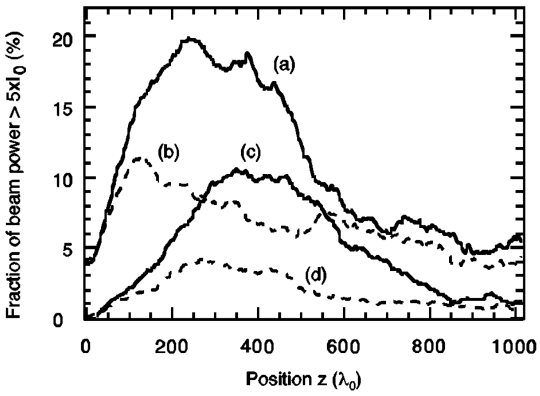

Figure 3.12: Fraction of the spatially modulated beam power which has intensity five times the average beam intensity $< I >$ as a function of the running time described here in terms of the longitudinal spatial coordinate z. The solid line a) refers to an RPP-produced beam and stands for our reference. Reprinted from Ref. [131].

3.3 Comparison to other works

In this section, we benchmark the results obtained with the semi-deterministic method against previous works, notably from Refs. [131] and [123]. In particular, we are interested in testing the tendency of intensity enhancement and modification of speckle intensity statistics obtained in our simulations.

In Ref. [131], the authors performed 3D electromagnetic simulations of speckles self-focusing and ponderomotive force-induced plasma density perturbations, while neglecting parametric instabilities. In this work, a laser with a wavelength $\lambda = 0.35$ μm is focused with a lens of $f/8$, giving rise to speckles of width $w_s \sim 3$ μm in the transverse dimension. Plasma parameters correspond to a plastic CH, with a homogeneous electron density of $n_{e0} = 0.1 n_c$ and an electron temperature T_e three times larger than ion temperature T_i, i.e. $T_e = 3T_i = 3$ keV. The average laser intensity is $I_0 = 2 \times 10^{15}$ W/cm^2. The simulation lasts 100 ps. Although the authors considered different smoothing techniques such as RPP, temporal smoothing and polarization smoothing, we discuss only the results concerning the RPP impact on laser self-focusing, illustrated by the curve a) in Fig. 3.12. This curve describes the fraction of the spatially modulated beam power which has intensity five times larger than the average beam intensity $< I >$ as a function of time defined in terms of the longitudinal spatial coordinate z. Different stages of laser self-focusing can be recognized: initially, only 4% of the beam carries such an amount of intensity. Then, speckles self-focus and the power fraction carried with high intensity speckles increases up to 20% at 200λ. Between 200λ and 400λ, generation of IAWs perturbs the dynamics, and the power fraction oscillates. After 400λ, plasma smoothing sets in and the power fraction is reduced to 7%, saturating at this value with slight fluctuations due to the IAW interference. The time-history of the power fraction is qualitatively retrieved in the dynamics of intensity enhancement of the most intense PCGO speckles: as displayed in Figs. 3.7a-3.7c, after an initial increase of the speckle intensity enhancement, this quantity falls down and then it reaches a steady state with small oscillations due to competition between plasma smoothing and single speckle self-focusing. The differences between Ref. [131] results and PCGO simulations mainly dwell on the time-scales at which density depletion and speckle contraction take place and on the dimension of the problem: the plasma

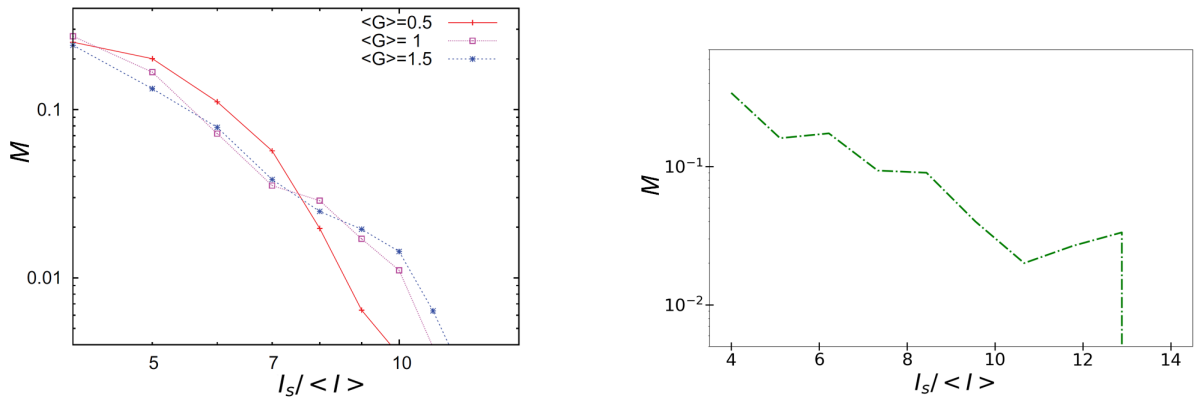

(a) (b)

Figure 3.13: a) Tail of speckle intensity distribution function obtained in HARMONY simulations as a function of the speckles intensity $I_s/ < I >$ (reprinted from Ref. [123]). b) Speckle intensity distribution obtained in PCGO simulations for $< I > /I_s^c = 2$ as a function of speckles intensity normalized to the same intensity as in the HARMONY simulations.

conditions are different, the time-scale of IAWs generation and propagation change, and the intensity oscillations occurs on times of the order of 100 laser periods. A further difference emerges from the regular distribution in space of PCGO speckles against the random speckle distribution in the electromagnetic simulations: this feature affects the smoothing effects, introducing larger oscillations in the intensity enhancement of PCGO speckles. Eventually, the dimension of the problem is different, and a more explosive self-focusing is expected in 3D than than in two-dimensions. However, despite such differences, the dynamics of the most intense PCGO speckles shows the same tendency as 3D real speckles.

Modification of speckle statistics due to both ponderomotive self-focusing and forward stimulated Brillouin scattering (FSBS) excited by plasma density perturbations has been numerically investigated in Ref. [123], in the particular case where strong self-focusing develops. In this work, the authors used 2D HARMONY simulations to study the variation of the speckle statistics in a homogeneous plasma. Since HARMONY solves a time-enveloped equation for the electric field in the paraxial approximation, speckle sizes are approximately equal to the size of real speckles, that is, a few times the laser wavelength. In this simulation, the number of speckles is around 2000, with an intensity ranging from 0.01 to 5 times the average beam intensity $< I >$ and the average beam intensity corresponds to a half of the speckles critical intensity.

In order to evaluate the effect of ion waves interference on the speckle dynamics as in PCGO simulations, we discuss here the case of weak IAW damping: $\nu_{\mathrm{IAW}}/\omega_0 = 0.01$. The plasma was weakly collisional and absorption did not affect the laser propagation. These conditions are in agreement with the plasma conditions as in our simulations. Furthermore, by considering that PCGO speckles are 10 times larger than HARMONY speckles and due to different normalization on the computation of the speckles power between CHIC and HARMONY, the HARMONY simulation under investigation corresponds to the PCGO-CHIC case where $< I > /I_s^c = 2$. Figure 3.13a shows the tail of of the speckle intensity distribution obtained in HARMONY simulations as a function of the speckles intensity $I_s/ < I >$. The dotted blue line corresponds to the case of weak IAW

damping $\nu_{\mathrm{IAW}}/\omega_0 = 0.01$. The tail of the distribution of HARMONY speckles can be qualitatively compared to the tail of the speckle abundance obtained in semi-deterministic PCGO simulations displayed in Fig. 3.11d for $< I > /I_s^c = 2$. In Ref. [123], the speckle intensity distribution is characterized by a power law with an exponent of -3.5. This behavior qualitatively agrees with PCGO simulations for $< I > /I_s^c = 2$, where the distribution function best fit correspond to a power law with an exponent of -3.1 (see Table 3.2). Then, it follows from a comparison of the blue curves in Fig. 3.13a and Fig.3.13b that the HARMONY and PCGO speckle distributions give the same percentage of speckle abundance for $4 < (< I > /I_s) < 6$ and for $(< I > /I_s) > 8$, whereas they differ in the central part, where PCGO overestimates the occurrences by a factor of 2. This is due to the fact that we are comparing the tail of a speckle pattern for 2000 speckles with an intensity distribution of only 15 PCGO speckles. Thus, one realization of PCGO statistics cannot quantitatively reproduce the entire speckle distribution. Despite that, at high intensities, the PCGO semi-deterministic algorithm presents the same trend of a 2D speckle distribution observed in electromagnetic simulations.

3.4 Comparison to the random speckle pattern

In this section, the self-focusing of a spatially modulated beam generated with the random algorithm is compared to results obtained with the semi-deterministic method for the same plasma conditions and by preserving the same number of beamlets and equal speckle size. To do so, simulations with the random beamlets initialization have been performed for an incident beam of $w_B \approx 350\lambda$ split in 45 beamlets near the plasma boundary. These beamlets are then focused inside the plasma in a box of comparable size as in the semi-deterministic case and placed at around $(500\lambda, 500\lambda)$. In this way, a pattern similar to the semi-deterministic case is created: the number of speckles is in average 12-15, with 3-4 beamlets per speckle. Also the average transverse speckle size is approximately the same as in the semi-deterministic pattern (compare Figs. 3.1b-3.2 and see Fig. 3.3a), whereas the longitudinal average size is smaller as a consequence of random inclination of beamlets. This breaks the speckles symmetry and reduces their self-focusing, as it is discussed below. The beam intensity considered is $< I > /I_c^s = 2$. As already seen in Sec. 3.3, the probability distribution of speckles for this beam intensity corresponds to the tail of a 2D speckle intensity distribution, and modification of the initial speckle statistics towards a power-dependence law due to strong speckle self-focusing is expected.

Figure 3.14a illustrates the transverse line-outs of the laser intensity for $t = 150$ ps and at around $x = 150\lambda$ for simulations performed with semi-deterministic algorithm (red line) and random algorithm (green line). The intensity is normalized to the initial beam intensity distribution in order to easily identify the intensity amplification of the speckles: for instance, a peak value of six means an intensity amplification of six times the initial speckle intensity. Weaker intensity enhancements are observed in speckles built while using the random method. As already pointed out in Sec. 2.3.1 when studying a single multi-beamlet speckle, such a reduction is due to beamlets crossing at uncontrolled random angles and consequently, short interaction length. Furthermore, the speckle-plasma coupling arising from collective effects is inhibited because the probability of beamlets overlapping around their maximum intensities is low. Then each beamlet affects the plasma dynamics almost independently, around its peak intensity. This suppresses the collective beamlets self-focusing and

reduces the overall speckle intensity enhancement. Therefore, with the random algorithm, one cannot retrieve the results on speckle statistics variation as in Ref. [123]: the probability of intensity distribution is shown in Fig. 3.14b by the solid green line, which refers to the time-averaged speckle abundance M evaluated from the random-initialized simulation. The dashed green line stands for the initial speckle intensity distribution while employing the random method, the dashed red line stands for initial statistics in case of deterministic algorithm as discussed in previous sections, the solid red line refers to time-average speckle abundance in case of deterministic algorithm (see green line in Fig. 3.11d), whereas the dashed blue line refers to the analytic exponential law Eq. (1.66), presented here as a reference. In case of random algorithm, the initial speckle distribution (dashed green line) displayes an approximately linearly decaying intensity distribution over all the speckles up to $I_s/ < I >= 3$, then drops to zero. Due to single beamlets self-focusing, speckles are modified, and new local maxima are formed (solid green line). The time-averaged intensity abundance of these maxima corresponds to an almost constant speckle distribution up to $I_s/ < I >= 3$. This is in contrast to what observed in deterministic (solid red line) and in two-dimensional electromagnetic simulations as in Ref [123]: the abundance of speckle intensities follows a power-dependence law as a consequence of strong speckles intensity enhancement. In conclusion, the semi-deterministic algorithm is a more appropriate method for describing of ponderomotive effects in Gaussian-like speckles unlike the random approach.

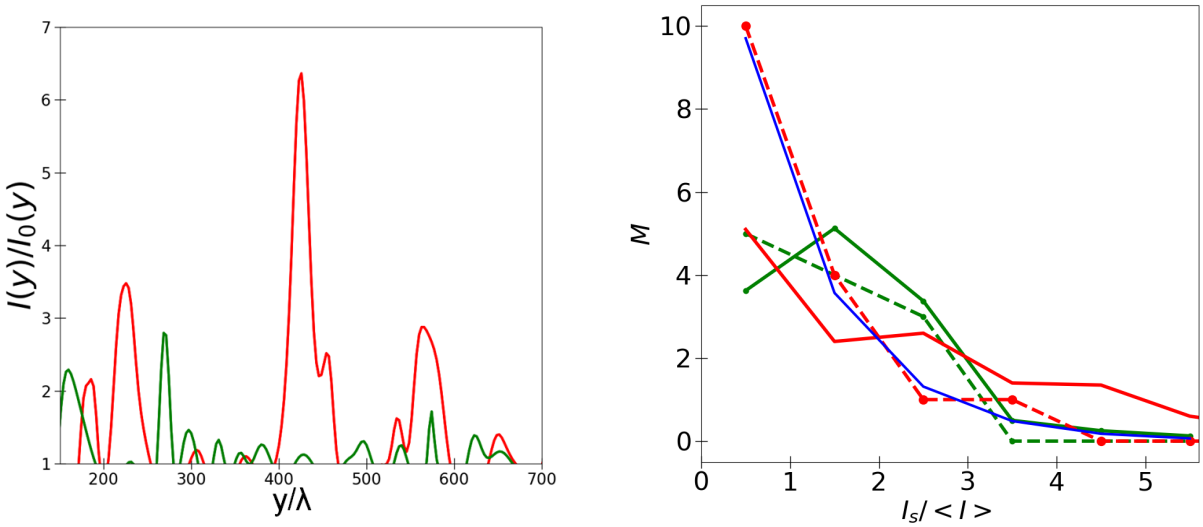

Figure 3.14: a) Transverse line-outs of laser intensity in plasma normalized to the initial beam intensity distribution at $t = 150$ ps for simulations performed with the semi-deterministic algorithm (red line) and random algorithm (green line). b) Time-averaged speckle abundance M evaluated from the random-inizialized simulation and represented by the solid green line. The dashed green line stands for the initial speckle intensity distribution, the dashed red line stands for the statistics in case of deterministic algorithm, the solid red line refers to time-average speckle abundance in case of deterministic algorithm (see green line in Fig. 3.11d), whereas the dashed blue line refers to the analytic exponential law Eq. (1.66).

3.5 Conclusion

In this Chapter, we studied ponderomotive self-focusing of a uniformly distributed speckle pattern within the PCGO-CHIC. A new approach consisting in predetermining the Gaussian-shaped speckle pattern geometry and the speckle intensity statistics has been developed: this consists in dividing the speckle intensity over three Gaussian beamlets while preserving the overall Gaussian shape. This approach provides the desired intensity enhancement reduction of PCGO speckles compared to the real speckles as discussed in Chapter 2. Ponderomotive self-focusing of speckles in a homogeneous plasma for average laser intensity ranging from $< I > /I_c^s$ =0.2-2.5 is studied. In this way, different regimes of plasma-speckles coupling and hydrodynamic-like inter-speckle interaction has been explored at short- and long-time scales.

At a short time-scale, independent speckle self-focusing is observed in agreement with the results obtained in Chapter 2: the three-beamlet speckles behave as Gaussian beamlets having a critical intensity two-times higher than the Gaussian beam critical intensity. For speckles with higher intensity, strong density perturbations induce a large beamlet divergence and the uncorrelated beamlets self-focusing independently. As a consequence, the speckle symmetry breaks behind the main self-focus position. Both effects result in a saturation of intensity enhancement of very intense speckles.

At longer time-scales, density perturbations produced in neighbor speckles interfere. That reduces the intensity enhancement in already self-focused speckles, and it triggers self-focusing in less intense speckles. This effect, coupled to the fact that intensity enhancement is saturated in the most intense speckles, produces oscillations of the intensity on a long time scale.

We define two regimes of multi-speckle beam self-focusing: for a low average intensity $(< I > /I_s) < 0.85 - 1.25$, no appreciable changing in speckle self-focusing is induced since the amplitude of plasma perturbations remains linear and the plasma-induced smoothing reduces the strong speckle intensity amplification. Thus the intensity statistics presents the exponential shape typical of the Gaussian statistics. For $(< I > /I_s) > 0.85 - 1.25$, speckle self-focusing dominates in the most intense speckles, whereas the highly nonlinear plasma perturbation prompts an intensity enhancement in less intensity speckles too. As a consequence, the speckle statistics shape changes because the number of intense speckles increases and the relation between the speckle abundance and the speckle intensity transforms into a power-dependence law. Therefore, by increasing the beam intensity of one order of magnitude from $< I > /I_s = 0.2$, the speckle-plasma coupling gradually becomes nonlinear, with the intensity interval $(< I > /I_s) = 0.85 - 1.25$ representing an indicative threshold between the linear and nonlinear regime.

For very intense speckles, such a departure from the standard exponential statistics, has been already reported in the literature in numerical simulations with an electromagnetic code. Our CHIC simulations qualitatively reproduce the modification of the speckle distribution tail observed in electromagnetic simulations. This confirms that our novel method can be used for in-line modelling of nonlinear laser plasma interaction with hydrodynamics codes when ponderomotive force becomes relevant.

Imposing a speckle statistics distribution and configuring a spatially regular speckle pattern leads to a more adequate description of ponderomotive phenomena. When these characteristics are not controlled, speckle self-focusing is less accurately described. This is the case of speckle initialization with the random algorithm, where

the speckle statistics is not controlled: the beamlets overlap area is small and the overall intensity enhancement is weak. Therefore, to correctly reproduce the collective beamlets action, it is preferable to resort to the semi-deterministic approach.

Chapter 4

Laser self-focusing in plasmas with a linear density profile

So far, we have considered ponderomotive laser self-focusing at moderate irradiances $I_0\lambda^2 < 10^{15}$ W/cm^2 μm^2 in homogeneous nonabsorbing plasmas. More realistic situations in ICF involve spatially-varying plasma density profiles where absorption takes place due to inverse bremsstrahlung. In these conditions, speckle self-focusing may drastically change because its critical power depends on the local plasma density. Furthermore, one needs to account for the ratio of a speckle length to the density scale length: in realistic cases, the longitudinal size of the speckle measures a few tens of microns, whereas in the PCGO algorithm speckle longitudinal size is a few hundreds of microns: longitudinal size of real optical speckles is one order of magnitude shorter than the characteristic plasma length, whereas PCGO speckles span over such a size. As a consequence, ponderomotive effects in longer PCGO speckles may be overestimated in inhomogeneous plasmas.

In this chapter, laser self-focusing in an inhomogeneous plasma and for intensities of interest for ICF are studied by means of hydrodynamic PCGO-CHIC simulations. The aim of this study is to extend the results obtained in the previous chapters to more realistic conditions for ICF. In particular, we investigate ponderomotive effects in plasmas with a linear density profile by varying the plasma longitudinal sizes and for several speckle powers aiming to understand the role of plasma absorption and to discuss the dependence of ponderomotive effects on plasma size. Values of plasma lengths and beam intensities are consistent with ICF and shock ignition conditions.

Following the structure of this thesis, we consider laser-plasma coupling for different PCGO beams. First, we treat self-focusing of a PCGO beamlet in order to analyze the consequences of laser absorption and plasma length on ponderomotively-induced beamlet intensity enhancement. The effect of thermal self-focusing is discussed as well. Then, self-focusing of a regularly-focused three-beamlet speckle is considered. Within this approach, the goal is to show that this speckle structure allows to mitigate ponderomotive effects in larger PCGO speckles. This is done by evaluating the reduction of speckle intensity enhancement for different plasma lengths and comparing it to the single-beamlet case. We show here that the three-beamlet configuration introduced in Chapter 2 allows to reduce the speckle intensity enhancement as it was demonstrated in a homogeneous plasma. At the end of

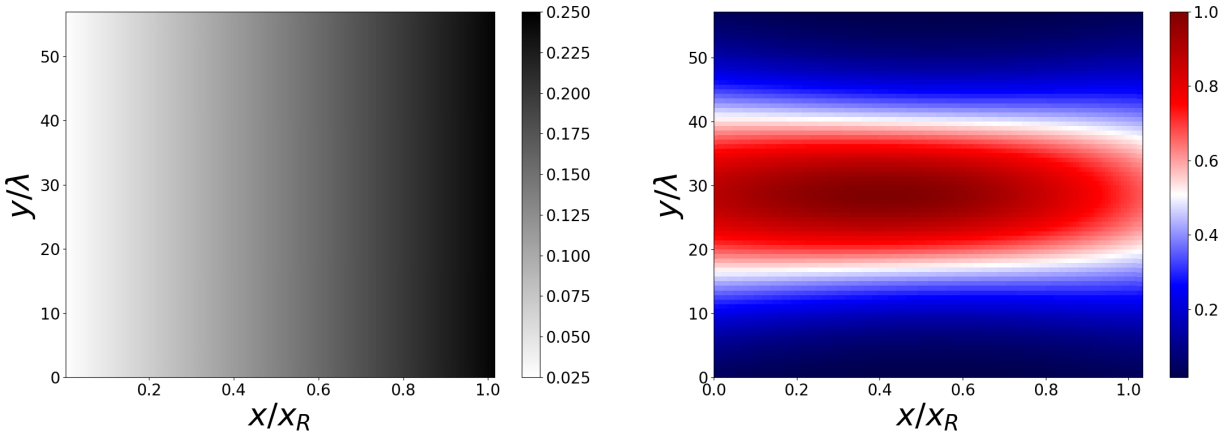

(a) (b)

Figure 4.1: a) Plasma density normalized to critical density n_c and b) initial laser intensity distribution normalized to the maximum laser intensity I_0 as a function of spatial coordinates: the transverse coordinate is normalized to the laser wavelength λ, whereas the longitudinal coordinate is normalized to the Rayleigh length x_R. Here, the plasma length L is 1500λ. In panel a) the laser propagates from the left.

this Chapter, we discuss the speckle statistics evolution of a multi-speckle beam initialized according to the algorithm introduced in Chapter 3.

4.1 Self-focusing of a Gaussian speckle: simulation conditions and results

In this section, we consider the self-focusing of beams having a Gaussian profile. In Sec. 4.1.1, we study the case of a PCGO Gaussian beamlet propagating in inhomogeneous plasma, whereas is Sec. 4.1.2 a regularly three-beamlet initialization of a PCGO speckle is considered with characteristics similar to a Gaussian beamlet. In both cases, to approach real ICF conditions, the laser wavelength λ is set to 0.35 μm, and the beam waist is $w_0 = 20\lambda \approx 7$ μm, which gives a Rayleigh length x_R of around 500 μm. PCGO-created speckle with the three-beamlet initialization of Sec. 4.1.2 has the same waist and longitudinal size. Thanks to the modular structure of PCGO laser-plasma coupling, modules which account for laser-plasma interaction can be easily switched on and off. This allows to clearly isolate and identify the importance of one phenomenon with respect to the others. Therefore, for all the laser configurations, three sets of runs are considered: the first set of runs concerns laser self-focusing only, then laser absorption is neglected and ponderomotive force module is on. In the second set of runs, laser absorption is turned on and the ponderomotive force is switched off, whereas the third set of runs includes ponderomotive force and laser absorption in collisional plasma. Plasma conditions are chosen as follows: a plastic CH fully ionized plasma ($Z = 3.5$), with a constant initial temperature and an electron temperature T_e three times the ion temperature T_i, $T_e = 3T_i = 3$ keV. The density in all the simulations varies from $0.25\%n_c$ to $25\%n_c$, where laser self-focusing may have repercussions on excitation of three-wave instabilities such as

SRS, TPD and SBS. However, in this preliminary study, competition between beam self-focusing and those instabilities is ignored. In all the simulations, the laser enters the plasma profile from the lowest density region. The spatial grid reproduces the typical resolutions considered in ICF hydrodynamics simulations, i.e. around 10λ. Duration of simulations is set to 100 ps, which is 6 times longer than the characteristic ion-acoustic time $t_{c_s} = w_0/c_s$ =17 ps.

An example of plasma density distribution n_{e0} normalized to the critical density n_c is illustrated in Fig. 4.1a. Figure 4.1b stands for a reference of how the laser intensity distribution looks like for all cases considered: the initial intensity peak I_0 is placed in the middle of plasma, i.e around $n_{e0}/n_c = 0.125$. The beam propagates from the left to the right. In both pictures, the transverse spatial coordinate is normalized to the laser wavelength λ, whereas the longitudinal coordinate is normalized to the Rayleigh length x_R. These figures refer to the case where the plasma size is equal to the beamlet Rayleigh length and stand for a reference for any other simulations.

4.1.1 Self-focusing of a PCGO beamlet: effects of absorption and dependence on the plasma length

We perform two-dimensional CHIC simulations for studying self-focusing of a PCGO beamlet in an inhomogeneous plasma in 2D planar geometry. Beamlet power P^{2D} and plasma sizes L are varied: P^{2D} = 0.5 TW; 1 TW; 5 TW, and $L/x_R = 0.2$; 0.5; 1, where we have expressed the plasma length in x_R units for convenience. The on-axis intensity I_0 related to the three powers can be recovered from Eq. (1.33) and from the value of beamlet waist $w_0 = 7$ μm: $I_0 = 0.5$ PW/cm^2; 1 PW/cm^2 and 5 PW/cm^2, respectively.

As mentioned above, the beamlet is always focused in the middle of the plasma simulation area, i.e. at (x,y)=$(0.1x_R,25\lambda)$ for $L/x_R = 0.2$, at (x,y)=$(0.25x_R,25\lambda)$ for $L/x_R = 0.5$, and (x,y)=$(0.5x_R,25\lambda)$ for $L/x_R = 1$, generating the intensity distribution similar to the one displayed in Fig. 4.1b.

The Gaussian beamlet critical power for ponderomotive self-focusing P_c^{2D} is evaluated by using these plasma and laser conditions in Eqs. (1.163) and (1.164): Figure 4.2a presents P_c^{2D} as a function of the plasma density (solid black line). The red, blue the green lines refer to P^{2D} = 0.5 TW; 1 TW; 5 TW, respectively. As already observed in Chapter 2, self-focusing threshold sensibly changes with respect to the density. For a low beam power, the critical power is almost one order of magnitude larger than the beam power across almost the whole density profile, and weak ponderomotive effects are expected. For a larger laser power, a ponderomotively-driven intensity enhancement plays an important role in the beamlet-plasma coupling. The dashed black line refers to the the critical power of thermal self-focusing $P_{c,th}^{2D} = \sqrt{\pi/2} I_0^{c,th} w_0 h$, being $I_0^{c,th}$ computed from Eq. (1.171). Thermal self-focusing arises from plasma heating when laser absorption is included in simulations: in case of inhomogeneous plasma, the beamlet intensity absorption occurs near the beamlet intensity profile, and especially along the beamlet axis. As a consequence, a local plasma heating develops in such a region. A transverse temperature gradient then establishes, which stands for the source of beamlet thermal self-focusing.

Comparing ponderomotive and thermal self-focusing thresholds, it can be predicted that thermal self-focusing would play a secondary role in the laser-plasma dynamics. Figure 4.2b shows the same thresholds for the conditions corresponding to a 2 μm speckle in a 3D geometry for the same plasma conditions. The solid black

lines refer to the critical power of ponderomotive self-focusing, whereas the dashed black lines refer to the critical power of thermal self-focusing. By keeping the same intensity I_0, the speckle powers in 3D reads $P^{3D} = 300$ MW (green line); 500 MW (blue line) and 3000 MW (red line). As already discussed in previous chapters and as evident from comparing Fig. 4.2a to Fig. 4.2b, the ratio between PCGO speckle power and beamlet power in 2D planar geometry is greater than the ratio between the real speckle power and its critical power. Therefore stronger intensity enhancement than in optical speckles may occur in PCGO-CHIC runs. Moreover, also in the 3D case, ponderomotive effects are expected to dominate.

From analytic considerations presented in Sec. 1.3.2.1, the importance of plasma length on laser self-focusing in collisionsless plasma can be estimated. Figure 4.3 presents the laser self-focusing length L_{sf} normalized to the Rayleigh length as a function of the laser power $p_{2c} = P^{2D}/P_c^{2D}$ (bottom axis) and plasma density (upper axis) in case of $P^{2D} = 0.5$ TW (green line) in panel a; $P^{2D} = 1$ TW (blue line) in panel b and $P^{2D} = 5$ TW (red line) in panel c and according to Eq. (1.166). The horizontal black lines refer to the plasma length $L/x_R = 0.2; 0.5; 1$. Ponderomotive force leads to laser self-focusing in plasma regions where $L_{sf}/x_R < L/x_R$ and for $p_{2c} > 1$. According to Fig. 4.3a, for $P^{2D} = 0.5$ TW self-focusing develops only in long plasmas, and is inducing a very weak intensity enhancement given that for $L_{sf}/x_R < 1$, $p_{2c} \sim 1$. Laser power of $P^{2D} = 1$ TW may induce laser self-focusing also at medium plasma length $L/x_R \sim 0.5$ as displayed by the blue line in Fig. 4.3b. At $P^{2D} = 5$ TW, the laser power is such that that the beamlet undergoes self-focusing for any plasma length.

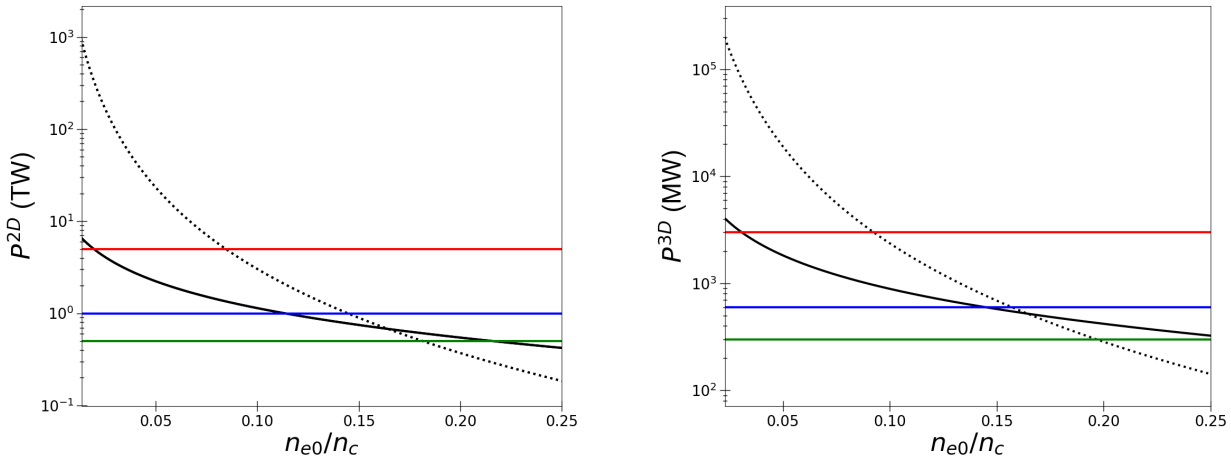

(a) (b)

Figure 4.2: Gaussian beam critical power in logarithmic scale as a function of plasma density for laser wavelength $\lambda = 0.35$ μm in 2D (panel a) and 3D (panel b). In both panels, the solid black lines refer to the critical power of ponderomotive self-focusing, whereas the dashed black lines refer to the critical power of thermal self-focusing. The green, blue and red lines correspond to single-beamlet speckle power used in CHIC-PCGO simulations: P^{2D}=0.5 TW; 1 TW and 5 TW, respectively, in panel a), and P^{3D}=300 MW; 500 MW and 3000 MW, respectively, in panel b).

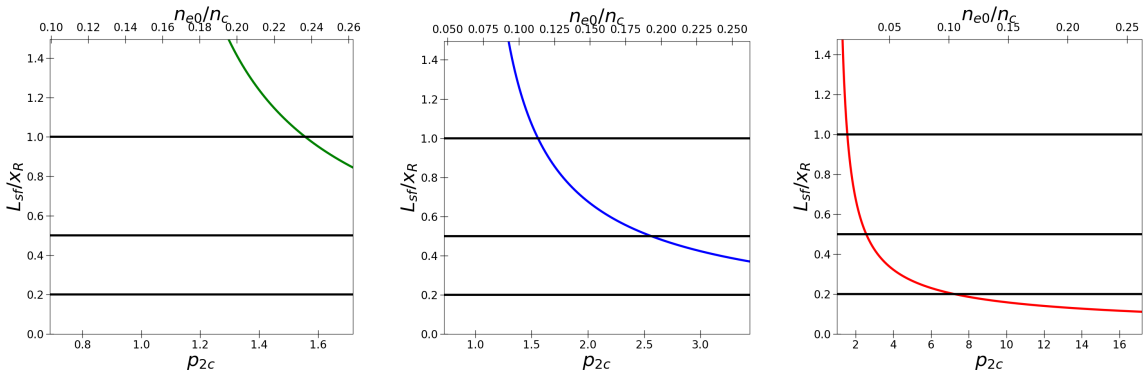

Figure 4.3: Self-focusing length normalized to beam Rayleigh length as a function of Gaussian beam power $p_{2c} = P^{2D}/P_c^{2D}$ (below x-axis) and as a function of the plasma density (upper x-axis) and in case of $P^{2D} = 0.5$ TW (green line) in panel a; $P^{2D} = 1$ TW (blue line) in panel b and $P^{2D} = 5$ TW (red line) in panel c and according to Eq. (1.166).

PCGO simulations of beamlet propagation in an inhomogeneous nonbasorbing plasma qualitatively confirm the theoretical estimations. This is shown in Fig. 4.4, which presents the beamlet intensity enhancement I_{max}/I_0 as a function of the plasma length L/x_R. Since the beamlet dynamics does not reach a stationary state and oscillations of the intensity appear, the values in the plots stand for the time-averaged intensity enhancement. The dashed green line refers to $P^{2D} = 0.5$ TW, the dashed blue line refers to $P^{2D} = 1$ TW whilst the dashed red line refers to $P^{2D} = 5$ TW. The error bars have been omitted for the sake of clarity. For $L/x_R = 0.2$, important intensity enhancement occurs only at a very high power, $P^{2D} = 5$ TW. For a medium and long plasma length, the time-averaged intensity enhancement increases almost proportionally with

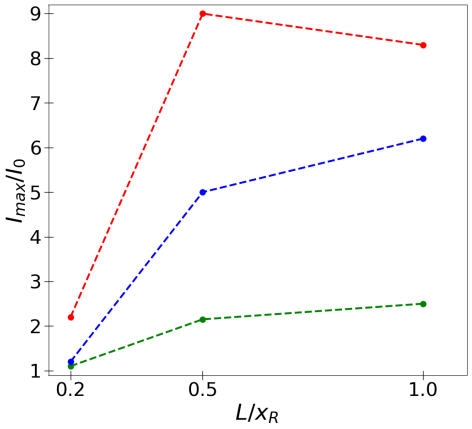

Figure 4.4: Time-averaged beamlet intensity enhancement I_{max}/I_0 as a function of the plasma lengths L/x_R. The green line refers to $P^{2D} = 0.5$ TW, the blue line refers to $P^{2D} = 1$ TW, and the red line refers to $P^{2D} = 5$ TW. Ponderomotive self-focusing in a collisionless plasma.

L/x_R	IB absorption (PCGO-CHIC)	IB absorption (analytic)
0.2	5.5%	6%
0.5	13%	14%
1	23%	25%

Table 4.1: Fraction of power absorbed due to collisional damping. First column: plasma length L normalized to Rayleigh range x_R; second column: time-averaged absorption evaluated from CHIC; Third column: inverse bremsstrahlung absorption calculated from Eq. (1.134)

the power, starting from around 2 for $P^{2D} = 0.5$ TW (green line) and reaching the highest values of 8-9 for $P^{2D} = 5$ TW (red line). Consequently, in a collisionless plasma the beamlet intensity enhancement strongly depends on the beamlet power but weakly varies with plasma length for $L \geq 0.5x_R$.

When considering beamlet propagation in inhomogeneous absorbing plasmas, another phenomenon may influence the laser-plasma interaction: the thermal self-focusing, which is expected to be a second order effect compared to the ponderomotive force (see Sec. 1.3.5 and Fig. 4.2a). To understand how thermal self-focusing competes with laser absorption, we performed the same set of simulations by switching off the ponderomotive force and allowing collisional absorption. The first quantity to consider is the fraction of laser power absorbed due to inverse Bremsstrahlung, outlined in Table 4.1: the first column refers to the plasma length, the second column refers to the time-averaged absorbed power evaluated from CHIC simulations, the third column refers to the absorbed fraction of laser power calculated from the analytic expression Eq. (1.135). For PCGO evaluation, the absorbed power has been time-averaged. As expected, at given density range, the larger is the plasma, the higher is the energy loss by the beamlet. CHIC computations are in good agreement with analytic calculations, differences come from the fact that the theoretical estimation considers a steady state beam, whereas in CHIC

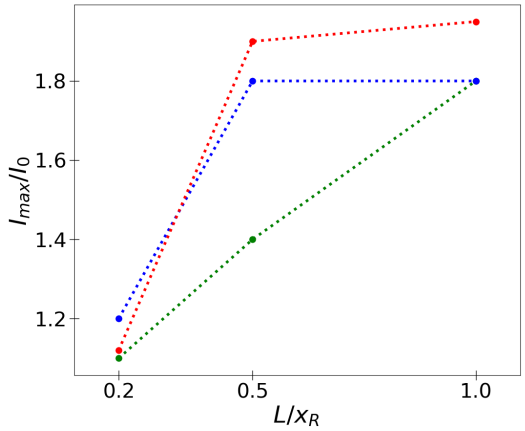

Figure 4.5: Time-averaged beamlet intensity enhancement I_{max}/I_0 as a function of the plasma lengths L/x_R. The green line refers to $P^{2D} = 0.5$ TW, the blue line refers to $P^{2D} = 1$ TW, and the red line refers to $P^{2D} = 5$ TW. Laser absorption is switched on and ponderomotive force is switched off.

the absorbed power is time-integrated. Laser absorption quasi-linearly increases with the plasma length: this brings to higher plasma heating and stronger temperature gradients in longer plasmas, inducing a greater feedback on the beamlet propagation due to the thermal self-focusing.

Figure 4.5 shows the time-averaged intensity enhancement I_{max}/I_0 when absorption is switched on and ponderomotive force is switched off. The dotted green line refers to $P^{2D} = 0.5$ TW, the dotted blue line refers to $P^{2D} = 1$ TW whilst the dotted red line refers to $P^{2D} = 5$ TW. The beamlet shows a less pronounced intensity enhancement than in nonbasorbing plasmas where only ponderomotive effects are activated (see Fig. 4.4). A weak influence on laser propagation only occurs in medium and long plasmas at moderate powers P^{2D} >1 TW, whereas it is practically absent at a short plasma. This confirms the fact that a higher absorption rate corresponds to larger spatial gains of the thermal self-focusing. At moderate and high powers, the intensity enhancement is very similar, and it reaches a maximum of 2 for $P^{2D} \geq 1$ TW and $L/x_R \geq 0.5$, i.e. thermal gradients become independent on plasma length and beamlet power. Above those values, the thermal-induced intensity amplification and the intensity loss due to laser absorption balance themselves, and no important variations are observable. Comparing to Figs. 4.4 and 4.6, we can notice that thermal self-focusing leads to an intensity enhancement between three and four times less important than ponderomotive-driven intensity enhancement, which means that thermal-induced effects play a secondary role in the beamlet dynamics.

This is confirmed in the last set of simulations, where we aim to highlight the role of thermal effects on beamlet self-focusing for the same plasma and laser parameters. For this purpose, collisional absorption is now allowed together with the ponderomotive force. Figure 4.6 shows the time-averaged beamlet intensity enhancement I_{max}/I_0 as a function of the speckle power for different plasma lengths. Overall, the nonlinear effects introduced by the ponderomotive force stand for the dominant phenomenon, whereas the laser absorption makes a small contribution to the beamlet dynamics given that it represents a linear process. As a consequence, the intensity enhancement preserves the same tendency observed when absorption effects were neglected. More

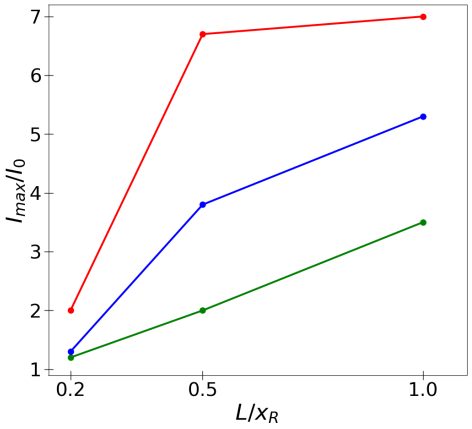

Figure 4.6: Time-averaged beamlet intensity enhancement I_{max}/I_0 as a function of plasma length L/x_R. The green lines refer to $P^{2D} = 0.5$ TW, the blue lines refer to $P^{2D} = 1$ TW, and the red lines refer to $P^{2D} = 5$ TW. Ponderomotive force is activated along with laser absorption.

in details, at short plasma length, collisions do not introduce any additional effect to laser-plasma interaction. This is due to the fact that the absorption is very low (see Table 4.1), and so is plasma heating. For medium and long plasmas the beamlet intensity reaches a value 7 times larger than the initial intensity for $P^{2D} = 5$ TW in a long plasma, which is around 25% less than in collisionless plasmas. This stands for a general trend in a collision plasma: interplay between the laser absorption, thermal and ponderomotive self-focusing still lead to large intensity amplifications, but reduced by a factor 15%-25% compared to the collisionless case in most situations. The case of $L/x_R = 1$ and $P^{2D} = 0.5$ TW represents the only exception: the intensity enhancement increases by 30% with respect the collisionless case. Only in this case in fact, the thermal-induced beamlet self-focusing overcomes the energy damped by inverse Bremsstrahlung and enforces the beamlet intensity amplification.

In conclusion, we have found that a relevant modification on beamlet propagation occurs only when the plasma size is greater than half of the beamlet Rayleigh range. At a given plasma length, intensity enhancement increases linearly with the beamlet power. Competition between collisional absorption and thermal self-focusing leads to a net mitigation of ponderomotive effects by a factor 0.85-0.75 compared to the collisionless case approximately. Such a behavior suggests that laser absorption is most important than thermal self-focusing in the regime studied. Despite that, at the highest power, the beamlet intensity still attains values 7-8 times larger than the initial intensity. These values are still two-times higher than the intensity amplification observed in a homogeneous plasma because the critical power depends on the plasma density.

4.1.2 Self-focusing of a three-beamlet speckle: relaxation of self-focusing effects

We demonstrated that in a homogeneous plasma ($n_{e0}/n_c = 0.1$) the dynamics of a three-beamlet speckle retraces the behavior of a Gaussian beam with a power twice lower. In order to confirm this observation in case of an inhomogeneous absorbing plasma, we performed simulations of a three-beamlet speckle evolution under the conditions similar to the single beamlet investigated in Sec. 4.1.1. Since in a short plasma and for a low power the single beamlet study has evidenced weak ponderomotive effects, we consider here only cases of three-beamlet speckle with powers $P^{2D} = 1$ TW and $P^{2D} = 5$ TW and for the plasma lengths $L/x_R = 0.5; 1$. Laser-plasma coupling conditions are varied by switching on and off the ponderomotive force and the collisional absorption modules, as previously done for a single beamlet. The beamlets have the same width as the speckle, carry a third of the speckle power each, and are focused in the plasma in such a way that the speckle has a shape similar to the single beamlet intensity distribution shown in Fig. 4.1b: the longitudinal distance among the beamlets focal points is $0.15x_R$, whereas the transverse distance is $0.5w_0$, similarly to the configuration studied in Chapter 2. The beamlet focal spots are placed such that the speckle is focused in the middle of the plasma density range, i.e. around $0.125n_c$. In case of $L/x_R = 0.5$, the speckle focus spot is located at $(x,y)=(0.125x_R,25\lambda)$, whereas for $L/x_R = 1$, the speckle focus spot is located at $(x,y)=(0.5x_R,25\lambda)$.

In an inhomogeneous plasma, and especially when both PCGO modules operate, the three-beamlet speckle dynamics is due to an entangled interplay among absorption, single beamlet ponderomotive effects, local plasma response, shared plasma density perturbation and overall hydrodynamic evolution due to local beamlet-plasma coupling. Leaving aside a detailed description of all these effects, we discuss the outcomes related to the intensity enhancement only. The main goal is to prove that in a three-beamlet speckle, the ponderomotive effects relax

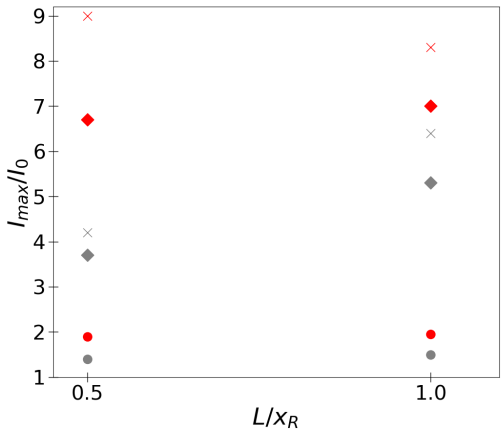

Figure 4.7: Time-averaged beamlet intensity enhancement I_{max}/I_0 as a function of plasma length L/x_R for $P^{2D} = 5$ TW. The red markers refer to the single beamlet, whereas the gray markers refer to the three-beamlet speckle. Circles correspond to the case where the ponderomotive force is switched off and collisional absorption is switched on, crosses refer to cases where only ponderomotive force module is switched on, whereas diamonds refer to collisional absorption and ponderomotive force modules both switched on.

the intensity amplification with respect a single beamlet. We present the results concerning only for $P^{2D} = 5$ TW because at moderate powers the intensity enhancement presents a similar trend.

Figure 4.7 displayes the time-averaged three-beamlet speckle intensity enhancement I_{max}/I_0 as a function of plasma length L/x_R for $P^{2D} = 5$ TW. The red markers refer to the single-beamlet, whereas the gray markers refer to the three-beamlet speckle. Circles corresponds to the case where the ponderomotive force is switched off and collisional absorption is switched on, crosses refer to cases where only ponderomotive force module is switched on, whereas diamonds refer to cases were collisional absorption and ponderomotive force modules are both switched on. When only absorption is activated, the fraction of power absorbed is close to the single beamlet measurements (see Table 4.1) when considering the whole speckle. However, thermal self-focusing appears mostly suppressed: similarly to the ponderomotive force, since the beamlets carry only a fraction of the total speckle power, their power is below of thermal self-focusing threshold, and the overall self-focusing effect is highly reduced.

When ponderomotive force operates, independently if laser absorption is considered or not, the three-beamlet speckle exhibits an intensity enhancement weaker than in the single beamlet case: such a decrease ranges between 22% for the case $L/x_R = 1$ and 53% for the case $L/x_R = 0.5$. Averaging over all the simulations, self-focusing effects are generally weaken of about 33% in the three-beamlet configuration with respect a single-beamlet speckle. Compared to the homogeneous plasma case, the three-beamlet configuration seems less efficient in decreasing intensity enhancement. This reduced efficiency in an inhomogeneous plasma is due to the fact that the longitudinal positions of the beamlets focus spots are shifted, and that the strength of ponderomotive effects depend on the plasma length. Therefore, they induce a ponderomotive pressure in different regions of the plasma density profile: the amplitude of the pressure depends on the local plasma density, and each beamlet undergoes

a self-focusing process of a different strength with respect the others. Then, as already discussed in Sec. 4.1.1 in Fig. 4.3, at a given beamlet power, a larger intensity enhancement is observed in longer plasmas, and the overall speckle intensity enhancement reduction is less important than in the single-beamlet case. For these reasons, when both ponderomotive forces and absorption act on the speckle for $L/x_R = 0.5$ the intensity enhancement of the three-beamlet speckle is reduced by 44% compared to the a single-beamlet case, whereas this reduction is less substantial in longer plasmas ($L/x_R = 1$), where it is only 30%. Nevertheless, this decreasing is still important when considering smoothing of self-focusing effects in two-dimensional PCGO speckles.

In summary, although the dynamics of three-beamlet speckle propagation in an inhomogeneous absorbing plasma is more complicated than in a homogeneous plasma, regular beamlets initialization allows to control and reduce the speckle intensity enhancement by a factor varying between 1/3 and 1/2 depending on the plasma and speckle conditions. This corresponds to an increasing of the critical power of a three-beamlet speckle of around 2-3, very close to the value of $\eta = 2$ found in Chapter 2 for homogeneous plasma and to the value desired to attain the reduction of ponderomotive effects in 2D (see Sec. 1.3.2.1).

4.1.3 Self-focusing time-scales and comparison to parametric instabilities time-scales

Before considering a multi-speckle beam and inter-speckle interaction, we discuss the potential impact of ponderomotive self-focusing on speckle-plasma coupling. Ponderomotive intensity enhancement has been considered for long time-scales while neglecting laser-plasma instabilities (LPIs). In integrated situations, excitation of parametric instabilities at short time-scales would introduce further laser energy loss besides collisional absorption because of light scattering or instability-induced pump depletion. These processes may occur on time-scales one order of magnitude shorter than the time-scales considered all along this chapter, or similarly at intervals several times smaller than the ion-acoustic transit time. This means that such instabilities generated before ponderomotive force can strongly influence laser-plasma coupling, and then laser intensity depletion due to saturation of LPIs may weaken the ponderomotive drive. Consequently, further reduction of the intensity enhancement can occur. One will account for all these phenomena when PCGO modules which account for LPIs are added. Here, we perform a preliminary analysis which is related to the development of self-focusing effects at time-scales comparable to LPIs time-scales, i.e for times around $t_{sf}/4$, in order to understand how they may influence LPIs at early time of laser-plasma interaction. In particular, our goal is to evidence a difference in ponderomotive intensity enhancement for a single-beamlet and a three-beamlet configuration.

Figure 4.8 shows the intensity enhancement I_{max}/I_0 as a function of plasma length L/x_R for $P^{2D} = 1$ TW (blue markers) and $P^{2D} = 5$ TW (red markers) at $t = t_{sf}/4$. The circles refer to a single-beamlet, whereas the crosses refer to a three-beamlet speckle. Here collisional absorption and ponderomotive force modules are both turned on. For $P^{2D} = 1$ TW (blue markers), passing from a single-beamlet (circles) to a the three-beamlet configuration (crosses) reduces the speckle intensity enhancement by a factor of 1.5-2, which is, consistent with what is observed at longer time-scales. Considering a three-beamlet speckle as a valid model of realistic speckles for what concerns ponderomotive effects, within this power interval the ponderomotive force is not expected to have a role in LPIs excitation. For $P^{2D} = 5$ TW instead (red markers), the PCGO beamlet (circles) exhibits a

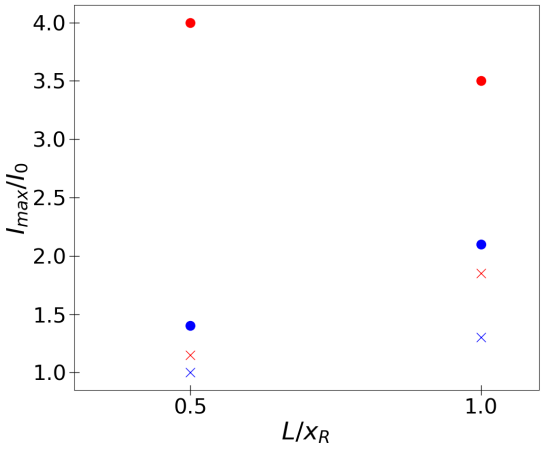

Figure 4.8: Intensity enhancement I_{max}/I_0 as a function of plasma length L/x_R at $t = t_{sf}/4$ for $P^{2D} = 5$ TW (red markers) and $P^{2D} = 1$ TW (blue markers). The circles refer to single-beamlet, whereas the crosses refer to three-beamlet speckle. Here collisional absorption and ponderomotive force modules are switched on.

very strong intensity enhancement, which may induce an overestimation of three-wave parametric instabilities in the time-interval considered. In this case, the three-beamlet speckle initialization (crosses) significantly moderates the development of ponderomotive self-focusing, which may influence LPIs excitation only in a long plasma. The speckle intensity is amplified by a factor 2 only. This strong intensity enhancement suppression is due to the increase of the speckle aspect ratio $x_R\lambda/\pi w_0^2$ as already discussed in Chapter 2.

In summary, at a short time-scale, i.e. a few picoseconds, the three-beamlet configuration predicts an increment of intensity enhancement only in a long plasma and for a high power. Concerning the conventional ICF conditions, long scales are attained at the end of laser pulse-target interaction. Then one may expect that self-focusing may appear later than other LPI processes thanks to the intensity speckle pattern which spatially modulates the beam intensity. It has been proved that with such a technique, nonlinear effects induced by the ponderomotive force can be avoided [115]. On the other hand, in the shock ignition scenario, the spike pulse irradiates a capsule surrounded by a long plasma corona. In this context, understanding of competition between the ponderomotive self-focusing development and excitation of parametric instabilities is very important. Indeed, considering a full-scale laser-plasma simulations with LPIs modules switched on, one needs to take into account that, since the ponderomotive self-focusing time-scale depends on the speckle width, in larger PCGO speckles ponderomotive force develops over a time ten times larger than in realistic speckles.

4.2 Self-focusing of a multi-speckle beam: statistics modification in inhomogeneous plasma and effects of absorption

In this section, we discuss self-focusing of a spatially modulated beam generated with the semi-deterministic algorithm. The speckle pattern extends over a transverse width as in Chapter 3, i.e. $w_B = 350$ μm. Preserving also the same ratio between the speckle waist and laser wavelength, i.e. $w_s = 20\lambda = 7$ μm, the algorithm

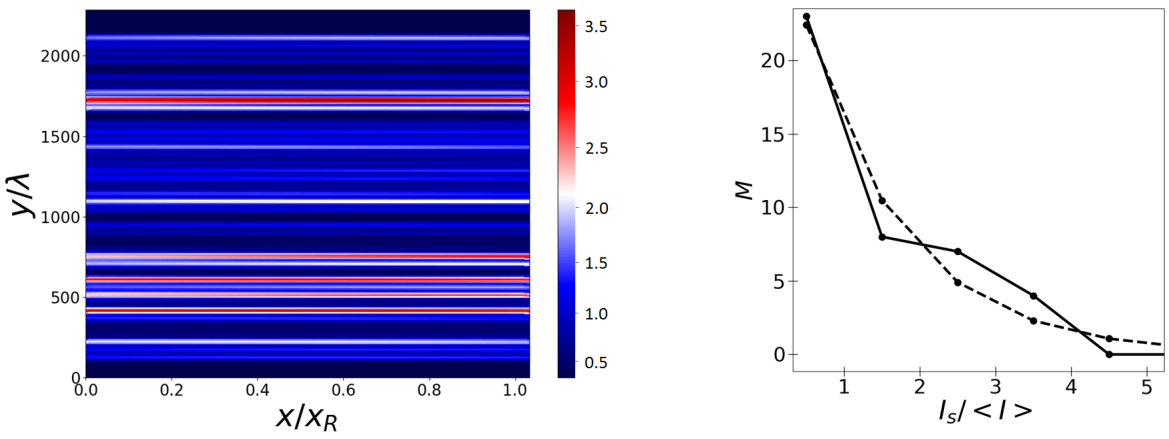

Figure 4.9: a) Initial laser intensity distribution in plasma normalized to the average beam intensity $< I >$. b) Initial speckle abundance M as a function of speckle intensity I_s normalized to the average beam intensity $< I >$ (solid line). The dashed line refers to the analytic expression (1.66). In panel a) laser propagates from the left to the right.

produces around 40 speckles, each composed by three beamlets of the same width. As in the previous sections, the plasma density spans in the interval $[0.025n_c, 0.25n_c]$. Here we consider only long plasmas, i.e. $L/x_R = 1$, of a transverse size $3w_B$. The beam is focused in the middle of the plasma profile.

We consider two average beam intensities $< I >$: $< I >= 10^{15}$ W/cm^2 and $< I >= 2.5 \times 10^{15}$ W/cm^2. In two-dimensional planar geometry, these values of beam intensity correspond to a beam power $P_B = 50$ TW and $P_B = 120$ TW respectively. Spatial configuration of the speckle pattern along with the intensity distribution normalized to the average beam intensity is shown in Fig. 4.9a. The solid black line in Fig. 4.9b represents the initial speckles intensity abundance calculated in PCGO runs, and the analytic exponential distribution (dashed line). As follows from the abundance function, the speckle intensities stretch from $I_s \approx 10^{14}$ W/cm^2 to $I_s \approx 3.5 \times 10^{15}$ W/cm^2 for the case $< I >= 10^{15}$ W/cm^2, and from $I_s \approx 2.5 \times 10^{14}$ W/cm^2 to $I_s \approx 10^{16}$ W/cm^2 for the case $< I >= 2.5 \times 10^{15}$ W/cm^2. The simulations last 100 ps, long enough to observe several inter-speckle interactions.

Considering plasma temperature $T_e = 3T_i = 3$ keV, and the critical power for a three-beamlet speckle twice higher than for a Gaussian beam, one can evaluate variation of the critical power of a three-beamlet speckle as a function of the plasma density: Figure 4.10a shows the speckle critical power as a function of plasma density for $< I >= 10^{15}$ W/cm^2, whereas Fig. 4.10b displayes the same quantity for $< I >= 2.5 \times 10^{15}$ W/cm^2. The red, blue, green and gray lines correspond to speckles with an intensity $I_s = 0.5$; 1; 2 and 5 times the average beam intensity $< I >$ (dotted lines in panel a, dashed lines in panel b). For $< I >= 10^{15}$ W/cm^2, considering that the speckles have the intensity abundance distribution shown in Fig. 4.9b, around 60% of the speckles have a power below the beam average intensity (dotted green line), whereas for the remaining 40% have a higher power. By considering the results obtained in Secs. 4.1.1-4.1.2, self-focusing effects are expected to be

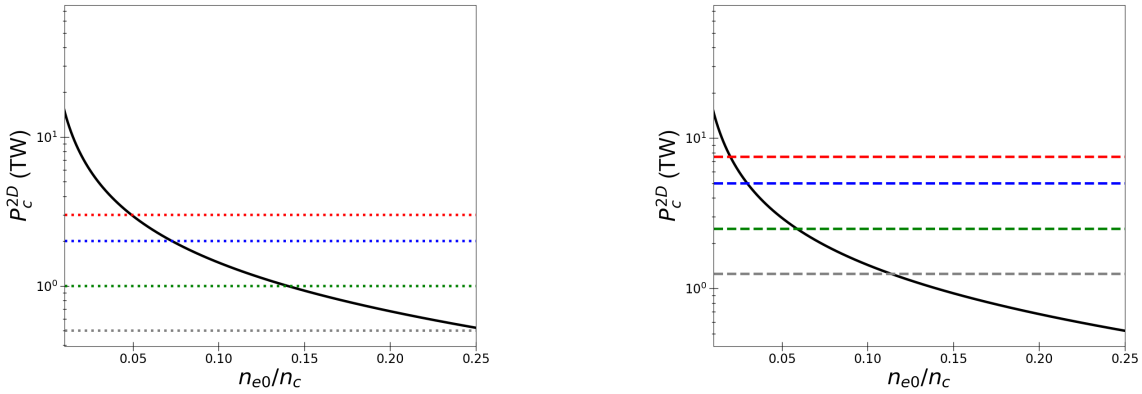

(a) (b)

Figure 4.10: Speckle critical power as a function of plasma density for a) $< I >= 10^{15}$ W/cm^2 and b) $< I >= 2.5 \times 10^{15}$ W/cm^2. The red, blue, green and gray lines correspond to speckles with an intensity $I_s = 0.5$; 1; 2 and 5 times the average beam intensity $< I >$ (dotted lines in panel a, dashed lines in panel b).

important for the 40% of speckles at the most. Instead, for $< I >= 2.5 \times 10^{15}$ W/cm^2, both the distribution of the speckle statistics displayed in Fig. 4.10b and Fig. 4.10b allow to predict that almost all the speckles have power at least comparable to the speckle critical power, and a strong modification of speckle intensity statistics due to ponderomotive effects may be expected.

A simulation set at each average laser intensity includes a run where only the ponderomotive force module is activated, a run where only the collisional absorption operates and a run where both the ponderomotive force and the collisional absorption modules are turned on. We characterize the strength of speckle self-focusing and the importance of absorption and thermal effects by analyzing the modification of the initial speckle intensity statistics. We have found out that when pondermotive effects are neglected, the intensity abundance of the speckle for any power is weakly modified, underlining a weak contribution of thermal self-focusing to speckle intensity enhancement. This is in agreement with the conclusion of Sec. 4.1.2 and for ICF direct-drive and shock ignition conditions. Therefore, in the following we investigate the time-averaged speckle intensity abundance of the speckles when only the ponderomotive force module operates and when collisional absorption module is added.

Figure 4.11 illustrates the speckle intensity abundance M as a function of speckle intensity bins averaged over all the simulation time: panel a shows the case where $< I >= 10^{15}$ W/cm^2, whereas panel b shows the case where $< I >= 2.5 \times 10^{15}$ W/cm^2. In both panels, the black lines stand for the initial speckle abundance, the green lines stand for time-averaged abundance in cases where laser absorption is disregarded, whereas the red lines refer to the time-averaged abundance in cases where absorption is taken into account. In the first case and for $< I >= 10^{15}$ W/cm^2 (green line in Fig. 4.11a), the abundance statistics may be fitted by two straight lines: a line with a steep slope up to $I_s \sim 2 - 3 < I >$ followed by a flat distribution up to $I_s \sim 6 - 7 < I >$, which is the upper limit of the speckle intensity enhancement. This evidences a strong self-focusing which affects speckles with intensity above $2< I >$. When laser absorption is considered (red line in Fig. 4.11a), the first part

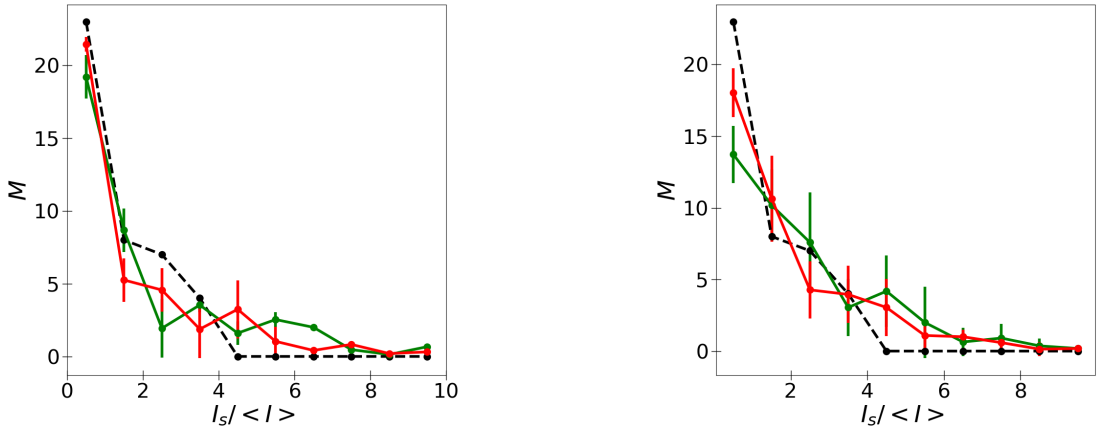

(a) (b)

Figure 4.11: Speckle intensity abundance M as a function of speckle intensity averaged over all the simulation time for (a) $< I >= 10^{15}$ W/cm^2 and (b) $< I >= 2.5 \times 10^{15}$ W/cm^2. In both panels, the black lines stand for the initial speckle abundance, the green lines stand for time-averaged abundance in a collisionless plasma, whereas the red lines refer to the time-averaged abundance in a collisional plasma.

of the distribution can be still represented by a steep straight line, but up to lower intensity compared to the collisionless case, i.e. up to $I_s \sim 1 - 2 < I >$. At higher intensities the probability distribution decreases much slower but steeper than in case without absorption. Moreover, the upper cut-off has a lower value compared to the case where absorption is neglected, reducing from 7 to 5 $< I >$, i.e. around 30%. Such a steeper probability distribution and a smaller upper cut-off in the collisional case is consistent with the results obtained in Sec. 4.1.2.

For $< I >= 2.5 \times 10^{15}$ W/cm^2, a stronger self-focusing develops in all speckles in case where the laser absorption module is switched off (green line in Fig. 4.11b) and the situation very similar to what observed in case of a homogeneous plasma: the speckle abundance can be interpolated by a power function with an exponent of -3.1. In case when laser absorption operates, the abundance in the central part of the distribution is slightly reduced, and the results may be approximated by a power law with an exponent of -3.3, with no influence on the cut-off intensity compared to the situation where absorption is neglected.

In general then, in all cases and for such high intensities, the initial exponential shape of the speckle intensity abundance is no longer preserved, as observed in homogeneous plasmas. Laser absorption slightly influences the ponderomotive self-focusing, the probability distribution of speckles is modified for intensities above 1-2 $< I >$, but its influence on speckles self-focusing reduces with the increase of the average beam intensity.

4.3 Conclusion

Laser propagation and self-focusing in an inhomogeneous and collisional plasma with different values of plasma scale length and laser intensity have been explored. Three types of PCGO beams have been considered: first we

investigated self-focusing of a single PCGO Gaussian beamlet in order to understand the role of plasma scale length and plasma heating on beamlet intensity enhancement. In agreement with theoretical considerations, it has been found that, at any beamlet intensity, beamlet self-focusing is more likely to develop when the plasma length is at least half of the speckle Rayleigh length for intensity above 0.5×10^{15} W/cm^2: below that, intensity enhancement is at maximum 2. In case of a large scale length plasmas, beamlet intensity enhancement is stronger. This means that for $L/x_R \geq 0.5$, ponderomotive effects no longer depend on plasma length. For $L/x_R \geq 0.5$, the intensity enhancement increases proportionally to the beamlet power. In cases when laser absorption is included, the same tendency as for the nonabsorbing case is observed. However, in this case a competition between thermal self-focusing and absorption contributes in different way to the beamlet evolution: temperature gradients tend to boost the intensity amplification, whereas inverse Bremsstrahlung decreases the beamlet intensity. Overall, absorption dominates over thermal self-focusing, and the net effect is a decreasing of intensity enhancement compared to the nonabsorbing case by 20% approximately.

Secondly, we have considered a three-beamlet regular initialization as studied in Chapter 2 to test if the intensity enhancement reduction works in inhomogeneous absorbing plasmas similarly as in a homogeneous plasma. Although the beamlet-plasma interaction presents a more complicate physics than in homogeneous plasmas, the intensity enhancement of a three-beamlet speckle diminishes by 30%-50% for all cases when compared to a single PCGO beamlet. This confirms the utility of modelling of real speckles by superposition of three beamlets: in this sense, the self-focusing of a real few-microns speckle can be more correctly reproduced by a PCGO three-beamlet speckle in plasmas with a linear density profile and for high intensity lasers. This effect corresponds to the critical power of a three-beamlet speckle multiplied by a factor 2-3 compared to a single Gaussian beamlet.

Third, we have studied how the plasma density ramp and absorption modify the speckle intensity distribution of a multi-speckle pattern. Similarly to single speckle cases, collisions decrease the ponderomotive speckle self-focusing, and the speckle abundance departs from its initial exponential shape: collisional absorption affects the speckles self-focusing, by increasing the steepness of the probability distribution and introducing an intensity cut-off about 30% smaller than in the collisionless case when $< I >= 10^{15}$ W/cm^2. At higher intensities, the effect of collisions on the speckle intensity statistics is weaker, and the intensity cut-off at about 6-7 times the beam average intensity does not depend on plasma conditions.

Conclusion

The implementation of Paraxial Complex Geometrical Optics (PCGO)-based methods in radiation-hydrodynamics codes may represent the key for describing in-line laser-plasma processes involved in inertial confinement fusion. Although this approach has been validated for several laser-plasma interaction experiments, a comprehensive treatment of ponderomotive effects has been left out so far. In a two-dimensional planar geometry, PCGO speckles are larger than real speckles and the intensity amplification in PCGO speckles may be overestimated by a factor 2 compared to the intensity enhancement of real speckles as it is demonstrated in Sec. 1.3.3. This PhD thesis aimed to solve this shortcoming by:

1. Benchmarking the PCGO-based method in describing laser self-focusing in the most representative case: a single PCGO Gaussian ray, called *beamlet*. This goal has been pursued by comparing PCGO-CHIC simulations to results obtained with the paraxial wave-based code HARMONY in a homogeneous nonabsorbing plasma.

2. Formulating a method which allows to control ponderomotive effects in large PCGO speckles in 2D planar geometry. This was achieved by studying different configurations of superposed Gaussian beamlets. This PCGO-like speckle configuration is referred to as *multi-beamlet speckle*. We identified the best beamlet initial configuration which fulfills the purpose of speckle intensity enhancement reduction in a homogeneous nonabsorbing plasma.

3. Adapting the best beamlets initialization geometry to a PCGO speckle pattern which mimics spatially modulated laser beams. Such PCGO-like spatially modulated beams are called *multi-speckle beams*. We have investigated the self-focusing of a multi-speckle beam in a homogeneous nonabsorbing plasma.

4. Extending to more realistic ICF situations all results described above by studying the self-focusing of PCGO-like beams in a plasma with a linear density ramp and accounting for laser absorption and induced thermal self-focusing. Three types of beams are considered: a single beamlet, a three-beamlet speckle and a multi-speckle beam.

The conclusions of this thesis are presented below:

1. Ponderomotive self-focusing of a single PCGO beamlet in a homogeneous non-absorbing plasma

Self-focusing of a Gaussian beamlet in a homogeneous nonabsorbing plasma within the PCGO framework has been investigated in the first part of Chapter 2. The accuracy in describing beamlet ponderomotive effects is benchmarked against ponderomotive self-focusing of a Gaussian-shaped beam modelled with the paraxial electromagnetic code HARMONY. This study is conducted for plasma density in the range $n_{e0}/n_c = 0.01 - 0.1$ and beamlet power in the range $p_{2d} = P^{2D}/P_c^{2D} = 1 - 6$ to explore different regimes of beamlet self-focusing. We found that at any density and at a low power, i.e. $p_{2d} \leq 2$, PCGO beamlet dynamics retrieves the behavior of a Gaussian beam as described by the electromagnetic code. Independently of the plasma density, analytic theory and full-wave simulations predict filamentation instability for $p_{2c} \geq 2.5$ which cannot be observed in PCGO-CHIC simulations. Despite that, PCGO reproduces the most important self-focusing characteristics of the dominant filament. The beamlet intensity enhancement due to ponderomotive self-focusing weakly depends on plasma density, however larger density perturbations are excited in a low density plasma, and their the coupling to the intensity enhancement is described less accurately by the PCGO model. This strongly nonlinear regime weakly influences the laser propagation in a realistic density profile as encountered in ICF corona: the beamlet critical power is inversely proportional to the density, and ponderomotive self-focusing is most likely to occur at higher densities.

2. Ponderomotive self-focusing of a PCGO multi-beamlet speckle in a homogeneous nonabsorbing plasma

In the second part of Chapter 2, two different beamlets configurations have been considered in order to create a PCGO speckle where ponderomotive effects are reduced compared to a single PCGO beamlet. The number of superposed beamlets N_b is chosen between three and five. The first approach consists in a random beamlets initialization. It was found that the ponderomotive drive is weakly affected and the speckle shape strongly depends on the number of beamlets and initial conditions. It is concluded that this initialization does not provide a control on the speckle self-focusing. The second configuration consists in a regularly-shaped speckle with a predefined Gaussian intensity profile. With this deterministic method, the ponderomotive effects are better controlled and the reduction of speckle self-focusing is attained by superposition of three and four PCGO beamlets. The case $N_b = 3$ shows a suppression of ponderomotive effects, accounted for by rescaling the three-beamlet speckle critical power by a factor $\eta = 2$. This suppression is explained by an increase of the speckle aspect ratio by the same factor. Since larger PCGO speckles overestimate real speckles self-focusing by approximately the same factor, the regular beamlets configuration represents the key to control intensity amplification in PCGO-CHIC simulations: as found by theoretical evaluation, 2D PCGO speckles present an intensity amplification twice larger than realistic speckles. The three-beamlet structure corrects this discrepancy, given that it behaves as its critical power would be twice as higher as the 2D single-beamlet critical power. In this way, the intensity enhancement of the three-beamlet speckles is two times weaker than the intensity enhancement of a 2D Gaussian beamlet, and thus recovering the same behavior of a real speckle.

3. Ponderomotive self-focusing of a PCGO multi-speckle in a homogeneous non-absorbing plasma

Based on results obtained in Chapter 2, in Chapter 3 the semi-deterministic algorithm of speckles generation has been introduced in PCGO-CHIC. It includes Gaussian-shaped speckles obtained by superposition of three beamlets. This novel algorithm generates a speckle pattern with two main properties: i) Gaussian speckles are regularly arranged at the far-field parallel to the beam propagation direction, and ii) the speckle intensity probability obeys to a Gaussian statistics. Self-focusing of spatially modulated beams in a homogeneous plasma is studied for average beam intensity $< I >$ ranging from $0.2I_c^s$ to $5I_c^s$, where I_c^s is the critical intensity of a three-beamlet speckle. At a short time-scale, self-focusing proceeds independently in each speckle. Three-beamlet speckles behave as Gaussian beamlets having a critical intensity twice higher than the Gaussian beam critical intensity and a saturation of speckle intensity enhancement of very intense speckles is observed. For long time-scales, interference of ion acoustic waves excited in neighbor speckles influences the speckle-plasma coupling leading to plasma smoothing effects.

Two regimes of multi-speckle beam self-focusing can be identified: the first one concerns low average intensity $(< I > /I_s) < 0.85 - 1.25$, where weak ponderomotive effects develop and plasma smoothing dominates, leading to a speckle statistics shape to the initial exponential form. Increasing the beam intensity induces an increase of nonlinear effects, which gradually become dominant: for $(< I > /I_s) > 0.85 - 1.25$, speckle self-focusing dominates, plasma behaves chaotically suppressing plasma smoothing and the speckles intensity enhancement is similar in all speckles. The intensity interval $(< I > /I_s) = 0.85 - 1.25$ represents an indicative threshold between the linear and nonlinear regime. At the highest intensity, the speckle abundance is better interpolated by a power law. Such a feature qualitatively agrees with simulations performed with a paraxial code Harmony.

4. Laser self-focusing in an inhomogeneous plasma with PCGO-CHIC

In Chapter 4, ponderomotively-induced self-focusing and its interplay with plasma heating are analyzed in an inhomogeneous and absorbing plasma with a linear density profile. We have considered different physical laser-plasma situations by switching on and off the modules modelling of the ponderomotive force and laser absorption, and by varying the plasma length. Beamlet self-focusing develops when plasma length is at least half of the speckle Rayleigh length, for intensity above 0.5×10^{15} W/cm^2. For plasma longer than half of the Rayleigh length the beamlet self-focusing depends essentially on the laser intensity. A competition between energy absorption and beamlet thermal self-focusing decreases a beamlet intensity enhancement by 20% in collisional plasmas.

Considering the three-beamlet speckle configuration, we have shown that the intensity enhancement of a three-beamlet speckle decreases by 30%-50% when compared to a single PCGO beamlet independently of plasma conditions and speckle intensity, as already observed in homogeneous plasmas. This feature confirms the utility of the three-beamlet speckle configuration for setting PCGO ponderomotive self-focusing at the same level of real speckles even in inhomogeneous plasmas.

Analyzing the statistics of multi-speckle beams, we have found that also in linear plasma density profiles

the speckle intensity statistics strongly is modified. Moreover, our simulations showed that laser absorption no longer affects the speckle statistics at a very high beam intensity.

General conclusion and perspectives

The general conclusion can be summarized as following:

- PCGO-CHIC accuracy in modelling of ponderomotive self-focusing of Gaussian beams has been tested in a homogeneous plasma for different plasma densities and beamlet powers. Good accuracy is obtained at low powers and high densities. In other regimes, difference with wave-based simulations are within the 20%, which is still satisfactory;
- A method for controlling and reducing ponderomotive effects in PCGO speckles has been developed: a superposition of three beamlets allows to reduce the PCGO speckle intensity enhancement by a factor 2. This is comparable with the factor needed for modelling of optical speckles with PCGO. This feature leads to a better reproduction in our 2D planar geometry of nonlinear ponderomotive effects developing in 3D geometry.
- The speckle pattern created within PCGO-CHIC has been modified in order to generate a speckle pattern with a controlled intensity probability distribution and intensity enhancement. We found that speckle self-focusing changes the intensity statistics to a power law at a high beam intensity in agreement with the results obtained with paraxial codes. These results are extended to more realistic ICF conditions of an inhomogeneous collisional plasma at laser intensities above 10^{15} W/cm^2 at the wavelength of 0.35 μm..

The semi-deterministic method has shown its utility in controlling and reducing ponderomotively-driven self-focusing in 2D PCGO speckles, improving the modelling of 3D effects in this simplified geometry. Further developments may comprise the following steps:

1. The semi-deterministic method can be improved by imposing additional constraints on the designing of spatially modulated beams such as a prescribed average intensity profile, a controlled beam contrast and a random inter-speckle distance. These features allow more control on the speckle intensity enhancement and may better describe temporal evolution of beam self-focusing.
2. The semi-deterministic method of initialization of speckle configuration and statistics may be extended to the temporal domain: the beamlet initialization could be changed at the end of a certain interval, corresponding to the speckle coherence time.
3. The PCGO approach can be applied to more realistic situations with non-stationary flowing plasmas: coupling multi-beamlet speckle self-focusing with transverse plasma flows may induce a deformation of the density channel and speckle bending.
4. Understanding the inter-play between multi-beamlet speckle self-focusing with other parametric instabilities and nonlinear laser-plasma coupling is necessary to model of realistic ICF conditions. Among all

issues, one can correlate the time-scale of speckle self-focusing to the reduced multi-scale model of SRS- and TPD-induced hot electrons generation. These modifications will improve the laser-plasma coupling, benefiting the overall predictability of PCGO-CHIC in analyzing full ICF processes.

Appendix: Three-wave parametric instabilities

In this appendix, we present the three-wave parametric instabilities occurring in ICF, notably stimulated Raman and Brillouin scattering. Both instabilities compete with the speckle self-focusing all along the plasma profile (SBS) or in certain part of it (SRS), and they are responsible for nonlinear effects in laser spike pulse-plasma coupling in the shock ignition context.

Stimulated Raman scattering (SRS)

The stimulated Raman scattering (SRS) consists in an excitation and amplification of a high frequency electron plasma wave, i.e. Langmuir wave (LW), along with a scattered electromagnetic wave. The three-wave matching conditions read

$$\omega = \omega_{LW} + \omega_R \tag{1}$$

$$\mathbf{k} = \mathbf{k}_{LW} + \mathbf{k}_R \tag{2}$$

where the subscript R refers to the electromagnetic scattered wave. Equations (1)-(2) are coupled to the LW and EM dispersion relations:

$$\omega_{LW}^2 = \omega_{pe}^2 + 3v_{Te}^2|\mathbf{k}_{LW}|^2; \tag{3}$$

$$\omega_0^2 = \omega_{pe}^2 + c^2|\mathbf{k}_0|^2; \tag{4}$$

$$\omega_R^2 = \omega_{pe}^2 + c^2|\mathbf{k}_R|^2. \tag{5}$$

Dependence on the plasma density through the term ω_{pe} introduces a cut-off on the density at which the instability can occur. We can find this cut-off by neglecting the thermal correction to the Langmuir wave, thus assuming $\omega_{LW} \sim \omega_{pe}$. Rewriting Eq. (5) as

$$\frac{\omega_R^2}{\omega_{LW}^2} = 1 + \frac{c^2|\mathbf{k}_R|^2}{\omega_{LW}^2}. \tag{6}$$

one obtains that $\omega_R \geq \omega_{LW}$. Thus, the minimum Raman frequency corresponds to $\omega_R = \omega_{LW}$, which implies that $\omega_R = \omega/2$. In terms of plasma densities, this last relation rewrites as $n_c^R = n_c/4$, where we have used the fact that $\omega_0^2 \propto n_c$. In inhomogeneous plasmas, the Raman instability can be excited for $n_e \leq n_c/4$. The lower density cut-off is determinated by the Landau damping of the Langmuir wave, measured by $k_{LW}\lambda_D$. Since $\lambda_D \propto \sqrt{n_e}^{-1}$, the lower cut-off is typically around 10%-1%n_c, depending on the plasma conditions.

In nonlinear regime, the saturation of the instability can be divided into two main categories [134–137]:

- fluid-like saturation: it consists in saturation of the Langmuir wave amplification due to wave-wave coupling. One of the most common process is the Langmuir decay instability (LDI): increasing of the Langmuir wave amplitude induces a secondary parametric instability corresponding to excitation of a secondary Langmuir wave and an ion acoustic wave. This process may generate a cascade of LW decays [138], so the first LW loses its energy to the other daughter waves and the SRS process is saturated.

- kinetic-like saturation: it consists in saturation of the Langmuir wave amplification because of wave-particle coupling. For example, an electron can be trapped inside the Langmuir wave potential, causing a LW frequency detuning and thus destroying the three-wave resonance. The Langmuir wave frequency shift $\Delta\omega_{LW}$ is proportional to the number of trapped electrons and the square root of the Langmuir wave potential.

The fluid-like saturation mechanism takes place in the long wavelength limit when the Landau damping is weak and the number of trapped particles is small, otherwise kinetic-like saturation prevails. It is considered that fluid-like saturation occurs for $k_{LW}\lambda_D < 0.29$, whereas kinetic-like saturation is more important above that, when the Langmuir wave is affected by the Landau damping [139, 140]. Another important aspect of the instability is its nature: as a three-wave instability, SRS can have an absolute or convective feature. The growth rates and the thresholds for the both modes have been investigated in several publications. The main results of the linear theory in inhomogeneous plasmas are:

- The absolute Raman instability is generated near the quarter critical density [141–143]. The growth rate γ_{SRS}^{abs} and instability excitation conditions evaluated with the linear theory [144, 145] in inhomogeneous plasmas for a backscattered light read

$$\gamma_{SRS}^{abs} = \frac{u_{osc}}{c}\omega \qquad \left(\frac{u_{osc}}{c}\right)^2 \left(k_0 L_{n_c/4}\right)^{4/3} > 1 \tag{7}$$

  From the right expression in Eq. (7), one obtains the intensity threshold I_{SRS}^{abs} in PW/cm^2

$$I_{SRS}^{abs} \approx \frac{1000}{\left(L_{n_c/4}^2\lambda\right)^{2/3}}, \tag{8}$$

  where $L_{n_c/4}$ is the density scale length at the quarter critical density in microns.

- The convective Raman instability is excited below the quarter critical density [143] Despite backscattered SRS often dominates, recent experiments have found a non negligible amount of side-scattered light having a convective feature [87]. As an example, the growth rate γ_{SRS}^{conv} and the intensity threshold I_{conv}^{thr} evaluated with the linear theory [87, 144] in inhomogeneous plasmas for convective backscattered light read:

$$\gamma_{SRS}^{conv} = \frac{u_{osc}}{c}\left(\omega\omega_{pe}\right)^{1/2} \qquad \left(\frac{u_{osc}}{c}\right)^2 k_0 L > 1, \tag{9}$$

  It is convenient to express the intensity threshold in terms of practical units:

$$I_{SRS}^{conv} \approx \frac{400}{L\lambda}, \tag{10}$$

  where the intensity threshold I_{SRS}^{conv} is in PW/cm^2, and L is the density scale length in microns at the corresponding point of the density profile where the instability is excited.

Scattered Raman light is detected by measuring the electromagnetic spectrum of the light coming out from the target. The SRS wavelength is related to the plasma density where the scattered wave has been generated by the relation [87]

$$\lambda_{SRS} = \lambda\left[1 - \sqrt{\frac{n_e}{n_c}\left(1 + 3k_{LW}^2\lambda_D^2\right)}\right]^{-1}. \tag{11}$$

Stimulated Brillouin scattering (SBS)

The stimulated Brillouin scattering (SBS) involves excitation and amplification of scattered electromagnetic waves coupled to a low-frequency ion acoustic wave (IAW). The three-wave matching conditions read

$$\omega = \omega_{IAW} + \omega_B \tag{12}$$

$$\mathbf{k} = \mathbf{k}_{IAW} + \mathbf{k}_B \tag{13}$$

where the subscript B refers to the electromagnetic scattered wave usually called "Brillouin" wave. Since $\omega_{IAW} << \omega_B$, $\omega \approx \omega_B$. The previous system must be coupled to Eq. (4) plus the following dispersion relations for the Brillouin and IAWs:

$$\omega_B^2 = \omega_{pe}^2 + c^2|\mathbf{k}_B|^2; \tag{14}$$

$$\omega_{IAW}^2 = k_s^2 c_s^2\left(\frac{1}{1 + k_s^2\lambda_D^2} + \frac{3T_i}{ZT_e}\right) - \mathbf{k}_S \cdot \mathbf{U} \tag{15}$$

where the IAW frequency has been evaluated in the laboratory frame, and the term $\mathbf{k}_S \cdot \mathbf{U}$ is related to the plasma flow with macroscopic fluid velocity $\mathbf{U}$. As a consequence of this last term, the SBS wave may be Doppler-shifted due to the hydrodynamic flow. Another consequence of Eqs. (12)-(15) is that the SBS cut-off is

at the critical density n_c, while the lower cut-off is related to the Landau damping by the condition $2k_0\lambda_{Di} > 1$. Thus the instability can occur all along the plasma profile where IAWs are not strongly affected by the Landau damping.

One can distringuish two main categories of SBS saturation [34]:

- fluid-like saturation: as in the SRS case, they are due to wave-wave interaction: a series of IAW harmonics are generated from the fundamental frequency ω_{IAW}. This harmonics generation dissipates the energy of the fundamental harmonic, saturating the instability;
- kinetic-like saturation: as in SRS kinetic-like saturation, the ions can be trapped inside the IAW potential. Thus, the IAW frequency is detuned destroying the SBS three-wave resonance.

Similarly to SRS, the fluid-like saturation mechanisms operates when the Landau damping is not so strong, otherwise kinetic-like saturation prevails. In terms of growth rate and intensity threshold in inhomogeneous plasmas, we consider here a backscattered SBS in range of laser intensities smaller than the ion acoustic frequency, the so-called *weak coupling regime*. In this regime, the SBS has a convective behavior, and its the growth rate γ_{SBS}^{con} evaluated from the linear theory [87] and in inhomogeneous plasmas reads

$$\gamma_{SBS}^{conv} = \frac{u_{osc}}{(2cc_s)^{1/2}}\omega_{pi} \tag{16}$$

The intensity threshold depends on the spatial density scale length of the region where the instability develops and on the scale length of the velocity gradient $L_V = c_s|dv/dx|$ and reads

$$\left(\frac{u_{osc}}{v_{te}}\right)^2 > \frac{16}{kL_V}\frac{n_c}{n_e} + \frac{8}{kL} \tag{17}$$

Since the effects of the flow dominates the SBS threshold, the first term on the right hand side is more important. Expressing Eq. (17) in practical units, one obtains:

$$I_{SBS}^{conv} \approx 7\frac{T_{keV}}{L_V\lambda}\frac{n_c}{n_e}, \tag{18}$$

where the intensity threshold I_{SBS}^{conv} is in PW/cm^2.

SBS is detected by measuring the spectrum of the light coming out from the target and with frequency close to ω, a shift in the spectrum of around 10^{-3} ω represents the SBS signature.

Résumé de la thèse en français: Modélisation de l'auto-focalisation pondéromotrice d'une impulsion laser dans un plasma avec un code hydrodynamique dans le cadre de la fusion par confinement inertiel en attaque directe

L'auto-focalisation laser due à la force pondéromotrice constitue un obstacle au succès du programme de fusion par confinement inertiel (FCI) étant donné qu'elle augmente localement l'intensité laser. Cette amplification d'intensité a deux effets néfastes: i) dégradation de l'uniformité de l'onde de choc lancée dans la cible, et ii) augmentation de la probabilité d'excitation des instabilités paramétriques. Bien que plusieurs techniques optiques aient été mises en œuvre pour atténuer les effets pondéromoteurs, elles restent une préoccupation en cas de croisement de faisceaux ou de l'utilisation des faisceaux laser avec une intensité élevée comme dans l'allumage par choc. Un module basé sur le Paraxial Complex Geometrical Optics (PCGO) a été implémenté dans le code hydrodynamique CHIC en géométrie plane bidimensionnelle : une telle méthode est une version améliorée de la technique standard du Ray-Tracing. PCGO tient compte de l'interaction non linéaire laser-plasma telle que la force pondéromotrice et la génération et la propagation d'électrons chauds, généralement négligés dans les simulations hydrodynamiques. Cette approche est également utilisée pour créer des faisceaux laser spatialement modulés par superposition de faisceaux gaussiens : l'enveloppe d'intensité de ces faisceaux génère des fluctuations d'intensité (" speckles ") dans le champ lointain. Bien que cette méthode basée sur PCGO ait amélioré la précision des simulations CHIC, la superposition de faisceaux PCGO produit des speckles laser plus grands et plus longs que les speckles réelles, et par conséquent leur auto-focalisation peut être surestimée.

Dans cette thèse, nous développons une méthode pour décrire et contrôler l'auto-focalisation pondéromotrice des speckles dans un plasma stationnaire en utilisant CHIC dans le formalisme PCGO. Dans le chapitre 1, nous présentons l'état de l'art de la modélisation de la propagation laser, de la théorie du plasma et de l'interaction laser-plasma. De plus, nous décrivons brièvement les outils numériques utilisés dans les études ICF.

Dans le chapitre 2, nous considérons l'auto-focalisation d'un seul faisceau gaussien, appelé beamlet, en le comparant aux résultats obtenus par le code électromagnétique Harmony. Nous avons constaté que le modèle PCGO décrit correctement l'autofocalisation des faisceaux dans un plasma homogène non absorbant pour des puissances allant jusqu'à quatre fois la puissance critique. Dans la même gamme de densité de plasma et de puissance de faisceau, nous étudions l'autofocalisation d'un speckle gaussien généré par la superposition de quelques beamlets, appelés speckle multi-beamlet. Ce speckle représente le prototype de tous les speckles générés par PCGO. L'augmentation de l'intensité induite par la force pondéromotrice est diminuée par rapport au cas du beamlet unique. Cette réduction peut être quantifiée en fonction du nombre de faisceaux superposés et en considérant deux stratégies pour la mise en forme de speckle multi-faisceaux: aléatoire et déterministe. Cette dernière configuration permet de mieux contrôler les effets pondéromoteurs lorsque trois beamlets composent le speckle.

Dans le chapitre 3, la méthode déterministe a été utilisée pour créer un faisceau multi-speckle, qui représente la version PCGO d'un faisceau modulé spatialement. Nous étudions l'auto-focalisation d'un tel faisceau dans

un plasma homogène non absorbant et nous montrons que les PCGO multi-beamlet speckle tiennent en compte des effets pondéromoteurs pour différentes intensités laser: cette méthode décrit la modification des statistiques d'intensité de speckle induite par l'auto-focalisation d'un speckle et l'interaction inter-speckle en accord avec ce qui a été observé dans des simulations électromagnétiques.

Dans le chapitre 4, tous ces résultats sont étendus aux plasmas absorbants dont la densité présente un profil linéaire. L'autofocalisation de différents faisceaux PCGO est étudiée ici pour des différentes longueurs de plasma, et l'effet de l'absorption laser est discuté.

Nous reprenons ici les principaux résultats obtenus dans cette thèse, illustrés dans les chapitres 2, 3 et 4.

- **Chapitre 2**

  L'absorption laser et le chauffage plasma ont été désactivés. De cette façon, les instabilités paramétriques, la génération d'électrons chauds et l'autofocalisation thermique sont exclus et la dynamique du plasma est uniquement dominée par la force pondéromotrice. Les paramètres d'entrée définis pour CHIC et HARMONY sont tels qu'ils génèrent un faisceau gaussien avec une taille initiale $w_0 \sim 20\lambda$.

  Nous avons trouvé qu'à n'importe quelle densité et à faible puissance la dynamique PCGO reproduit le comportement d'un faisceau gaussien tel que décrit par Harmony, surtout en terme de surintensité. Indépendamment de la densité du plasma, le modèle theorique prédit une instabilité de filamentation pour $p_{2c} \geq 2,5$ qui ne peut pas être observée dans les simulations PCGO-CHIC. Malgré cela, PCGO reproduit les caractéristiques d'autofocalisation les plus importantes du filament dominant.

  Dans la deuxième partie du chapitre 2, deux configurations différentes ont été envisagées afin de créer un speckle PCGO où les effets pondéromoteurs sont réduits par rapport à un seul beamlet PCGO. Le nombre de faisceaux superposés N_b est choisi entre trois et cinq. La première approche consiste en une initialisation aléatoire des beamlets. Nous avons constaté que les effets pondéromoteurs sont faiblement affecté dans ce cadre car la forme du speckle ne peut être controllée. En effet, elle dépend fortement du nombre de faisceaux et des conditions initiales. On conclut que cette initialisation ne fournit pas de contrôle sur l'auto-focalisation du speckle. La deuxième configuration consiste en un speckle de forme régulière avec un profil d'intensité gaussien prédéfini. Avec cette méthode déterministe, les effets pondéromoteurs sont mieux contrôlés et la réduction de l'autofocalisation du speckle est atteinte par superposition de trois et quatre faisceaux PCGO. Le cas $N_b = 3$ montre que la suppression des effets pondéromoteurs est diminuée, ce qui est expliqué par le redimensionnement de la puissance critique du speckle à trois faisceaux par un facteur 2. Cette suppression s'explique par l'augmentation du rapport d'aspect ratio du même facteur. Étant donné que les plus gros speckle de PCGO surestiment les taches réelles d'environ le même facteur, la configuration déterministe représente la clé pour contrôler l'amplification de l'intensité des speckles réels dans PCGO-CHIC.

- **Chapitre 3**

  Dans ce chapitre, nous décrivons une nouvelle méthode pour générer un distribution de speckles dans PCGO-CHIC sur la base des résultats obtenus dans le chapitre 2. Dans cette nouvelle approche, les speckles sont créées par superposition régulière de trois faisceaux gaussiens dont l'intensité est choisie de

telle sorte que la distribution d'intensité des speckles obéit à une loi exponentielle. Une telle méthode est appelée *algorithme semi-déterministe*, contrairement à la méthode PCGO standard appelée *algorithme aléatoire*. Nous montrons ici que l'approche semi-déterministe améliore la description du couplage laser-plasma dans les régimes où se développent des effets pondéromoteurs, permettant de traiter correctement l'amplification des effets pondéromoteurs dans de plus grands speckles 2D par rapport aux vrais speckles. Le nouvel algorithme de création d'un speckle composé de trois faisceaux fonctionne comme suit: premièrement, le nombre de speckles N_s et la largeur de faisceau w_B sont fixés en entrée. Ensuite, la largeur du speckle w_s est calculée. En règle générale, le nombre de speckles PCGO est compris entre 15 et 60 en fonction de la longuer d'onde.

Le comportement de la distribution des speckles est exploré en considérant différentes intensités laser moyennes. Pour les speckles très intenses, un tel écart par rapport aux statistiques exponentielles standard, qui caractérise les speckles gaussiens, a déjà été rapporté dans la littérature, où des simulations HARMONY d'interaction plasma-speckles ont été effectuées. Ces simulations ont montré que la queue de distribution des speckles, c'est-à-dire la distribution d'intensité des speckles les plus intenses, s'écarte de la forme exponentielle initiale, et une loi de puissance décrit mieux la relation entre l'abondance et l'intensité des speckles. Étant donné que les speckles PCGO semi-déterministes sont conçues comme des faisceaux gaussiens avec une distribution d'intensité prescrite, nos résultats reproduisent qualitativement la modification de la queue de distribution de speckle observée dans les simulations électromagnétiques HARMONY.

- **Chapitre 4**

Dans ce chapitre, l'autofocalisation laser dans un plasma inhomogène et les intensités d'intérêt pour l'ICF sont étudiées par es simulations hydrodynamiques PCGO-CHIC. Le but de cette étude est d'étendre les résultats obtenus dans les chapitres précédents à des conditions plus pertinentes pour l'ICF. En particulier, nous étudions les effets pondéromoteurs dans les plasmas avec des profils linéaires de densité et pour des puissances lasers qui sont relèvent de celles utilisées en FCI. Nous cherchons à comprendre le rôle de l'absorption du plasma sur l'autofocalisation du faisceau et à discuter de la dépendance des effets pondéromoteurs avec la taille du plasma. Les valeurs des longueurs de plasma et des intensités de faisceau sont cohérentes avec les longueurs d'échelle de plasma et les intensités laser des schémas conventionnels de FCI et d'allumage par choc. Grâce à la structure modulaire du couplage laser-plasma PCGO, les modules qui prennent en compte l'interaction laser-plasma peuvent être facilement allumés et éteints. Cela permet d'isoler et d'identifier clairement l'importance d'un phénomène par rapport aux autres, notamment les effets ponderomoteur et d'absorption laser. L'intervalle de densité fixé dans toutes les simulations est compris entre 0,25%n_c et 25%n_c. Nous considerons l'autofocalisation d'un beamlet unique, d'un speckle composé de 3 faisceaux et d'un multi-speckle beam. Pour le premier type de faisceau PCGO, en accord avec les considérations théoriques, nous constatons que son auto-focalisation est plus susceptible de se développer lorsque la longueur du plasma est au moins la moitié de la longueur de Rayleigh du speckle et pour une intensité supérieure à 0,5 $\times 10^{15}$ W/cm^2. Lorsque nous considérons l'autofocalisation d'un

speckle à trois beamlets, la sur-intensité d'un speckle est plus basse d'un facteur entre 1.5 et 2 par rapport à la surintensité d'un beamlet unique. Cela montre que la puissance critique est à-peu-prés 1.5-2 fois plus élevé que la puissance critique d'un beamlet, ce qui confirme les conclusions trouvées dans le chapitre 2 pour un plasma homogène.

- **Conclusions et perspectives**

  La conclusion générale peut être résumée comme suit:

  - La précision PCGO-CHIC pour la modélisation de l'autofocalisation pondéromotrice des faisceaux gaussiens a été testée dans un plasma homogène pour différentes densités de plasma et différentes puissances de faisceaux. Des résultats très satisfaisants sont obtenus à faibles puissances et hautes densités. Dans les autres régimes, la différence avec les simulations electromagnetiques se situe dans les 20%, ce qui est satisfaisant pour notre objectif;
  - Une méthode pour contrôler et réduire les effets pondéromoteurs dans les plus speckles PCGO qui sont plus grands par rapport aux speckles réelles: la superposition de trois beamlets permet de réduire l'augmentation d'intensité de la speckle PCGO d'un facteur 2, ce qui est comparable à la surestimation constatée lors de la modélisation des speckles optiques en utilisant speckles PCGO;
  - La distribution de speckles créée dans PCGO-CHIC a été modifiéée afin de générer une nouvelle configuration où que la statistique d'intensité de speckle satisfait a priori à la loi theorique exponentielle. Plusieurs effets liés à la pondération sont étudiés au sein de cette méthode dans des plasmas homogènes: nous avons notamment constaté que les statistiques d'intensité tendent vers des statistiques d'intensité de speckle non exponentielles pour une intensité de faisceau très élevée. Les résultats trouvés dans la littérature confirment également cette tendance.
  - Tous les résultats précédents sont généralisés et confirmés dans des conditions de plasma plus réalistes, c'est-à-dire dans des profils de plasma linéaires absorbants, et des intensités laser plus élevées, c'est-à-dire au-dessus de 10^{15} W/cm^2. Dans cette dernière partie, nous avons également considéré l'effet de l'absorption laser: comme prévu, ce phénomène a tendance à réduire l'amplification d'intensité induite par la pondéromotrice.

  Une amélioration supplémentaire comprendrait les étapes suivantes:

  1. La méthode semi-déterministe peut être améliorée en imposant d'autres contraintes à la conception de faisceaux modulés spatialement. Les exigences de configuration spatiale peuvent inclure le profil d'intensité transversale, un certain nombre de faisceaux par speckles, un contraste de faisceau contrôlé et modifier la distance inter-speckle de façon aléatoire.
  2. La méthode d'initialisation de la configuration et des statistiques du speckle peut être étendue au domaine temporel. afin de reproduire la méthode de lissage temporelle.
  3. L'approche PCGO peut être appliqué à des situations plus réalistes avec des plasmas non stationnaires, et le bending du faisceau et sa connexion aux effets pondéromoteurs peut être étudiées au sein de PCGO.

4. Finalement, on devrait coupler tous les effets précédemment étudiés ici aux instabilités paramétriques pour se rapprocher des conditions réalistes de la FCI.

Bibliography

[1] Statistical Review of World Energy, Workbook (xlsx), London, (2016), https://www.eia.gov/

[2] https://www.euronuclear.org/glossary/fuel-comparison/;
https://www.ocean.washington.edu/courses/envir215/energynumbers.pdf

[3] D. Meade, "*50 years of fusion research*", Nucl. Fusion 50 014004 (2010) . doi: doi10.1088/0029-5515/50/1/014004;

[4] S. Pfalzner, "*An Introduction to Inertial Confinement Fusion*", CRC Press (2006).

[5] K. S. Krane, "*Introductory Nuclear Physics*", John Wiley and Sons (1955).

[6] A. Lépine-Szily and P. Descouvemont, "*Nuclear astrophysics: nucleosynthesis in the Universe*", International Journal of Astrobiology, Volume 11, Issue 4 (special issue) (2011). doi: doi10.1017/S1473550412000158.

[7] R. S. Craxton, K. S. Anderson, T. R. Boehly, V. N. Goncharov, D. R. Harding, J. P. Knauer, R. L. McCrory, P. W. McKenty, D. D. Meyerhofer, J. F. Myatt, A. J. Schmitt, J. D. Sethian, R. W. Short, S. Skupsky, W. Theobald, W. L. Kruer, K. Tanaka, R. Betti, T. J. B. Collins, J. A. Delettrez, S. X. Hu, J. A. Marozas, A. V. Maximov, D. T. Michel, P. B. Radha, S. P. Regan, T. C. Sangster, W. Seka, A. A. Solodov, J. M. Soures, C. Stoeckl, and J. D.Zuegel, "*Direct-drive inertial confinement fusion: A review*", Physics of Plasmas 22, 110501 (2015). doi: doi10.1063/1.4934714.

[8] C. D. Zhou and R. Betti, "*Hydrodynamic relations for direct-drive fast-ignition and conventional inertial confinement fusion implosions*", Physics of plasmas **14**, 072703 (2007).doi: doi10.1063/1.3380857.

[9] J. D. Lindl, "*Inertial Confinement Fusion: The Quest for Ignition and Energy Gain Using Indirect Drive*", AIP-Press (1998).

[10] S. Atzeni, J. Meyer-ter-Vehn, "*The physics of Inertial Fusion*", Oxford University Press Canada, (2009).

[11] T. J. B. Collins, J. A. Marozas, K. S. Anderson, R. Betti, R. S. Craxton, J. A. Delettrez, V. N. Goncharov, D. R. Harding, F. J. Marshall, R. L. McCrory et al, "*A polar-drive–ignition design for the National Ignition Facility*", Physics of Plasmas **19** 056308 (2012). doi: doi10.1063/1.3693969

[12] O. V. Gotchev, N. W. Jang, J. P. Knauer, M. D. Barbero, R. Bett, C. K. Li and R. D. Petraso, "*Magneto-inertial approach to direct-drive laser fusion*", Journal of Fusion Energy **27** 25–31 (2008). doi: doi10.1007/s10894-007-9112-3.

[13] J. Meyer-ter-Vehn,"*Fast ignition of ICF targets: an overview*", Plasma Physics and Controlled Fusion, Volume **43**, Number 12A (2001). doi: doi10.1088/0741-3335/43/12A/308.

[14] R. Betti, C. D. Zhou, K. S. Anderson, L. J. Perkins, W. Theobald, and A. A. Solodov, "*Shock Ignition of Thermonuclear Fuel with High Areal Density*", Phys. Rev. Lett. 98, 155001 (2017). doi: doi10.1103/PhysRevLett.98.155001.

[15] S. Atzeni, A. Marocchino and A. Schiavi, "*Shock ignition: a brief overview and progress in the design of robust targets*", Plasma Physics and Controlled Fusion, Volume 57, Number 1 (2015). doi: doi10.1063/1.5003814.

[16] V T Tikhonchuk, A Colaïtis, A Vallet,, E Llor Aisa, G Duchateau, Ph Nicolaï and X Ribeyre, "*Physics of laser-plasma interaction for shock ignition of fusion reactions*", Plasma Physics and Controlled Fusion, Volume 58, Number 1 (2005). doi: doi10.1088/0741-3335/58/1/014018.

[17] S. Atzeni, J.R. Davies, L. Hallo, J.J. Honrubia, P.H. Maire, M. Olazabal-Loumé, J.L. Feugeas, X. Ribeyre, A. Schiavi, G. Schurtz, J. Breil and Ph. Nicolaï, "*Studies on targets for inertial fusion ignition demonstration at the HiPER facility*", Nuclear Fusion, Volume 49, Number 5 (2009). doi: doi10.1088/0029-5515/49/5/055008.

[18] T. R. Boehly, D. Munro, P. M. Celliers, R. E. Olson, D. G. Hicks, V. N. Goncharov, G. W. Collins, H. F. Robey, S. X. Hu, J. A. Morozas, T. C. Sangster, O. L. Landen, and D. D. Meyerhofer, "*Demonstration of the shock-timing technique for ignition targets on the National Ignition Facility*", Physics of Plasmas 16, 056302 (2009). doi: doi10.1063/1.3078422.

[19] S. Guskov, X. Ribeyre, M. Touati, J.L. Feugeas, P. Nicolaï, V. Tikhonchuk, "*Ablation pressure driven by an energetic electron beam in a dense plasma*", Phys Rev Lett. **109** 255004(2012). doi: doi10.1103/PhysRevLett.109.255004.

[20] E Aisa, X. Ribeyre, G. Duchateau, T. Nguyen-Bui, V. Tikhonchuk, A.Colaïtis, R. Betti, A. Bose, W. Theobald, "*The role of hot electrons in the dynamics of alaser-driven strong converging shock*", Physics of Plasmas **24**, 112711 (2017). doi: doi10.1063/1.5003814.

[21] W. Theobald et al., "*Enhanced hot-electron production and strong-shock generation in hydrogen-rich ablators for shock ignition*", Physics of Plasmas **24**, 120702 (2017). doi: doi10.1063/1.4986797.

[22] S. I. Anisimov, V. A. Khokhlov, "*Instabilities in Laser-Matter Interaction*", CRC Press (1995)

[23] R. H. Stolen and A. Ashkin, "*Optical Kerr effect in glass waveguide*", Appl. Phys. Lett. **22**, 294 (1973). doi: doi10.1063/1.1654644.

[24] C.E. Max, "*Strong self-focusing due to the ponderomotive force in plasmas*", Physics of Fluids **19**, 74 (1976). doi: doi10.1063/1.861305.

[25] Y. Kato, K. Mima, *N*. Miyanaga, S. Arinaga, Y. Kitagawa, M. Nakatsuka, and C. Yamanaka, "*Random Phasing of High-Power Lasers for Uniform Target Acceleration and Plasma-Instability Suppression*", Phys. Rev. Lett. **53**, 1057 (1984). doi: doi10.1103/PhysRevLett.53.1057.

[26] S. N. Dixit, J. K. Lawson, K. R. Manes, H. T. Powell, and K. A. Nugent, "*Kinoform phase plates for focal plane irradiance profile control*", Optics Letters Vol. **19**, No. 6 (1994). doi: doi10.1364/OL.19.000417.

[27] S. Skupsky, R. W. Short, T. Kessler, R. S. Craxton, S. Letzring, and J. M. Soures, "*Improved laser-beam uniformity using the angular dispersion of frequency-modulated light*", J. Appl. Phys. **66**, 3456 (1989). doi: doi10.1063/1.344101.

[28] E. A. Williams, "*On the control of filamentation of intense laser beams propagating in underdense plasma*, Physics of Plasmas **13**, 056310 (2006). doi: doi10.1063/1.2179051.

[29] C. J. Randall, J. R. Albritton, and J. J. Thomson, "*Theory and simulation of stimulated brillouin scatter excited by non-absorbed light in laser fusion systems*", Phys. Fluids **24**, 1474 (1981). doi: doi10.1063/1.863551.

[30] W. Seka, D. H. Edgell, J. P. Knauer, J. F. Myatt, A. V. Maximov, R. W. Short, T. C. Sangster, C. Stoeckl, R. E. Bahr, R. S. Craxton, J. A. Delettrez, V. N. Goncharov, I. V. Igumenshchev, and D. Shvarts, "*Time-resolved absorption in cryogenic and room-temperature direct-drive implosions*", Physics of Plasmas **15**, 056312 (2008). doi: doi10.1063/1.2898405.

[31] S. Hüller, G. Raj, W. Rozmus, and D. Pesme, "*Crossed beam energy transfer in the presence of laser speckle ponderomotive self-focusing and nonlinear sound waves*", Physics of Plasmas **27**, 022703 (2020). doi: doi10.1063/1.5125759.

[32] D. Batani, S. Baton, A. Casner, S. Depierreux, M. Hohenberger, O. Klimo, M. Koenig, C. Labaune, X. Ribeyre, C. Rousseaux, G. Schurtz, W. Theobald and V.T. Tikhonchuk, "*Physics issues for shock ignition*" Nucl. Fusion **54**, 054009 (2014). doi: doi10.1088/0029-5515/54/5/054009.

[33] P. Michel, C. Labaune, S. Weber, V. T. Tikhonchuk, G. Bonnaud, G. Riazuelo, and F. Walraet, "*Studies of the laser filament instability in a semicollisional plasma*, Physics of Plasmas 10, 3545 (2003). doi: doi10.1063/1.1598204.

[34] S. Hüller, P. E. Masson-Laborde, D. Pesme, M. Casanova, F. Detering and A. Maximov, "*Harmonic decomposition to describe the nonlinear evolution of stimulated Brillouin scattering*", Phys. Plasmas **13**, 022703 (2006). doi: doi10.1063/1.2168403.

[35] Ph. Ballereau, M. Casanova, F. Duboc, D. Dureau, H. Jourdren, P. Loiseau, J. Metral, O. Morice, and R. Sentis, "*Simulation of the Paraxial Laser Propagation Coupled with Hydrodynamics in 3D Geometry*", Journal of Scientific Computing, , Vol. **33**, No. 1, October (2007). doi: doi10.1007/s10915-007-9135-y.

[36] J. F.Myatt, J. G.Shaw, R. K.Follett, D. H. Dustin, H. Froula, J. P.Palastro, V. N.Goncharov, "*LPSE: A 3-D wave-based model of cross-beam energy transfer in laser-irradiated plasmas*", Journal of Computational Physics Volume **399**, 108916 (2019). doi: doi10.1016/j.jcp.2019.108916.

[37] T.B. Kaiser, "*Laser ray tracing and power deposition on an unstructured three-dimensional grid*",Phys. Rev. E, **89**, 1 (2000). doi: doi10.1103/PhysRevE.61.895.

[38] J. Breil, S.Galera and P.H. Maire, "*Multi-material ALE computation in inertial confinement fusion code CHIC*" Computers Fluids **46**, 161-167 (2011). doi: doi10.1016/J.COMPFLUID.2010.06.017.

[39] Y. A. Kravtsov, Y. I Orlov, "Geometrical Optics of Inhomogeneous Media", Springer-Verlag, (1990).

[40] A. Colaïtis, G. Duchateau, Ph. Nicolaï and V. Tikhonchuk, "*Towards modeling of nonlinear laser-plasma interactions with hydrocodes: The thick-ray approach*" Phys. Rev. E **89**, 033101 (2014). doi: doi10.1103/PhysRevE.89.033101.

[41] A. Colaïtis,, "Multi-scale description of the laser-plasma interaction: application to the physics of shock ignition in inertial confinement fusion", PhD thesis, University of Bordeaux (2016).

[42] E. L. Dewald, F. Harteman, P. Michel, J. Milovich, M. Hohenberger, A. Pak, O. L. Landen, L. Divol, H. F. Robey, O. A. Hurricane, T. Döppner, F. Albert, B. Bachmann, N. B. Meezan, A. J. Mackinno, D. Callahan, and M. J. Edwards, "*Generation and Beaming of Early Hot Electrons onto the Capsule in Laser-Driven Ignition Hohlraums*" Phys. Rev. Lett. **116**, 075003. doi: doi10.1103/PhysRevLett.116.075003.

[43] J. D. Jackson, "Classical Electrodynamics", John Wiley and Sons (1999).

[44] B. E. A. Saleh, M. C. Teich, "Fundamentals of Photonics", Wiley-Blackwell: Wiley Series in Pure and Applied Optics (1991).

[45] W. Kruer, "The Physics Of Laser Plasma Interactions", CRC Press (2003).

[46] V. K. Tripathi, C. S. Liu, "Interaction of Electromagnetic Waves with Electron Beams and Plasmas", World Scientific Publishing Co Pte Ltd (1994).

[47] M. Born, E. Wolf, A. B. Bhatia, P. C. Clemmow, D. Gabor, A. R. Stokes, A. M. Taylor, P. A. Wayman, W. L. Wilcock "Principles of Optics", Cambridge University Press (1999).

[48] R. J. Goldston and P. H. Rutherford, "Introduction to Plasma Physics", Routledge (1995).

[49] A. E. Siegman, "Lasers", University Science Books (1986).

[50] H. Goldstein, "Classical Mechanics", Addison-Wesley (1980).

[51] M. M. Popov. "*A new method for computing wave fields in a high-frequency approximation*", Journal of Soviet Mathematics volume **20** (1982). doi: doi10.1007/BF01119372.

[52] D.S. Montgomery, "*Two decades of progress in understanding and control of laser plasma instabilities in indirect drive inertial fusion*", Phys. Rev. Lett. **53**, 1057 (1984). doi: doi10.1063/1.4946016.

[53] S. Chandrasekhar, "Hydrodynamic and Hydromagnetic Stability", Dover Publications (1981).

[54] J. Neauport, X. Ribeyre, J. Daurios, D. Valla, M. Lavergne, V. Beau, and L. Videau, "*Design and optical characterization of a large continuous phase plate for Laser Integration Line and laser Megajoule facilities*", *2003 Optical Society of America 1 May 2003 Vol. **42**, No. 13 Applied Optics*, (1997). doi: doi10.1364/AO.42.002377.

[55] H. Rose, D. F. Dubois, "*Statistical properties of laser hot spots produced by a random phase plate*" Phys. Fluids B**5**, 590 (1993). doi: doi10.1063/1.860545.

[56] J. Garnier, "*Statistics of the hot spots of smoothed beams produced by random phase plates revisited*" Physics of Plasmas **6**, 1601 (1999). doi: doi10.1063/1.873413.

[57] M. N. Saha, "*On a Physical Theory of Stellar Spectra*". Proceedings of the Royal Society A: Mathematical, Physical and Engineering Sciences, 99 (697) (1921). doi: doi10.1098/rspa.1921.0029.

[58] K. Kingdon, I. Langmuir, "*The Removal of Thorium from the Surface of a Thoriated Tungsten Filament by Positive Ion Bombardment*", Physical Review **22**, (1923). doi: doi10.1103/PhysRev.22.148.

[59] Y. B. Zel'dovich and Y. P. Raizer, "Physics of Shock Waves and High-Temperature Hydrodynamic Phenomena", Hayes W D and R F Probstein (New York: Academic Press) (1967).

[60] S. Eliezer, "The Interaction of High-Power Lasers with Plasmas", CRC Press, (2002).

[61] T. R. Boehly, D. L. Brown, R. S. Craxton, R. L. Keck, J. P. Knauer, J. H. Kelly, T. J. Kessler, S. A. Kumpan, S. J. Loucks, S. A. Letzring et al., "*Initial performance results of the OMEGA laser system*", Opt. Commun. **133**, 495 (1997). doi: doi10.1016/S0030-4018(96)00325-2.

[62] S. Laffite and P. Loiseau, "*Design of an ignition target for the laser megajoule, mitigating parametric instabilities*", Physics of Plasmas **17**, 102704 (2010). doi: doi10.1063/1.3489309.

[63] D. R. Nicholson, "Introduction to Plasma Theory", John Wiley and Sons (1983)

[64] F. F. Chen, "Introduction to Plasma Physics and Controlled Fusion", Kluwer Academic/Plenum Publishers (1984).

[65] A. I. Akhiezer, "Plasma Electrodynamics: Linear Theory", Pergamon (2013).

[66] A.A. Vlasov, "*On the kinetic theory of an assembly of particles with collective interaction*", Journal of Physics (USSR) 9, (1945).

[67] P. L. Bhatnagar, E. P. Gross, and M. Krook, "*A Model for Collision Processes in Gases. I. Small Amplitude Processes in Charged and Neutral One-Component Systems*", Phys. Rev. **94**, 511 (1954). doi: doi10.1103/PhysRev.94.511.

[68] L.D. Landau and E.M. Lifshitz, "Electrodynamics of Continuous Media", New York: Interscience Publishers (1984).

[69] L. Spitzer and R. Härm, "*Transport Phenomena in a Completely Ionized Gas*", Physical Review **89** pp. 977–981. (1953). doi: doi10.1103/PhysRev.89.977.

[70] S. Weber, G. Riazuelo, P. Michel, R. Loubére, F. Walreat, V.T. Tikhonchuk, V. Malka, J. Ovadia, and G. Bonnaud, "*Modeling of laser–plasma interaction on hydrodynamic scales: Physics development and comparison with experiments*", Laser and Particle Beams **22**, 189–195 (2004). doi: doi10.10170S0263034604222157.

[71] P. Kaw, G. Schmidt, and T. Wilcox, "*Filamentation and trapping of electromagnetic radiation in plasmas*" Physics of Fluids **16**, 1522 (1973). doi: doi10.1063/1.1694552.

[72] P. L. Kelley, " *Self-Focusing of Optical Beams*", Phys. Rev. Lett. **15**, 1005 (1965). doi: doi10.1103/PhysRevLett.15.1005.

[73] S. A. Akhmanov, A. P. Sukhorukov and R. V. Khokhlov, "*Self-focusing and Diffraction of Light in a Nonlinear Medium*", Soviet Physics Uspekhi, Volume **10**, Number 5 (1968). doi: doi10.1070/PU1968v010n05ABEH005849.

[74] R. Y. Chiao, E. Garmire, and C. H. Townes, "*Self-Trapping of Optical Beams*", Phys. Rev. Lett. **13**, 479 (1964). doi: doi10.1103/PhysRevLett.13.479.

[75] C.E. Max, J. Arons, and A. B. Langdon, "*Self-Modulation and Self-Focusing of Electromagnetic Waves in Plasmas*", Phys. Rev. Lett. **33**, 209 (1974)). doi: doi10.1103/PhysRevLett.33.209.

[76] J. F. Lam, B. Lippmann, F. Tappert, "*Self-trapped Laser Beams in Plasma*", Physics of Fluids **20**, 1176 (1977). doi: doi10.1063/1.861679.

[77] A. J. Palmer, "*Stimulated Scattering and Self-Focusing in Laser-Produced Plasmas* ", Physics of Fluids **14**, 2714 (1971). doi: doi10.1063/1.1693396.

[78] L. C. Johnson and T. K. Chu, "*Measurements of electron density evolution and beam self-focusing in a laser-produced plasma*", Phys. Rev. Lett. **32**, 517 – (1974). doi: doi10.1103/PhysRevLett.32.517.

[79] J. W. Shearer and J. L. Eddleman , "*Laser light forces and self-focusing in fully ionized plasmas* ", Physics of Fluids **16**, 1753 (1973). doi: doi10.1103/PhysRevLett.32.517.

[80] R. M. Corless, G. H. Gonnet, D. E. G. Hare, D. J. Jeffrey and D. E. Knuth , "*On the Lambert W function*, Adv. Comput. Math., vol. 5, (1996). doi: doi10.1007/BF02124750.

[81] H. A. Rose and D. F. DuBois, "*Initial development of ponderomotive filaments in plasma from intense hot spots produced by a random phase plate*", Physics of Fluids B **5**, 3337 (1993). doi: doi10.1063/1.860629.

[82] V. Tikhonchuk, S. Hüller, P. Mounaix, "*Effect of the speckle self-focusing on the stationary stimulated Brillouin scattering reflectivity from a randomized laser beam in an inhomogeneous plasma*", Physics of Plasmas **4**, 4369 (1997). doi: doi10.1063/1.872599.

[83] M. Weinstein, "*Nonlinear Schroedinger equations and sharp interpolation estimates*", Commun. Math, Phys. **87**, 567-576 (1983).

[84] J. H. Marburger and E. Dawes, "*Dynamical formation of a small-scale filament*", Phys. Rev. Lett. **21**, 556–558 (1968). doi: doi10.1103/PhysRevLett.21.556.

[85] A. Couairon and A. Mysyrowicz, "*Femtosecond filamentation in transparent media*", Physics Reports Volume 441, Issues 2–4 (2007). doi: doi10.1016/j.physrep.2006.12.005.

[86] E. M. Epperlein, "*Kinetic theory of laser filamentation in plasmas*", Phys. Rev. Lett. **65**, 2145 (1990). doi: doi10.1103/PhysRevLett.65.2145.

[87] D. Pesme, G. Bonnaud, M. Casanova, et al., "La fusion thermonucléaire inertielle par laser: l'interaction laser-matiére" part. 1, vol. 1. (French Edition). Synthèses. 61, BoulevardSaint-Germain: Eyrolles (1993).

[88] R. Bingham, R. Short, E. Williams, D. Villeneuve and M. C. Richardson, "*The filamentation instability at short wavelengths*", Plasma Physics and Controlled Fusion **26** 1077 (1986). doi: doi10.1088/0741-3335/26/9/003.

[89] R.J. Briggs, "*Electron-stream Interaction with Plasmas*", Research monographs, MIT (1964).

[90] M. N. Rosenbluth, R. B. White, and C. S. Liu. "*Temporal Evolution of a Three-Wave Parametric Instability*", Physical Review Letters *31* (1973). doi: doi10.1103/PhysRevLett.31.1190.

[91] M. N. Rosenbluth. "*Parametric Instabilities in Inhomogeneous Media*", Phys. Rev. Lett. **29** (1972). doi: doiPhysRevLett.29.565.

[92] C. S. Liu and M. N. Rosenbluth, "*Parametric decay of electromagnetic waves into two plasmons and its consequences*", Physics of Fluids **19** (1976). doi: doi10.1063/1.861591.269.

[93] S. Weber, C. Riconda, and V. T. Tikhonchuk, "*Low-Level Saturation of Brillouin Backscattering due to Cavity Formation in High-Intensity Laser-Plasma Interaction*", Phys. Rev. Lett. **94**, 055005 (2005). doi: doi10.1103/PhysRevLett.94.055005.

[94] C. Riconda, S. Weber, V. T. Tikhonchuk, and A. Héron, "*Kinetic simulations of stimulated Raman backscattering and related processes for the shock-ignition approach to inertial confinement fusion*", Physics of Plasmas **18**, 092701 (2011). doi: doi10.1063/1.3630937.

[95] H. Figueroa, C. Joshi, H. Azechi, et al. "*Stimulated Raman scattering, two-plasmon decay, and hot electron generation from underdense plasmas at 0.35 μm*", Physics of Fluids **27** (1984). doi: doi10.1063/1.864801.

[96] Zhang Jia-tai et al., "*Mechanism of hot electron generation and Stimulated Raman Scattering in laser cavity target plasma*", Acta Phys. Sin. (Overseas Edn) 3 279 (1994). doi: doi10.1088/1004-423X/3/4/005.

[97] S. J. Gitomer, R. D. Jones, F. Begay, A. W. Ehler, J. F. Kephart, and R. Kristal, "*Fast ions and hot electrons in the laser–plasma interaction*", Physics of Fluids **29**, 2679 (1986). doi: doi10.1063/1.865510.

[98] R. Yan, C. Ren, J. Li, A. V. Maximov, W. B. Mori, Z.-M. Sheng, and F. S. Tsung, "*Generating energetic electrons through staged acceleration in the two-plasmon-decay instability in inertial confinement fusion*", Phys. Rev. Lett. **108**, 175002 (2012). doi: doi10.1103/PhysRevLett.108.175002.

[99] D. T. Michel, A. V. Maximov, R. W. Short, J. A. Delettrez, D. Edgell, S. X. Hu, I. V. Igumenshchev, J. F. Myatt, A. A. Solodov, C. Stoeckl, B. Yaakobi, and D. H. Froula, "*Measured hot-electron intensity thresholds quantified by a two-plasmon-decay resonant common-wave gain in various experimental configurations*", Physics of Plasmas **20**, 055703 (2013). doi: doi10.1063/1.4803090.

[100] D. W. Forslund, J. M. Kindel, and E. L. Lindman, "*Nonlinear Behavior of Stimulated Brillouin and Raman Scattering in Laser-Irradiated Plasmas*",Phys. Rev. Lett. **30**, 739 (1973). doi: doi10.1103/PhysRevLett.30.739.

[101] P. E. Young, "*Experimental study of filamentation in laser–plasma interactions*", Physics of Fluids B: Plasma Physics **3**, 2331 (1991). doi: doi10.1063/1.859600.

[102] P. E. Young, H. A. Baldis, R. P. Drake, E. M. Campbell, and K. G. Estabrook, "*Direct Evidence of Ponderomotive Filamentation in a Laser-Produced Plasma*", Phys. Rev. Lett. **61**, 2336 (1988). doi: doi10.1103/PhysRevLett.61.2336.

[103] S. Wilks, P. E. Young, J. Hammer, M. Tabak, and W. L. Kruer, "*Spreading of Intense Laser Beams Due to Filamentation*", Phys. Rev. Lett. **73**, 2994 (1994). doi: doi10.1103/PhysRevLett.73.2994.

[104] I. V. Igumenshchev, W. Seka, D. H. Edgell, D. T. Michel, D. H. Froula, V. N. Goncharov, R. S. Craxton, L. Divol, R. Epstein, R. Follett, J. H. Kelly, T. Z. Kosc, A. V. Maximov, R. L. McCrory, D. D. Meyerhofer, P. Michel, J. F. Myatt, T. C. Sangster, A. Shvydky, S. Skupsky, and C. Stoeckl , "*Crossed-beam energy transfer in direct-drive implosions*", Physics of Plasmas **19**, 056314 (2012). doi: doi10.1063/1.4718594.

[105] F. W. Perkins and E. J. Valeo, "*Thermal Self-Focusing of Electromagnetic Waves in Plasmas*", Phys. Rev. Lett. **32**, 1234 (1974). doi: doi10.1103/PhysRevLett.32.1234.

[106] W. L. Kruer, "*Ponderomotive and thermal filamentation of laser light*", Comments Plasma Phys. Controlled Fusion **9** (1985).

[107] A. J. Schmitt, " *Three-dimensional filamentation of light in laser plasmas*", Physics of Fluids B: Plasma Physics **3** 186 (1991). doi: doi10.1063/1.859936.

[108] G. Cristoforetti et al., "*Time evolution of stimulated Raman scattering and two-plasmon decay at laser intensities relevant for shock ignition in a hot plasma*", High Power Laser Science and Engineering Volume 7 2019 (2019). doi: doi10.1017/hpl.2019.37.

[109] D. Batani, L. Antonelli, F. Barbato, G. Boutoux, A. Colaïtis, J.-L. Feugeas, G. Folpini, D. Mancelli, Ph. Nicolaï, J. Santos, J. Trela, V. Tikhonchuk, J. Badziak, T. Chodukowski, K. Jakubowska, Z. Kalinowska, T. Pisarczyk, M. Rosinski, M. Sawicka, F. Baffigi, G. Cristoforetti, F. D'Amato, P. Koester, L.A. Gizzi, S. Viciani, S. Atzeni, A. Schiavi, M. Skoric, S. Gus'kov, J. Honrubia, J. Limpouch, O. Klimo, J. Skala,

Y.J. Gu, E. Krousky, O. Renner, M. Smid, S. Weber, R. Dudzak, M. Krus and J. Ullschmied, "*Progress in understanding the role of hot electrons for the shock ignition approach to inertial confinement fusion*", Nuclear Fusion, Volume 59, Number 3 (2018). doi: doi10.1088/1741-4326/aaf0ed.

[110] S. Weber, C. Riconda, O. Klimo, A. Héron, and V. T. Tikhonchuk, "*Fast saturation of the two-plasmon-decay instability for shock-ignition conditions*", Phys. Rev. E **85**, 016403 (2012). doi: doi10.1103/PhysRevE.85.016403.

[111] E. Llor Aisa, X. Ribeyre, G. Duchateau, T. Nguyen-Bui, V. T. Tikhonchuk, A. Colaïtis, R. Betti, A. Bose, and W. Theobald, "*The role of hot electrons in the dynamics of a laser-driven strong converging shock*", Physics of Plasmas **24**, 112711 (2017. doi: doi10.1063/1.5003814.

[112] A. Colaïtis, X. Ribeyre, E. Le Bel, G. Duchateau, Ph. Nicolaï, and V. Tikhonchuk , "*Influence of laser induced hot electrons on the threshold for shock ignition of fusion reactions*", Physics of Plasmas **23**, 072703 (2016). doi: doi10.1063/1.4958808.

[113] W. Theobald. et al., "*Spherical shock-ignition experiments with the 40 + 20-beam configuration on OMEGA*", Physics of Plasmas **19**, 102706 (2012). doi: doi10.1063/1.4763556.

[114] S. Skupsky and R. S. Craxton. "*Irradiation uniformity for high-compression laser-fusion experiments*". Physics of Plasmas **65**, 2157 (1999). doi: doi10.1063/1.873501.

[115] A. J. Schmitt, "*The effects of optical smoothing techniques on filamentation in laser plasmas*", Physics of Fluids **31**, 3079 (1988). doi: doi10.1063/1.866964.

[116] E. Lefebvre, R. L. Berger, A. B. Langdon, B. J. MacGowan, J. E. Rothenberg, and E. A. Williams, "*Reduction of laser self-focusing in plasma by polarization smoothing*", Physics of Plasmas **5**, 2701 (1998). doi: doi10.1063/1.872957.

[117] V. T. Tikhonchuk, J. Fuchs, C. Labaune, S. Depierreux, S. Hüller and J. Myatt, and H. A. Baldis, "*Stimulated Brillouin and Raman scattering from a randomized laser beam in large inhomogeneous collisional plasmas. II. Model description and comparison with experiments*", Physics of Plasmas **8**, 1636 (2001). doi: doi10.1063/1.1357218.

[118] B. Wattellier et al., "*Generation of a single hot spot by use of a deformable mirror and study of its propagation in an underdense plasma*", Journal of Optics Society of America B Vol. **20**, No. 8 (2003). doi: doi10.1364/JOSAB.20.001632.

[119] K. Glize, C. Rousseaux, D. Bénisti, V. Dervieux, L. Gremillet, S. D. Baton, and L. Lancia, "*Stimulated backward Raman scattering driven collectively by two picosecond laser pulses in a bi- or multi-speckle configuration*", Physics of Plasmas **24**, 032708 (2017). doi: doi10.1063/1.4978879.

[120] R. K. Follett, J. G. Shaw, J. F. Myatt, C. Dorrer, D. H. Froula, and J. P. Palastro, "*Thresholds of absolute instabilities driven by a broadband laser*", Physics of Plasmas **26**, 062111 (2019). doi: doi10.1063/1.5098479.

[121] B. J. Albright, L. Yin and B. Afeyan, "*Control of stimulated Raman scattering in the strongly nonlinear and kinetic regime using spike trains of uneven duration and delay*", Phys. Rev. Lett. **113**, 045002 (2014). doi: doi10.1103/PhysRevLett.113.045002.

[122] A. V. Maximov, I. G. Ourdev, D. Pesme, W. Rozmus, V. T. Tikhonchuk, and C. E. Capjack, "*Plasma induced smoothing of a spatially incoherent laser beam and reduction of backward stimulated Brillouin scattering*", Phys. of Plasmas **8**, 1319 (2001). doi: doi10.1063/1.1352056.

[123] S. Hüller, A. Porzio and J. Robiche, "*Order statistics of high-intensity speckles in stimulated Brillouin scattering and plasma-induced laser beam smoothing*", New Journal of Physics **15**, 025003 (2013). doi: doi10.1088/1367-2630/15/2/025003.

[124] C. Labaune, S. Baton, T. Jalinaud, H. A. Baldis, and D. Pesme, "*Filamentation in long scale lengthplasmas: Experimental evidence andeffects of laser spatial incoherence*", Physics of Fluids B: Plasma Physics **4**, 2224 (1992). doi: doi10.1063/1.860027.

[125] A. Schmitt and B. Afeyan, "*Time-dependent filamentation and stimulated Brillouin forward scattering in inertialconfinement fusion plasma*", Physics of Plasmas **5**, 503 (1998). doi: doi10.1063/1.872733.

[126] A. Colaïtis, S. Hüller, D. Pesme, G. Duchateau, and V. T. Tikhonchuk, "*Crossed beam energy transfer: Assessment of the paraxial complex geometrical optics approach versus a time-dependent paraxial method to describe experimental results* ", Physics of Plasmas **23**, 032118 (2016). doi: doi10.1063/1.4944496.

[127] A. Colaïtis, G. Duchateau, X. Ribeyre, Y. Maheut, G. Boutoux, L. Antonelli, Ph. Nicolaï,, D. Batani, V. T. Tikhonchuk, "*Coupled hydrodynamic model for laser-plasma interaction and hot electron generation*", Physical Review E **92** (4), 041101 (2015). doi: doi10.1103/PhysRevE.92.041101.

[128] D. W. Forslund, J. M. Kindel, and K. Lee. "*Theory of hot-electron spectra at high laser intensity*", Phys. Rev. Lett. **39**, 284 (1977). doi: doi10.1103/PhysRevLett.39.284.

[129] G. Cristoforetti, L. Antonelli, S. Atzeni, F. Baffigi, F. Barbato, D. Batani, G. Boutoux, A. Colaïtis, J. Dosta, R. Dudzak, L. Juha, P. Koester, A. Marocchino, D. Mancelli, Ph. Nicolai, O. Renner, J. J. Santos, A. Schiavi, M. M. Skoric, M. Smid, P. Straka, and L. A. Gizzi, "*Measurements of parametric instabilities at laser intensities relevant to strong shock generation*", Physics of Plasmas **25**, 012702 (2018). doi: doidoi.org/10.1063/1.5006021.

[130] A. Colaïtis, G. Duchateau, X. Ribeyre and V. Tikhonchuk, "*Modeling of the cross-beam energy transfer with realistic inertial-confinement-fusion beams in a large-scale hydrocode*" Phys. Rev. E **91**, 013102 (2015). doi: doi10.1103/PhysRevE.89.033101.

[131] E. Lefebvre, R. L. Berger, A. B. Langdon, B. J. MacGowan, J. E. Rothenberg, and E. A. Williams, *Reduction of laser self-focusing in plasma by polarization smoothing*, Physics of Plasmas **5**, 2701 (1998. doi: doi10.1063/1.872957.

[132] S. H. Glenzer, L. J. Suter, R. L. Berger, K. G. Estabrook, B. A. Hammel, R. L. Kauffman, R. K. Kirkwood, B. J. MacGowan, J. D. Moody, J. E. Rothenberg, and R. E. Turner, *Hohlraum energetics with smoothed laser beams*, Physics of Plasmas **7**, 2585 (2000). doi: doi10.1063/1.872957.

[133] J. D. Moody, H. A. Baldis, D. S. Montgomery, R. L. Berger, K. Estabrook, W. L. Kruer, B. F. Lasinski, E. A. Williams, S. Dixit, and C. Labaune, *Beam smoothing effects on the stimulated Brillouin scattering (SBS) instability in Nova exploding foil plasmas*, Physics of Plasmas **2**, 4285 (1995). doi: doi10.1063/1.872957.

[134] T. Kolber, W. Rozmus, and V. T. Tikhonchuk, "*Saturation of stimulated Raman scattering by Langmuir and ion-acoustic wave coupling*", Physics of Fluids B: Plasma Physics **5**, 138 (1993). doi: doi10.1063/1.860861.

[135] L. Yin, B. J. Albright, K. J. Bowers, W. Daughton, and H. A. Rose , "*Saturation of Backward Stimulated Scattering of a Laser Beam in the Kinetic Regime*", Phys. Rev. Lett. **99**, 265004 (2007). doi: doi10.1103/PhysRevLett.99.265004.

[136] L. Yin, B. J. Albright, K. J. Bowers, W. Daughton, and H. A. Rose , "*Saturation of backward stimulated scattering of laser in kinetic regime: Wavefront bowing, trapped particle modulational instability, and trapped particle self-focusing of plasma waves*", Physics of Plasmas **15**, 013109 (2008). doi: doi10.1063/1.2825663.

[137] D. T. Michel, S. Depierreux, C. Stenz, V. Tassin, and C. Labaune , "*Exploring the Saturation Levels of Stimulated Raman Scattering in the Absolute Regime*", Phys. Rev. Lett. **104**, 255001 (2010). doi: doi10.1103/PhysRevLett.104.255001.

[138] S. Depierreux, C. Labaune, J. Fuchs, D. Pesme, V. T. Tikhonchuk, and H. A. Baldis, "*Langmuir Decay Instability Cascade in Laser-Plasma Experiments*", Phys. Rev. Lett. **89**, 045001 (2002). doi: doi10.1103/PhysRevLett.89.045001.

[139] J. L. Kline, D. S. Montgomery, B. Bezzerides, J. A. Cobble, D. F. DuBois, R. P. Johnson, H. A. Rose, L. Yin, and H. X. Vu, "*Observation of a Transition from Fluid to Kinetic Nonlinearities for Langmuir Waves Driven by Stimulated Raman Backscatter*", Phys. Rev. Lett. 94, 175003 (2005). doi: doi10.1103/PhysRevLett.94.175003.

[140] D. A. Russell, D. F. DuBois and Harvey A. Rose L. Yin, and H. X. Vu, "*Nonlinear saturation of stimulated Raman scattering in laser hot spots* ", Physics of Plasmas **6**, 1294 (1999). doi: doi10.1063/1.873371.

[141] J. F. Drake and Y. C. Lee. "*Temporally growing Raman backscattering instabilities in an inhomogeneous plasma*", Physical Review Letters **31**, 1197 (1973). doi: doi10.1103/PhysRevLett.31.1197.

[142] Y. C. Lee and P. K. Kaw. "*Temporal electrostatic instabilities in inhomogeneous plasmas*", Physical Review Letters **32**, 135 (1974). doi: doi10.1103/PhysRevLett.32.135.

[143] C. S. Liu. "Parametric instabilities in an inhomogeneous unmagnetized plasma", Advances in Plasma Physics. Ed. by A. Simon and W. B. Thompson. John Wiley and Sons, Inc. (1976).